Jonas Augusto Kunzler

Development and Analysis of Mathematical Methods for Estimating Statistical Parameters in Sensor Array-based Systems

Goiânia

2020

sistema de ufg

PRPG

UFG

TERMO DE CIÊNCIA E DE AUTORIZAÇÃO PARA DISPONIBILIZAR VERSÕES ELETRÔNICAS DE TESES E DISSERTAÇÕES NA BIBLIOTECA DIGITAL DA UFG

Na qualidade de titular dos direitos de autor, autorizo a Universidade Federal de Goiás (UFG) a disponibilizar, gratuitamente, por meio da Biblioteca Digital de Teses e Dissertações (BDTD/UFG), regulamentada pela Resolução CEPEC nº 832/2007, sem ressarcimento dos direitos autorais, de acordo com a Lei nº 9610/98, o documento conforme permissões assinaladas abaixo, para fins de leitura, impressão e/ou *download*, a título de divulgação da produção científica brasileira, a partir desta data.

O conteúdo das dissertações e teses disponibilizados são de responsabilidade exclusiva dos autores. Ao encaminhar(em) o produto final, o autor e o orientador firmam o compromisso de que ele não contém nenhuma violação de quaisquer direitos autorais ou outro direito de terceiros.

1. Identificação do material bibliográfico: ☐ **Dissertação** ☒ **Tese**

2. Identificação da Tese ou Dissertação:

Nome completo do autor: Jonas Augusto Kunzler

Título do trabalho: Development and Analyses of Mathematical Methods for Estimating Statistical Parameters in Sensor Array-based Systems

3. Informações de acesso ao documento:

Concorda com a liberação total do documento ☐ SIM ☒ NÃO[1]

Independente da concordância com a disponibilização eletrônica, é imprescindível o envio do(s) arquivo(s) em formato digital PDF da tese ou dissertação.

Jonas Augusto Kunzler

Assinatura do(a) autor(a)[2]

Ciente e de acordo:

Assinatura do(a) orientador(a)[2]

Data: 06 / 03 / 2020

---

[1] Neste caso o documento será embargado por até um ano a partir da data de defesa. O documento não será disponibilizado durante o período de embargo.

Casos de embargo:

- Solicitação de registro de patente;
- Submissão de artigo em revista científica;
- Publicação como capítulo de livro;
- Publicação da dissertação/tese em livro.

[2] As assinaturas devem ser originais sendo assinadas no próprio documento, imagens coladas não serão aceitas.

sibi
sistema de bibliotecas ufg

UFG

TERMO DE CIÊNCIA E DE AUTORIZAÇÃO PARA DISPONIBILIZAR AS TESES E DISSERTAÇÕES ELETRÔNICAS NA BIBLIOTECA DIGITAL DA UFG

Na qualidade de titular dos direitos de autor, autorizo a Universidade Federal de Goiás (UFG) a disponibilizar, gratuitamente, por meio da Biblioteca Digital de Teses e Dissertações (BDTD/UFG), regulamentada pela Resolução CEPEC nº 832/2007, sem ressarcimento dos direitos autorais, de acordo com a Lei nº 9610/98, o documento conforme permissões assinaladas abaixo, para fins de leitura, impressão e/ou *download*, a título de divulgação da produção científica brasileira, a partir desta data.

1. Identificação do material bibliográfico: **[ ] Dissertação** **[X] Tese**

2. Identificação da Tese ou Dissertação

Nome completo do autor: Jonas Augusto Kunzler

Título do trabalho: Development and Analysis of Mathematical Methods for Estimating Statistical Parameters in Sensor Array-based Systems

3. Informações de acesso ao documento:

Concorda com a liberação total do documento [X] SIM [ ] NÃO[1]

Havendo concordância com a disponibilização eletrônica, torna-se imprescindível o envio do(s) arquivo(s) em formato digital PDF da tese ou dissertação.

Jonas Augusto Kunzler
Assinatura do (a) autor (a) [2]

Data: 29 / 12 / 2022

---

[1] Neste caso o documento será embargado por até um ano a partir da data de defesa. A extensão deste prazo suscita justificativa junto à coordenação do curso. Os dados do documento não serão disponibilizados durante o período de embargo.

[2] A assinatura deve ser escaneada.

Jonas Augusto Kunzler

Development and Analysis of Mathematical Methods for Estimating Statistical Parameters in Sensor Array-based Systems

A thesis submitted to the Doctoral Program in Electrical and Computer Engineering of Escola de Engenharia Elétrica, Mecânica e de Computação (EMC), Universidade Federal de Goiás - UFG, in partial fulfillment of the requirements for the degree of Doctor of Science in Computer Engineering.

Universidade Federal de Goiás (UFG)

Escola de Engenharia Elétrica, Mecânica e de Computação (EMC)

Programa de Pós-Graduação em Engenharia Elétrica e de Computação

Supervisor: Prof. Dr. Rodrigo Pinto Lemos
Co-supervisor: Dr.-Ing. Oliver Sander

Goiânia
2020

Identification sheet of the work prepared by the author, through the Program for Automatic Generation of the UFG Library System.

Kunzler, Jonas Augusto

Development and Analysis of Mathematical Methods for Estimating Statistical Parameters in Sensor Array-based Systems/ Jonas Augusto Kunzler. – Goiânia, 2020-

214 p. : il. (color).

Supervisor: Prof. Dr. Rodrigo Pinto Lemos; Co-supervisor: Dr.-Ing. Oliver Sander

Thesis (Doctorate) – Universidade Federal de Goiás (UFG)
Escola de Engenharia Elétrica, Mecânica e de Computação (EMC)
Programa de Pós-Graduação em Engenharia Elétrica e de Computação, Goiânia, 2020.

1. doa estimation. 2. eigenvalue decomposition. 3. matrix norms. 4. signal processing. 5. microwave squid multiplexer. 6. metallic magnetic calorimeters. I. Supervisor: Prof. Dr. Rodrigo Pinto Lemos. II. Federal University of Goiás (UFG). III. School of Electrical, Mechanical and Computer Engineering (EMC). IV. Doctorate Thesis

CDU 621.3

UNIVERSIDADE FEDERAL DE GOIÁS - UFG
SCHOOL OF ELECTRICAL, MECHANICAL AND COMPUTER ENGINEERING

THESIS DEFENSE REPORT

Report No. 01/2020 of the Thesis Defense session of **Jonas Augusto Kunzler**, which awarded him the title of **Doctor of Electrical and Computer Engineering**, in the field of **Electrical Engineering**.

On **February seventh, two thousand and twenty**, at **9:00 am**, in the **Caryocar brasiliensis room** of the School of Electrical, Mechanical and Computer Engineering, **Jonas Augusto Kunzler** performed the public defense of his thesis entitled "**Development and Analysis of Mathematical Methods for Estimating Statistical Parameters in Sensor Array-based Systems**". The works were opened by the chair and Advisor, Professor **Rodrigo Pinto Lemos, D.Sc. (EMC / UFG)** and, after the candidate completed the presentation, the following members of the Examining Committee inquired him about his work: Professor **Oliver Sander, Ph.D. (IPE/ KIT)**, Co-advisor, Professor **Claudio Afonso Fleury, D.Sc. (DAA IV/IFG)**, external member, **Robson Domingos Vieira, D.Sc. (FAPEG)**, external member, Professor **Marcelo Stehling de Castro, D.Sc. (EMC/UFG)**, external member, Professor **Mário José de Souza, D.Sc. (IME/UFG)**, external member, Professor **Flávio Henrique Teles Vieira, D.Sc. (EMC/UFG)**, internal member. During the inquiry the committee members did not suggest changing the title of the Thesis. In the following, the Examining Committee met in secret session to finalize the Thesis judgment and decided to **approve** the candidate. After the results were proclaimed by the chair **Professor Rodrigo Pinto Lemos, D.Sc.**, the session was adjourned and these report was drawn up and signed by the Examining Committee members, on **February seventh, two thousand and twenty**.

Rodrigo Pinto Lemos
Rodrigo Pinto Lemos – Advisor (EMC/UFG)

Oliver Sander – Co-avisor (IPE/KIT, Germany)

Fleury.
Claudio Afonso Fleury – (DAA IV/IFG)

Robson Domingos Vieira – (FAPEG)

Marcelo Stehling de Castro
Marcelo Stehling de Castro – (EMC/UFG)

Mário José de Souza
Mário José de Souza – (IME/UFG)

FH Vieira
Flávio Henrique Teles Vieira – (EMC/UFG)

Jonas Augusto Kunzler
candidate

Este trabalho é dedicado às crianças adultas que,
quando pequenas, sonharam em se tornar cientistas.
I dedicate this work to those adults who
dreamed of becoming scientist in the youth.

Acknowledgements

I thank God for life and for supporting me in every situation. I would like to express my gratitude for my wife Jordana, who supports me and makes life more beautiful and joyful. To my parents Paulo and Neli, and my parents-in-law João Bosco and Enia my deepest thanks for accompanying me in this journey.

I want to thank especially my advisor Prof. Dr. Rodrigo Pinto Lemos, who believed in my work and provided the opportunity to continuously grow in knowledge and as a person. I also want to thank my colleagues at *Escola de Engenharia Elétrica, Mecânica e de Computação* in *Universidade Federal de Goiás* for being kind and for the atmosphere of harmony created by everyone.

The period in Germany was of great value for my development as a researcher and as a person. I would like to thank my advisor abroad Dr.-Ing. Oliver Sander and my colleague Nick Karcher for their warming reception and for allowing me to learn and to be a part of the team in *Karlsruher Institut für Technologie*. I met great people during the internship and I am very glad I had such an exquisite experience.

Lastly, but not least, I would like to thank CAPES for granting me the scholarship funding through the PDSE program, and to ERASMUS for granting me the scholarship funding through the BEMUNDUS program. I had the privilege of spending 18 months in Europe thanks to the citizens of Brazil and the European Union, thus I am very grateful for the opportunity, and I am looking forward to work for my country and to contribute with the scientific progress.

Um inteiro se torna real quando diante das adversidades, as quais intentam inverter a sua função que está definida no domínio do conjunto universo, encontra sua identidade e se torna a imagem conforme a semelhança do que é verdadeiro. Diferenciado e íntegro. Seu comportamento se torna um modelo, o qual apresenta a menor probabilidade de erro. Se torna a referência. Seus valores são próprios e singulares, e seus vetores apontam na direção e sentido correto, com intensidade bem proporcionada. Não oscila e não apresenta sombra de incerteza, mas segue a trajetória do equilíbrio quando seu tempo tende ao infinito.

Abstract

The direction of arrival estimation and the estimation of energy pulses in x-ray spectroscopy are based on the same parameter, the phase shift of measured signals relative to a reference. This work demonstrates the possibility of applying well-established direction-of-arrival estimation techniques to the problem of spectroscopy. The two themes are correlated in an introductory part and, then, they are discussed separately giving emphasis on the intrinsic characteristics of each topic. In the problem of direction of arrival estimation, the signal model for the sensor array is presented as well as some maximum likelihood-based methods. It consists of a uniform linear array of half-wavelength spaced sensors, which produce phase-shifted copies of a reference signal in each circuit. The time lag is closely related to the direction of arrival of a planar wave. The spatial domain shows complex exponentials whose frequencies should be estimated. The main estimation methods are MODE, MODEX, modified MODEX, and SEAD. They are discussed along this work, but special attention lies on the SEAD method, which is based on the eigenvalue decomposition of the modified spatial correlation matrix. The difference between the two largest eigenvalues constitute an interesting measure, it provides an initial guess for the estimates by presenting prominent peaks near the true direction of arrival positions. By sweeping the entire angular interval with a test angle and calculating the eigenvalues the differential spectrum can be traced. A mathematical analysis of the differential spectrum has shown that it is basically a matrix norm calculation, leading to the definition of the total differential spectrum. Therefore, a matrix-based approach is proposed to estimate the arriving angles. This procedure allows to express the angular spectrum in terms of the true angles, a test angle, the correlation between the signals, the number of sources, and the number of sensors. This mathematical formulation is general and demonstrates the principles of operation of the SEAD method, it is one of the main contributions of the present work. The use of the norm-based approach avoided the need of performing the eigenvalue-decomposition, consequently reducing the overall runtime while enhancing the performance for widely-spaced sources. SEAD method based on matrix norms outperformed the MODE method and its derivatives regarding the root mean square error. However, for a number of sources less than 4, the execution time of SEAD-based method is more time consuming than MODEX and modified MODEX. The estimation of energy pulses in x-ray spectroscopy is not a new topic, however, the microwave SQUID multiplexer is a relatively new approach and it is currently a thriving research subject. The objective of the system is to simultaneously read out the energy of energetic particles that fall into detectors for a large amount of resonators. The detectors may be a transition edge sensor or a metallic magnetic calorimeter. Metallic calorimeters are paramagnetic sensors that are situated in a weak magnetic field. They translate temperature variation into magnetic flux variation. To readout the magnetic flux variations due to charged particles, a superconducting quantum interference device is used. The SQUID is an extremely sensitive interferometer and behaves as a variable inductor. The SQUID is coupled to a termination of a superconducting transmission line and produces changes in the resonant frequency of the circuit. Therefore, particle energy can be readout electronically by demodulating a radio frequency that travels through the resonator. Modulation occurs at the amplitude and phase of the complex carrier. After the discard of intermediate frequencies, mixing down the carrier, a complex low frequency carrier is obtained. The signal can be recovered by demodulating the carrier phase. Due to the similarity with the direction of arrival estimation problem, it is proposed a sensor array-based approach, which profits from the spatial correlation matrix decomposition into its eigenvalues. In this way, an analogy is established between the two problems. For obtaining the correlation matrix, a virtual reference vector is considered, whose phase does not depend on the incidence of particles, i.e. when the system is idle. This reference vector is compared by means of the correlation function with the received data sample by sample. A convenient data vector length is defined, so that a snapshot matrix with two sensors is obtained and, consequently, a 2×2 dimension correlation matrix is set. The eigenvalue decomposition can be explicitly solved as a function of the matrix entries, such that a general formulation for the method is presented. In addition, simplifications were imposed that allows its implementation on dedicated hardware. The estimation error is analyzed for the proposed method and the maximum likelihood method. The eigenvalue-based method presented greater robustness against the effects of noise. In some specific cases, in which the maximum likelihood method was not able to properly estimate the energy pulse, the proposed method proved to be quite efficient.

Keywords: doa estimation. eigenvalue decomposition. matrix norms. signal processing. microwave squid multiplexer. metallic magnetic calorimeters.

Resumo

A estimação da direção de chegada e a estimação de pulsos de energia na espectroscopia de raios-x são baseadas no mesmo parâmetro, o deslocamento de fase de sinais em relação a uma referência. Neste trabalho é demonstrada a possibilidade de aplicar técnicas já estabelecidas para a estimação da direção de chegada ao problema de espectroscopia. Os dois temas são correlacionados em uma parte introdutória e em seguida eles são discutidos separadamente dando ênfase nas características intrínsecas de cada um. No problema de estimação da direção de chegada, inicialmente apresenta-se o modelo de sinal para o arranjo de sensores e alguns métodos baseados no estimador de máxima verossimilhança. Considerando um arranjo de sensores linearmente distribuídos e com espaçamento uniforme entre os elementos, os sinais induzidos em cada circuito serão cópias defasadas de um sinal de referência. O defasamento está intimamente relacionado com a direção de chegada. No domínio espacial, as direções de chegada representam frequências de funções exponenciais complexas, as quais deverão ser estimadas. Os principais métodos de estimação são o MODE, MODEX, o MODEX modificado, e o SEAD. Atenção especial é dispensada ao método SEAD que é baseado na decomposição em autovalores da matriz de correlação espacial modificada. A diferença entre os dois maiores autovalores gera uma curva com picos proeminentes indicando as direções de chegada de ondas planas. A esta curva dá-se o nome de espectro diferencial. Uma análise matemática do espectro diferencial, denominada de espectro diferencial total, é desenvolvida e demonstra-se que a norma matricial induzida pela norma-2 vetorial é a principal componente do cálculo. Portanto, propõe-se uma abordagem baseada em normas matriciais para a estimação das direções de chegada. Uma descrição matemática geral foi desenvolvida, a qual explicita a relação entre os verdadeiros ângulos de chegada e um ângulo sintético usado para varrer todo o espectro, a correlação entre as fontes, o número de fontes e o número de sensores. Demonstra-se que a diferença entre os ângulos determina a amplitude do pico gerado. A formulação matemática do espectro angular constitui em uma das principais contribuições deste trabalho, porém, outros aprimoramentos foram alcançados através da proposta de uso de normas matriciais. A utilização da abordagem baseada em normas evita a necessidade de realização da decomposição da matriz em autovalores e, consequentemente, o tempo de execução total do método é reduzido e o erro quadrático médio é reduzido para situação de fontes afastadas. Comparando as propostas com os métodos estabelecidos na literatura, a abordagem de normas supera o método MODE e seus derivados com relação ao erro quadrático médio. Porém, com relação ao tempo de execução os métodos baseados no SEAD são mais custosos computacionalmente para um número de fontes menor do que 4. A estimação de pulsos de energia na espectroscopia de raios-x não é um tema novo, porém, o multiplexador SQUID de micro-ondas é uma abordagem relativamente nova e, atualmente, ele consiste em um tema de pesquisa pujante. O objetivo do sistema é estimar a energia de partículas energéticas que incidem em detectores, os quais podem ser do tipo *transition edge sensor* ou *metallic magnetic calorimeters*. Os calorímetros metálicos são sensores paramagnéticos que estão situados em um campo magnético fraco, eles traduzem variação de temperatura em variação de fluxo magnético. Para realizar a leitura das variação de fluxo magnético decorrente da incidência de partículas emprega-se um componente supercondutor denominado de *superconducting quantum interference device* (SQUID). O SQUID é um interferômetro de extrema sensibilidade e se comporta como um indutor variável. O SQUID é acoplado a uma terminação de uma linha de transmissão supercondutora e produz alterações na frequência de ressonância do circuito. Portanto, a energia de partículas pode ser lida eletronicamente através da demodulação de uma onda de rádio que percorre o ressonador. A modulação ocorre na amplitude e fase de uma portadora complexa. Após a exclusão de frequências intermediárias, resultado do processo de mixagem da portadora, obtem-se uma portadora complexa de frequência baixa sobre a qual métodos de estimação de fase são aplicados. Pela semelhança com o problema de estimação da direção de chegada, propõe-se uma abordagem baseada em arranjo de sensores e decomposição da matriz de correlação espacial em autovalores. Desta forma, estabelece-se uma analogia entre os dois problemas. Para a obtenção da matriz de correlação, considera-se a existência de um vetor de referência cuja fase não depende da incidência de partículas, i.e., quando o sistema está em repouso. Este vetor de referência é comparado por meio da função de correlação com os dados que são recebidos a cada instante. Define-se um comprimento do vetor de dados que seja conveniente e, desta forma, obtem-se uma matriz de *snapshots* com dois sensores e uma matriz de correlação de dimensões 2×2. A decomposição em autovalores pode ser resolvida explicitamente em função das entradas da matriz, de tal maneira, que uma formulação geral para o método é apresentada. Além disso, simplificações podem ser impostas com o objetivo de implementação em hardware dedicado. O erro de estimação é analisado para o método proposto e o método de máxima verossimilhança. O método de autovalores apresentou maior robustez ao ruído e em algumas circunstâncias consegue resolver o problema de estimação sem artifícios externos, algo que não ocorre para o método de máxima verossimilhança.

Palavras-chave: estimação doa. decomposição em autovalores. normas matriciais. processamento de sinais. multiplexador squid de micro-ondas. calorímetros metálicos magnéticos.

Zusammenfassung

Die Schätzung der Ankunftsrichtung und die Energieimpulsschätzung in der Röntgenspektroskopie basieren auf demselben Parameter, der Phasenverschiebung von Signalen relativ zu einer Referenz. Diese Arbeit demonstriert die Möglichkeit, bereits etablierte Techniken zur Abschätzung der Ankunftsrichtung auf das Spektroskopie Problem anzuwenden. Die beiden Themen werden in einem einleitenden Teil miteinander korreliert und dann separat diskutiert, wobei die spezifischen Merkmale der einzelnen Themen hervorgehoben werden. In dem Problem der Abschätzung der Ankunftsrichtung präsentieren wir zunächst das Signalmodell für die Sensoranordnung und einige Methoden, die auf dem Maximum-Likelihood-Schätzer basieren. Betrachtet man eine Anordnung linear verteilter Sensoren mit gleichmäßigem Abstand zwischen den Elementen, so sind die induzierten Signale in jeder Schaltung Kopien eines Referenzsignals mit Verzögerung. Die Verzögerung ist eng mit der Ankunftsrichtung verbunden. In der räumlichen Domäne stellen Ankunftsrichtungen Frequenzen komplexer Exponentialfunktionen dar, die geschätzt werden sollten. Die wichtigsten Schätzmethoden sind MODE, MODEX, Modifiziert MODEX und SEAD. Besonderes Augenmerk wird auf die SEAD-Methode gelegt, die auf der Eigenwertzerlegung der modifizierten räumlichen Korrelationsmatrix basiert. Die Differenz zwischen den beiden größten Eigenwerten erzeugt eine Kurve mit markanten Spitzenwert, die die Ankunftsrichtungen flacher Wellen angeben. Diese Kurve wird als Differenzspektrum bezeichnet. Eine mathematische Analyse des Differentialspektrums, das als Gesamtdifferentialspektrum bezeichnet wird, wird entwickelt und es wird gezeigt, dass die durch die euklidische Vektornorm induzierte Matrixnorm die Hauptkomponente der Berechnung ist. Daher schlagen wir einen Ansatz vor, der auf Matrixnormen für die Schätzung der Ankunftsrichtungen basiert. Es wurde eine allgemeine mathematische Beschreibung entwickelt, die die Beziehung zwischen tatsächlichen Einfallswinkeln und einem synthetischen Winkel erläutert, der zum Abtasten des gesamten Spektrums, der Korrelation zwischen Quellen, der Anzahl von Quellen und der Anzahl von Sensoren verwendet wird. Die Differenz zwischen den Winkeln wird angezeigt, um die Amplitude des erzeugten Peaks zu bestimmen. Die mathematische Formulierung des Winkelspektrums ist einer der Hauptbeiträge dieser Arbeit, aber andere Verbesserungen wurden durch die vorgeschlagene Verwendung von Matrixnormen erreicht. Die Verwendung des auf Standards basierenden Ansatzes vermeidet die Notwendigkeit, eine Matrixzerlegung in Eigenwerten durchzuführen, und folglich wird die Gesamtzeit der Ausführung der Methode reduziert und der mittlere quadratische Fehler für Situationen mit entfernten Quellen reduziert. Vergleicht man die Vorschläge mit den in der Literatur etablierten Methoden, übertrifft der Standardansatz die MODE-Methode und ihre Ableitungen in Bezug auf den mittleren quadratischen Fehler. In Bezug auf die Laufzeit sind SEAD-basierte Methoden für eine Reihe von Quellen unter 4 jedoch rechenintensiver. Die Schätzung von Energieimpulsen in der Röntgenspektroskopie ist kein neues Thema, der Mikrowellen-SQUID-Multiplexer ist jedoch ein relativ neuer Ansatz und derzeit ein florierendes Forschungsthema. Das Ziel des Systems ist es, die Energie von energetischen Partikeln zu schätzen, die in Detektoren fallen. Die Detektoren können die *transition edge sensor* oder metallische magnetische Kalorimeter sein. Metallische magnetische Kalorimeter sind energiedispersive Teilchendetektoren, deren Detektionsprinzip auf dem ersten Hauptsatz der Thermodynamik beruht. Sie sind paramagnetische Sensoren, die sich in einem schwachen Magnetfeld befinden und Temperaturschwankungen in Schwankungen der magnetische Flusses umsetzen. Um die Magnetflussvariation aufgrund des Teilcheneinfalls zu lesen, wird eine supraleitende Komponente, die als supraleitende Quanteninterferenzvorrichtung bezeichnet wird, verwendet. Das SQUID ist ein äußerst empfindliches Interferometer und verhält sich wie ein variabler Induktor. Der SQUID ist mit einem Abschluss einer supraleitenden Übertragungsleitung verbunden und erzeugt Änderungen in der Resonanzfrequenz des Schaltkreises. Daher kann die Teilchenenergie elektronisch gelesen werden, indem eine Funkwelle, die sich durch den Resonator ausbreitet, demoduliert wird. Die Modulation erfolgt an der Amplitude und Phase eines komplexen Trägers. Nach dem Ausschluss von Zwischenfrequenzen infolge des Trägermischprozesses wird ein komplexer Niederfrequenzträger erhalten, auf den Phasenschätzungsverfahren angewendet werden. Aufgrund der Ähnlichkeit mit dem Ankunftsrichtungsschätzungsproblem schlagen wir einen Ansatz vor, der auf der Sensoranordnung und der räumlichen Korrelationsmatrix in Eigenwertezerlegung basiert. Auf diese Weise wird eine Analogie zwischen den beiden Problemen hergestellt. Um die Korrelationsmatrix zu erhalten, wird angenommen, dass ein Referenzvektor existiert, dessen Phase nicht vom Einfall von Partikeln abhängt, d.h., wenn das System in Ruhe ist. Dieser Referenzvektor wird mittels der Korrelationsfunktion mit den zu jedem Zeitpunkt empfangenen Daten verglichen. Eine geeignete Datenvektorlänge wird definiert und somit eine Zwei-Sensor-Matrix (*snapshots*) und eine 2×2-Korrelationsmatrix erhalten. Die Eigenwertzerlegung kann explizit in Abhängigkeit von den Eingaben gelöst werden, so dass eine allgemeine Formulierung für die Methode vorgestellt wird. Darüber hinaus können Vereinfachungen zum Zweck der Implementierung auf dedizierter Hardware eingeführt werden. Der Schätzfehler wird für die vorgeschlagene Methode und die Maximum-Likelihood-Methode analysiert. Die Eigenwertmethode zeigte eine größere Robustheit gegenüber Rauschen und kann unter Umständen das Schätzproblem ohne externe Geräte lösen, was bei der Maximum-Likelihood-Methode nicht der Fall ist.

Schlüsselworte: Ankunftsrichtungschätzung. eigenwertzerlegung. matrixnormen. signalverarbeitung. mikrowellen-squid-multiplexer. metallische magnetische kalorimeter.

Resumen

La estimación de la dirección de llegada y la estimación del pulso de energía en la espectroscopia de rayos X se basan en el mismo parámetro, el desplazamiento de fase de las señales en relación con una referencia. Este trabajo demuestra la posibilidad de aplicar técnicas ya establecidas para la estimación de la dirección de llegada al problema de espectroscopia. Los dos temas se relacionan en una parte introductoria y luego se discuten por separado con énfasis en las características intrínsecas de cada uno. En el problema de estimación de la dirección de llegada, inicialmente presentamos el modelo de señal para la disposición del sensor y anlgunos métodos basados en el estimador de máxima verosimilitud. Considerando un conjunto de sensores distribuidos linealmente con espaciado uniforme entre los elementos, las señales inducidas en cada circuito serán copias rezagadas de una señal de referencia. El retraso está estrechamente relacionado con la dirección de llegada. En el dominio espacial, las direcciones de llegada representan frecuencias de funciones exponenciales complejas, que deben estimarse. Los principales métodos de estimación son MODE, MODEX, MODEX modificado y SEAD. Se presta especial atención al método SEAD que se basa en la descomposición del valor propio de la matriz de correlación espacial modificada. La diferencia entre los dos valores propios más grandes genera una curva con picos prominentes que indican las direcciones de llegada de las ondas planas. Esta curva se llama espectro diferencial. Se desarrolla un análisis matemático del espectro diferencial, llamado espectro diferencial total, y se muestra que la norma de la matriz inducida por el vector norma-2 es el componente principal del cálculo. Por lo tanto, proponemos un enfoque basado en reglas de matriz para la estimación de las direcciones de llegada. Se ha desarrollado una descripción matemática general que explica la relación entre los ángulos de llegada verdaderos y un ángulo sintético utilizado para escanear todo el espectro, la correlación entre las fuentes, la cantidad de fuentes y la cantidad de sensores. La diferencia entre los ángulos se muestra para determinar la amplitud del pico generado. La formulación matemática del espectro angular es una de las principales contribuciones de este trabajo, pero se lograron otras mejoras mediante el uso propuesto de reglas de matriz. El uso del enfoque basado en estándares evita la necesidad de realizar la descomposición de la matriz en valores propios y, en consecuencia, el tiempo total de ejecución del método se reduce y el error cuadrado medio se reduce para la situación de fuentes remotas. Comparando las propuestas con los métodos establecidos en la literatura, el enfoque estándar supera el método MODE y sus derivados en relación con el error cuadrático medio. Sin embargo, con respecto al tiempo de ejecución, los métodos basados en SEAD son más costosos desde el punto de vista informático para varias fuentes de menos de 4. La estimación de los pulsos de energía en la espectroscopia de rayos X no es un tema nuevo, sin embargo, el multiplexor SQUID de microondas es un enfoque relativamente nuevo y actualmente es un tema de investigación próspero. El objetivo del sistema es estimar la energía de las partículas energéticas que caen en los detectores, que pueden ser de tipo *transition edge sensor* o *metallic magnetic calorimeters.* Los calorímetros metálicos son sensores para-magnéticos que se encuentran en un campo magnético débil, traducen la variación de temperatura en variación de flujo magnético. Para leer las variaciones del flujo magnético debido a la incidencia de partículas, se utiliza un componente superconductor llamado *superconducting quantum interference device.* El SQUID es un interferómetro extremadamente sensible y se comporta como un inductor variable. El SQUID está acoplado a una terminación de una línea de transmisión superconductora y produce cambios en la frecuencia de resonancia del circuito. Por lo tanto, la energía de las partículas puede leerse electrónicamente demodulando una onda de radio que viaja a través del resonador. La modulación ocurre en la amplitud y fase de un portador complejo. Después de la exclusión de frecuencias intermedias como resultado del proceso de mezcla de portadora, se obtiene una portadora compleja de baja frecuencia sobre la cual se aplican los métodos de estimación de fase. Debido a la similitud con el problema de estimación de la dirección de llegada, proponemos un enfoque basado en la disposición del sensor y la descomposición de la matriz de correlación espacial en valores propios. De esta manera, se establece una analogía entre los dos problemas. Para obtener la matriz de correlación, se considera que existe un vector de referencia cuya fase no depende de la incidencia de partículas, es decir, cuando el sistema está en reposo. Este vector de referencia se compara mediante la función de correlación con los datos que se reciben en cada momento. Se define una longitud de vector de datos conveniente, por lo que obtiene una matriz de instantáneas con dos sensores y una matriz de correlación de dimensiones 2×2. La descomposición del valor propio se puede resolver explícitamente en función de las entradas de la matriz, de modo que se presente una formulación general para el método. Además, se pueden imponer simplificaciones con el fin de implementarlas en *hardware* dedicado. El error de estimación se analiza para el método propuesto y el método de máxima verosimilitud. El método de valores propios presentó una mayor robustez al ruido y, en algunas circunstancias, puede resolver el problema de estimación sin dispositivos externos, algo que no ocurre con el método de máxima verosimilitud.

Palabras clave: estimación doa. descomposición en autovalores. normas matriciales. procesamiento de señales. multiplexor squid de microondas. calorímetro metálico magnético.

List of Figures

List of Tables

List of abbreviations and acronyms

ADC	Analog-to-Digital Converter
CDM	Code Division Multiplexing
CE	Computational Effort
CERN	European Organization for Nuclear Research
CML	Conditional Maximum Likelihood
CRB	Cramér-Rao Bound
DAC	Digital-to-Analog Converter
DAQ	Data Acquisition
DDC	Digital Down Conversion
DOA	Direction of Arrival
DS	Differential Spectrum
DTFT	Discrete Time Fourier Transform
ECHo	Electron Capture in Holmium
EVD	Eigenvalue Decomposition
FDM	Frequency Division Multiplexing
FIR	Finite Impulse Response
FPGA	Field Programmable Gate Array
HEMT	High Electron Mobility Transistor
LHC	Large Hadron Collider
MKID	Microwave Kinetic Inductance Detectors
MLE	Maximum Likelihood Estimator
MMC	Metallic Magnetic Calorimeter
MODE	Method of Direction Estimation

MODEX	MODE with Extra Roots
MSE	Mean Square Error
RMSE	Root Mean Square Error
SDM	Spatial Division Multiplexing
SEAD	Search of Direction by Differential Spectrum
SNR	Signal-to-Noise Ratio
SQUID	Superconducting Quantum Interference Device
SVD	Singular Value Decomposition
TDM	Time Division Multiplexing
TDS	Total Differential Spectrum
TES	Transition Edge Sensor
ULA	Uniform Linear Array

List of symbols

$(\bullet)^*$	Complex transpose conjugate of scalar, vector or matrix
$\delta(n,i)$	Kronecker delta
$\mathrm{E}(\bullet)$	Statistical expectation
$\mathbf{I}$	Identity matrix
M	Number of signal sources
K	Number of sensors
N	Number of snapshots
$\mathrm{tr}(\bullet)$	Trace operator
$(\bullet)^T$	Real transpose operation of scalar, vector or matrix
r_k	Distance between a planar wave and the origin
ϕ_k	Polar angle
θ_k	Azimuth angle
θ_R	Reference vector initial phase
θ_T	Transmitted vector initial phase
ω	Angular frequency
ϑ	Wavelength relative to the angular frequency ω
τ_k	Delay between the k-th signal and the reference signal
τ_{rise}	Rise time of energetic scattering pulse
Φ_0	Quantum magnetic flux
$\hbar$	Reduced Plank constant

Contents

Part I

Overview of Problems, Employed Methods and State of the Art

1 Linking the Sensor Array Approach to X-ray Spectroscopy

1.1 Introduction and Motivation

This work focuses on the analysis and proposition of mathematical methods for digital signal processing. Two topics of great relevance are investigated: the direction of arrival (DOA) estimation and the readout of energy pulses in X-ray spectroscopy.

The concept of sensor array will be employed to establish a relationship between the two themes. Thus, the techniques that are already known in the literature for DOA estimation can be applied to the problem of X-ray spectroscopy. In this chapter, the two themes are introduced by a brief exposition of their main features. The state of the art of each problem is highlighted and some questions that remain open are posed.

1.2 Sensor Array and Applications

Sensor array is currently a widely used concept. It arises from the use of multiple transducer elements arbitrarily arranged in space in a manner that meets the design purposes. There are several possible distributions, such as uniform or nonuniform linear, circular, planar, volumetric, among others (TREES, 2002). Assuming the system is narrow-banded, the electrical signals induced in each circuit will simply be shifted copies of a properly selected reference signal. In this way, a sample vector is obtained in the array output, called snapshot. By sampling the electrical signals periodically, a data matrix with multiple snapshots can be set.

This technique provides to the systems a spatial division multiplexing (SDM) capability, which allows the direction-of-propagation measurement of incoming wavefronts. However, it is not restricted to DOA estimation. There are several applications in a variety of areas of human knowledge, among them are radars, astronomy, sonar, communications, seismology, and medical treatment and diagnosis (TREES, 2002).

The digital signal processing play an important role in such systems. The estimation of parameters is based on the reconstruction of intrinsic signal information, such as DOA parameters, carrier wave propagation velocity, temporal and spectral signal components such as amplitude, phase and frequency (TREES, 2002; PILLAI, 1989). In order to do that, it is assumed that the number of incident wavefronts, the array geometry and the statistical signal and noise models are known. The parameter estimation is hampered by the decrease in signal-to-noise ratio (SNR), spacing between sources, and the amount of available snapshots (ALVES, 2004).

Although frequency estimation goes back to the early days of parameter estimation, where a sensitive element alone was responsible for the signal transduction, there is a direct correspondence between DOA estimation and signal frequency estimation. To this relationship is attributed the benefits (ALVES, 2004):

- expand the possibilities of application of DOA and frequency estimation techniques;
- use the previously developed theory in order to solve new arising problems with the aid of relationships that are already established.

Consequently, both approaches share the same limitations:

- the estimate resolution is limited by the signal observation time, the number of stored samples.
- noise power can change the characteristics of the signals and lead to an erroneous decision.

To obtain DOA estimates, several mathematical and statistical techniques are used, such as Fourier transform, subspace decomposition, Maximum Likelihood (ML) criterion, hypothesis testing, and many others. It is important to classify the available methods as spectral or parametric methods. Spectral methods are characterized by the assignment of a function whose maxima represent DOA estimates. These methods have as their main tool the Fourier transform. The greatest limitation is the frequency resolution, which is a function of the number of samples available. The parametric methods assume a statistical model for the signals, resulting in a certain structure for the autocorrelation matrix of the array output signals. In these methods, the estimate is obtained through a finite set of model parameters. They are generally more efficient and robust to noise effects, on the other hand, the computational effort is usually higher. Currently the methods that perform a maximum likelihood function reparametrization present the best results in terms of noise robustness, i.e., the variance of the estimates. This present work explore the parametric methods, which take advantage of the characteristics of the correlation matrix to estimate the parameters of interest.

1.3 DOA Estimation Problem and Signal Model

This section deals with the mathematical formulation of the DOA problem from a broad perspective, considering the sensor array with a generic geometric distribution. The number of sources M are assumed to be known and they are spread in the space. It is also considered the existence of noise and interfering sources in some region. The number of sources M should be less than the number of sensors K, i.e., $M < K$.

The wave source can be acoustic, electromagnetic, tectonic or others and the types of sensors can be microphones, dipole antennas, accelerometers or seismographs, etc. (TREES, 2002).

The array is used to filter the signals in the time-space field by surveying their spatial characteristics. Filtering is expressed in terms of angle or wavelength. In the frequency domain this filtering represents the emphasis or rejection of the signals according to their spatial dependence. Complex weights are used to combine the signals in the various array circuits and to provide the desired response.

Firstly, a coordinate system should be established to enable sensor position in space. The spherical coordinate system is convenient in this situation. The relationship between cartesian and spherical coordinates is given by (TREES, 2002):

$$x = r\sin(\phi)\cos(\theta); \tag{1.1}$$

$$y = r\sin(\phi)\sin(\theta); \tag{1.2}$$

$$z = r\cos(\phi); \tag{1.3}$$

and

$$r = \sqrt{x^2 + y^2 + z^2}, \quad r \geq 0; \tag{1.4}$$

$$\phi = \arccos\left(\frac{z}{r}\right), \quad 0 \leq \phi \leq \pi; \tag{1.5}$$

$$\theta = \arctan\left(\frac{y}{x}\right); \quad 0 \leq \theta \leq 2\pi \tag{1.6}$$

where, $r \in \mathbb{R}^+$ is the distance between the surface of a sphere and its center, which is located at the origin of the coordinate system, $\phi \in [0, \pi]$ is the angle formed from the z-axis towards the xy plane and $\theta \in [0, 2\pi]$ is the angle formed between the x-axis and any vector of the xy plane, which are respectively called **radius**, **polar angle** and **azimuthal angle**. A generic point of the space $\mathbf{P}(x,\, y,\, z)$ is associated with a vector that is given by $\mathbf{p} = (x,\, y,\, z) = (r\sin(\phi)\cos(\theta),\, r\sin(\phi)\sin(\theta),\, r\cos(\phi))$.

Figure 1 shows a diagram of a generic arrangement in three-dimensional space containing two sensors. In this example, there is a flat wavefront generated by a generic source m in the far field relative to the sensors. It propagates in a direction defined by the angles, ϕ_m and θ_m, which are assigned by the two points in space: the origin of the coordinate system and the source location. This sets a unitary vector $\mathbf{a}_m$, which is normal to the defined plan and given by:

$$\mathbf{a}_m = \begin{bmatrix} -\sin(\phi_m)\cos(\theta_m) \\ -\sin(\phi_m)\sin(\theta_m) \\ -\cos(\phi_m) \end{bmatrix}, \tag{1.7}$$

the negative sign indicates that $\mathbf{a}_m$ has the opposite direction relative to the coordinate system. The figure was obtained with the help of Geogebra® software (www.geogebra.org).

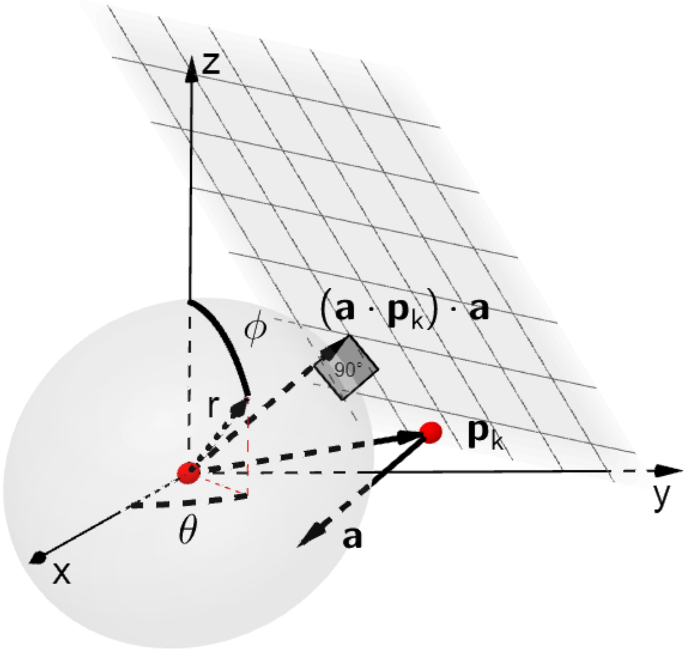

Figure 1 – Representation of a sensor array in three-dimensional space. Two sensors are presented, one at the origin and the other at the point $\mathbf{P}_k$, which is hit by the flat wave at a given instant. Source: Author.

To a sensor k located at any point in space there will be a vector $\mathbf{p}_k$ that will link it to the origin of the coordinate system by determining a distance $r_k = |\mathbf{p}_k|$. The scalar $d_{k,m}(\mathbf{O},\psi)$ represents the traveled distance by the m-th source wavefront, represented by the ψ plane, from the moment it impinges on the sensor positioned at the point $\mathbf{P}_k$ until it reaches the origin, on $\mathbf{O}(0,0,0)$, and it is given as:

$$d_{k,m}(\mathbf{O},\psi) = r_k\{\sin(\phi_m)\sin(\phi_k)\cos(\theta_m - \theta_k) + \cos(\phi_m)\cos(\phi_k)\}. \tag{1.8}$$

It is assumed that the array consists of isotropic sensors positioned at $\mathbf{p}$. Parsing the array response to an external signal yields a function vector $\mathbf{f}(t,\mathbf{p})$ with temporal and spatial dependence. The sensors sample the signal spatially at the positions $\mathbf{p}_k$, $k = [0,1,\ldots,K-1]$, $K \in \mathbb{N}$, such that $\mathbf{f}(t,\mathbf{p})$ is denoted by:

$$\mathbf{f}(t,\mathbf{p}) = \begin{bmatrix} f(t,\mathbf{p}_0) \\ f(t,\mathbf{p}_1) \\ \vdots \\ f(t,\mathbf{p}_{K-1}) \end{bmatrix}. \tag{1.9}$$

Each circuit works as a time-invariant linear system consisting of a finite impulse response filter (FIR) with impulse response $h_k(\tau)$, where τ is the time lag, and then the processed signals are summed up to obtain an output $y(t)$. The observation time is assumed to last long enough. Therefore, one can express $y(t)$ as a convolution integral in vector notation as:

$$y(t) = \int_{-\infty}^{\infty} \mathbf{h}^T(t-\tau)\mathbf{f}(\tau, \mathbf{p}_k)d\tau, \tag{1.10}$$

where

$$\mathbf{h}(t) = \begin{bmatrix} h_0(t) \\ h_1(t) \\ \vdots \\ h_{K-1}(t) \end{bmatrix}. \tag{1.11}$$

In the time domain, the wave travels with frequency ω given in radians, so that the functions $\mathbf{f}(t, \mathbf{p}_k)$ can be written as shifted-phase signals relative to the reference signal on the origin of the coordinate system (TREES, 2002):

$$\mathbf{f}(t, \mathbf{p}) = \begin{bmatrix} f(t-\tau_0) \\ f(t-\tau_1) \\ \vdots \\ f(t-\tau_{K-1}) \end{bmatrix}. \tag{1.12}$$

with τ_k given by:

$$\tau_k = \frac{\mathbf{a}_m^T \mathbf{p}_k}{c}, \tag{1.13}$$

where c is the speed of light in vacuum.

The signal lag for each sensor can be given as:

$$\begin{aligned} \tau_k &= -\frac{1}{c}\left[\sin(\phi)\cos(\theta)p_{x_k} + \sin(\phi)\sin(\theta)p_{y_k} + \cos(\phi)p_{z_k}\right] \\ &= -\frac{d_{k,m}}{c}. \end{aligned} \tag{1.14}$$

Considering the baseband signal in 1.12, the k-th component of the Fourier transform $\mathbf{F}(\omega)$ is:

$$F_k(\omega) = \int_{-\infty}^{\infty} f(t-\tau_k)\exp(-j\omega t)\mathrm{d}t = \exp(-j\omega\tau_k)F(\omega), \tag{1.15}$$

where

$$\omega\tau_k = \frac{\omega}{c}\mathbf{a}_m^T\mathbf{p}_k, \tag{1.16}$$

and $F(\omega)$ is the Fourier transform from the original signal.

Then, one can define the **wavenumber**, $\boldsymbol{\kappa}$, as:

$$\boldsymbol{\kappa} = \frac{\omega}{c}\mathbf{a} = \frac{2\pi}{\vartheta}\mathbf{a}, \tag{1.17}$$

where ϑ is the wavelength relative to the frequency ω.

From 1.13 and 1.17, the *array manifold vector* containing all the spatial characteristics of the array is defined by:

$$\mathbf{v}(\boldsymbol{\kappa}) = \begin{bmatrix} \exp\left(-j\boldsymbol{\kappa}^T\mathbf{p}_0\right) \\ \exp\left(-j\boldsymbol{\kappa}^T\mathbf{p}_1\right) \\ \vdots \\ \exp\left(-j\boldsymbol{\kappa}^T\mathbf{p}_{K-1}\right) \end{bmatrix}, \tag{1.18}$$

where $\omega\tau_k = \boldsymbol{\kappa}^T\mathbf{p}_k$.

It follows then that the received signal frequency components, $\mathbf{F}(\omega)$, is directly related to the original signal spectrum, $F(\omega)$, and expressed as (TREES, 2002):

$$\mathbf{F}(\omega) = F(\omega)\mathbf{v}(\boldsymbol{\kappa}). \tag{1.19}$$

This approach profits from the phase shift of the received signals at each sensor in order to align them in time and then sum them to recover a stronger version of the original signal. This processor is known as *delay-and-sum beamformer* (TREES, 2002).

Some simplifications can be applied to the array geometry and signal properties. The specific case that considers the sensors arranged linearly in the xy plane with uniform distance will be addressed in Part II.

The organization of Part II of the work is as follows: Chapter 2 discusses the DOA estimation in the xy plane and establishes the simplifications relative to the general model. The main estimation methods are briefly discussed, for instance, method of direction estimation (MODE), MODE with extra roots (MODEX) and an improved version of the search of direction by differential spectrum (SEAD). Chapter 3 brings an alternative approach to the SEAD method, which uses matrix norms for tracing an angular spectrum, and its mathematical fundamentals is described in detail. The SEAD method based on the differential spectrum is shown to be a particular case of the matrix norms approach. Finally, in Chapter 4 the simulation results are discussed in terms of the performance evaluation criteria of DOA estimation methods.

1.3.1 Evaluation Criteria for DOA Estimation Methods

This section describes the main performance indexes used in the simulations of DOA estimation methods. This evaluation takes into account the comparison between the indexes obtained by the methods and the theoretical limits of parameter estimation.

The Cramér-Rao Bound (CRB) is the main theoretical reference in parameter estimation and it represents the minimum theoretical value of the estimates variance by a unbiased estimator. This value is calculated as (ALVES, 2004), where the parameters are the number of samples, number of sensors, number of signals, spacing between frequencies, SNR, etc. Due to the frequency and DOA equivalence, it is necessary to calculate the CRB for only one of these parameters.

The estimation variance curve or simply the performance curve is one of the most common ways to perform the evaluation or comparison between estimation methods. One can also assess the performance surface by considering two parameters at the same time. For example, it can be obtained as a function of the SNR and the distance between the sources on DOA estimation. Each point on this surface (or curve) is obtained from the root mean square error (RMSE) over the set of estimates with respect to the true parameters. In this work, the performance surfaces of the estimation methods are generated as a function of the SNR and the difference between DOA angles. The RMSE for the angles θ_m and ϕ_m is defined as:

$$\mathrm{RMSE}(\hat{\theta}_m,\hat{\phi}_m) \equiv \sqrt{\mathrm{E}\left[(\hat{\theta}_{rm}-\theta_m)^2+(\hat{\phi}_{rm}-\phi_m)^2\right]} \qquad [\mathrm{rad}]\,, \tag{1.20}$$

where $\hat{\theta}_{rm}$ is the r-th estimate of θ_m and $\hat{\phi}_{rm}$ is the r-th estimate of ϕ_m.

The **asymptotic efficiency** of the estimator, defined by the performance as a function of the number of snapshots, is also an important metric. A desired property for an estimator is that the variance continuously decreases as the number of snapshots tends to infinity. The estimator that meets this property is said to be consistent (ALVES, 2004).

Considering high SNR values and in case of estimation methods that are asymptotically efficient, the performance surfaces tend to overlap the CRB surface. However, as the SNR decreases the **threshold breakdown effect** is reached, which represents another important merit index for method evaluation. It is the SNR value that shows rapidly degradation of performance, hence the method fails to estimate the parameters (ALVES, 2004).

The **correlation factor** represents an important parameter because some categories of estimation methods do not perform well when signals are partially or fully correlated (coherent). Parametric methods, when applied to coherent signal estimation, have similar performances compared to those obtained if the signals are uncorrelated (ALVES, 2004).

Computational effort (CE) is another important metric, especially when one finds that the main DOA estimation methods are derived from an estimator that has significant CE, the ML criterion. CE is directly associated with the feasibility of real-time applications (ALVES, 2004).

In short, the ideal estimation method should generate unbiased estimates and have the lowest possible threshold breakdown effect. The performance curve should be as close as possible to the CRB curve for all relevant DOA situations, correlation factor, number of snapshots, etc.. Finally, the computational effort should be as small as possible, i.e., equal to or less than the current methods (ALVES, 2004).

Current estimation methods only partially meet the characteristics of an ideal estimator. It is therefore important to develop new methods or make improvements to existing methods to meet the growing demand for applications.

1.4 Microwave SQUID Multiplexer

To draw a parallel between DOA estimation and X-ray spectroscopy, this section presents the basic concepts that support the use of the microwave SQUID multiplexer.

Spectroscopy has always contributed to the understanding of nature. It provides essential stimuli for the development of new theories and frequently leads to unexpected discoveries, such as the description of new chemical elements, e.g., Helium, Cesium and Rubidium. Several detectors have been developed in the past to obtain spectral characteristics through spectroscopy. The developed systems allowed the recording of incident particle energy in the detectors, i.e. the wavelength of electromagnetic radiation (KEMPF, 2012). The list of detector types is endless and applications go through a variety of areas.

In general, the traditional detectors in use are made of semiconductor materials such as high purity silicon and germanium. The minimum energy resolution achieved by these detectors is in the order of $\Delta E_{FWHM} > 100$ eV. Although this resolution is sufficient for a wide range of applications, even better resolutions are often required. This is the case when the goal is to visualize the basic structure of an X-ray fluorescence line or to precisely establish the energy of an X-ray domain (KEMPF, 2012).

With the development of particle detectors at very low-temperature levels, it was possible to break through this energy resolution barrier. Physically, they are called microcalorimeters because they are based on the principle of calorimetry measurement. This means that the energy of an incident particle can be measured by monitoring the temperature variation of a particle absorbing element. The use of microcalorimeters in the context of cryogenics ensures a wide temperature range for system operation and, on the other hand, drastically reduces the thermal noise in the signal (KEMPF, 2012).

The detectors are operated at very low-temperatures to obtain maximum sensitivity and are widely used for this purpose: Transition-Edge Sensor (TES), Metallic Magnetic Calorimeter (MMC), Microwave Kinetic Inductance Detectors (MKID), among others (MATES, 2011). They have enabled a technical enhancement of spectrometry by increasing the estimated energy range up to 10 keV as well as an improvement in energy resolution in the 1.6 eV to 3.2 eV range (KEMPF, 2012).

The benefits of cryogenic detection are combined with the discovery of the superconductivity phenomenon. Superconducting devices are used as an intermediate amplification stage, they receive the signal from the detector/sensor assembly, amplify it and then direct the signal to an external amplifier at room temperature, such as the High Electron Mobility Transistor (HEMT). The Superconducting QUantum Interference Device (SQUID) is an example of such devices that makes this interface between the cryogenic world and the world of room temperature. There are two types: the direct current SQUID (dc-SQUID), which is driven by direct current and the radio frequency SQUID (rf-SQUID), which is operated under the alternating current regime. In the past dc-SQUID has been widely used for the amplification of particle detector signals, nowadays the rf-SQUID is gaining attention.

The rf-SQUID is currently employed in frequency division multiplexing systems. MMC detectors associated with rf-SQUIDs consists on the second study topic of the present work. They are an essential part of the microwave SQUID multiplexer. Its purpose is to simultaneously readout the energy pulses in arrays of thousands of transducer elements (IRWIN et al., 2006; MATES et al., 2008; KEMPF et al., 2017a; KEMPF et al., 2017b).

Some benefits of the system are listed below:

- The device works at very low noise levels;
- The power dissipated in the circuitry is extremely low;
- The scalability of the system is very high and can reach thousands of detectors;
- The number of connectors is reduced for frequency multiplexing schemes.

Performing signal multiplexing is not an easy task, as each scheme requires specific techniques and accurate design. There are three commonly used types: time division multiplexing (TDM), frequency division multiplexing (FDM) and code division multiplexing (CDM). Furthermore, field programmable gate array (FPGA) devices are currently widely used for generating carriers and processing the received information, so that analog and digital stages should be employed.

The first demonstrations of SQUID multiplexing were proven to be feasible by the TDM technique together with the dc-SQUID (BANDLER et al., 2012; PORST et al., 2013). However, for system scaling the complexity is very high, the heating due to the load is an issue and the cost with the increasing number of detectors make it difficult to simultaneously readout large arrays. In addition, the TDM scheme does not conserve pulse rise information because the effective bandwidth is small. The transition from idle to active level is extremely fast ($\tau_{rise} < 400ns$). This has led to the development of FDM-based systems, which use a rf-SQUID for simultaneous reading a large number of channels (KEMPF et al., 2017a).

Preliminary experiments have recently been conducted with detectors arranged in small arrays of up to 64 elements. For future applications it is expected to read larger arrays, around 400 channels. Some authors make estimates for reading thousands of channels. However, as this concept is new, multiplexing and readout techniques are in full development (MATES, 2011).

In the microwave SQUID multiplexer, an MMC-type sensor is sited in a weak magnetic field and converts detector temperature variations into magnetization variations, which in turn can be measured by the varying magnetic flux threading a SQUID. All SQUIDs are readout simultaneously through superconducting resonator circuits that are tuned to a specific frequency, featuring a high performance notch filter. The resonators are driven by a common power line, such that two coaxial cables connect the cryostat to room temperature equipment (MATES et al., 2008). Each resonant circuit is assigned a carrier that is constantly modulated by the total magnetic flux crossing the SQUID. The individual flows that contribute to the operating state of the circuit are: two opposite polarity paramagnetic sensors, a SQUID modulation wave (e.g., sine, sawtooth, triangular, etc.) and the mutual inductance between inductive couplings.

The baseband signal to be estimated may be obtained from the amplitude or phase of the modulated carrier after discarding the intermediate frequencies. These carriers will have real and imaginary components, represented shortly by I/Q, which refers to in-phase and quadrature. Whenever there is a particle impinging on the detector, the magnitude and phase of this complex function will vary, otherwise the complex function will behave proportionally to the SQUID modulating wave.

From this point, it is worth mentioning the congruence of the energy estimation problem to the DOA estimation. Both solutions lie in the phase shift of a sinusoidal wave.

In the DOA estimation problem, there are as many time series as sensors in the array. The reference signal is elected from one sensor among the several sensors, typically the one located at the origin of the coordinate system, representing null delay.

On the other hand, in the microwave SQUID multiplexer, there is just one time series relative to each source, the SQUID. Thus, it requires a special procedure to obtain a reference signal in order to compare it with the upcoming data throughout the experiment. The reference signal is defined as the SQUID response for an idle system (there is no incidence of charged particles). Once the analogy is settled, there will be two sensors in the system, one would be virtually a zero-delayed wave and the second wave would be delayed as a function of the incident energy in the detector.

Consequently, the techniques employed for sensor array parameter estimation can also be applied to the energy estimation problem in X-ray spectroscopy.

The organization of Part III is as follows: Chapter 5 introduces the motivation for researching particle physics and the microwave SQUID multiplexer. In Chapter 6 the operation of the microwave SQUID multiplexer is detailed and Chapter 7 presents a new approach to the readout of energy pulses, which is supported by simulated and experimental results. The method is inspired in the SEAD method and is, therefore, based on the eigenvalue decomposition of the covariance/correlation matrix. A mathematical formulation for estimating the pulse was developed based on a signal model with white Gaussian additive noise. It allows to understand the eigenvalues behavior considering several scenarios.

Finally, Chapter 8 presents the conclusions and discusses future work perspectives.

1.5 Published Works

The total scientific production is listed below according to the publication/activity type. The list contemplates published papers, book chapters and attended events.

Two funding programs were granted for an internship abroad, one from Bemundus/Erasmus Mundus program which was held between January 2017 and June 2017, and the other from PDSE/CAPES which was held between June 2017 and June 2018. Both were developed in Karlsruhe, Germany, in the facilities of the *Karlsruher Institut für Technologie* under the supervision of advisor Dr.-Ing. Oliver Sander. The main research topic was the readout of signals in the microwave SQUID multiplexer.

1.5.1 Journal Papers

1. LEMOS, Rodrigo P.; KUNZLER, Jonas A.; BURGOS B., Diego F.; DE SOUZA, Mário J.; SILVA, Hugo V.L. e; FERREIRA, Yroá R.; FLÔRES, Edna L.; SANDER, Oliver. Using matrix norms to estimate the direction of arrival of planar waves on an ULA. JOURNAL OF THE FRANKLIN INSTITUTE-ENGINEERING AND APPLIED MATHEMATICS, v. 356, p. 4949-4969, 2019.

2. BURGOS B., Diego F.; LEMOS, Rodrigo P.; SILVA, Hugo V.L. e; KUNZLER, Jonas A.; FLÔRES, Edna. L. Adaptive Beamforming for Moving Targets Using Genetic Algorithms. Ingeniería, v. 21, p. 214, 2016.

3. LEMOS, Rodrigo P.; SILVA, Hugo V.L. e; FLÔRES, Edna L.; KUNZLER, Jonas A.; BURGOS B., Diego F. Spatial Filtering Based On Differential Spectrum For Improving ML DOA Estimation Performance. IEEE SIGNAL PROCESSING LETTERS, v. 99, p. 1-1, 2016.

1.5.2 Book Chapter

1. CRUZ, Lucas F.; MAGALHÃES, Marcela G.; KUNZLER, Jonas A.; COELHO, André A.S. ; Lemos, Rodrigo P. A New Approach for Brain Source Position Estimation Based on the Eigenvalues of the EEG Sensors Spatial Covariance Matrix. IFMBE Proceedings. 1ed.: Springer Singapore, 2019, v. 68/2, p. 271-274.

1.5.3 Events

1. 4th Annual Matter and Technologies Meeting. Metallic magnetic calorimeter: system simulation and signal analysis. 2018. (Meeting).
2. CRUZ, L. F. ; MAGALHÃES, M. G. ; KUNZLER, J. A. ; COELHO, A. A. S. ; LEMOS, R. P. . A New Approach for Brain Source Position Estimation Based on the Eigenvalues of the EEG Sensors Spatial Covariance Matrix. 2018. (Paper presentation/Congress).

Part II

Proposal of Using Matrix Norms as DOA Estimators in a Uniform Linear Array

2 The DOA Estimation Problem for Uniform Linear Arrays

The first part of the present work dealt with establishing the relationship between DOA estimation and x-ray spectroscopy using the sensor array concept. In this second part, the focus relays on the DOA estimation of wavefronts that hit a uniform linear array (ULA). Some methods used for DOA estimation which employ the maximum likelihood function are discussed.

2.1 Introduction

The DOA estimation problem uses the concept of sensor array to obtain spatial sensibility. This feature has been widely exploited and has a leading role in signal processing. Due to the spatial sensitivity of the system, several applications have become possible lately.

The ULA consists of half-wavelength spaced elements which are linearly distributed over a plane. The DOA angles are obtained by the angular distance between the wave propagation direction and the normal vector relative to the array (TREES, 2002; SILVA et al., 2013).

The signals are induced in the electrical circuits through the sensors and are synchronously spatially sampled. The dataset sampled over the spatial domain at each instant is called a **snapshot**. It is periodically obtained and results in a matrix with dimensions that depend on the number of sensors and snapshots.

This chapter will present the theoretical foundations that enable the development of methods with the ability to estimate the parameters of interest.

2.2 Signal Models and Criteria for Performance Evaluation

Signal models for the uniform linear array follow simplifications in the general model discussed in Section 1.3. Figure 2 illustrates the case of an ULA with K sensors and 1 wavefront traveling in the direction θ_m.

Considering the sensors distributed along a horizontal line on the y-axis, i.e., $x = 0$ and $z = 0$ (equivalent to $\phi_k = \frac{\pi}{2}$ and $\theta_k = \frac{\pi}{2}$), the distance from the k-th sensor to the origin is equal to $r_k = \frac{k\vartheta}{2}$ ($\frac{\vartheta}{2}$ spacing between the elements), the direction vector components can be simplified and the calculation of the angle θ_m comes down to the

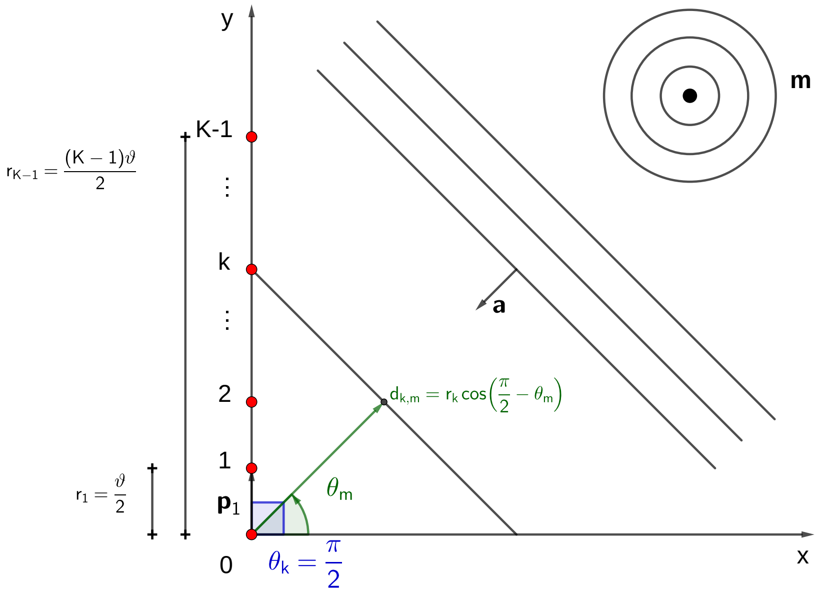

Figure 2 – Uniform linear array composed of K sensors located on the y-axis and a wavefront that hits it with an angle θ_m. Source: Author.

angular distance between the wave propagation direction and the normal vector relative to the array, according to Equation 1.8. Thus, the distance traveled by the wavefront, from the moment it hits the k-th sensor until it arrives at the origin, is given by:

$$\begin{aligned} d_{k,m} &= r_k \cos(\theta_k - \theta_m) \overset{(\theta_k = \frac{\pi}{2})}{=} \\ &= r_k \sin(\theta_m). \end{aligned} \tag{2.1}$$

Assuming all signals have the same carrier (reflected signals) or co-channel interfering signals with frequency ω_C^m, the wavelength will be the same for all wavefronts. Thus, an electrical angle given as a function of the mechanical angle can be defined as the angular frequency:

$$\begin{aligned} \omega_m &= \frac{2\pi}{\vartheta} r_1 \sin(\theta_m) \overset{(r_1 = \frac{\vartheta}{2})}{=} \\ &= \pi \sin(\theta_m). \end{aligned} \tag{2.2}$$

It follows that the modulated signal in each sensor is given by:

$$x_k(t) = \sum_{m=1}^{M} f_m(t) \exp\left(j\omega_C^m t\right) \exp\left[j\varphi_m(t)\right] \exp\left(jk\omega_m\right). \tag{2.3}$$

Before sampling, the signal is demodulated and the term $\exp(j\omega_C^m t)$ is discarded, converting it to the baseband. The baseband signal is expressed by:

$$x_k(t) = \sum_{m=1}^{M} f_m(t) \exp\left[j\varphi_m(t)\right] \exp\left(jk\omega_m\right). \tag{2.4}$$

Equation 2.4 describes the components of the induced signal in each sensor, which has M complex exponentials with the normalized frequencies ω_m, phases $\varphi_m(t)$ and complex amplitudes $f_m(t)$.

2.2.1 The Signal Model for a ULA

Handling the expression 2.4, a variable change can be performed to simplify the notation and to highlight the signal components.

Let,

$$a_k(\omega_m) = \exp\left(jk\omega_m\right); \tag{2.5}$$

$$s_m(t) = f_m(t)\exp\left[j\varphi_m(t)\right], \tag{2.6}$$

be two vectors describing the spatial and time characteristics respectively, the signal can be now expressed by:

$$x_k(t) = \sum_{m=1}^{M} a_k\left(\omega_m\right) s_m(t). \tag{2.7}$$

In matrix notation:

$$\mathbf{x}(t) \equiv \begin{bmatrix} x_0(t) \\ x_1(t) \\ \vdots \\ x_{K-1}(t) \end{bmatrix} = \sum_{m=1}^{M} \begin{bmatrix} a_0(\omega_m) \\ a_1(\omega_m) \\ \vdots \\ a_{K-1}(\omega_m) \end{bmatrix} s_m(t) \qquad \in \mathbb{C}^{K\times 1}, \tag{2.8}$$

which is equivalent to:

$$\mathbf{x}(t) = \sum_{m=1}^{M} \mathbf{a}\left(\omega_m\right) s_m(t). \tag{2.9}$$

The vector $\mathbf{a}(\omega_m)$ is called the steering vector, in analogy to the classic beamforming method, where the array is adjusted to have predetermined gain in a certain direction or angle of incidence (VIBERG; KRIM, 1996). One can also write the $\mathbf{x}(t)$ vector in matrix notation as:

$$\mathbf{x}(t) = \mathbf{A}(\boldsymbol{\omega})\mathbf{s}(t), \tag{2.10}$$

where

$$\mathbf{s}(t) = \begin{bmatrix} s_1(t) & s_2(t) & \dots & s_M(t) \end{bmatrix}^T \qquad \in \mathbb{C}^{M\times 1} \tag{2.11}$$

is the vector of complex signal amplitudes, $\mathbf{x}(t)$ contains the incoming signals, $\boldsymbol{\omega} = [\omega_1\ \omega_2\ \dots\ \omega_M]$ are the electrical angles and $\mathbf{A}(\boldsymbol{\omega})$ is the steering matrix, which is given by (ALVES, 2004):

$$\mathbf{A}\left(\boldsymbol{\omega}\right) = \begin{bmatrix} \mathbf{a}\left(\omega_1\right) & \mathbf{a}\left(\omega_2\right) & \dots & \mathbf{a}\left(\omega_M\right) \end{bmatrix} \in \mathbb{C}^{K\times M}. \tag{2.12}$$

Thus, the matrix $\mathbf{A}(\boldsymbol{\omega})$ has Vandermonde structure and the matrix entries are given by:

$$\mathbf{A}(\boldsymbol{\omega}) = \begin{bmatrix} 1 & \dots & 1 \\ \exp(j\omega_1) & \dots & \exp(j\omega_M) \\ \exp(j2\omega_1) & \dots & \exp(j2\omega_M) \\ \exp\left[j(K-1)\omega_1\right] & \dots & \exp\left[j(K-1)\omega_M\right] \end{bmatrix}. \tag{2.13}$$

Due to digitization, the amount of data available for signal processing is limited and each sample follows the sequence $t = n \cdot T_S$, $\forall\ n \in \{0,\ 1,\ 2, \dots,\ N-1\}$, where N is the total number of snapshots and T_S is the sampling period. Considering the signals after the sampling process, we use the n index instead of t.

The whole system is contaminated by additive noise, so we introduce the array output vector $\mathbf{y}(n)$ as:

$$\begin{aligned} \mathbf{y}(n) &= \mathbf{x}(n) + \mathbf{e}(n) \\ &= \mathbf{A}(\boldsymbol{\omega})\mathbf{s}(n) + \mathbf{e}(n) \quad \in \mathbb{C}^{K\times 1}. \end{aligned} \tag{2.14}$$

where $\mathbf{e}(n)$ is a complex noise vector.

2.2.2 Stochastic Signal Models

As stated in (STOICA; NEHORAI, 1990), signals are considered zero-mean random variables, which can be expressed by:

$$\mathrm{E}\left\{\mathbf{s}(n)\right\} = 0, \tag{2.15}$$

where $\mathrm{E}\{\bullet\}$ is the statistical mathematical expectation. Additionally, the following statements are true:

$$\mathrm{E}\left\{\mathbf{s}(n)\mathbf{s}^*(i)\right\} = \mathbf{P}_{M\times M}\ \delta_{n,i}; \tag{2.16}$$

$$\mathrm{E}\left\{\mathbf{s}(n)\mathbf{s}^T(i)\right\} = \mathbf{0}, \qquad \forall\ n,\ i \in \mathbb{N}, \tag{2.17}$$

where $\delta_{n,i}$ is the Kronecker's delta function, which implies $\delta_{n,n} = 1$, and $\delta_{n,i} = 0$ whenever $n \neq i$, the conjugate transpose operator is denoted by $(\bullet)^*$, and $(\bullet)^T$ is the ordinary transpose operator. The expressions 2.16 and 2.17 imply a complete uncorrelation between the real and imaginary parts of the signals and that their variances are the same. These conditions ensure time uncorrelation between the signals.

Matrix $\mathbf{P}$ is the data correlation matrix within the same snapshot. It is hermitian and its rank lays between 1 and M. The $[\mathbf{P}]_{r,c} = \rho_{r,c}$ element outside its main diagonal indicates the cross correlation between the r-th and c-th signals and it is called the correlation factor.

If the matrix $\mathbf{P}$ is proportional to the identity matrix $\mathbf{I}$, the signals have the same power and are uncorrelated. Consequently, $\mathrm{rank}(\mathbf{P}) = M$. This condition is obtained whenever the vectors of complex signal amplitudes are independent of each other in the snapshot. It is possible to have $0 < \rho_{r,c} < 1$, which corresponds to partially correlated signals, with correlation factor $\rho_{r,c}$. Finally, a third situation that deserves attention is when the signals are called coherent or fully correlated, that is, the vector elements of the signals are a proportional and/or shifted versions of one of its components (reflected signals). In this case $1 < \mathrm{rank}(\mathbf{P}) < M$.

Stochastic signal models can be classified as conditional or unconditional.

2.2.2.1 Conditional Model (CM)

In this model, the signal amplitudes in a given snapshot are independent random variables. Also, the distinct snapshot vectors are independent, i.e.:

$$\mathbf{s}(n) \neq \mathbf{s}(i) \qquad \forall\; n \neq i. \tag{2.18}$$

Therefore, the vector $\mathbf{s}(n)$ is stochastic in space (along one snapshot) and in time (in different snapshots). In other realizations, this vector sequence is kept fixed by varying only the additive noise. The term *conditional* arises from the fact that the statistical properties of the data vector $\mathbf{y}(n)$, as in 2.14, are conditioned by the signal vectors $\mathbf{s}(n)$ (STOICA; NEHORAI, 1990).

A specific case of this model is the **deterministic model** which employs the same signal vector in all snapshots. It is often used in frequency estimation when only one sequence of samples is used. The signal in this case is considered unknown and fixed in all realization (KUMARESAN; SHAW, 1986; HUA, 1994). This signal model is used by classical estimators, such as the maximum likelihood criterion, the deterministic maximum likelihood follows from it.

2.2.2.2 Unconditional Model (UM)

In this model the randomness in space and time of the signal vectors are maintained and additionally, in each realization, a new sequence of vectors $\mathbf{s}(n)$ is generated (STOICA; NEHORAI, 1990). The term *unconditional* is used because the statistical properties of the data vectors $\mathbf{y}(n)$ are unconditional, since the sequence $\mathbf{s}(n)$ varies with each realization. In the simulations to be performed, the UM will be used, due to its widespread use in more recent bibliographic references and because it is the most realistic signal model.

2.2.3 Noise Model

Noise in a practical system comes from a variety of sources, such as environmental influence, transducer stages, preprocessing and sampling steps, and non-distinguishable low intensity sources (PILLAI, 1989). It is generated by several identical and independent sources and the application of the central limit theorem (CLT) allows us to model it as a zero-mean Gaussian random variable. Thus, the noise vectors satisfy the expressions:

$$\mathrm{E}\left\{\mathbf{e}(n)\mathbf{e}^{*}(i)\right\} = \sigma^{2}\mathbf{I}_{K\times K}\ \delta_{n,i}; \tag{2.19}$$

$$\mathrm{E}\left\{\mathbf{e}(n)\mathbf{e}^{T}(i)\right\} = \mathbf{0},\ \forall\ n,\ i \in \mathbb{N}, \tag{2.20}$$

where σ^2 is the noise variance. Equation 2.20 indicates the orthogonality between the real and imaginary parts of the noise vector. Also, there is no correlation either between the samples of a noise vector or between the distinct snapshots noise vectors, that is, there are no correlation in space and time.

2.2.4 Spatial Correlation Matrix

The spatial correlation matrix is the basis of the estimation methods here treated. It is obtained from the array output vectors, expression 2.14:

$$\mathbf{R}(n,i) = \mathrm{E}\left\{\mathbf{y}(n)\mathbf{y}^{*}(i)\right\}, \tag{2.21}$$

which turns on:

$$\mathbf{R}(n,i) = \mathbf{A}\mathrm{E}\left\{\mathbf{s}(n)\mathbf{s}^{*}(i)\right\}\mathbf{A}^{*} + \mathrm{E}\left\{\mathbf{e}(n)\mathbf{e}^{*}(i)\right\}, \tag{2.22}$$

where $n,\ i = \{0,\ 1,\ 2, \ldots,\ N-1\}$.

Considering the expressions 2.16 of the signal model and 2.19 of noise, as well as the correlation between the signal and noise vectors, the matrix $\mathbf{R}(n,i)$ will only be nonzero for $n = i$, when it then takes the following form:

$$\mathbf{R} = \mathbf{APA}^{*} + \sigma^{2}\mathbf{I} \qquad \in \mathbb{C}^{K\times K}, \tag{2.23}$$

There is also the possibility of performing the spectral decomposition of the matrix $\mathbf{R}$ through the EVD:

$$\mathbf{R} = \mathbf{U}\boldsymbol{\Lambda}\mathbf{U}^{*}, \tag{2.24}$$

where $\mathbf{U}$ is a unit matrix whose columns are the eigenvectors of $\mathbf{R}$ and $\boldsymbol{\Lambda}$ is a diagonal matrix whose elements are the eigenvalues of $\mathbf{R}$. It is assumed they are sorted in a decreasing order. Considering M independent wave sources and white noise with variance σ^2 in an ULA with K sensors where $M < K$, the diagonalization process yields $\boldsymbol{\Lambda} = \mathrm{diag}\left\{\lambda_1,\ \lambda_2, \ldots,\ \lambda_K\right\}$. By grouping the M first columns of eigenvectors relative to the M largest eigenvalues in a matrix $\mathbf{U}_S$ and the remaining eigenvectors in the matrix $\mathbf{U}_N$, 2.24 is rewritten as:

$$\mathbf{R} = \mathbf{U}_S\boldsymbol{\Lambda}_S\mathbf{U}_S^{*} + \mathbf{U}_N\boldsymbol{\Lambda}_N\mathbf{U}_N^{*}, \tag{2.25}$$

where $\mathbf{U}_S \in \mathbb{C}^{K\times M}$ and $\boldsymbol{\Lambda}_S = \mathrm{diag}\left\{\lambda_1,\ \lambda_2, \ldots,\ \lambda_M\right\} \in \mathbb{R}^{M\times M}$ span the signal subspace and $\mathbf{U}_N \in \mathbb{C}^{K\times(K-M)}$ and $\mathbf{\Lambda}_N = \sigma^2\mathbf{I} \in \mathbb{R}^{(K-M)\times(K-M)}$ are the noise subspace eigenvectors and eigenvalues, respectively.

In the case of a finite number of snapshots, statistical expectations are replaced by algebraic averages and $\hat{\mathbf{R}}$ is an estimated version of the asymptotic spatial correlation matrix. Considering N snapshots it follows that:

$$\begin{aligned}\hat{\mathbf{R}} &= \frac{1}{N}\sum_{n=1}^{N}\mathbf{y}(n)\mathbf{y}^*(n)\\ &= \mathbf{A}\left[\frac{1}{N}\sum_{n=1}^{N}\mathbf{s}(n)\mathbf{s}^*(n)\right]\mathbf{A}^* + \frac{1}{N}\sum_{n=1}^{N}\mathbf{e}(n)\mathbf{e}^*(n). \end{aligned} \tag{2.26}$$

Similarly to expression 2.25 the EVD produces:

$$\hat{\mathbf{R}} = \hat{\mathbf{U}}_S\hat{\mathbf{\Lambda}}_S\hat{\mathbf{U}}_S^* + \hat{\mathbf{U}}_N\hat{\mathbf{\Lambda}}_N\hat{\mathbf{U}}_N^*, \tag{2.27}$$

where $\hat{\mathbf{U}}_S$, $\hat{\mathbf{\Lambda}}_S$ are the signal subspace eigenvectors and eigenvalues, and $\hat{\mathbf{U}}_N$, $\hat{\mathbf{\Lambda}}_N$ are the eigenvectors and eigenvalues associated with the noise subspace.

The SNR for the m-th signal is defined as (PILLAI, 1989):

$$\mathrm{SNR}_m = 10\cdot\log_{10}\left\{\frac{\mathrm{E}\left\{|s_m(n)|^2\right\}}{\sigma^2}\right\} \qquad [\mathrm{dB}]. \tag{2.28}$$

2.3 Maximum Likelihood Estimator

Maximum Likelihood Estimator (MLE) is a classical parameter estimation method. The estimates are obtained directly from noise-contaminated signal samples, but require high computational effort and their direct implementation is not a commonly used alternative.

This chapter introduces some MLE expressions for DOA estimation in the context of stochastic signal models. The objective is to analyze some characteristics of this estimator to allow a better understanding of the estimation methods that are derived from MLE, which will be presented in the following chapters. These methods achieve performance close to MLE with considerably low CE due to simpler equations.

The MLE is obtained from the probability density function of data vector $\mathbf{y}(n)$. Its advantage is that it can be used for many complicated estimation problems (KAY, 1993), as it exploits data with relative efficiency.

Specifically when applied to frequency estimation or DOA in ULA, MLE performance is asymptotically optimal. It approaches the CRB as the number of snapshots becomes larger. Additionally, there is no limitations in estimating coherent signals, some methods generally fail.

The vector gathering all parameter estimates is calculated by a M-dimensional search while seeking the minimum point of a cost function. The computational effort required is then prohibitive.

MLE has two versions (OTTERSTEN; VIBERG, 1989), the first is the deterministic maximum likelihood estimator (DMLE) for the conditional model. The second version is the stochastic maximum likelihood estimate (SMLE) for the unconditional model.

2.3.1 Deterministic Maximum Likelihood Estimator

DMLE assumes that the signal is properly represented by the conditional model, where the signal parameters are random in snapshots, but in the different realizations, the same sequence is always used.

The DMLE expression is obtained from the probability density function of the sample vector and a parameter vector in the so-called likelihood function, $L(\boldsymbol{\theta})$. This function is maximized, i.e., the goal is to get a $\boldsymbol{\theta}$ parameter vector that makes it to have the largest possible value (BRESLER; MACOVSKI, 1986). Alternatively, this expression can be obtained from the mean square error function (KUMARESAN; SHAW, 1986), from which an estimate of the complex amplitude is obtained. This estimate is replaced with the original error function, resulting in a modified error function, equal to the DMLE cost function.

In this model, the noise in data vector is white and zero-mean Gaussian. As a consequence, the data vector $\mathbf{y}(n)$ is also a Gaussian random process, with mean equal to $\mathbf{A}(\boldsymbol{\omega})\mathbf{s}(n)$ and correlation matrix given by $\sigma^2\mathbf{I}$. The likelihood function is given by (VIBERG; KRIM, 1996):

$$L_{DMLE}(\boldsymbol{\omega},\mathbf{s}(n),\sigma^2) = \prod_{n=1}^{N} (\pi\sigma^2)^{-K} \exp\left[\frac{-\|\mathbf{y}(n) - \mathbf{A}(\boldsymbol{\omega})\mathbf{s}(n)\|^2}{\sigma^2}\right], \tag{2.29}$$

where $\| \bullet \|$ denotes the Euclidean vector norm, $\boldsymbol{\omega}$ is the signal frequencies vector, $\mathbf{s}(n)$ is the complex amplitudes vector for the n-th snapshot and σ^2 is the noise variance. For convenience, ML estimates are calculated over the arguments of the logarithm of 2.29, i.e.:

$$l_{DMLE}\left[\boldsymbol{\omega},\mathbf{s}(n),\sigma^2\right] = -\ln\left\{L_{DMLE}\left[\boldsymbol{\omega},\mathbf{s}(n),\sigma^2\right]\right\}. \tag{2.30}$$

Normalizing by N and ignoring the constant term $K \cdot \ln(\pi)$, it follows that:

$$l_{DMLE}\left[\boldsymbol{\omega},\mathbf{s}(n),\sigma^2\right] = K\ln\sigma^2 + \frac{1}{\sigma^2 N}\sum_{n=1}^{N} \|\mathbf{y}(n) - \mathbf{A}(\boldsymbol{\omega})\mathbf{s}(n)\|^2. \tag{2.31}$$

The parameters are σ^2, $\mathbf{s}(n)$ and $\boldsymbol{\omega}$. The ML estimates are the values that minimize the expression 2.31.

A procedure often used in this minimization is setting $\boldsymbol{\omega}$ constant and minimizing the two other parameters, since all three are independent. Then replace the minimum values in 2.31 and next minimize relative to $\boldsymbol{\omega}$. This produces (VIBERG; KRIM, 1996), omitting the argument for the sake of simplicity, the following equations:

$$\hat{\sigma}^2_{DMLE} = \frac{1}{K}\mathrm{tr}\left(\mathbf{P}_A^{\perp}\hat{\mathbf{R}}\right), \tag{2.32}$$

and

$$\hat{\mathbf{s}}_{DMLE}(n) = \left(\mathbf{A}^*\mathbf{A}\right)^{-1}\mathbf{A}^*\mathbf{y}(n). \tag{2.33}$$

Substituting the expressions 2.32 and 2.33 into 2.31, and noting that $\frac{1}{N}\sum_{n=1}^{N}\|\mathbf{P}_A^{\perp}\mathbf{y}(n)\|^2 = \mathrm{tr}(\mathbf{P}_A^{\perp}\hat{\mathbf{R}})$, it is shown that frequency estimates are obtained by solving the following minimization problem (VIBERG; KRIM, 1996):

$$\hat{\boldsymbol{\omega}}_{DMLE} = \arg\min_{\boldsymbol{\omega}}\left\{F_{DMLE}(\boldsymbol{\omega})\right\}, \tag{2.34}$$

where

$$F_{DMLE}(\boldsymbol{\omega}) = \mathrm{tr}(\mathbf{P}_A^{\perp}\hat{\mathbf{R}}) \tag{2.35}$$

is the DMLE cost function for the frequency parameter.

2.3.2 Stochastic Maximum Likelihood Estimator

The SMLE is obtained when signal parameters are modeled as Gaussian random variables for the unconditional model.

The parameter set to be estimated consists of the frequencies $\boldsymbol{\omega}$, the correlation matrix of the signals $\mathbf{P}$ and the noise variance σ^2. The likelihood function for this model is given by (KAY, 1993):

$$L_{SMLE}\left(\boldsymbol{\omega},\mathbf{P},\sigma^2\right) = \prod_{n=1}^{N}\pi^{-K}\det(\mathbf{R})^{-K}\exp\left[-\mathbf{y}^T(n)\mathbf{R}^{-1}\mathbf{y}(n)\right]. \tag{2.36}$$

Following the same steps as DMLE and assuming the parameters are independent, $\boldsymbol{\omega}$ is fixed so that the estimates of σ^2 and $\mathbf{P}$ can be calculated by (VIBERG; KRIM, 1996):

$$\hat{\sigma}^2_{SMLE}(\boldsymbol{\omega}) = \frac{1}{M-K}\mathrm{tr}\left(\mathbf{P}_A^{\perp}\hat{\mathbf{R}}\right), \tag{2.37}$$

and

$$\hat{\mathbf{P}}_{SMLE}(\boldsymbol{\omega}) = \left(\mathbf{A}^*\mathbf{A}\right)^{-1}\mathbf{A}^*\left[\hat{\mathbf{R}} - \hat{\sigma}^2_{SMLE}(\boldsymbol{\omega})\mathbf{I}\right]\left[\left(\mathbf{A}^*\mathbf{A}\right)^{-1}\mathbf{A}^*\right]^*. \tag{2.38}$$

By substituting these estimates in the modified likelihood function of SMLE and performing some simplifications, the frequency estimates are obtained from the following expression (VIBERG; KRIM, 1996):

$$\hat{\boldsymbol{\omega}}_{SMLE} = \arg\min_{\boldsymbol{\omega}}\left\{F_{SMLE}(\boldsymbol{\omega})\right\}, \tag{2.39}$$

where

$$F_{SMLE}(\boldsymbol{\omega}) = \ln\{\det\left[\mathbf{A}\hat{\mathbf{P}}_{SMLE}(\boldsymbol{\omega})\mathbf{A}^* + \hat{\sigma}^2_{SMLE}(\boldsymbol{\omega})\mathbf{I}\right]\} \tag{2.40}$$

is the SMLE cost function.

The term performance will refer to the RMSE of the estimates. CRB is a parameter for the quality of the estimates obtained, as it provides the lower limit for RMSE of unbiased estimates. Therefore, the comparison between the methods evaluated with the CRB is extremely relevant, however, this evaluation can be extremely complex given the number of parameters and the evaluation ranges. Therefore, it is common to explore the asymptotic behavior of methods (when the number of snapshots is large enough) to have an idea about the general behavior of methods. Expressions of asymptotic performance of ML methods are analyzed in (STOICA; SHARMAN, 1990; STOICA; NEHORAI, 1990).

2.4 DMLE Derived Methods

DMLE has high resolution capability and presents no difficulties for application in different types of sensor arrays with different geometric characteristics. It also features asymptotic performance consistent with CRB, but its direct implementation requires a prohibitive computational effort for many applications. In order to bypass the implementation problem, iterative methods were developed, which perform parameter estimation by minimizing a modified version of the DMLE objective function. The great advantage of using this procedure is that the implementations of these methods have reduced computational effort, and the performances presented are not inferior to those obtained with the original method (ALVES, 2004).

The first method of great relevance uses an iterative procedure on a quadratic function obtained from the parameterization of the DMLE cost function, which is called iterative quadratic maximum likelihood (IQML) (BRESLER; MACOVSKI, 1986; KUMARESAN; SHAW, 1986). To revise inaccuracies in the IQML method, the modified IQML (M-IQML) method became alive, which performs a correction in the data matrix to reduce the effect of noise on estimates (ALVES, 2004).

Other extremely important methods are the MODE method and its derivatives. The MODE method uses the DMLE cost function parameterized in terms of the polynomial that forms a basis for the null space of $\mathbf{A}(\boldsymbol{\omega})$. However, it additionally truncates the estimated correlation matrix $\hat{\mathbf{R}}$ to discard the eigenvalues and eigenvectors of the noise subspace, known as weighted subspace fitting (WSF) (STOICA; SHARMAN, 1990). MODEX uses MODE as the basis for obtaining candidate angles, which are applied to a selection criterion in order to choose the best estimates. Modified MODEX uses MODE to obtain three sets of candidate angles based on different criteria (constraints imposed on the $\hat{\mathbf{b}}$ vector) and then applies the selection criteria to choose the best estimates (ALVES, 2004).

The MODEX and Modified MODEX methods will be used in the analysis as a basis for comparison of the proposed methods. They were considered the best estimators of DOA in ULA.

2.4.1 Basic Formulation for DMLE Derivative Methods

The reparametrization of the DMLE cost function takes advantage of the null subspace of **A** in such a manner that 2.31 is written in terms of a linear prediction polynomial $b(z)$, as presented in the following expression:

$$b(z) \triangleq \sum_{m=0}^{M} b_m z^{(M-m)} = b_0 z^M + b_1 z^{(M-1)} + \cdots + b_M = b_0 \prod_{m=1}^{M} (z - \varrho_m). \tag{2.41}$$

If the roots of this polynomial assume the form $\varrho_m = \exp(j\omega_m)$, i.e. equal to the DOA angles, the coefficients will be unequivocally determined. Then,

$$\sum_{m=0}^{M} b_m \exp\left[j(M-m)\omega_i\right] = 0, \; \forall \; i \in \mathbb{N} \mid 1 \leq i \leq M. \tag{2.42}$$

the index i refers to each polynomial root individually.

From the vector of coefficients $\mathbf{b} = [b_0, b_1, \ldots, b_M]^T$, the band matrix **B** is obtained (BRESLER; MACOVSKI, 1986):

$$\mathbf{B} = \begin{bmatrix} b_M^* & \ldots & 0 & \ldots & 0 \\ \vdots & \ddots & \ddots & \ddots & \vdots \\ b_0^* & \ldots & b_M^* & \ldots & 0 \\ \vdots & \ddots & \ddots & \ddots & \vdots \\ 0 & \ldots & b_0^* & \ldots & b_M^* \\ \vdots & \ddots & \ddots & \ddots & \vdots \\ 0 & \ldots & 0 & \ldots & b_0^* \end{bmatrix} \in \mathbb{C}^{K\times(K-M)}. \tag{2.43}$$

The expression 2.42 in matrix notation turns into:

$$\mathbf{B}^*\mathbf{A} = \mathbf{0}. \tag{2.44}$$

Let $\text{rank}(\mathbf{A}) = \bar{M}$ and $\text{rank}(\mathbf{B}) = K - \bar{M}$ be the number of independent rows of each matrix, the columns of **B** are assumed to belong to the null space of $\mathbf{A}^*$ (BRESLER; MACOVSKI, 1986). It follows that (section A.3):

$$\mathbf{P}_B = \mathbf{B}\mathbf{B}^+ = \mathbf{B}\left(\mathbf{B}^*\mathbf{B}\right)^{-1}\mathbf{B}^* = \mathbf{I} - \mathbf{A}\left(\mathbf{A}^*\mathbf{A}\right)^{-1}\mathbf{A}^* = \mathbf{I} - \mathbf{A}\mathbf{A}^+ = \mathbf{P}_A^{\perp}; \tag{2.45}$$

$$\mathbf{P}_A = \mathbf{A}\mathbf{A}^+ = \mathbf{A}\left(\mathbf{A}^*\mathbf{A}\right)^{-1}\mathbf{A}^* = \mathbf{I} - \mathbf{B}\left(\mathbf{B}^*\mathbf{B}\right)^{-1}\mathbf{B}^* = \mathbf{I} - \mathbf{B}\mathbf{B}^+ = \mathbf{P}_B^{\perp}, \tag{2.46}$$

where $\mathbf{P}_B$ and $\mathbf{P}_A^{\perp}$ are orthogonal projectors to the column space of $\mathbf{A}$ (ALVES, 2004).

The ML estimates can be obtained by solving the following constrained linear optimization problem:

$$\hat{\mathbf{b}} = \underset{\mathbf{b}\,\in\, D}{\arg\min}[F_{DMLE2}(\mathbf{b})], \tag{2.47}$$

where the term $F_{DMLE2}(\mathbf{b})$ refers ot the DMLE's reparameterized objective function in terms of $\mathbf{b}$, as follows:

$$\begin{aligned} F_{DMLE2}(\mathbf{b}) &= \operatorname{tr}\left[\mathbf{B}\left(\mathbf{B}^*\mathbf{B}\right)^{-1}\mathbf{B}^*\hat{\mathbf{R}}\right] \\ &= \operatorname{tr}\left(\mathbf{P}_B\hat{\mathbf{R}}\right). \end{aligned} \tag{2.48}$$

To ensure the method's convergence it is essential to establish some constraints on the polynomial coefficients set D in 2.47 (ALVES, 2004):

- $\mathbf{b} \neq \mathbf{0}$: non-triviality constraint. This ensures the two-way match between $\mathbf{b}$ and the angular frequency vector $\boldsymbol{\omega}$, such that the inversion of $\mathbf{B}^*\mathbf{B}$ exists (BRESLER; MACOVSKI, 1986). To implement the constraint, one can impose on the $\mathbf{b}$ vector that one of the elements is equal to one or it has unit norm;
- $b(z)$ roots on the unit circle: imposes that complex exponentials are undamped functions.

2.4.2 MODE Method

The basic idea behind MODE method is to approximate the cost function locally around the optimal vector $\mathbf{b}_0$, by a quadratic function. This function is obtained by replacing the $\hat{\mathbf{R}}$ matrix in terms of its eigenvalues and eigenvectors decomposition and assuming the signal subspace as an estimate for the correlation matrix, which results in:

$$\hat{\mathbf{R}} = \hat{\mathbf{U}}_S\hat{\mathbf{\Lambda}}_S\hat{\mathbf{U}}_S^* + \hat{\mathbf{U}}_N\hat{\mathbf{\Lambda}}_N\hat{\mathbf{U}}_N^*, \tag{2.49}$$

where $\hat{\mathbf{U}}_S$ and $\hat{\mathbf{\Lambda}}_S$ are the eigenvectors and eigenvalues of the signal subspace and $\hat{\mathbf{U}}_N$ and $\hat{\mathbf{\Lambda}}_N$ are the eigenvalues and eigenvalues of the noise subspace, respectively.

Considering the asymptotic situation (number of snapshots tends to infinity or N is large) and, ideally, $\mathbf{B}^*\hat{\mathbf{U}}_S = \mathbf{0}$, the expression of the MODE cost function is given by (STOICA; SHARMAN, 1990):

$$F_{MODE}(\mathbf{b}) = \operatorname{tr}\left[\mathbf{B}\left(\hat{\mathbf{B}}^*\hat{\mathbf{B}}\right)^{-1}\mathbf{B}^*\hat{\mathbf{U}}_S\hat{\mathbf{\Psi}}_{MODE}\hat{\mathbf{U}}_S^*\right], \tag{2.50}$$

the $\hat{\mathbf{\Psi}}_{MODE}$ is an optimal matrix, so that the estimator variance parameter is minimal and it is given by:

$$\hat{\mathbf{\Psi}}_{MODE} = \operatorname{diag}\left\{\frac{\left(\hat{\lambda}_1 - \hat{\sigma}^2\right)^2}{\hat{\lambda}_1}, \frac{\left(\hat{\lambda}_2 - \hat{\sigma}^2\right)^2}{\hat{\lambda}_2}, \ldots, \frac{\left(\hat{\lambda}_{\bar{M}} - \hat{\sigma}^2\right)^2}{\hat{\lambda}_{\bar{M}}}\right\}, \tag{2.51}$$

where $\bar{M} = \min\{M, \mathrm{rank}(\mathbf{P})\}$, $\hat{\lambda}_i$ is the i-th eigenvalue of $\hat{\mathbf{R}}$ and

$$\hat{\sigma}^2 = \frac{1}{K - \bar{M}} \left[\mathrm{tr}\left(\hat{\mathbf{R}}\right) - \sum_{m=1}^{\bar{M}} \hat{\lambda}_m \right] \tag{2.52}$$

is the noise variance estimate.

Making the appropriate substitutions in the cost function 2.50, the expression to be minimized turns into:

$$\hat{\boldsymbol{\beta}}_{MODE} = \underset{\boldsymbol{\beta}\, \in\, D}{\arg\min} \left\{ \boldsymbol{\beta}^T \boldsymbol{\Omega}_{MODE} \boldsymbol{\beta} \right\}, \tag{2.53}$$

with $\boldsymbol{\Omega}_{MODE}$ dependent on the constraint set D that is imposed on the $\boldsymbol{\beta}$ vector, as described in (STOICA; SHARMAN, 1990).

The sequence for obtaining estimates in MODE method can be summarized as (STOICA; SHARMAN, 1990):

1. Estimate the spatial correlation matrix $\hat{\mathbf{R}}$ and the $\bar{M}$ eigenvalues and eigenvectors from signal subspace. Estimate the noise power σ^2 and set the matrix $\hat{\boldsymbol{\Psi}}_{MODE}$.
2. Get an initial estimate $\boldsymbol{\beta}_0$ by minimizing the cost function:

$$F^0_{MODE} = \mathrm{tr}\left[\mathbf{B}^* \hat{\mathbf{S}} \hat{\boldsymbol{\Psi}} \hat{\mathbf{S}}^* \mathbf{B} \right], \tag{2.54}$$

   which can be calculated by (ALVES, 2004):

$$\hat{\boldsymbol{\beta}}_0 = \underset{\boldsymbol{\beta}\, \in\, D}{\arg\min} \{ \boldsymbol{\beta}^* \mathbf{W}^* \left[\sum_{m=1}^{M} \tilde{\mathbf{S}}^*_m \tilde{\mathbf{S}}_m \right] \mathbf{W} \boldsymbol{\beta} \}. \tag{2.55}$$

3. Estimate $\boldsymbol{\beta}_{MODE}$, performing $(\hat{\mathbf{B}}^* \hat{\mathbf{B}})$ where the initial estimate $\boldsymbol{\beta}_0$ is used, which was found on step 2.
4. Estimate the frequency $\hat{\boldsymbol{\omega}}$ by searching the roots of $b(z)$, where the coefficients are $\hat{\mathbf{b}}$ obtained from $\hat{\beta}_{MODE}$ which was calculated on step 3.

Repeating step 3 a few times by updating the most recent estimation matrix of the $\hat{\mathbf{b}}$ vector to improve estimates is also possible. However, values greater than three are irrelevant (LI; STOICA; LIU, 1998).

The minimizations in steps 2 and 3 refer to quadratic functions, since $(\mathbf{B}^*\mathbf{B})$ has been replaced by an independent estimate of the vector $\mathbf{b}$. Thus, these minimizations can be solved using norm constraints or linear constraints (ALVES, 2004).

The MODE method presents some performance issues for small amount of snapshots and the threshold breakdown effect is affected by improper estimation of signal and noise subspaces. To get around these problems, the MODEX method was developed.

2.4.3 MODEX Method

The MODEX (GERSHMAN; STOICA, 1999) method is based on MODE, but is considerably more complex. Its advantages over MODE are a lower threshold breakdown effect for very low SNRs, and good performance also on the condition of a few snapshots.

MODEX has the principle of obtaining two sets of estimates. One of these sets is formed by the estimates obtained with the MODE method. The second set is obtained with a modified version of this same method, but with the order of the parameter vector **b** equal to $(M+Q)$, with Q being an integer such that $0 < Q < K-M$. The K roots from MODE and the $(M+Q)$ roots from the modified version are gathered together, forming a set of $(2M+Q)$ roots. In the following, combinations of M distinct roots are formed which are called the candidate estimates. The best candidate minimizes the selection criteria which could be one of the two MLE equations, the DMLE as stated in 2.29 or the SMLE as stated in 2.36.

The use of MODE method estimates aims to provide MODEX with its excellent asymptotic performance. The introduction of the order vector $(M+Q)$ extends the degree of freedom to obtain the roots, which can avoid misuse of the noise subspace in place of the signal subspace.

The first set of MODEX estimates are the root angles of the polynomial formed by the $\hat{\boldsymbol{\beta}}_{MODE}$ vector, as in 2.53. The second set of estimates is obtained by extending the coefficient vector by Q and minimizing a function similar to MODE. From this, an extended parameter array $\mathbf{b}_{EX}$ is defined:

$$\mathbf{b}_{EX} = \left[b_0,\, b_1, \ldots,\, b_{M+Q}\right]^T . \tag{2.56}$$

The matrix of corrected eigenvalues must be expanded so that it is given by:

$$\hat{\boldsymbol{\Psi}}_{MODEX} = \operatorname{diag}\left\{\hat{\boldsymbol{\Psi}}_{MODE},\, 0, \ldots,\, 0\right\} \in \mathbb{C}^{(M+Q)\times(M+Q)}. \tag{2.57}$$

The matrix $\mathbf{B}_{EX}$ is:

$$\mathbf{B}_{EX} = \begin{bmatrix} b^*_{M+Q} & \ldots & 0 & \ldots & 0 \\ \vdots & \ddots & \ddots & \ddots & \vdots \\ b^*_0 & \ldots & b^*_{M+Q} & \ldots & 0 \\ \vdots & \ddots & \ddots & \ddots & \vdots \\ 0 & \ldots & b^*_0 & \ldots & b^*_{M+Q} \\ \vdots & \ddots & \ddots & \ddots & \vdots \\ 0 & \ldots & 0 & \ldots & b^*_0 \end{bmatrix} \in \mathbb{C}^{K\times(K-M-Q)}. \tag{2.58}$$

Due to the extra elements in $\hat{\boldsymbol{\Psi}}_{MODEX}$, the signal eigenvectors matrix has now $(M+Q)$ columns. Thus, the final expression of the parameter vector is given by:

$$\hat{\boldsymbol{\beta}}_{EX} = \underset{\beta\,\in\,D}{\arg\min}\left\{\mathrm{tr}\left[\left(\hat{\mathbf{U}}_{S,EX}^{*}\mathbf{B}_{EX}\right)\left(\hat{\mathbf{B}}_{EX}^{*}\hat{\mathbf{B}}_{EX}\right)^{-1}\left(\mathbf{B}_{EX}^{*}\hat{\mathbf{U}}_{S,EX}\right)\hat{\boldsymbol{\Psi}}_{MODEX}\right]\right\}. \tag{2.59}$$

However, it is worth noting that:

$$\hat{\mathbf{U}}_{S,EX}\hat{\boldsymbol{\Psi}}_{MODEX}\hat{\mathbf{U}}_{S,EX}^{*} = \hat{\mathbf{U}}_{S}\hat{\boldsymbol{\Psi}}_{MODE}\hat{\mathbf{U}}_{S}^{*}, \tag{2.60}$$

and therefore, 2.59 can be written as:

$$\hat{\boldsymbol{\beta}}_{EX} = \underset{\beta\,\in\,D}{\arg\min}\left\{\mathrm{tr}\left[\left(\hat{\mathbf{U}}_{S}^{*}\mathbf{B}_{EX}\right)\left(\hat{\mathbf{B}}_{EX}^{*}\hat{\mathbf{B}}_{EX}\right)^{-1}\left(\mathbf{B}_{EX}^{*}\hat{\mathbf{U}}_{S}\right)\hat{\boldsymbol{\Psi}}_{MODE}\right]\right\}. \tag{2.61}$$

In summary, this step of the MODEX method allows the $b(z)$ polynomial to provide a greater number of roots than the number of frequencies to be estimated. A greater number of roots ensure a greater degree of freedom to accommodate them at the unit circle. With this in mind, it is intended to have better estimates.

The minimization of 2.61 is done using the same procedure used in MODE. Convergence is rapid, requiring also few iterations. The next step is to select, according to 2.29 or 2.36, the best M roots from the $2M+Q$ set of polynomials roots formed by the $\hat{\mathbf{b}}_{MODE}$ and $\hat{\mathbf{b}}_{EX}$ vectors, which will be considered the final estimates in MODEX method.

This selection of the subsets of estimates requires extra computational effort compared to the MODE method. The second step of MODEX runs the MODE method once again, so that, the whole runtime is greater than twice the original one.

Although Q can be freely chosen, it should be used with discretion, as the higher it is, the more extra roots there will be and the greater the number of subsets to evaluate. In (GERSHMAN; STOICA, 1999) a brief experimental analysis of this simulation parameter is performed and it is found that values above four do not significantly improve the MODEX performance curve when the number of signals is equal to two. The number of subsets formed is given by:

$$N_m = \frac{(2M+Q)!}{M!\,(M+Q)!}. \tag{2.62}$$

MODEX method is recommended when the number of signals is small as its complexity increases considerably as the number of signals increases.

2.4.4 Modified MODEX method

Not all MODEX extra roots are suitable for DOA estimation. By simply increasing the order of the $b(z)$ polynomial leads to the assignment of M roots associated with the signal subspace near the global minimum and Q roots associated with the noise subspace far away from the global minimum. In general, this last set of roots does not estimate the DOA angles in a suitable manner (LOPES et al., 2003).

Considering this, Modified MODEX was proposed (LOPES et al., 2003). This estimator is capable of generating roots closer to true values, generating three vectors of estimates which add up to $3M$ roots. Each of these vectors is calculated from a MODE estimation vector by applying different constraints to avoid the trivial solution $\hat{\mathbf{b}} = 0$.

It was observed that noise disturbs the estimates in different ways in each of the three estimation vectors. Thus, it is assumed that, out of the $3M$ calculated estimates, at least M are of good quality. In other words, when applying different constraints, not all roots are always affected at the same time. In addition, noise does not disturb the same DOA estimate for the same signal source in all estimate vectors.

The operation of Modified MODEX is briefly explained. First of all, a MODE solution is computed using the unit-norm non-triviality constraint $|\boldsymbol{\beta}| = 1$ (LOPES et al., 2003; KRUMMENAUER et al., 2010) vector. For M pair, $\hat{\mathbf{b}}$ has the following form:

$$\hat{\mathbf{b}} = \begin{bmatrix} \hat{b}_0 & \hat{b}_1 & \dots & \hat{b}_{\left(\frac{M}{2}-1\right)} & \hat{b}_{\frac{M}{2}} & \hat{b}^*_{\left(\frac{M}{2}-1\right)} & \dots & \hat{b}^*_1 & \hat{b}^*_0 \end{bmatrix}^T \tag{2.63}$$

and if M is odd:

$$\hat{\mathbf{b}} = \begin{bmatrix} \hat{b}_0 & \hat{b}_1 & \dots & \hat{b}_{\left(\frac{M-1}{2}\right)} & \hat{b}^*_{\left(\frac{M-1}{2}\right)} & \dots & \hat{b}^*_1 & \hat{b}^*_0 \end{bmatrix}^T . \tag{2.64}$$

From the $\hat{\mathbf{b}}$ vector, the second step generates other estimates by imposing two non-triviality constraints while minimizing Equation 2.61. The actual linear constraint is equivalent to imposing $\mathrm{Re}\left\{\hat{b}_0\right\} = 1$. However, numerical instabilities may occur when imposing this restriction, although this is not common.When this happens, the minimization of Equation 2.61 is simply repeated under the $\mathrm{Im}\left\{\hat{b}_M\right\} = 1$ constraint. This constraint is called the imaginary linear constraint. The use of these two linear constraints is sufficient to cover all practical situations and one of these solutions is always correct for all values of $\mathbf{b}$ (SILVA, 2017).

After that, the $3M$ roots are extracted from the three polynomials generated through the above mentioned process. The roots are then combined into M-tuples (or estimate vectors) and stored in the $\boldsymbol{\Omega}_c$ matrix. Thus, to select the best root combination the ML expressions 2.31 or 2.40 can be used (GERSHMAN; STOICA, 1999).

2.5 SEAD-based Methods

SEAD method was introduced in 2005 based on the distance between the two largest eigenvalues of matrix $\mathbf{R}$, a procedure that brings the differential spectrum (DS) into life (FERREIRA; LEMOS, 2005). The DS is the method's first step, it is used to indicate the DOA positions in a ULA, the set of candidate directions consists on the initial estimates. The former SEAD method showed to be robust against the harmful effects of noise, however, its algorithm did not provide accurate estimates for high SNR values, their variance did not follow the CRB.

To overcome this limitation, improved SEAD was introduced in 2009, in which an iterative strategy based on the so-called *branch-and-bound* technique was implemented to provide more accurate estimates (SILVA et al., 2013). The result was excellent, improved SEAD surpasses the performance of methods which are already well known in the literature, such as MODE and MODEX, and its performance curve overlaps the CRB curve for low SNRs.

Nevertheless, until this moment, it was not clear how DS could indicate DOA angles. This section presents the fundamental concepts for understanding SEAD-based methods.

2.5.1 Sweep Procedure

An extremely important concept in SEAD-based methods is the **sweep procedure**. It consists of arbitrating values for a test angle over a suitable angle range in order to sample the DS curve. It has emerged from the observation that the eigenvalues distribution of the estimated correlation matrix, $\hat{\mathbf{R}}$, changes accordingly with the direction of arrival angles.

For analysis purposes, the ideal correlation matrix is assumed to be available, which is presented in 2.23. The matrix $\mathbf{R}$ can be decomposed in terms of its eigenvalues (or singular values) and eigenvectors, which exhibit the same behavior as those for the $\hat{\mathbf{R}}$ matrix, as in 2.24.

An illustrative way to have a general idea of how the eigenvalues behave is through the spectral stems. In Figure 3 three situations are shown, where the sources are located at (a) (10°,45°), (b) (10°,15°) and (c) (10°,10°). As the sources get closer, the distance between the eigenvalues tends to increase, it reaches the maximum value when the two DOA angles overlap.

This observation is the key for adding a test source to the spatial correlation matrix. The test source has the same structure of the other sources, i.e., $\mathbf{a}_t(\omega_t) = \{1,\ \exp(j\omega_t), \ldots,\ \exp\left[j(K-1)\omega_t\right]\}^T$, where the index t refers to test. It is added to the system through its autocorrelation matrix, which is given by:

$$\mathbf{R}_t(\omega_t) = \sigma_t^2 \mathbf{a}_t(\omega_t)\mathbf{a}_t^*(\omega_t), \tag{2.65}$$

where, σ_t^2 is the test source power. In practical situations, the test source power is the average of the real sources, $\hat{\sigma}_t^2 = \frac{1}{MK}\sum_{m=1}^{M}\hat{\lambda}_m$.

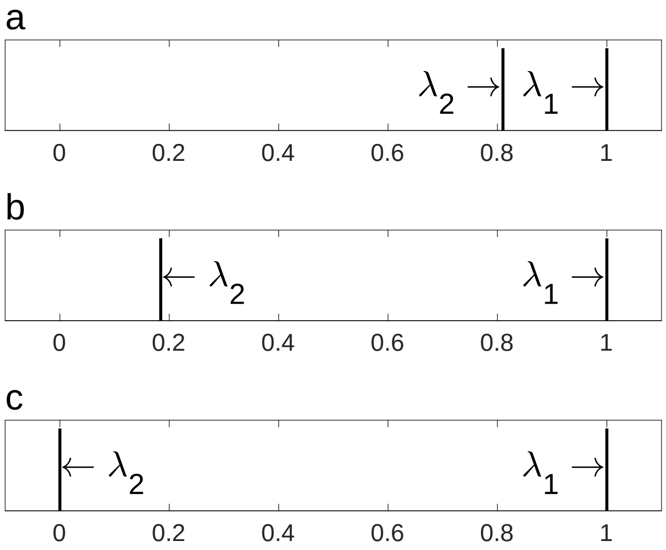

Figure 3 – The eigenvalues are strongly dependent on the flat waves direction. Normalized eigenvalues for (a) widely-spaced sources, (b) closely-spaced sources, and (c) overlapped sources. Source: Author.

Let $\mathbf{R}$ be the spatial correlation matrix, and let $\mathbf{R}_t(\omega_t)$ be the test matrix, where both matrices have dimensions $K \times K$. The modified spatial correlation matrix is defined as:

$$\mathbf{R}_m(\omega_t) = \mathbf{R} + \mathbf{R}_t(\omega_t). \tag{2.66}$$

It can be proved that the trace of the modified spatial correlation matrix is constant for all test angles.

Theorem 2.5.1 *The trace of* $\boldsymbol{R}_m(\omega_t)$ *is constant.*

Proof. By the definition of the modified spatial correlation matrix and through the knowledge that the trace of a sum is the sum of traces (subsection A.1), calculating the trace turns into:

$$\begin{aligned} \mathrm{tr}[\mathbf{R}_m(\omega_t)] &= \mathrm{tr}[\mathbf{R} + \mathbf{R}_t(\omega_t)] \\ &= \mathrm{tr}(\mathbf{R}) + \mathrm{Tr}[\mathbf{R}_t(\omega_t)]. \end{aligned} \tag{2.67}$$

First, since $\mathbf{R}$ is always the same for each test frequency its trace remains unchanged. On the other hand, $\mathbf{R}_t(\omega_t)$ changes for each test frequency, however, all terms in its main diagonal are zero-exponents, then $\mathrm{tr}[\mathbf{R}_t(\omega_t)]$ is the same for all ω_t. It is concluded that $\mathrm{tr}[\mathbf{R}_m(\omega_t)]$ is constant. $\square$

2.5.2 Differential Spectrum

After obtaining the matrix $\mathbf{R}_m$, the eigenvalue decomposition is applied for each test angle and the DS is traced. The DS is of fundamental importance for SEAD method, its prominent peaks indicates DOA positions.

Definition 2.5.1 *Considering a modified spatial correlation matrix, $\boldsymbol{R}_m(\omega_t)$, the differential spectrum is given by the difference between its largest, λ_1, and second-largest, λ_2, eigenvalues for each test angle:*

$$\mathrm{DS}(\omega_t) = \lambda_1(\omega_t) - \lambda_2(\omega_t). \tag{2.68}$$

An expression to calculate the DS in terms of a single DOA angle, denoted by ω_{DOA}, has been presented in (SILVA et al., 2013). The formulation follows from the characteristic polynomial of $\mathbf{R}_m(\omega_t)$ and it considers an array of K sensors under noise:

$$\mathrm{DS}(\omega_t) = 2\left\{K + 2\sum_{k=1}^{K-1} k\cos\left[(K-k)(\omega_{DOA} - \omega_t)\right]\right\}^{\frac{1}{2}} \tag{2.69}$$

In case ω_t is assumed to be another DOA angle, the spectrum produced represents the interaction between both throughout the search range. In this way, the difference between the two DOA angles is denoted by $\Delta\omega$, and rewriting the term inside the square root of (2.69) using Euler's formula, it follows that:

$$\begin{aligned}\mathrm{DS}(\Delta\omega) = 2\Bigg\{ & K\exp\{(j0)\} + \sum_{k=1}^{K-1} k\exp\{[-j(K-k)\Delta\omega]\} + \\ & + \sum_{k=1}^{K-1} k\exp\{[j(K-k)\Delta\omega]\}\Bigg\}^{\frac{1}{2}}.\end{aligned} \tag{2.70}$$

Then, making $n = K - k$,

$$\begin{aligned}\sum_{n=1}^{K}(K-n)\exp\{(-j(-n)\Delta\omega)\} + \sum_{n=0}^{K}(K-n)\exp\{(-jn\Delta\omega)\} &= \\ = \sum_{n=-K}^{K}(K-|n|)\exp\{(-jn\Delta\omega)\}&,\end{aligned} \tag{2.71}$$

which corresponds to the DTFT of a triangular sequence:

$$\mathrm{DTFT}\left\{K \cdot \mathrm{triang}\left(\frac{n}{K}\right)\right\} = \frac{\sin^2(K \cdot \Delta\omega/2)}{\sin^2(\Delta\omega/2)}. \tag{2.72}$$

In conclusion, the interaction between the DOA angles in an ULA produces a behavior similar to the absolute value of the sinc function with respect to $\Delta\omega$:

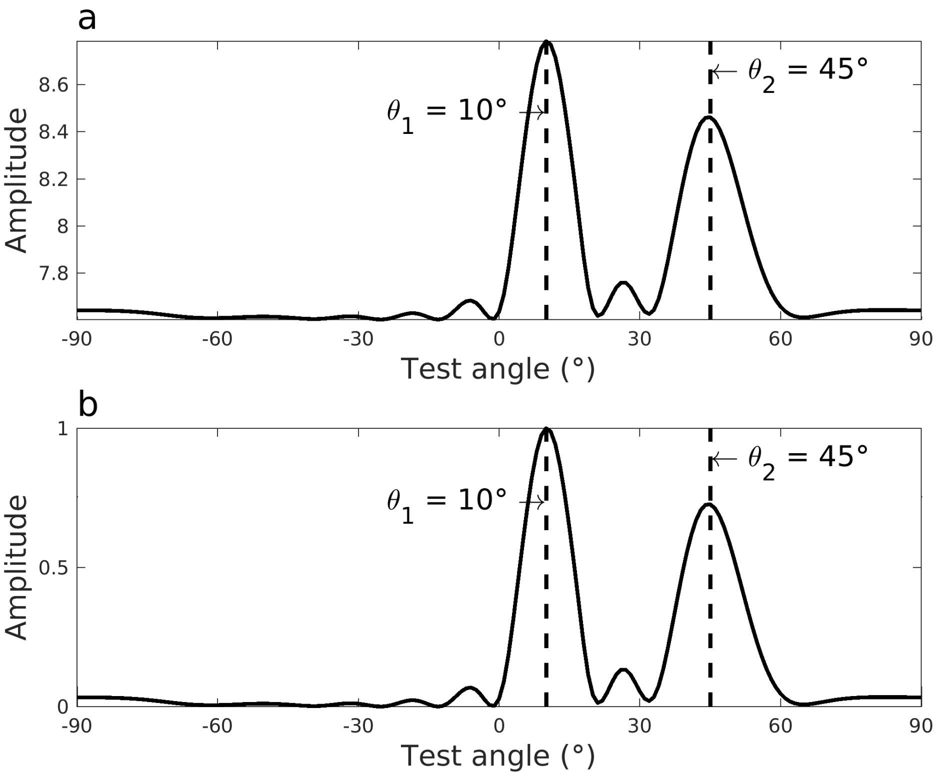

Figure 4 – Differential spectrum in its (a) original form and (b) resized form. Source: Author.

$$\mathrm{DS}(\Delta\omega) = 2\left|\frac{\sin\left(K \cdot \Delta\omega/2\right)}{\sin\left(\Delta\omega/2\right)}\right|. \tag{2.73}$$

Figure 4 (a) presents the differential spectrum in its original form with amplitudes according to the signal model formulation for uncorrelated sources positioned at 10° and 45° in the absence of noise. In Figure 4 (b) the DS values are presented in a resized manner distributed in the range [0,1]. After obtaining the difference vector, the smallest value is subtracted and then the resulting vector is divided by its largest value for the sake of better visualization. The DS in this case is the superposition of two sinc functions.

As it can be seen in Figure 4, the SEAD method does not posses good resolution due to the fact that there is a limited number of sensors, which results in one large base peak to indicate the angle. Furthermore, two sources apart from each other by 10° and located, for instance, at 10° and 20° will have only one peak indicating both angles. For shorter distances, angles are even less likely to be identified individually (SILVA et al., 2013).

2.5.3 Estimates Selection

After tracing the DS, the candidate angles should be determined. The two earlier mentioned implementations of the SEAD method can be distinguished according to the strategies chosen for the selection of estimates.

1. **First Implementation:** in the former method, the initial guesses were selected by simply differentiating the DS. The prominent peaks, which surpass an amplitude threshold, settled a search region. A second step consisted of dividing these regions into tenths of a degree and of assigning candidate angles to these positions (FERREIRA; LEMOS, 2005). Finally, the set of candidate angles were applied to 2.31 and the set of M-tuples that minimized the function was selected.
2. **Second implementation:** For better estimates at high SNR, (SILVA et al., 2013) proposed a modification on the method's estimates selection based on the *branch-and-bound* technique. This technique consists on the use of an iterative approach rather than an exhaustive search, so the time required to perform this step of the SEAD method has been dramatically reduced. The global minimum of the objective function was estimated by dividing the search range into smaller, non-overlapping sets forming a search tree. At each iteration, new boundaries were defined for the ranges and the outer values were discarded. Convergence to the global minimum is achieved when a set containing 1 element was obtained (SILVA, 2017).

The second implementation remains in use currently and a brief description of the procedure is presented in the following.

The first implementation settled an amplitude threshold to assign peaks to real DOA angles and the second implementation proceeds likewise. In (SILVA et al., 2013) a new detection threshold function is proposed, which is based on the DS and on the number of sources:

$$T_D(\omega_t) = \frac{1 - \mathrm{DS}(\omega_t)}{M}. \tag{2.74}$$

Two steps are foreseen at the refinement stage: the **preselection** and the **iterative selection**.

Preselection aims to reject spurious peaks and compare the amount of peaks with the number of sources, and thereby, generate a vector of initial estimates. To achieve this goal, the number of detected peaks is denoted by a parameter Q. It may occur that the number of candidate angles produced by the prominent peaks above T_D is different from the number of sources, one peak can also be relative to noise or more than one source (SILVA et al., 2013).

Thus, there are three possible situations given an amplitude threshold: $Q > M$, $Q = M$ or $Q < M$ (SILVA et al., 2013).

1. $Q > M$: the detected frequencies are combined M by M and stored in $\boldsymbol{\Omega}_c$. This process evaluates $C = {}^{Q!}/_{M!(M-Q)!}$ combinations;
2. $Q = M$: initial estimates are the detected frequencies. In this case $C = 0$;
3. $Q < M$: all detected peaks are assumed as incident signals. Initially, the left and right valleys points $(\omega_{(v,q,l)},\omega_{(v,q,r)})$ are stored and also the pinnacle of the q-th detected peak $(\omega_{(p,q)})$, $q = 1, 2, \ldots, Q$. Hence, each peak is assumed to refer to one or more frequencies. Denoting each peak as a bin, each bin will contain at least one frequency, represented by $b_q = 1$ and at most $b_q = M - Q + 1$, such that $\sum_{q=1}^{Q} b_q = M$. The amount of required combinations is $C = {}^{(M-1)!}/_{(M-Q)!(Q-1)!}$. Additional estimates for each peak are calculated by:

$$\hat{\omega}_{(l,q,n)} = \omega_{(p,q)} - \frac{n\Delta\omega_{(l,q)}}{2(N_q + 1)}; \tag{2.75}$$

$$\hat{\omega}_{(r,q,n)} = \omega_{(p,q)} + \frac{n\Delta\omega_{(r,q)}}{2(N_q + 1)}, \tag{2.76}$$

where $n = \{1, 2, \ldots, N_q\}$, $N_q = {}^{(b_q-1)}/_2$ if b_q is odd and $N_q = {}^{b_q}/_2$ if b_q is even, $\Delta\omega_{(l,q)} = \omega_{(p,q)} - \omega_{(v,q,l)}$ and $\Delta\omega_{(r,q)} = \omega_{(v,q,r)} - \omega_{(p,q)}$ are the left and right width, respectively.

The best combination of M-tuples in $\boldsymbol{\Omega}_c$ is selected as the initial guesses using the ML expressions 2.31 or 2.40. Once it is determined, the next step is to apply the *branch-and-bound* technique in the iterative selection stage (SILVA et al., 2013).

This procedure branches each $\hat{\omega}_m$ estimate in the initial guesses vector by generating two candidate estimates, one on the left $(\hat{\omega}_{(l,m)})$ and another on the right $(\hat{\omega}_{(r,m)})$ of ω_m. Thus, for each signal source a group with the frequencies $\left\{\hat{\omega}_{(l,m)},\hat{\omega}_m,\hat{\omega}_{(r,m)}\right\}$ is settled. In the first iteration, $\hat{\omega}_{(l,m)}$ and $\hat{\omega}_{(r,m)}$ are calculated as follows:

$$\hat{\omega}_{(l,m)} = \hat{\omega}_m - \frac{\Delta\omega_{(l,q)}}{4(N_q + 1)}; \tag{2.77}$$

$$\hat{\omega}_{(r,m)} = \hat{\omega}_m - \frac{\Delta\omega_{(r,q)}}{4(N_q + 1)}, \tag{2.78}$$

with $q = \{1, 2, \ldots, Q\}$ and $\Delta\omega_{(l,q)}$ and $\Delta\omega_{(r,q)}$ are associated with the q-th peak. The steps ${}^{\Delta\omega_{(l,i)}}/_{4(n+1)}$ and ${}^{\Delta\omega_{(r,i)}}/_{4(n+1)}$ correspond to half the width between frequencies on the same side of the peak to avoid overlapping of the adjacent groups.

In the following, these groups are combined and generate new estimates, which are later stored in $\boldsymbol{\Omega}_c$. However, it is important to note that frequencies belonging to the same group are not combined in order to avoid ineffective combinations. Then, the best combination in $\boldsymbol{\Omega}_c$ is selected using the procedures 2.31 or 2.40. This process is repeated to an arbitrary limit and the steps are halved at each iteration to improve resolution. Finally, the DOA estimate vector $\hat{\boldsymbol{\Theta}}$ is calculated from the combination of the selected frequencies.

3 Differential Spectrum Analysis and the Use of Matrix Norms in SEAD-based Methods

The DS, as defined in 2.68, has no theoretical framework, the definition is based on the observations and it is empirically motivated. This chapter presents the mathematical fundamentals that support the use of DS as a DOA estimator and discusses how the components on DS contribute for rising peaks on DOA positions.

3.1 Investigating the Differential Spectrum Components

By definition, the DS is obtained from the difference between the two largest eigenvalues of the modified spatial correlation matrix. However, a concern arises as to understand why only these specific eigenvalues are used. The total differential spectrum (TDS) emerged in this context as an attempt to deeply understand the contribution given by each eigenvalue. In TDS not only the second-largest eigenvalue is subtracted from the first, but all the others as well.

Definition 3.1.1 *For a modified spatial correlation matrix, $\boldsymbol{R}_m(\omega_t)$, the total differential spectrum is defined as the difference between the largest eigenvalue, λ_1, and the sum of the other eigenvalues, $\sum_{k=2}^{K}\lambda_k$. In mathematical terms:*

$$\mathrm{TDS}(\omega_t) = \lambda_1(\omega_t) - \lambda_2(\omega_t) - \cdots - \lambda_K(\omega_t). \tag{3.1}$$

Theorem 3.1.1 *The TDS is equivalent to a matrix norm calculation.*

Proof. The TDS can be rewritten as follows:

$$\mathrm{TDS} = 2\|\mathbf{R}_m\|_{2_i} - \mathrm{tr}\left(\mathbf{R}_m\right), \tag{3.2}$$

where $\| \bullet \|_{2_i}$ stands for the matrix norm induced by the vector 2-norm (MEYER, 2001; BOLDRINI et al., 1980).

Theorem 2.5.1 guarantees the $\mathrm{tr}(\mathbf{R}_m)$ is constant, and since the factor 2 is only a scaling factor, it does not contribute to the emerging peaks in the spectrum. Thus, the matrix norm is the only responsible for the rising peaks in the TDS. ☐

Figure 5 presents this behavior for two uncorrelated sources (10°,15°) impinging on a ULA with 10 omnidirectional sensors in the absence of noise.

From this fact, it is straightforward to consider the use of other matrix norm types in order to trace the angular spectrum.

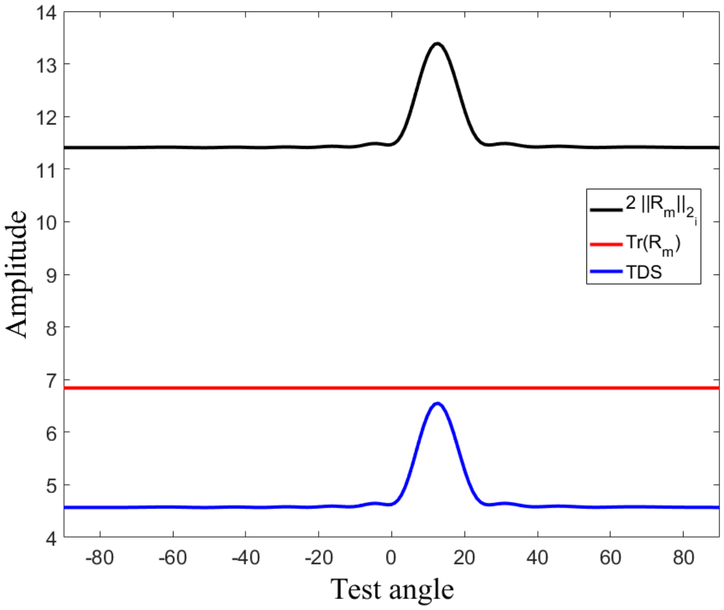

Figure 5 – TDS behavior and its components. Source: Author.

3.2 Matrix **R** and the Behavior of Different Norms

In the last section, it was shown that the first eigenvalue, which is also a matrix norm, increases near true DOA positions. Now the main matrix norms are assessed in order to verify how they behave in different DOA situations.

Table 1 shows a comparison between the norm values considering the 1-norm, 1_i-norm, 2-norm and 2_i-norm for the cases of great interest: widely-spaced, closely-spaced and overlapped sources.

Table 1 – Norm values of **R** for specific cases: widely-spaced, closely-spaced and overlapped sources.

Norms	(10°,45°)	(10°,15°)	(10°,10°)
1-norm	128,02	172,15	200
1_i-norm	13,73	18,51	20
2-norm	14,24	17,50	20
2_i-norm	11,16	17,29	20

According to the Table 1, all matrix norms increase as the sources get closer. This means that they can also indicate candidate angles in SEAD-based methods.

As a consequence, it is reasonable to propose a new approach based on matrix norms to replace the procedure using DS. The proposal consists of modifying only the initial guess stage, therefore, the refinement process remains unchanged. The main objective now is to prove that matrix norms are DOA estimators.

3.3 Mathematical Analysis of DOA Estimation by Matrix Norms

This section discusses the matrix norms as estimators and presents the mathematical fundamentals that support this statement, which express their capability to perform DOA estimation. Not all norms will be assessed and the reason is as follows.

Subsection A.2 lists the most commonly used types of norms. From the six possibilities, only four norm types will be evaluated as estimators, which are the 1-norm, the 1_i-norm, the 2-norm and 2_i-norm. The others are excluded because of two observations:

- for symmetrical or hermitian matrices the rows and columns are interchangeable, so that:

$$\|\mathbf{A}\|_1 = \|\mathbf{A}\|_\infty, \tag{3.3}$$

  where $\mathbf{A}$ is a square matrix, thus the 1-norm is sufficient.
- The ∞_i-norm needs some algebraic manipulation to fulfill all norm properties and, as noted in previous experiments, it does not provide consistent estimates.

Considering the elected four matrix norms, there is a very relevant common feature, they rely on the absolute value of the entries. According to the equations A.4, A.5 A.7, the norms are calculated exactly over the absolute value of the matrix entries, followed by different combinations in order to obtain the specific matrix norm value. However, the matrix 2_i-norm does not express a straightforward relationship with the entries, but it will be shown later that the same analysis, which is developed in Theorem 3.3.1, is valid.

Theorem 3.3.1 *Given a modified spatial correlation matrix, $\boldsymbol{R}_m(\omega_t)$, the matrix norms are direction of arrival estimators.*

Proof. Firstly, as presented along the Appendix B, the matrices in (2.66) should be rewritten in terms of the angular frequencies, such that the general term of $\mathbf{R}_m$ is:

$$[\mathbf{R}_m(\omega_t)]_{rc} = \left[\sum_{\beta=1}^{M}\sum_{\alpha=1}^{M} \rho_{\alpha\beta} \exp\{-j[(c-1)\omega_\alpha - (r-1)\omega_\beta]\}\right] + \exp[-j(c-r)\omega_t], \tag{3.4}$$

where, ω_α and ω_β stand the DOA angles. The indexes r and c are relative to the row and columns of the matrix, respectively.

Performing a change of variables by expressing $\Gamma = (c-1)\omega_\alpha - (r-1)\omega_\beta$ and $\gamma = (c-r)\omega_t$, it follows that:

$$\begin{aligned} |\,[\mathbf{R}_m]_{rc}\,| &= \left| \left(\sum_{\beta=1}^{M} \sum_{\alpha=1}^{M} \rho_{\alpha\beta} \exp\{(-j\Gamma)\} \right) + \exp\{(-j\gamma)\} \right| \\ &= \left| \left\{ \sum_{\beta=1}^{M} \sum_{\alpha=1}^{M} \rho_{\alpha\beta} \left[\cos(\Gamma) - j\sin(\Gamma)\right] \right\} + \left[\cos(\gamma) - j\sin(\gamma)\right] \right|. \end{aligned} \tag{3.5}$$

But the entries of $\mathbf{R}_m$ are complex numbers. Therefore, the absolute value definition of a complex number is applied on the entries to obtain:

$$|\,[\mathbf{R}_m]_{rc}\,| = \left\{ \left[\sum_{\beta=1}^{M} \sum_{\alpha=1}^{M} \rho_{\alpha\beta} \cos(\Gamma) + \cos(\gamma) \right]^2 + \left[\sum_{\beta=1}^{M} \sum_{\alpha=1}^{M} \rho_{\alpha\beta} \sin(\Gamma) + \sin(\gamma) \right]^2 \right\}^{1/2}. \tag{3.6}$$

Solving the squares within the square root follows that:

$$\begin{aligned} |\,[\mathbf{R}_m]_{rc}\,| = \Bigg\{ & \left[\sum_{\beta=1}^{M} \sum_{\alpha=1}^{M} \rho_{\alpha\beta} \cos(\Gamma) \right]^2 + 2 \sum_{\beta=1}^{M} \sum_{\alpha=1}^{M} \rho_{\alpha\beta} \cos(\Gamma)\cos(\gamma) + \cos^2(\gamma) + \\ & + \left[\sum_{\beta=1}^{M} \sum_{\alpha=1}^{M} \rho_{\alpha\beta} \sin(\Gamma) \right]^2 + 2 \sum_{\beta=1}^{M} \sum_{\alpha=1}^{M} \rho_{\alpha\beta} \sin(\Gamma)\sin(\gamma) + \sin^2(\gamma) \Bigg\}^{1/2}. \end{aligned} \tag{3.7}$$

Considering the trigonometric identities:

$$\cos(\Gamma + \gamma) = \cos(\Gamma)\cos(\gamma) - \sin(\Gamma)\sin(\gamma); \tag{3.8}$$

$$\cos(\Gamma - \gamma) = \cos(\Gamma)\cos(\gamma) + \sin(\Gamma)\sin(\gamma), \tag{3.9}$$

followed by the addition and subtraction of the expressions 3.8 and 3.9, it results in:

$$\cos(\Gamma)\cos(\gamma) = \frac{1}{2}\left[\cos(\Gamma+\gamma) + \cos(\Gamma-\gamma)\right]; \tag{3.10}$$

$$\sin(\Gamma)\sin(\gamma) = \frac{-1}{2}\left[\cos(\Gamma+\gamma) - \cos(\Gamma-\gamma)\right], \tag{3.11}$$

then replacing 3.10 and 3.11 in 3.7 yields:

$$\begin{aligned} |\,[\mathbf{R}_m]_{rc}\,| = \Bigg\{ & \left[\sum_{\beta=1}^{M} \sum_{\alpha=1}^{M} \rho_{\alpha\beta} \cos(\Gamma) \right]^2 + \left[\sum_{\beta=1}^{M} \sum_{\alpha=1}^{M} \rho_{\alpha\beta} \sin(\Gamma) \right]^2 + \\ & + \sum_{\beta=1}^{M} \sum_{\alpha=1}^{M} \rho_{\alpha\beta} \left[\cos(\Gamma+\gamma) + \cos(\Gamma-\gamma)\right] - \\ & - \sum_{\beta=1}^{M} \sum_{\alpha=1}^{M} \rho_{\alpha\beta} \left[\cos(\Gamma+\gamma) - \cos(\Gamma-\gamma)\right] + 1 \Bigg\}^{1/2}. \end{aligned} \tag{3.12}$$

Finally, excluding null terms, the following equation is reached:

$$\begin{aligned} |\,[\mathbf{R}_m]_{rc}\,| = \Bigg\{ & \left[\sum_{\beta=1}^{M} \sum_{\alpha=1}^{M} \rho_{\alpha\beta} \cos(\Gamma) \right]^2 + \left[\sum_{\beta=1}^{M} \sum_{\alpha=1}^{M} \rho_{\alpha\beta} \sin(\Gamma) \right]^2 + \\ & + 2 \left[\sum_{\beta=1}^{M} \sum_{\alpha=1}^{M} \rho_{\alpha\beta} \cos(\Gamma-\gamma) \right] + 1 \Bigg\}^{1/2}, \end{aligned} \tag{3.13}$$

which express that the values of $|\,[\mathbf{R}_m]_{rc}\,|$ are given by the DOA angles, the test angle, and the correlation between the sources. Worth to note is that the only term that interrelates ω_t and the DOA angles is:

$$\cos(\Gamma-\gamma)=\cos\left[(c-1)\omega_\alpha-(r-1)\omega_\beta-(c-r)\omega_t\right] \tag{3.14}$$

The DOA angles in Γ are always the same throughout the spectrum tracing process, they are independent of ω_t. Thus, the other terms remain constant, such that $|[\mathbf{R}_m]_{rc}|$ is maximum whenever $\cos(\Gamma-\gamma)$ reaches its maximum value. $\square$

Remark 1 *Regarding the influence of the correlation between the sources, two possibilities should be highlighted:*

- *for uncorrelated sources ($\rho_{\alpha\beta}=0$, whenever $\alpha\neq\beta$)*

$$\begin{aligned}\sum_{\beta=1}^{M}\sum_{\alpha=1}^{M}\rho_{\alpha\beta}\cos(\Gamma-\gamma) &= \sum_{\alpha=\beta=1}^{M}\rho_{\alpha\alpha}\cos\left[(c-1)\omega_\alpha-(r-1)\omega_\alpha-(c-r)\omega_t\right]\\ &=\sum_{\alpha=1}^{M}\cos\left[(c-r)\omega_\alpha-(c-r)\omega_t\right]\\ &=\sum_{\alpha=1}^{M}\cos\left[(c-r)\left(\omega_\alpha-\omega_t\right)\right].\end{aligned} \tag{3.15}$$

  The absolute value of each input depends on the difference between the DOA and the test angle, and if $\omega_t=\omega_\alpha$, the cosine function will be maximum. The other DOA angles will contribute to the sum according to their distances from ω_t. This occurs for every ω_t in the $(-\pi,\pi)$ range, for instance.

- *for correlated sources (at least one $\rho_{\alpha\beta}\neq 0$, for any $\alpha\neq\beta$)*

$$\begin{aligned}\sum_{\beta=1}^{M}\sum_{\alpha=1}^{M}\rho_{\alpha\beta}\cos(\Gamma-\gamma) &= \sum_{\alpha=\beta=1}^{M}\rho_{\alpha\alpha}\cos(\Gamma-\gamma)+\sum_{\beta=1}^{M}\sum_{\alpha=1}^{M}\rho_{\alpha\beta}\cos(\Gamma-\gamma)\\ &=\sum_{\alpha=\beta=1}^{M}\cos\left[(c-r)\left(\omega_\alpha-\omega_t\right)\right]\\ &\quad+\sum_{\beta=1}^{M}\sum_{\alpha=1}^{M}\rho_{\alpha\beta}\cos\left[(c-1)\omega_\alpha-(r-1)\omega_\beta-(c-r)\omega_t\right].\end{aligned} \tag{3.16}$$

  The absolute value of each entry is related to the difference between DOA and ω_t, however, there are other terms that contribute to the sum. Consequently the peaks relative to the DOA angles are reinforced and tend to produce more consistent initial estimates when compared to the uncorrelated situation. It will be discussed later in the section 4.3.

For the 2_i-norm it is possible to establish a relationship with the analysis performed in 3.3.1, although this norm is not directly calculated over the absolute values of the matrix entries. To establish this connection, the singular value decomposition is considered. The SVD is based in the concept of linear transformation, where the original matrix is decomposed into a full-rank diagonal $\mathbf{\Lambda}$ matrix and two adjacent orthonormal matrices, $\mathbf{U}$ and $\mathbf{V}^*$. This process is commonly performed by the rotation method or alternatively by the Gram-Schmidt procedure, which the latter can be described as:

$$\mathbf{R}_m = \mathbf{U}\ \mathbf{T}, \tag{3.17}$$

where, $\mathbf{U} = (\mathbf{u}_1|\mathbf{u}_2|\ldots|\mathbf{u}_K)$,

$$\mathbf{T} = \begin{pmatrix} t_1 & \mathbf{u}_1^*\mathbf{r}_2 & \ldots & \mathbf{u}_1^*\mathbf{r}_K \\ 0 & t_2 & \ldots & \mathbf{u}_2^*\mathbf{r}_K \\ \vdots & \vdots & \ddots & \vdots \\ 0 & 0 & \ldots & t_K \end{pmatrix}$$

$t_1 = |\mathbf{r}_1|$, $t_i = |\mathbf{r}_i - \sum_{k=1}^{K-1}(\mathbf{u}_k^*\mathbf{r}_i)\mathbf{u}_k|$, $\forall\ i > 1$.

Then the same procedure is applied to $\mathbf{T}^*$ resulting in:

$$\mathbf{R}_m = \mathbf{U}\begin{pmatrix} \mathbf{\Lambda}_{M\times M} & \mathbf{0} \\ \mathbf{0} & \mathbf{0} \end{pmatrix}\mathbf{V}^*. \tag{3.18}$$

During the execution of the Gram-Schmidt procedure, the matrix $\mathbf{T}$ stores the Euclidian norm of the column vector from matrix $\mathbf{R}_m$, represented by t_1, and the projected versions of the other column vectors, t_i, in its main diagonal. Thus, it is evident that the same behavior demonstrated by 3.3.1 holds when calculating the 2_i-norm. It is then concluded that the peaks produced in its angular spectrum depends on the distance between the DOA and the test angle.

3.4 Eigenvalues Behavior

It is known that the trace of the matrix $\mathbf{R}_m(\omega_t)$ is constant, in addition, it is true that:

$$\mathrm{tr}\left[\mathbf{R}_m(\omega_t)\right] = \sum_{k=1}^{K}\lambda_i(\omega_t). \tag{3.19}$$

As the largest eigenvalue increases, the remaining eigenvalues should decrease. Hence, the following statements are true:

- λ_1 has the greatest magnitude among the eigenvalues and presents peaks at DOA positions;
- the eigenvalues $\{\lambda_2, \ldots, \lambda_{M+1}\}$ show valleys on DOA positions;

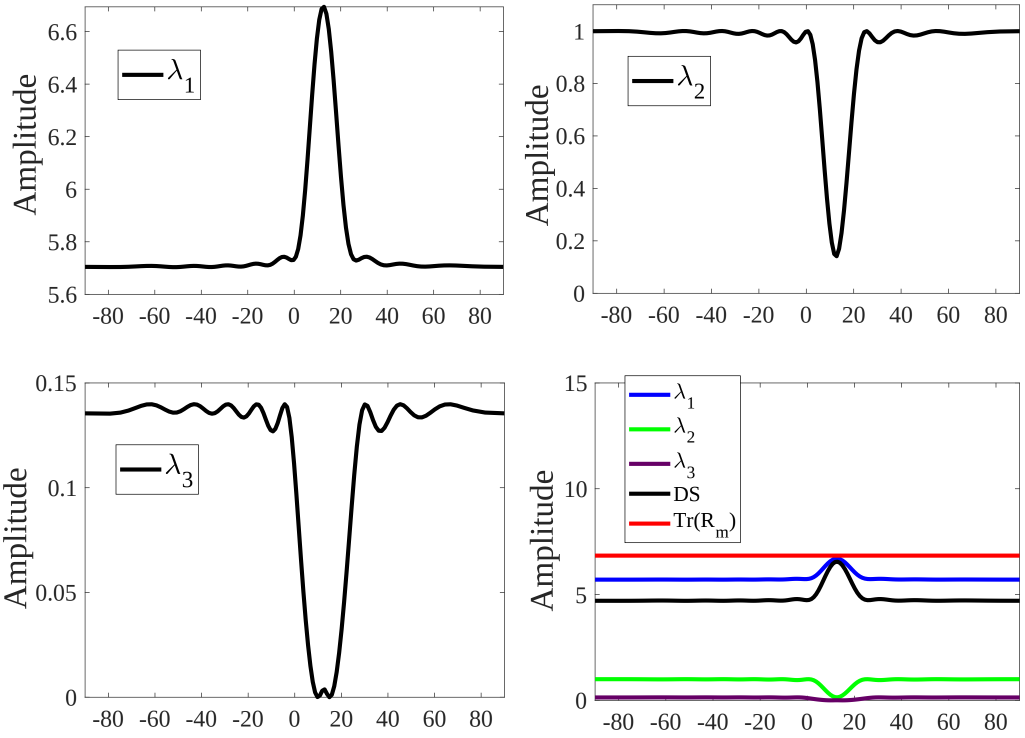

Figure 6 – Eigenvalues behavior for two uncorrelated sources located at (10°,15°). Source: Author.

- the other eigenvalues $\{\lambda_{M+2}, \ldots, \lambda_K\}$ are equal to zero in the absence of noise, i.e. for $\mathbf{R} = \mathbf{APA}^*$, or equal to the noise power σ^2, when $\mathbf{R} = \mathbf{APA}^* + \sigma^2\mathbf{I}$.

The Figure 6 presents the behavior of eigenvalues for the case of uncorrelated sources located at 10° and 15° and in the absence of noise.

The subtraction of the eigenvalues in DS implies on the amplification of the peak, which motivates the following remark.

Remark 2 *The DS is actually a norm estimator with an additional term, the second-largest eigenvalue, that amplifies the peaks and reduces the noise influence.*

3.5 Chapter Conclusion

Within this chapter, it was discussed the motivation to perform a detailed analysis over the differential spectrum components. The differential spectrum was empirically supported, but it had no theoretical framework. The operations over the eigenvalues were argued resulting in the total differential spectrum, which proven to be a matrix norm calculation. The matrix norms were investigated and had proven to be estimators for the direction of arrival of planar waves. A mathematical formulation was delivered, which describes the relationship among the real direction of arrival angles and the test angle. It is a general expression, so that it holds for any number of sources, any number of sensors, any correlation factor and for direction of arrival angles. It is worth mentioning that the matrix norm approach profit from the correlation among sources, which is a big advantage for in-door and urban communication systems where the probability of reflected signals is very high. The eigenvalues also play an important role on the differential spectrum calculation. The first eigenvalue shows peaks in positions relative to existing sources directions and the other eigenvalues in the signal subspace show valleys, such that, the difference between the largest and the second-largest eigenvalues will emphasize the peaks.

4 Simulated Results

In order to evaluate the accuracy of DOA estimates obtained from the methods discussed in the last chapter, 1000 Monte Carlo simulations were performed for each SNR in the range of -15 to 15 dB with steps of 1.25 dB. It is assumed $M = 2$ planar waves impinging on a ULA composed of $K = 10$ half-wavelength spaced sensors and that $N = 100$ snapshots.

The comparison is performed considering the proposed norm matrix alternatives to the DS and three other methods that are already established in the literature. The first is the MODEX (GERSHMAN; STOICA, 1999) method, the second is its enhanced version, the Modified MODEX (LOPES et al., 2003). The third method used in the comparison is the Improved SEAD (SILVA, 2017), which is the second implementation of SEAD method.

All simulations were performed on MATLAB® version R2016b, running on an Intel Core i7-6800K, 32 GB RAM with Microsoft Windows 10 64-bit operating system.

4.1 Norm Spectra

Similar to what happens in the differential spectrum, each matrix norm generates the angular spectra, such that, the initial estimates are obtained by peaks in the generated spectrum.

Figure 7 shows the possible spectrum types, where the sources are close to each other and located at (10°,15°) for three different SNR values ($0, -10$ and -15 dB).

The spectra are found to be very similar to each other, except for the 1_i-norm. All spectra were useful for indicating the position of sources through the prominent peaks, which have higher amplitude than other existing peaks.

There is little difference between the DS, 2-norm, and 2_i-norm spectra. The relationship between the DS and the 2_i-norm is evident, both depend on the largest eigenvalue, which determines the position of the peak. The 2-norm is also the Frobenius norm, which has a close relationship with the eigenvalues because it is the sum of all squared eigenvalues, as seen in (MEYER, 2001; KUNZLER et al., 2015).

There are 10 sensors recording complex amplitude values implying in poor resolution of the spectra and it is not ideal for separating close sources. It can be observed in Figure 7 that the same peak represents two distinct sources, however, they will be individualized in the refinement process.

Due to noise added to the signals, there are spurious peaks that arise on random

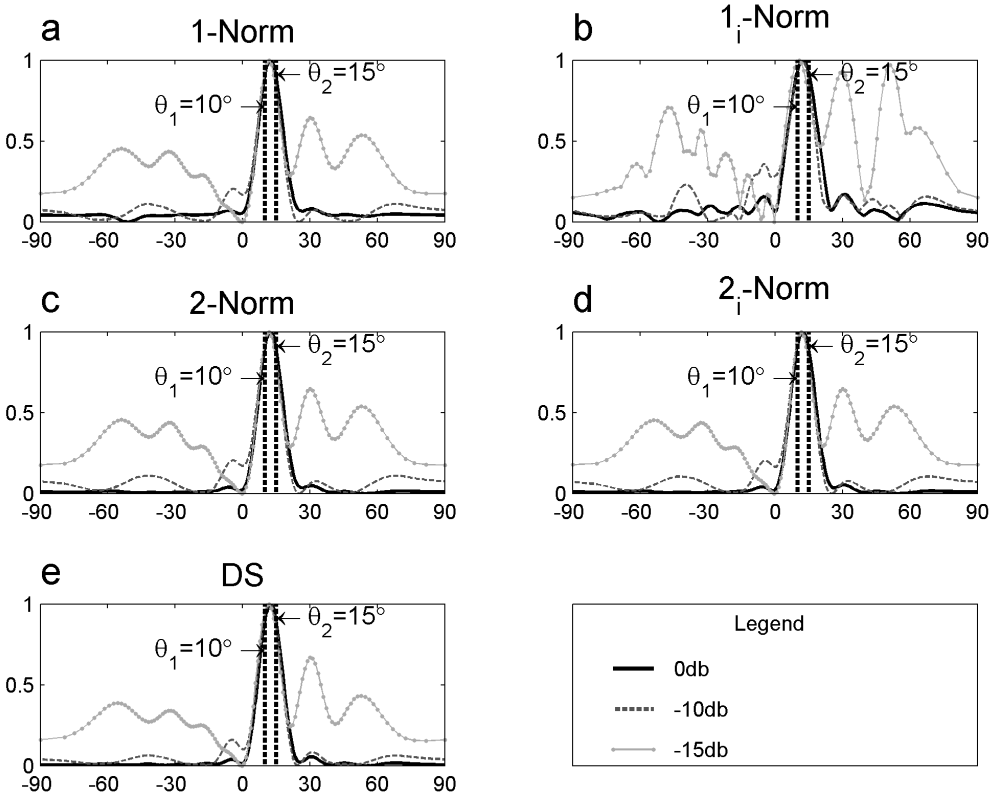

Figure 7 – Spectra produced by (a) $\|\mathbf{R}_m\|_1$, (b) $\|\mathbf{R}_m\|_{1_i}$, (c) $\|\mathbf{R}_m\|_2$, (d) $\|\mathbf{R}_m\|_{2_i}$ and (e) DS for closely-spaced sources located at 10° and 15° for SNR values equal to -15 dB, -10 dB, and 0 dB. Source: Author.

positions, they can increase and may even exceed peaks relative to real sources. The refinement process selects the larger peaks to perform the optimization and some concerns may arise regarding the spurious peaks which have a high amplitude, they can induce the method to false estimates.

Another case to consider is when the sources are widely-spaced. Figure 8 shows the spectra for sources at (10°,45°) for three different SNR scenarios.

The spectra are also very similar to each other. The direction in which a planar wave travels is indicated by large peaks that rise on DOA positions, but the noise disturbs tracing the spectrum.

The 2-norm and 2_i-norm provide very similar spectra, on the other hand, the DS shows slightly different behavior in this case. The second eigenvalue in the DS calculation changes the peaks amplitude ratio, it can be seen that the peak relative to the source on (45°) is attenuated when compared to 1-norm, 2-norm and 2_i-norm. There is still a strong relationship between DS and other norms for higher SNR values.

For widely distant sources the spectrum shows two distinct peaks relative to each

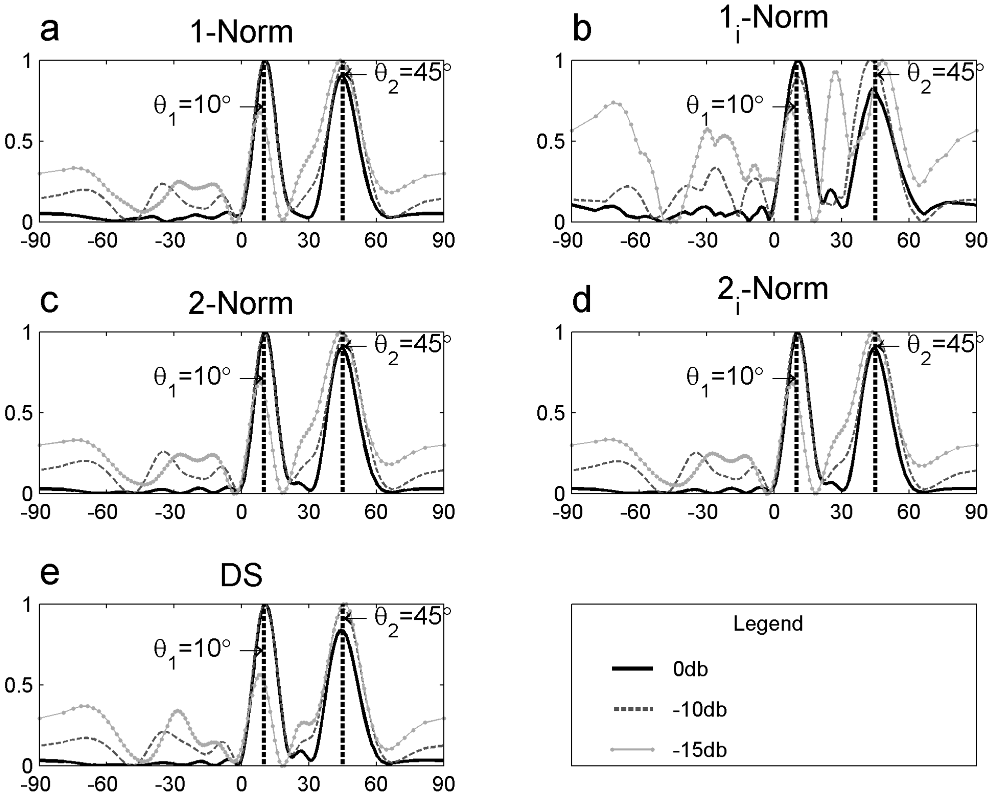

Figure 8 – Spectra produced by (a) $\|\mathbf{R}_m\|_1$, (b) $\|\mathbf{R}_m\|_{1_i}$, (c) $\|\mathbf{R}_m\|_2$, (d) $\|\mathbf{R}_m\|_{2_i}$ and (e) DS for widely-spaced sources located at 10° and 45° for SNR values equal to −15 dB, −10 dB, and 0 dB. Source: Author.

signal source. Even in this situation, the refinement process is necessary because the peaks are displaced from the correct position and the estimation accuracy should be improved.

4.2 Performance Comparison

The simulations were performed by setting one source at 10° and varying the other in the range −40° to 60°. Two dashed lines highlight the most relevant cases in the DOA estimation problem, which are two closely-spaced sources located at (10°,15°) and two widely-spaced sources located at (10°,45°).

The simulations were performed using the $\|\mathbf{R}_m\|_1$, $\|\mathbf{R}_m\|_{1_i}$, $\|\mathbf{R}_m\|_2$ and $\|\mathbf{R}_m\|_{2_i}$. In the following, the results for uncorrelated and correlated sources will be discussed.

4.2.1 Uncorrelated Sources

Figures 9, 10, 11, 12, 13, 14, and 15 present the performances of each method in terms of the error surface given by the RMSE for each estimate.

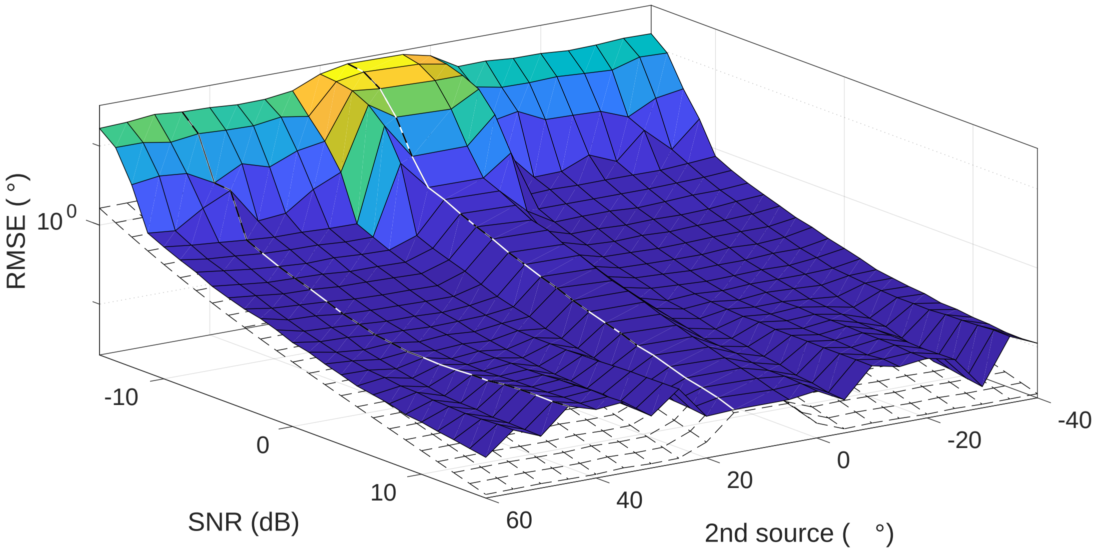

Figure 9 – RMSE of 1-norm for uncorrelated sources. One source is fixed at 10° and another sweeps the range from 60° until −40°. The SNR is in the range (−15,15) dB. Two representative situations are highlighted by dashed lines, where the sources are located at (10°,15°) and (10°,45°). Source: Author.

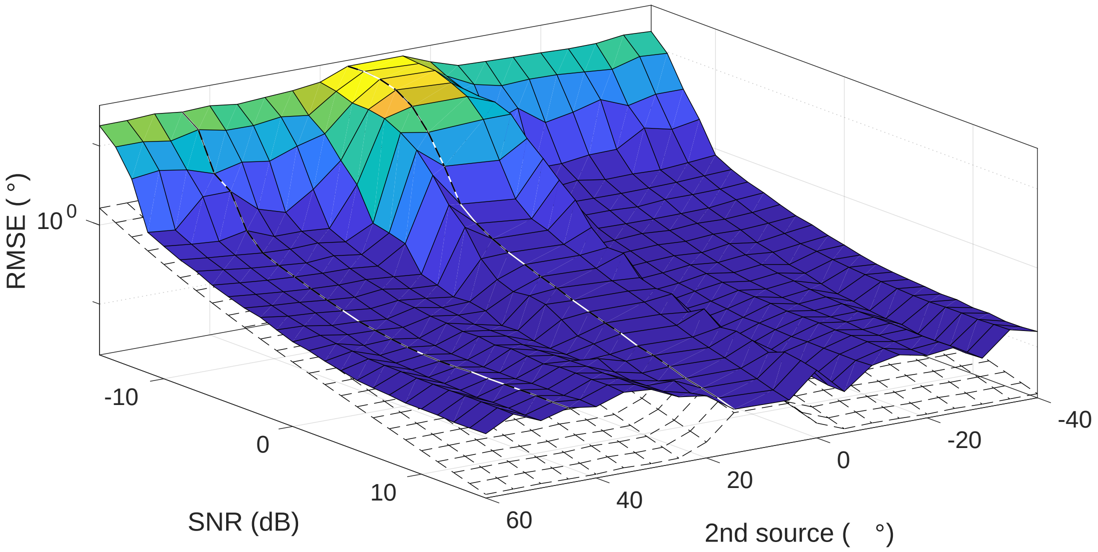

Figure 10 – RMSE of 1_i-norm for uncorrelated sources. One source is fixed at 10° and another sweeps the range from 60° until −40°. The SNR is in the range (−15,15) dB. Two representative situations are highlighted by dashed lines, where the sources are located at (10°,15°) and (10°,45°). Source: Author.

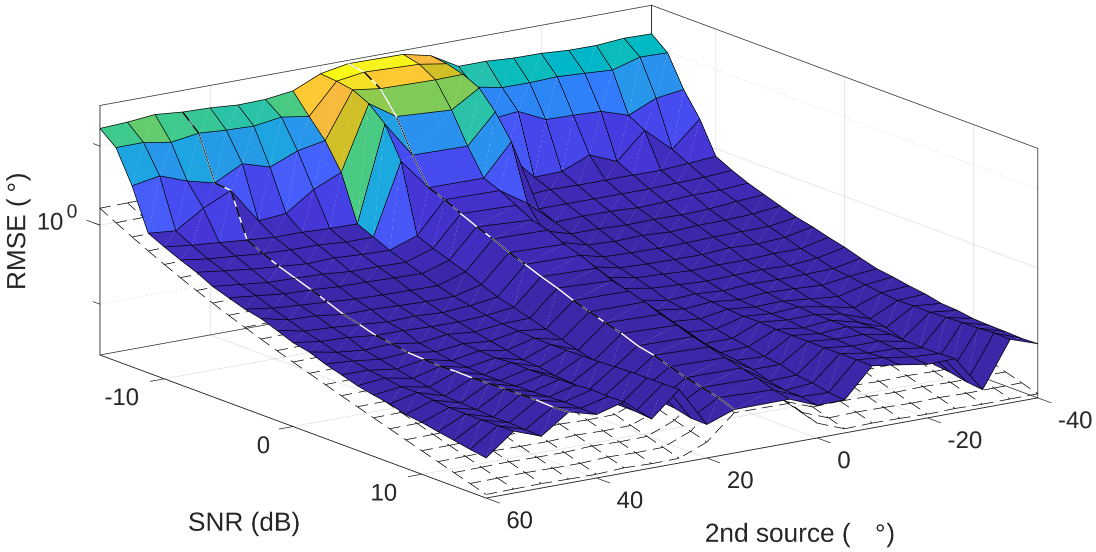

Figure 11 – RMSE of 2-norm for uncorrelated sources. One source is fixed at 10° and another sweeps the range from 60° until −40°. The SNR is in the range (−15,15) dB. Two representative situations are highlighted by dashed lines, where the sources are located at (10°,15°) and (10°,45°). Source: Author.

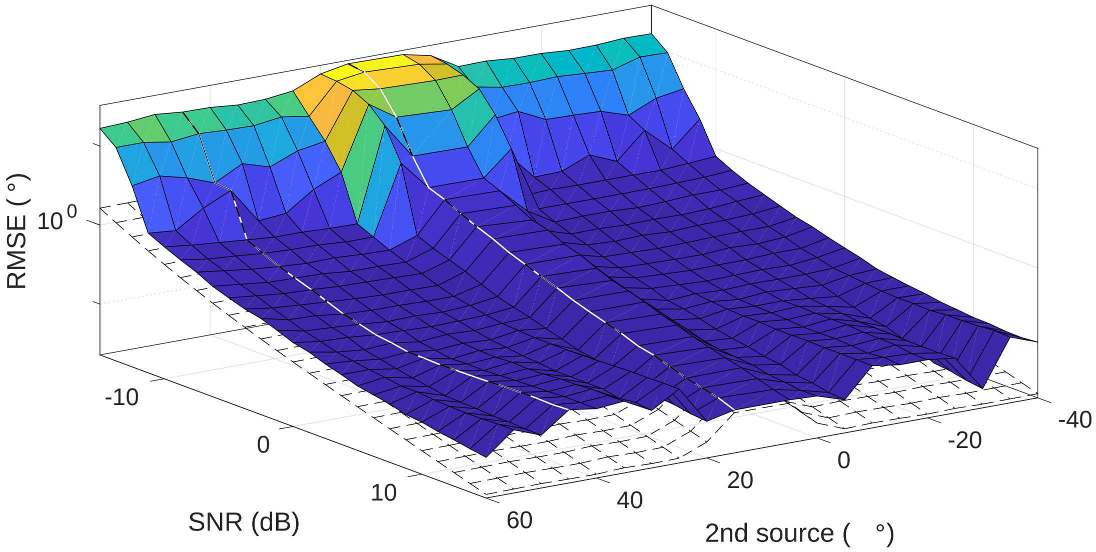

Figure 12 – RMSE of 2_i-norm for uncorrelated sources. One source is fixed at 10° and another sweeps the range from 60° until −40°. The SNR is in the range (−15,15) dB. Two representative situations are highlighted by dashed lines, where the sources are located at (10°,15°) and (10°,45°). Source: Author.

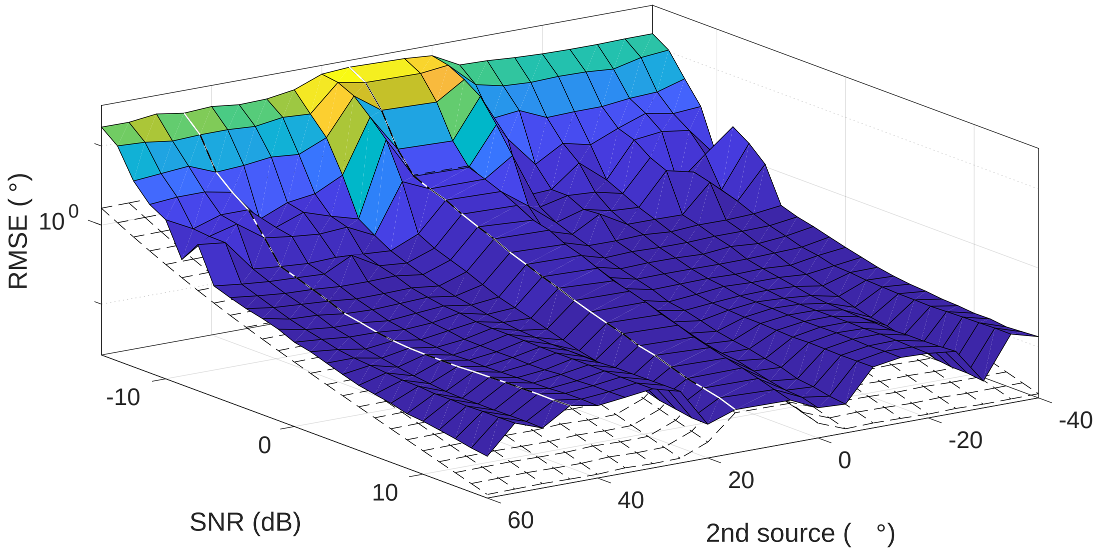

Figure 13 – RMSE of Improved SEAD for uncorrelated sources. One source is fixed at 10° and another sweeps the range from 60° until −40°. The SNR is in the range (−15,15) dB. Two representative situations are highlighted by dashed lines, where the sources are located at (10°,15°) and (10°,45°). Source: Author.

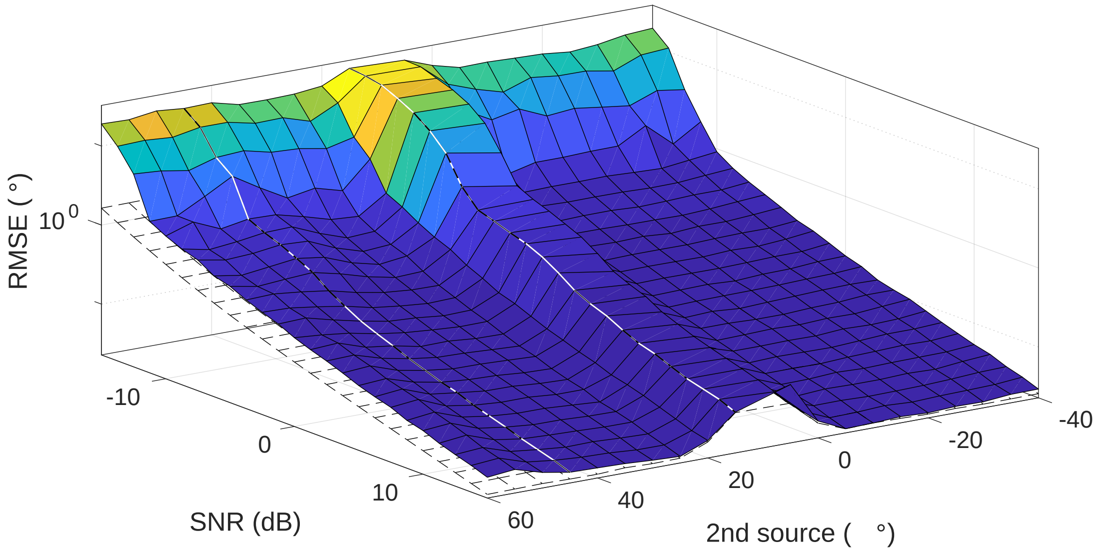

Figure 14 – RMSE of MODEX for uncorrelated sources. One source is fixed at 10° and another sweeps the range from 60° until −40°. The SNR is in the range (−15,15) dB. Two representative situations are highlighted by dashed lines, where the sources are located at (10°,15°) and (10°,45°). Source: Author.

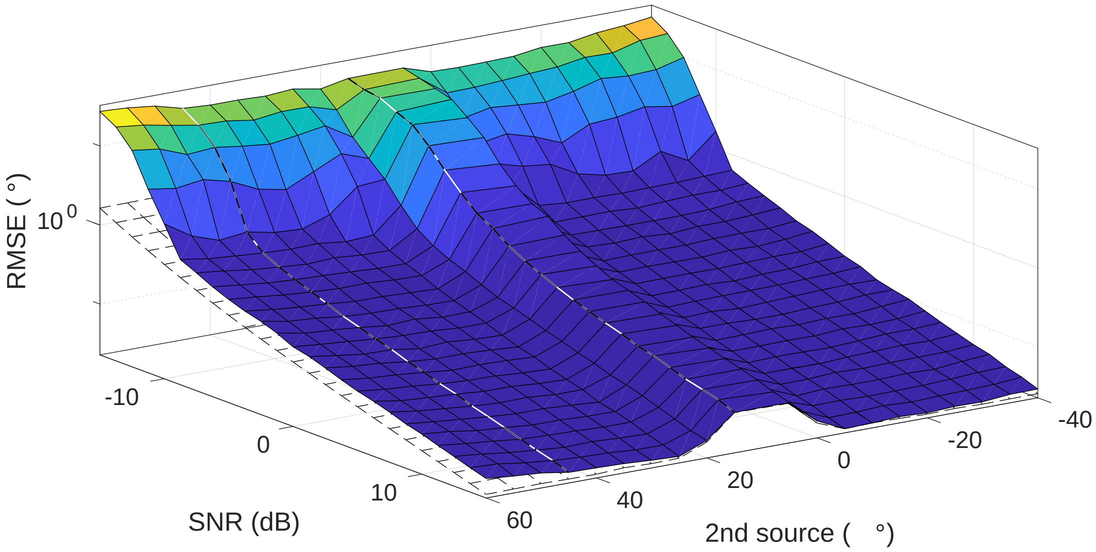

Figure 15 – RMSE of Modified MODEX for uncorrelated sources. One source is fixed at 10° and another sweeps the range from 60° until -40°. The SNR is in the range (-15,15) dB. Two representative situations are highlighted by dashed lines, where the sources are located at (10°,15°) and (10°,45°). Source: Author.

Considering closely-spaced sources, the estimators achieved optimal CRB-compatible performance for high SNRs until the point where the breakdown effect is recognized. Improved SEAD provided better estimates with a threshold SNR in the proximity of -10 dB, while SEAD using the 1_i-norm performed worse among SEAD-based methods, with threshold SNR at -7.5 dB. Although not as effective as the other norms, the 1_i-norm outperformed the MODEX method for a wide range of SNRs values.

Except the 1_i-norm, the matrix norms had similar results. All spectra effectively indicated DOA positions and has shown to be robust against the harmful effects of noise. It is important to point out that for nearby sources the second eigenvalue played an important role, a considerable gain in the improved-SEAD can be observed.

For widely-spaced sources, the SEAD method using matrix norms outperformed the MODEX and improved-SEAD methods for low SNRs. All SEAD-based methods have limitations on high SNRs range, their performance tends to stagnate in a certain error level, which is dependent on the distance between the sources.

Among the methods using norms, their performances were similar. In contrast to closely-spaced sources, for widely-spaced sources the methods using norms provide more consistent estimates, even outperforming the improved-SEAD method. In general, they have shown threshold SNR at -10 dB, whilst the previous version presents the instabilities from -7.5 dB on. All methods outperformed MODEX and Modified MODEX methods on the low SNR range.

4.2.2 Correlated Sources

Figure 16, 17, 18, 19, 20, 21, and 22 show the methods' performances for correlated sources, where ($\rho_{12} = \rho_{21} = 0{,}9$). All SEAD-based methods performed better when compared to the case of uncorrelated sources.

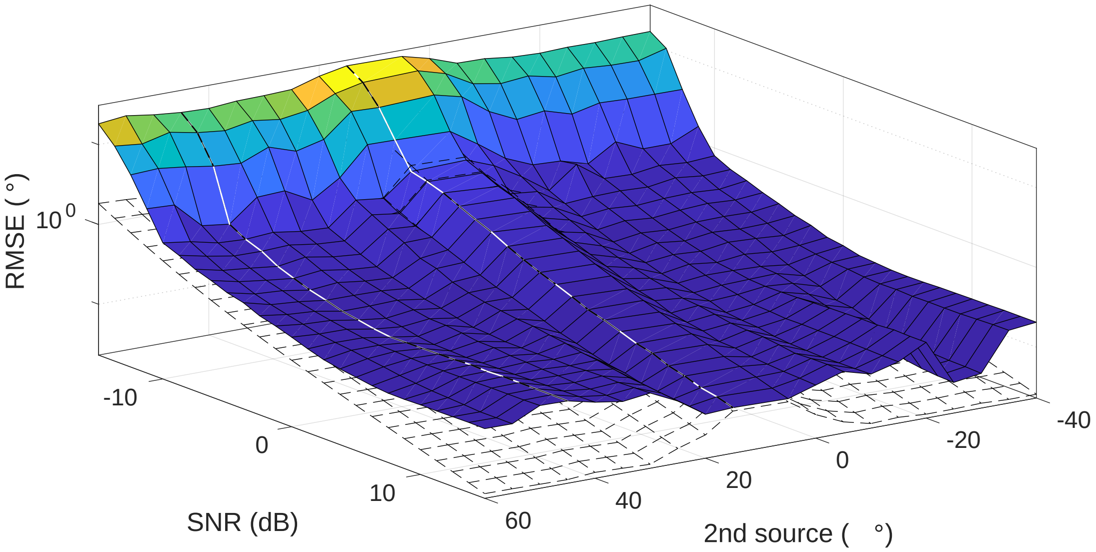

Figure 16 – RMSE of 1-norm for correlated sources. One source is fixed at 10° and another sweeps the range from 60° until −40°. The SNR is in the range (−15,15) dB. Two representative situations are highlighted by dashed lines, where the sources are located at (10°,15°) and (10°,45°). Source: Author.

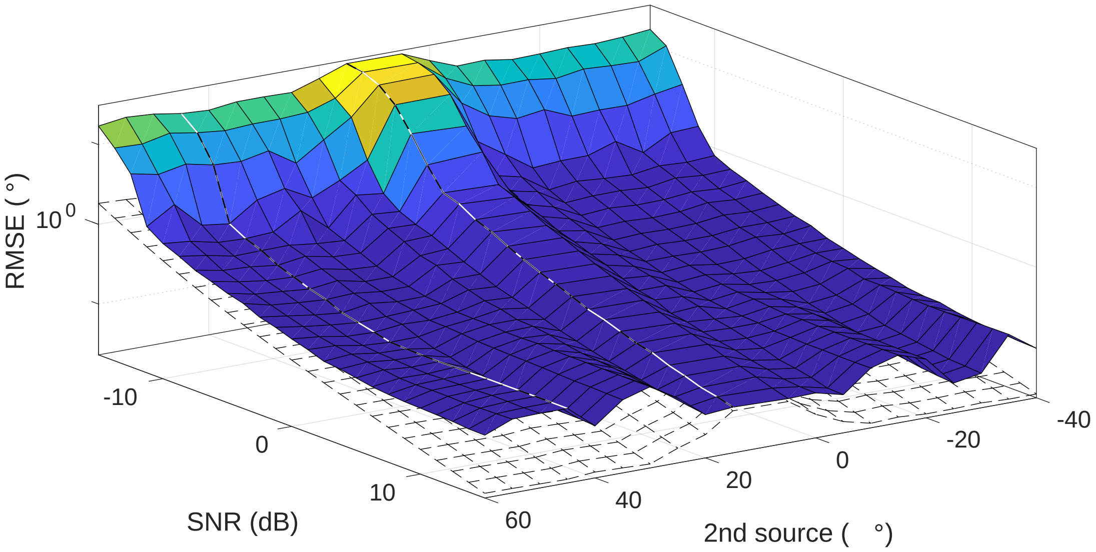

Figure 17 – RMSE of 1_i-norm for correlated sources. One source is fixed at 10° and another sweeps the range from 60° until −40°. The SNR is in the range (−15,15) dB. Two representative situations are highlighted by dashed lines, where the sources are located at (10°,15°) and (10°,45°). Source: Author.

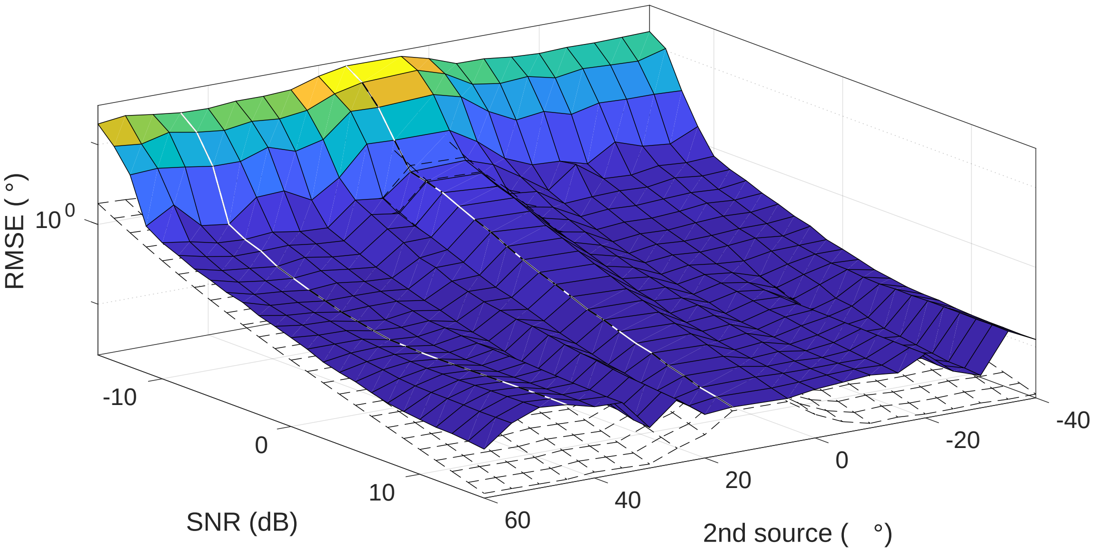

Figure 18 – RMSE of 2-norm for correlated sources. One source is fixed at 10° and another sweeps the range from 60° until −40°. The SNR is in the range (−15,15) dB. Two representative situations are highlighted by dashed lines, where the sources are located at (10°,15°) and (10°,45°). Source: Author.

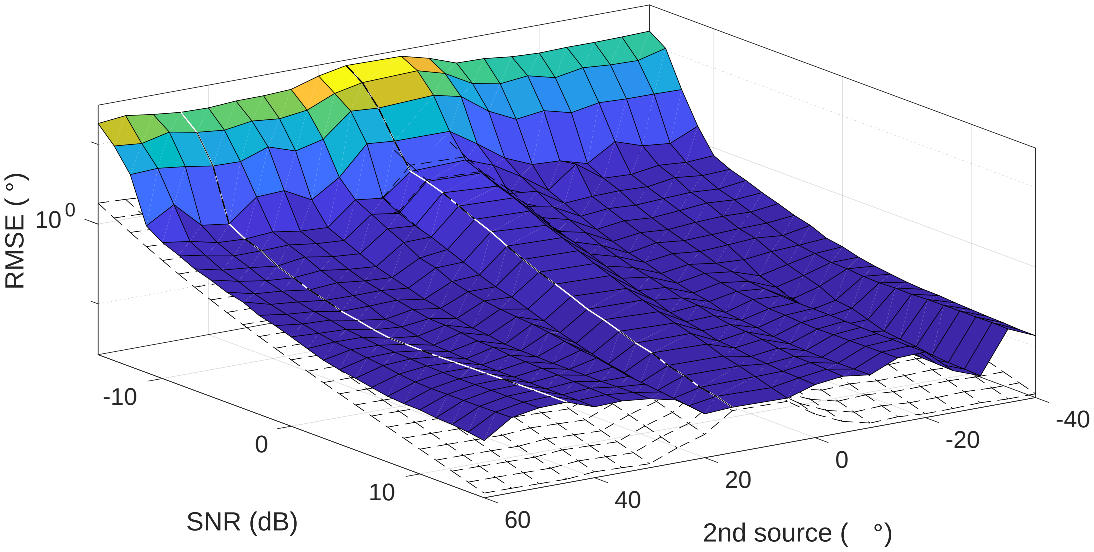

Figure 19 – RMSE of 2_i-norm for correlated sources. One source is fixed at 10° and another sweeps the range from 60° until −40°. The SNR is in the range (−15,15) dB. Two representative situations are highlighted by dashed lines, where the sources are located at (10°,15°) and (10°,45°). Source: Author.

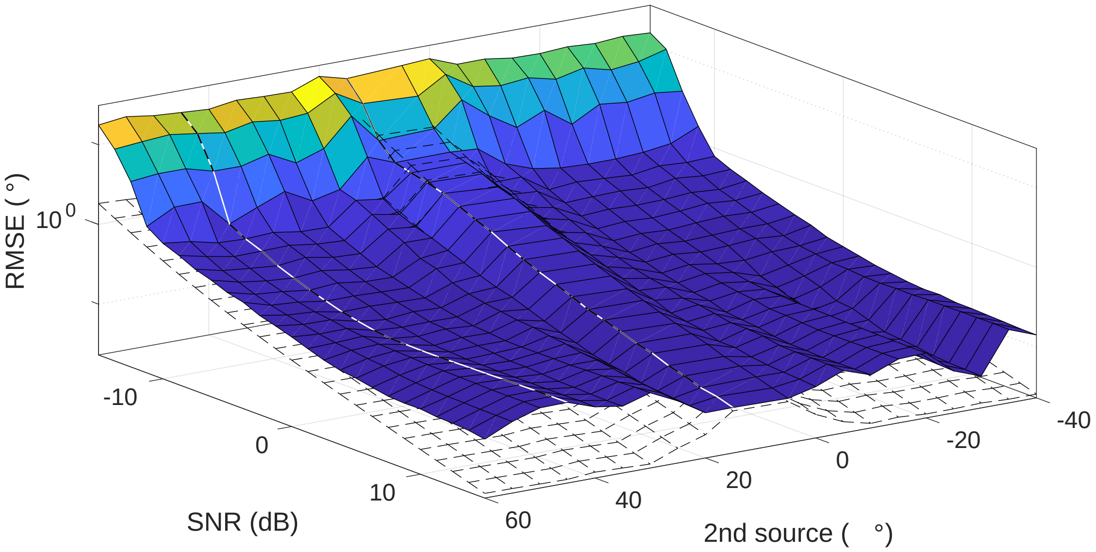

Figure 20 – RMSE of Improved SEAD for correlated sources. One source is fixed at 10° and another sweeps the range from 60° until −40°. The SNR is in the range (−15,15) dB. Two representative situations are highlighted by dashed lines, where the sources are located at (10°,15°) and (10°,45°). Source: Author.

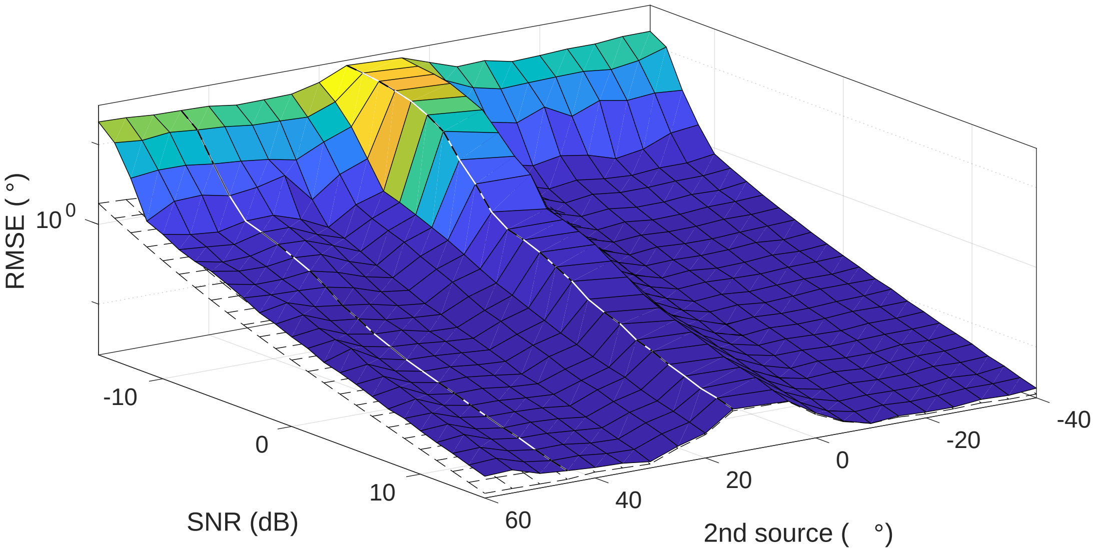

Figure 21 – RMSE of MODEX for correlated sources. One source is fixed at 10° and another sweeps the range from 60° until −40°. The SNR is in the range (−15,15) dB. Two representative situations are highlighted by dashed lines, where the sources are located at (10°,15°) and (10°,45°). Source: Author.

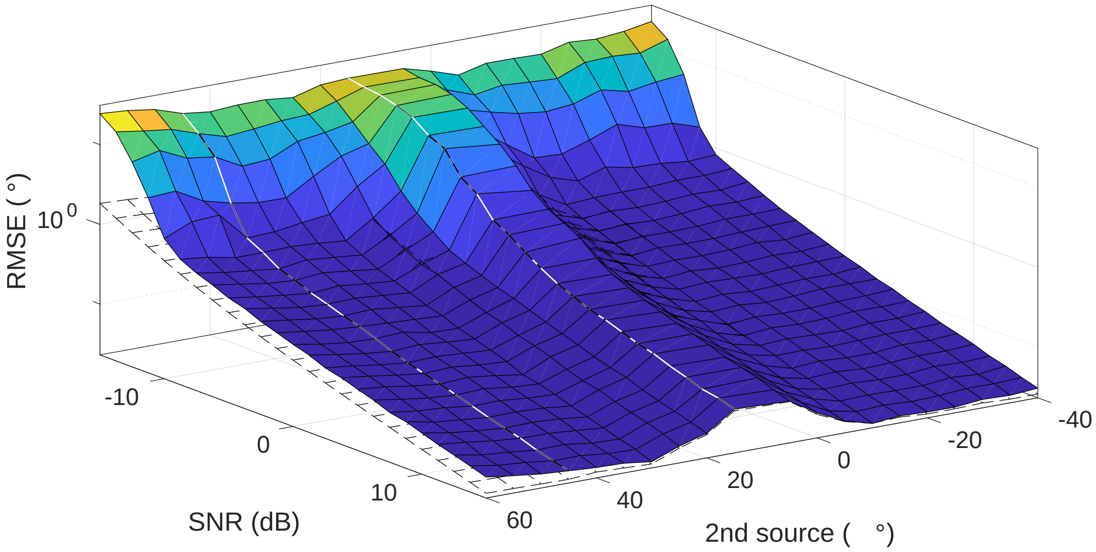

Figure 22 – RMSE of Modified MODEX for correlated sources. One source is fixed at 10° and another sweeps the range from 60° until −40°. The SNR is in the range (−15,15) dB. Two representative situations are highlighted by dashed lines, where the sources are located at (10°,15°) and (10°,45°). Source: Author.

For close sources, SEAD-based methods performed very close to CRB. For low SNRs these methods obtained even better results, and in some regions the surface is below the CRB surface.

Despite the subtle differences, SEAD methods had very similar performances, however, improved-SEAD presented an outstanding performance with threshold SNR at −12.5 dB, below the level reached by the 1-norm, 2-norm, and 2_i-norm methods, which had shown a breakdown effect at −10 dB. The method with the 1_i-norm again showed the worst performance among the matrix norms, with threshold SNR of −8.75 dB. The MODEX and Modified MODEX methods were outperformed by SEAD-based methods, they have shown a threshold SNR at −5 dB and −6.25 dB, respectively.

For widely-spaced sources the performance was even better. Improved-SEAD no longer presented instability for uncorrelated sources and performed similarly to norm methods. All SEAD-based methods performed well, presenting threshold SNR around −10 dB. On the other hand, for high SNRs, SEAD-based methods tended to stagnate at an error value. MODEX and Modified MODEX had performances very close to the CRB for high SNRs, but they presented worse performance for low SNR, close to −8.75 dB.

In short, improved-SEAD has shown the best performance for close sources, but it is unstable when they are distant and uncorrelated. SEAD using matrix norms showed very competitive results and their performances were stable in all cases. They also present consistent results outperforming the improved-SEAD for widely-spaced sources, and MODEX-based methods for closely-spaced uncorrelated and correlated sources.

4.2.3 Runtime

The efficiency of a computational method can also be measured in terms of its execution time. Different sets of DOA angles are considered for several number of sources in the range $M = \{1, 2, 3, 4, 5\}$, $K = 10$ and $L = 181$ samples of the angular spectrum.

SEAD-based methods should be analyzed taking into account their two processing stages: the initial guess and the refinement process. The norm approach directly affects the initial guess stage, more precisely in the spectrum generation. As a consequence, the number of sensors will be determinant for the computational effort employed in the calculation of the initial estimates.

The computational complexities of DS and the 2_i-norm are equivalent to the SVD complexity, which can be expressed by $\mathrm{O}(K^3)$. For the other matrix norms the complexity can be expressed by $\mathrm{O}(K^2)$. Despite the similarity of expressions, MATLAB has specific implementations for each norm, such that the algorithms present significantly different runtime. For a single calculation, the time required for calculating the SVD is 2.195 ms, 0.855 ms for 1-norm, 0.954 ms for 1_i-norm, 0.527 ms for 2-norm and 2.510 ms for 2_i-norm.

The runtime reduction is remarkable when considering the use of matrix norms. In addition, it is important to mention that the 2-norm performed faster, requiring only a quarter of the SVD runtime.

To compare the total runtime of the evaluated methods, a maximum number of iterations equal to 5 for SEAD-based methods was set, MODEX has 4 extra roots and at least 2 iterations for MODEX and Modified MODEX are considered.

Table 2 presents the computational complexity of each method, in addition, it shows the average runtime for two uncorrelated sources in 1000 simulations. The runtime is independent of the correlation between sources.

Table 2 – Runtime for two uncorrelated sources ($\rho_{\alpha\beta} = 0$)

Methods	Complexity	Mean (ms)
MODEX	$O\left[\left(\frac{(2M+X)!}{M!(M+X)!}\right)MK^2\right]$	0,2027
Modified MODEX	$O\left[\left(\frac{(3M)!}{M!(2M)!}\right)MK^2\right]$	0,1174
Improved SEAD	$O\left[LK^3+\left(D+IE^M\right)MK^2\right]$	0,4609
1-norm	$O\left[LK^2+\left(D+IE^M\right)MK^2\right]$	0,3117
1_i-norm	$O\left[LK^2+\left(D+IE^M\right)MK^2\right]$	0,3215
2-norm	$O\left[LK^2+\left(D+IE^M\right)MK^2\right]$	0,2778
2_i-norm	$O\left[LK^3+\left(D+IE^M\right)MK^2\right]$	0,4815

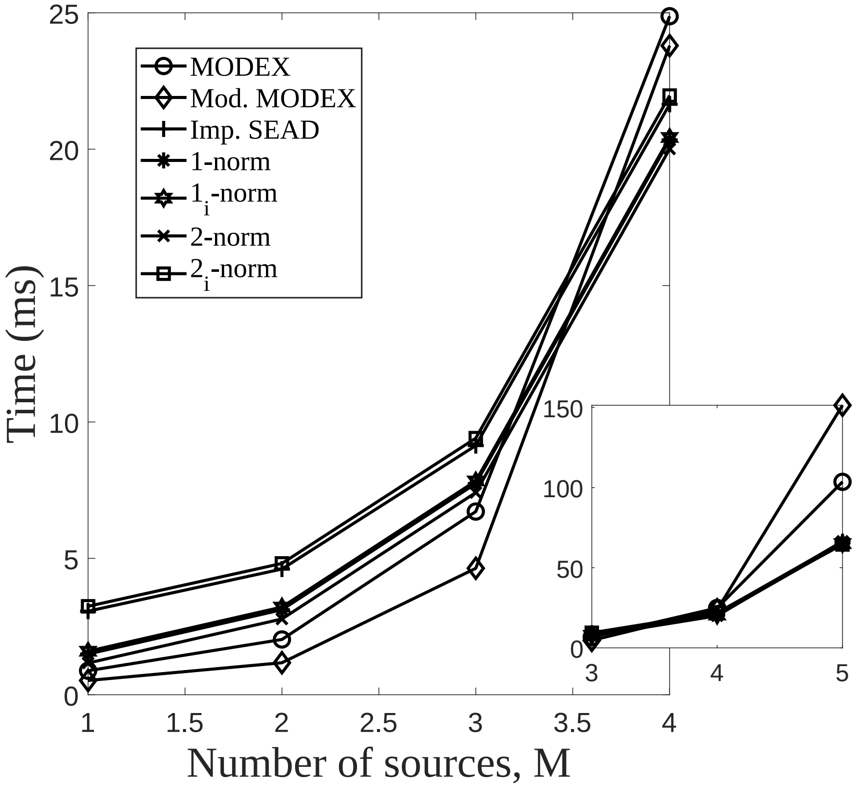

Figure 23 – Runtime evolution according to number of sources. Source: Author.

The computational complexity is given in terms of the number of sources M and the number of sensors K for all methods. In particular, the number of extra root in MODEX method is represented by the parameter X. In case of SEAD-based methods, the parameter L stands for the number of points used to trace the angular spectrum for each approach, D is the total number of candidate angles combinations evaluated by the DMLE cost function in the first stage of the selection procedure, I is the number of iterations performed in the refinement procedure, and E refers to number of candidate frequencies used in the final process, where the best estimates are selected.

In short, the SEAD method using 2-norm reduced the runtime around 40%, but despite this enhancement, the MODEX method still perform faster in the context of two sources. However, as stated in (SILVA et al., 2013), this behavior changes dramatically for more than three sources. Figure 23 shows the evolution of the runtime according to the number of sources in the system.

Both MODE-based methods are faster for less than three sources, it becomes more time consuming for $M \geq 4$. On the other hand, SEAD-based methods runtime slightly increases as the number of sources increases. For 5 sources, the proposed methods required half the time than MODEX and one-third of the Modified MODEX.

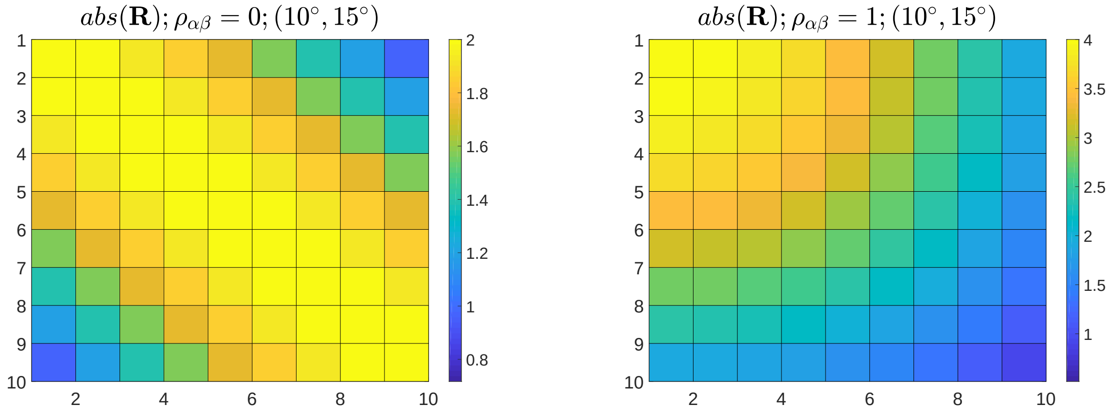

(a) Magnitude of **R** for uncorrelated and closely-spaced sources.

(b) Magnitude of **R** for correlated and closely-spaced sources.

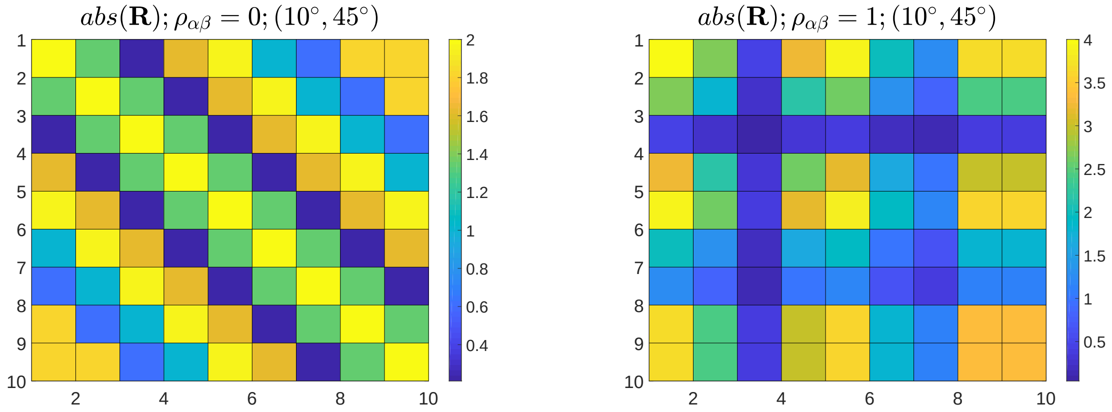

(c) Magnitude of **R** for uncorrelated and widely-spaced sources.

(d) Magnitude of **R** for correlated and widely-spaced sources.

Figure 24 – Magnitude of the spatial correlation matrix entries for (a) uncorrelated and (b) correlated closely-spaced sources and for (c) uncorrelated and (d) correlated widely-spaced sources. Source: Author.

4.3 Correlation Influence

As seen in the Section 3.3, correlation plays an important role in the stability of SEAD-based methods. It has been mathematically demonstrated, for correlated signals, that there are additional terms on the norm calculation compared to the uncorrelated case. For each test source there is a greater number of cumulative terms in the sum. This corroborates the results in the performances comparison of the error surfaces obtained for the estimates in Subsection 4.2.2. This means that correlation is an advantageous factor for obtaining estimates, unlike other methods used in DOA estimation.

Figure 24 presents the magnitude's color map of the spatial correlation matrix entries $[\mathbf{R}]_{rc}$. Two cases are considered, closely-spaced sources at (10°,15°) and widely-spaced sources at (10°,45°) according to the correlation between the signals.

From Figure 24 it is remarkable that the values are significantly amplified when there is correlation between the sources. In Figure 24b it is observed that the values are in the range $(0, 4)$.

In the case of distant sources, the same effect can be observed when there is correlation between the sources. The absolute values of the matrix entries in Figure 24 (c) range from 0 to 2, this range practically doubles when the sources are fully correlated ($\rho_{\alpha\beta} = 1$).

4.4 Chapter Conclusions

The matrix norms are suitable for obtaining candidate angles and all spectra were useful for indicating the position of sources through the prominent peaks, which have higher amplitude than other existing peaks. The same resolution issue on the differential spectrum is present in matrix norms spectra, the number of sensors limits the thickness of the peaks.

In the uncorrelated case and considering closely-spaced sources, the estimators achieved optimal CRB-compatible performance for high SNRs until the point where the breakdown effect is recognized. Improved SEAD provided better estimates with a threshold SNR in the proximity of -10 dB. For widely-spaced sources on the uncorrelated situation, SEAD-based methods using matrix norms outperformed the MODEX and improved-SEAD methods for low SNRs. All SEAD-based methods have limitations on high SNRs range, their performance tends to stagnate in a certain error level.

Considering the correlated case, the instability were fixed regarding the error surface on improved-SEAD. The other SEAD-based methods performed slightly better for closely-spaced sources. For widely-spaced sources, the performance did not change dramatically and the stagnation on the error still exists for high SNRs.

Beyond these benefits, the proposal using matrix norms reduces the runtime on the initial guess stage. By avoiding the EVD or SVD calculation, the overall runtime of the method was reduced and it was shown that for a number of sources greater than 4, the SEAD-based methods perform faster than MODEX-based methods. An astonishing result was reached by the 2-norm, it reduced the runtime of SEAD method around 40%.

Part III

Proposal of Sensor Array-based Approach for Readout of Energy Pulses in the Microwave SQUID Multiplexer

5 High Energy Physics

5.1 Introduction

High energy physics arises in the context of human restlessness to understand how matter was formed. These questions already bothered the Greek philosophers and reach the present time as an object of research for scientists from the most varied knowledge areas. They are trying to explain what the universe is made of and how the various elements interact with each other. Therefore, a standard model was proposed in particle physics field in order to unify the theory that allows the interpretation of observed phenomena in the universe (AMSTUTZ, 2016). Particle physics can be termed equivalently as high energy physics, since knowledge of the components of matter at its most basic levels is possible only when energies of the order of MeV and TeV are achieved.

Knowledge about the subject has been unveiled and expanded relatively recently. The embryo of the current standard model takes back to 1911 when Rutherford proposed a planetary atomic model, in which the nucleus had a positive charge and the electrons traveled elliptical orbits revolving around the nucleus. Rutherford's model had a flaw that made it inconsistent with the theory of electromagnetism. His student, Niels Bohr, worked on the subject and using the quantum descriptions of electromagnetic radiation, proposed by Alber Einstein and Max Plank, completed his master's theory. It is now called the Rutherford-Bohr atomic-molecular model. (HALLIDAY; RESNICK; WALKER, 2011).

By this time, it was already agreed that the molecules were composed of atoms that contained elements with positive and negative electric charges, called protons and electrons respectively. In 1897 Joseph John Thomson had discovered the electron, the proton was discovered by Rutherford in 1911 while developing his theory of the planetary atomic model and named in 1920 (proton comes from the Greek *protos*, which means first), whereas the neutron was a Chadwick's discovery in 1932. There was a belief that these were the smallest parts of an atom. This has been questioned over the time and new particles have been discovered and demonstrated through physical experiments, such as those performed on particle colliders (HALLIDAY; RESNICK; WALKER, 2011).

The Large Hadron Collider (LHC) is currently the largest and most powerful particle accelerator/collider of the world, this experimentation machine is available in the European Organization for Nuclear Research (CERN) facilities. Important discoveries are being made since CERN began operating in 2008. The developed research at LHC is a major challenge for physicists and engineers because of the magnitude of this project. An extraordinary amount of data is generated within one experiment, and the design of new equipment, technologies as well as the analysis of the generated data goes through the integration of knowledge from various areas (AMSTUTZ, 2016).

The common understanding among scientists is that there are four types of forces governing the behavior of the particles that make up the universe, they are the weak and strong forces, the electromagnetic force and the gravitational force. The last two produce long-range interactions whose effects are seen in everyday life, while the first two produce their effects at subatomic levels and govern nuclear interactions (HALLIDAY; RESNICK; WALKER, 2011).

5.2 The European Organization for Nuclear Research - CERN

CERN was established to offer a research institution that would unite Europe and North America to promote and develop research in the area of particle physics (CERN-HISTORY, Accessed: 2019-06-15). Since the laboratory began in 1954, CERN has made significant strides in both particle physics and technologies that help improve daily activities.

One of the most important discoveries made at CERN, which has become the apple of scientists' eyes, is the so-called Higgs boson. It was discovered in 2012 by CERN scientists in the powerful LHC, more specifically in the Compact Muon Solenoid (CMS) experiment. In addition to the CMS, there are six other extremely important experiments in LHC, which are A Large Ion Collider Experiment (ALICE), A Toroidal LHC Apparatus (ATLAS), Large Hadron Collider beauty (LHCb), TOTal cross section, Elastic scattering and diffraction dissociation Measurement (TOTEM), Large Hadron Collider forward (LHCf) and Monopole and Exotics Detector At the LHC (MoEDAL) (AMSTUTZ, 2016; CERN-SCIENCE, Accessed: 2019-06-15).

The biggest experiments are ATLAS and CMS. They employ general purpose detectors to investigate the widest range of possibilities for physical phenomena. Two other experiments have a specific purpose and focus on specific phenomena, namely ALICE and LHCb. These four experiments stay underground in the LHC and are located in large LHC ring caves. The other three experiments are smaller and are associated with one of the larger experiments focusing on very specific phenomena (AMSTUTZ, 2016).

The LHC rings are located in a tunnel with a circumference of 27km on the border between Switzerland and France at a depth of 100m on average. The LHC accelerates hadrons in two ring beams that travel in opposite directions. These beams intersect at the four interaction points that provide the performance of the four main experiments cited. If the accelerated particles are hadrons, and so are non-elemental, what actually collides with the sensors are quarks and gluons, which once formed a composed particle (AMSTUTZ, 2016).

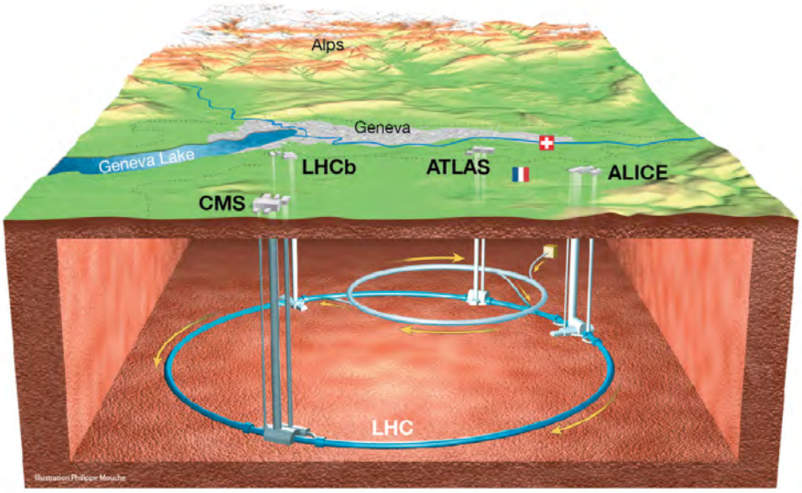

Figure 25 – Main Experiments on LHC. Source: (AMSTUTZ, 2016).

Through the tunnels the bursts of particles move in a vacuum tube with a diameter of 56mm. To keep the particles in a circular path, there are 1232 superconducting magnets installed in the tunnel. Each is cooled to 1.9K and produces a 8.33 T magnetic field. In addition, different magnetic systems keep the beams focused and 16 radio frequency superconducting cavities accelerate the particles.

As an example of an experiment performed in LHC, Figure 26 shows two collisions for the pile-up visualization, which is the name given to simultaneous collisions, under conditions encountered in LHC and, in the future, in HL-LHC.

The particles collide in the LHC at nanosecond intervals and the amount of data generated is enormous. However, interesting physical processes rarely occur and it is sufficient that only data containing relevant information be stored and analyzed. (AMSTUTZ, 2016).

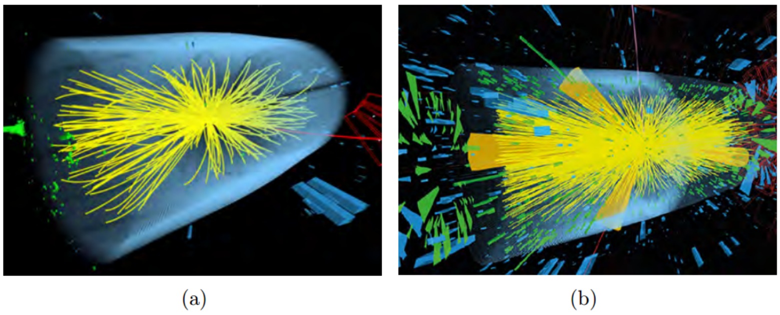
(a) (b)

Figure 26 – (a) Particle collision registered in May 2016 at the LHC and (b) Simulation of a particle collision in 2025 in the context of the HL-LHC. Each yellow line corresponds to a charged particle. Source: (AMSTUTZ, 2016).

5.2.1 Particle Classification

The name "atom" is derived from the Greek word *atomos*, consisting of the prefix *a-* (not) and the adjective *tomos* (cut or divided), which means indivisible. In addition to the known particles, such as the proton, electron and neutron, several particles have been discovered and others are suggested. Figure 27 shows the particles in the standard model (AMSTUTZ, 2016).

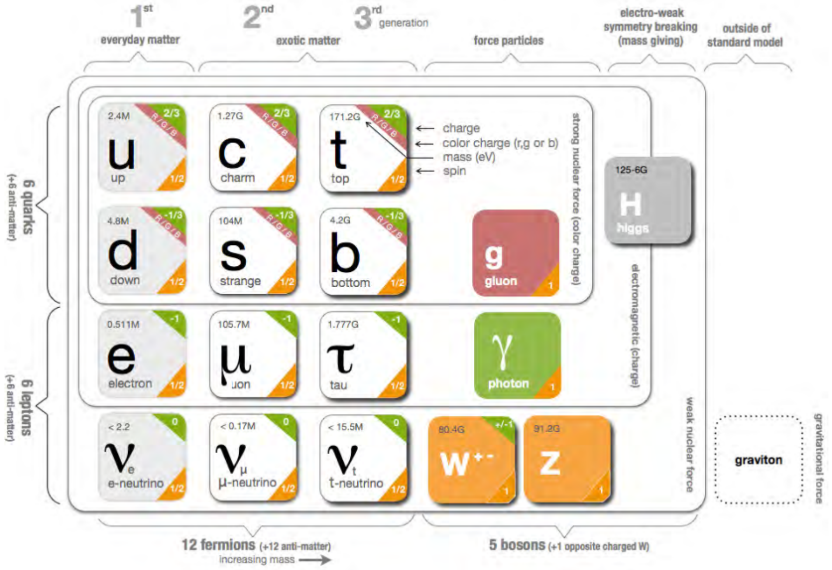

Figure 27 – Standard Model. Source: (AMSTUTZ, 2016).

Quarks are particles that interact through the strong nuclear force and form compound particles called hadrons. The most common hadrons are the proton and neutron which are made up of three quarks each. On the other hand, charged leptons interact by electromagnetism and through weak nuclear force, an example is the electron. Additionally, there is an antiparticle for each of the particles of matter. Antiparticles behave the same as the corresponding particles, have the same mass but have opposite charge.

5.2.2 A LHC Experiment Example

The detection system in CMS can be mentioned as an example of an experiment in the LHC. The detectors are disposed in an onion like shape around the collision point. Figure 28 presents an internal view of the experiment.

All detectors are distributed in two parts. First, there is a cylindrical section around the collision point. Then, there are endcaps which consist of sensor disks that encase the cylinders at both ends. A very important part of the detector is the 4T magnetic coil, which has an internal diameter of 6m and it is the largest superconducting magnet ever built (AMSTUTZ, 2016).

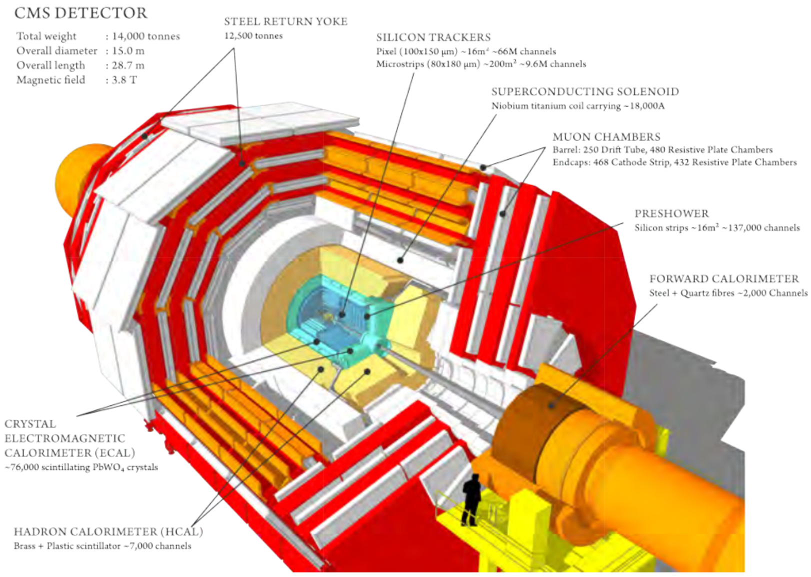

Figure 28 – CMS detection system composition. Source: (AMSTUTZ, 2016).

The detector located in the innermost part of the experiment is the silicon tracker. It consists of thin silicon blades that are able to detect the charged particles crossing the section area. Multiple layers of these sensors enable to trace the path described by the charged particle.

CMS silicon tracker consists of an internal and an external tracker. The internal tracker consists of pixel modules that allow fine spatial resolution. They sum up to 1440 modules with 66 million pixels. The external tracker consists of over 15000 modules in 10 layers with an active area of approximately $198m^2$.

The particles that crossed the silicon tracker follow their path and hit the next detector, the electromagnetic calorimeter (ECAL). They are used to measure the particles energy, particularly photons and electrons. The last detector inside the superconducting coil is the hadron calorimeter (HCAL), which measures the energy of hadrons, e.g. protons, neutrons, pions and kaons. In addition, the HCAL is important for indirectly detecting neutrinos or unknown particles that do not interact with other detectors (AMSTUTZ, 2016).

Muons do not easily interact with matter, consequently, muon detection systems can be positioned outside the superconducting coil. The muon detection system is complex and consists of 1400 muon chambers of three different types. The main detection system is the drift tube (DT) wire chamber which is located in the cylindrical section and the cathode strip chambers (CSCs) positioned at the endcaps. The third type of muon detector is the resistive plate chambers (RPCs) which consist of two conductive plates separated by a gas.

5.2.2.1 CMS Trigger Level 1

When particles collide, new particles are created and they decay into others. Processes occur with a certain probability, but processes of interest occur rarely. For this reason, most experiments in high energy physics include triggers that select events that have interesting characteristics. It is also possible to implement a multi-level triggers system (AMSTUTZ, 2016).

The CMS track trigger consists of two levels: level 1 trigger (L1 trigger) and high-level trigger (HLT). L1 trigger processes data from calorimeters and muon chambers with poor resolution. To process data within the time frame corresponding to the data storage latency period (3.2 μs), the L1 trigger algorithms are implemented on dedicated hardware, especially FPGAs.

5.2.2.2 CMS High-level Trigger and its Data Acquisition System

In the CMS experiment, the HLT is closely coupled to the data acquisition system (DAQ). After receiving the trigger signal, the event data that has been stored in different pipelines steps is fed to the event builder network (EBN). From it, the data is destined for a computer in a computing section. Each computer runs a builder unit (BU) and a filter unit (FU), where BU reformats the data to create the final event type and stores it until the FU is ready to process them. HLT algorithms are executed by the FU. The average time to process an event is 200 ms. After that, the data is stored and can be used for off-line analysis. The main idea in silicon tracker is to get a spatial representation of the particle behavior right after the collision. Sensors are positioned around the point of occurrence of events in such a way that a signal is generated at each particle-matter interaction. This signal is processed and the results enable the researcher to infer about the particle's trajectory (AMSTUTZ, 2016).

Silicon trackers store 3D images of a particle collision in high-energy physics experiments, high rates as 40 MHz are required. The analysis of these images is helpful to determine the trajectory and momentum of charged particles. The charged particles produce a signal at the position where they crossed the sensor, which is called a *hit*.

An important feature of silicon trackers is the measurement of the momentum of charged particles, which can be determined by the curvature of their path. In CMS the Lorentz force caused by the magnetic field of a superconducting solenoid (3.8 T) imposes a curvilinear path to the charged particles. The particle polarity is determined according to the direction in which the particle follows, whether clockwise or counterclockwise. The radius of curvature is a measure for the transverse momentum of the particle, almost straight trajectory means high momentum (AMSTUTZ, 2016).

5.2.2.3 Particle Detection by Silicon Sensors

Although silicon detectors are more expensive to produce and offer opposition to the particle trajectory because of dense matter, they have several advantages (AMSTUTZ, 2016):

- silicon is widely used in electronic devices and production processes are well known and available;
- small elements (pixels) can be produced in a silicon wafer, so detectors can have fine resolution;
- the small size of the detector and the high speed of silicon charge carriers lead to very fast detectors;
- since detectors are produced by the same electronics process, circuits can be integrated with the sensor.

The particles thread a silicon sensor and generate around 80 pairs of electron-gap per μm. Generally, the thickness of a silicon sensor is in the order of a few hundred micrometers. Electrodes are positioned on either side of the sensor and a voltage applied to them collects the electrons and free gaps. Subsequently, the resulting current is amplified, digitized and can then be processed. By segmenting the electrodes, either in the form of strips or in the form of pixels, sensors with spatial sensitivity can be created. A thicker sensor produces a larger signal as it has a larger number of charge carriers, however, a larger amount of material will interfere with particle trajectory and therefore the accuracy of external detectors may be degraded. In addition, a high voltage must be applied to produce the same electric field in the sensor. The problem with these sensors is that in order to achieve very fast readings, a very high current circulation is required (AMSTUTZ, 2016).

5.2.2.4 Stack Detector Modules

The total amount of particles reaching a silicon tracker is in the order of ten thousand. Most particles have small transverse momentum and are irrelevant. However, events including particles with high transverse momentum may be interesting physical processes and deserve to receive focus.

To identify these events, the idea of stack detectors was developed. When charged particles cross the detector, they intercept both silicon sensors. Depending on its transverse moment the location of the interceptions on each sensor will be different. The distance between these points also depends on the configuration of the silicon detectors regarding their subdivisions, the distance between the modules and the point where particles collides and the magnitude of the magnetic field. The distance between the previous and backside sensors is called bend (AMSTUTZ, 2016).

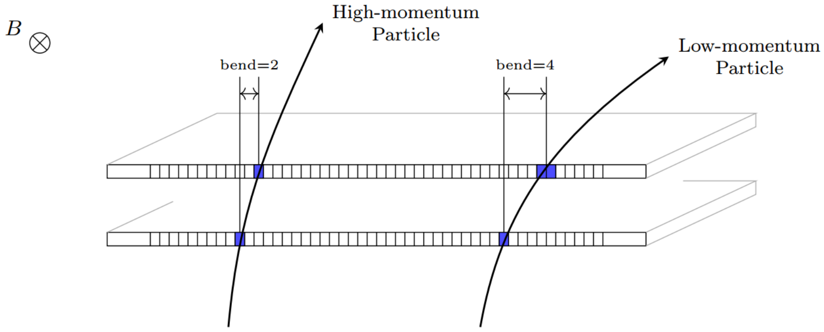

Figure 29 – The distance between the excited sensors sets the momentum of the particle. The smaller the bend the bigger the moment. Source: (AMSTUTZ, 2016).

Figure 29 illustrates the process of recording the points at which particles intersect each sensor. The two points at which the particle intercepts the stack sensor determine a specific path taken by this particle, these two points are called stub. A stub consists of two elements: the location and the bend. The location corresponds to the relative position in the agglomeration on the internal silicon sensor. The bend is the distance between the intersections in the inner and outer sensor. It is measured in number of strips along the detector and is a gross measure for transverse momentum.

6 Microwave SQUID Multiplexer

Low-temperature microcalorimeters such as metallic magnetic calorimeters or transition edge sensors are already well established and widely used in several experiments in fields ranging from atomic and nuclear physics to X-ray spectroscopy, astrophysics laboratory or materials science (KEMPF et al., 2014).

Generally speaking, these calorimeters consist of a particle sensor connected to a thermometer that monitors the variation of the detector temperature due to the absorption of energy particles. Specifically in the case of MMCs, the thermometer is a paramagnetic metal sited in a weak magnetic field, it converts detector temperature variations into sensor magnetization, which in turn can be measured by a SQUID (KEMPF et al., 2014). There are two different interferometer types, the dc-SQUID and rf-SQUID. A non-dissipative rf-SQUID consists of a single Josephson junction breaking a superconducting loop, which will be considered in the context of this work (MATES et al., 2008).

Several preliminary experiments confirm the applicability of single or small array detectors (IRWIN et al., 2006; MATES et al., 2008; KEMPF et al., 2014), but systems with a large number of detectors will be required for future applications. To achieve this goal, multiplication techniques suitable for MMC arrays are under development.

A current approach to the readout of large arrays is the SQUID-based multiplexers, they consist of non-hysteretic rf-SQUID exploiting the non-linear behavior of SQUID response, which can be assumed to be a controlled inductance. Each SQUID is magnetically coupled to a superconducting transmission line resonator in order to provoke subtle frequency shifts, which modulate a complex carrier on amplitude and phase. In the end of the day, the signal demodulation provides the energy of the particle.

Some important features of MMCs: They have very high power resolution, their nature of operation is intrinsically non-dissipative, rapid pulse rise and excellent linearity (KEMPF et al., 2014; KEMPF et al., 2014).

6.1 Microwave SQUID Multiplexer Principles of Operation

This section will discuss the physical and electrical characteristics of the microwave SQUID multiplexer. Each input channel corresponds to a non-dissipative rf-SQUID coupled to a quarter-wave superconducting resonator. The channels are combined into a common feed line that is capacitively coupled individually to each resonator.

6.1.1 Metallic Magnetic Calorimeter

Magnetic Metallic Calorimeters are energy dispersive-based particle detectors, which join in the set of detectors that embrace thermodynamics as a fundamental principle. This type of device uses temperature sensors that absorb charged particles. The particle detector, which has thermal capacity C, and the thermal sensor are directly connected to each other and to a temperature bath T_b through the thermal conductance G. Monitoring the sensor temperature provides the power, P, following the equation (MATES et al., 2008):

$$T = T_b + \frac{P}{G}. \tag{6.1}$$

The same device can act as a calorimeter if it measures the incident energy, E, as follows:

$$T = T_b + \frac{E}{C}. \tag{6.2}$$

Figure 30 presents a diagram of the detector and energy pulse after the incidence of a charged particle.

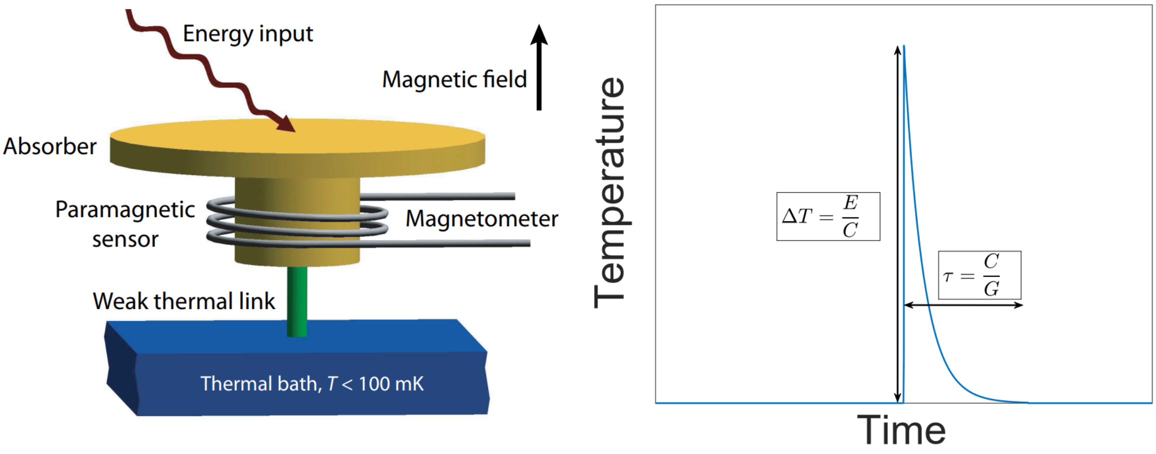

Figure 30 – Incidence of a charged particle at the MMC detector. An energy input increases the sensor temperature which will be readout by a magnetometer. Source: (SANDER et al., 2017).

The correct operation of the calorimeter is achieved at very low-temperatures around the absolute zero, some systems can achieve a temperature of 100 mK. For this purpose, a cryostat is employed to control the temperature to the lowest desired level and isolating the system from external interference. The thermal noise is severely reduced and consequently the detector signal is maximized (KEMPF et al., 2014).

6.1.2 The Readout of Magnetic Calorimeters by Non-dissipative rf-SQUID

In Figure 31 it is presented a schematic circuit diagram of the multiplexer. It employs non-hysteretic rf-SQUIDs to convert the detector signal into a frequency shift of

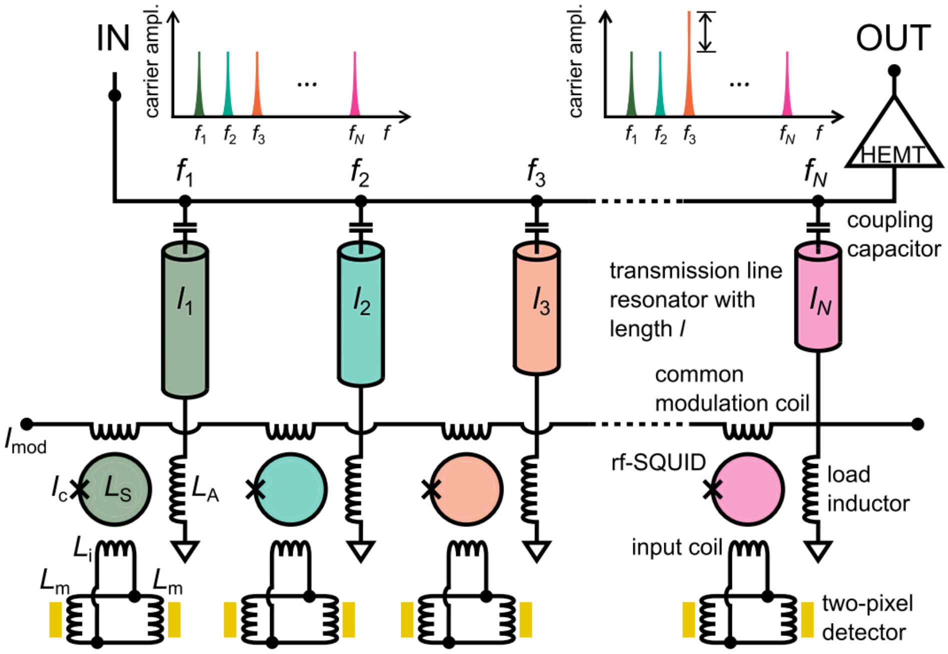

Figure 31 – Frequency multiplexing system schematic using rf-SQUIDs. Source: (KEMPF et al., 2017a).

an associated microwave resonator. Each SQUID has a specific loop inductance L_S and junction critical current I_c (KEMPF et al., 2014).

It is observed that an arbitrary number of carriers could be inserted in the common feed line. At the output, the signals are amplified using a high electron mobility transistor (HEMT). In the diagram, resonator l_3 acknowledges the existence of energy input as the carrier power increases. The energy inputs come from the pixels, the yellow rectangles at the bottom of the diagram, that capture the energetic particle and modify the magnetization of the coil L_m, subsequently introducing the signal into the SQUID via L_i. The SQUID is also coupled to a modulation coil that provides the optimum operating point of the device through the current I_{mod}. The SQUID response is coupled to the transmission line termination by coil L_A (KEMPF et al., 2017a).

6.1.2.1 Josephson Junction Inductance

The electrical current that flows through the Josephson junction depends on the phase difference of the superconducting wave function, comparing both sides of the junction (MATES, 2011):

$$I = I_c \sin(\phi), \tag{6.3}$$

where I_c is the critical junction current and ϕ is the phase difference across the junction.

A voltage difference between the junction terminals causes the phase to develop faster on the high voltage side than on the lower voltage side. Therefore the variation of the phase difference over time across the junction is given by (MATES, 2011):

$$\frac{\mathrm{d}\phi}{\mathrm{d}t} = \frac{2eV}{\hbar}. \tag{6.4}$$

These two expressions are named as Josephson relations and have been experimentally proven on several occasions (MATES, 2011). It follows from the combination of (6.3) and (6.4) that there is a self-inductive characteristic described by the junction. The rate of change in the current across the junction is given by:

$$\frac{\mathrm{d}I}{\mathrm{d}t} = I_c \cos(\phi)\frac{\mathrm{d}\phi}{\mathrm{d}t}, \tag{6.5}$$

which implies that

$$V = \frac{\hbar}{2eI_c\cos(\phi)}\frac{\mathrm{d}I}{\mathrm{d}t}, \tag{6.6}$$

and therefore, the variable inductance referring to the Josephson junction can be defined as:

$$L(\phi) = L_j \sec(\phi), \tag{6.7}$$

where $L_j \equiv \frac{\hbar}{2eI_c} = \frac{\Phi_0}{2\pi I_c}$ is the Josephson inductance. The quantum magnetic flux is defined as $\Phi_0 = {}^{h}/_{2e} \approx 2 \times 10^{-15}$ Webers. It is important to note that the values of L_j are adjusted by I_c and that the ratio is valid only for small values of ϕ.

The rf-SQUID contains a Josephson junction in which the magnetic flux is given by (MATES, 2011):

$$\phi = \frac{2e}{\hbar}\int \frac{\mathrm{d}\Phi}{\mathrm{d}t}\mathrm{d}t = \frac{2e\Phi}{\hbar} = 2\pi\frac{\Phi}{\Phi_0}. \tag{6.8}$$

Because the loop has its own L_S inductance, the current flowing through the junction interferes with the loop's magnetic flux, so that Φ is not a value solely determined by the external magnetic flux Φ_e, which can be expressed by:

$$\Phi_e = \Phi - I_c L_S \sin\left(2\pi\frac{\Phi}{\Phi_0}\right). \tag{6.9}$$

For hysteresis to be avoided, total flux must be a unique value function for a given applied flux. Thus, $\Phi_e(\Phi)$ should be monotonous.

$$\begin{aligned}
0 &< \frac{\mathrm{d}\Phi_e}{\mathrm{d}\Phi}\\
0 &< 1 - I_c L_S \cos\left(2\pi\frac{\Phi}{\Phi_0}\right)\frac{2\pi}{\Phi_0}\\
0 &< 1 - \frac{2\pi I_c L_S}{\Phi_0}\\
0 &< 1 - \frac{L_S}{L_j},
\end{aligned} \tag{6.10}$$

where $\eta \equiv \frac{L_S}{L_j}$ is defined, meaning that when $\eta < 1$, rf-SQUID is non-hysteretic. Whenever $\eta > 1$, SQUID-rf is hysteretic and can perform flux jumps between metastable states (MATES, 2011).

6.1.2.2 The SQUID Inductance

To measure the equivalent inductance, the non-hysteretic rf-SQUID is coupled to another inductor, which is already known and can allow to set a relationship between the total flux and the equivalent inductance. The inductor $L(\Phi)$ therefore has an effective flux-variable inductance given by (MATES, 2011):

$$\begin{aligned} L(\Phi) &= L_c - \frac{M_c^2}{L_S + L_j \sec\left({}^{2\pi\Phi}/_{\Phi_0}\right)} \\ &= L_c - \frac{\eta M_c^2 \cos\left({}^{2\pi\Phi}/_{\Phi_0}\right)}{L_S \left(1 + \eta \cos\left({}^{2\pi\Phi}/_{\Phi_0}\right)\right)}. \end{aligned} \tag{6.11}$$

6.1.3 Resonant Frequency

Aiming to read several detectors simultaneously, it is necessary to use a multiplexing technique. The microwave SQUID multiplexer employs a frequency division multiplexing. The main components of the resonator circuit are discussed in the following.

6.1.3.1 Ideal Quarter-wave Resonator

A quarter-wave resonator is a non-dissipative transmission line that is an electrically open circuit at one end and a short-circuit at the other end. Therefore, there is no current in one terminal and no voltage in the other. The only non-attenuated standing waves under these conditions are those for which the transmission line length, l, is directly related to its wavelength, ϑ, so that l is an odd multiple of a quarter of the wavelength, $\forall\ n \in \mathbb{N}$.

Considering the phase speed, v_p, the first mode frequency will be given by (POZAR, 2012):

$$f_1 = \frac{v_p}{4l}. \tag{6.12}$$

Based on Maxwell's equations, the voltage and current expressions that go through a transmission line have angular frequency ω and phase speed v_p. They can be modeled as (POZAR, 2012):

$$V(z) = V_0^+ e^{-i\beta z} + V_0^- e^{i\beta z}, \tag{6.13}$$

and

$$I(z) = \frac{V_0^+}{Z_1} e^{-i\beta z} - \frac{V_0^-}{Z_1} e^{i\beta z}, \tag{6.14}$$

where $\beta \equiv {}^{\omega}/_{v_p}$. If a short-circuit is considered at $z = 0$, then:

$$V(0) = V_0^+ + V_0^- = 0; \tag{6.15}$$

and

$$I(0) = \frac{V_0^+}{Z_1} - \frac{V_0^-}{Z_1} \equiv 0, \tag{6.16}$$

where I is the magnitude of the current wave at the shorted terminal of the transmission line. Hence, it follows that the configuration of the standing wave fields along the transmission line is:

$$V(z) = -iIZ_1 \sin(\beta z); \tag{6.17}$$

and

$$I(z) = I\cos(\beta z). \tag{6.18}$$

6.1.3.2 Capacitive Coupling

The resonator is coupled to the transmission line using a small capacitance C_c. The resonant frequency of this set will be at the point of operation where the total reactance is equal to zero. The load impedance can be given by (MATES, 2011):

$$Z = Z_1 \frac{Z_L + iZ_1 \tan\left({}^{\omega l}/_{v_p}\right)}{Z_1 + iZ_L \tan\left({}^{\omega l}/_{v_p}\right)}. \tag{6.19}$$

If the transmission line is short-circuited, it follows that:

$$Z = iZ_1 \tan\left(\frac{\omega l}{v_p}\right). \tag{6.20}$$

This impedance in series with the capacitor impedance yields the resonance condition as:

$$\begin{aligned} 0 &= \frac{1}{i\omega_0 C_c} + iZ_1 \tan\left(\frac{\omega_0 l}{v_p}\right) \\ \omega_0 C_c Z_1 &= \cot\left(\omega_0 \frac{\pi}{2\omega_1}\right), \end{aligned} \tag{6.21}$$

where $\omega_1 = \frac{\pi v_p}{2l}$ is the resonant frequency of the decoupled resonator. The above equation cannot be solved by elementary functions as it is a transcendent equation. However, considering $\omega_0 C_c Z_1$ very small and expanding the cotangent around $\frac{\pi}{2}$, follows (MATES, 2011):

$$\begin{aligned} \omega_0 C_c Z_1 &= \cot\left[\frac{\pi}{2} + \frac{\pi}{2\omega_1}(\omega_0 - \omega_1)\right] \\ &= 0 - \frac{\pi}{2\omega_1}(\omega_0 - \omega_1) + O\left[(\omega_0 - \omega_1)^2\right] \\ \frac{2\omega_0\omega_1 C_c Z_1}{\pi} &\approx (\omega_1 - \omega_0) \\ \omega_0\left(1 + \frac{2\omega_1 C_c Z_1}{\pi}\right) &\approx \omega_1 \\ \omega_0 &\approx \frac{\omega_1}{1 + \frac{2\omega_1 C_c Z_1}{\pi}}. \end{aligned} \tag{6.22}$$

Thus, the charged resonant frequency is close to the resonator nominal resonant frequency of the fourth-wavelength transmission line, but it is reduced by the coupling capacitor and the oscillation frequency can be expressed as:

$$f_0 = \frac{f_1}{1 + 4 f_1 C_c Z_1}. \tag{6.23}$$

6.1.3.3 Inductive Load

Instead of short-circuiting the resonator terminal, an inductor is inserted at the termination of the transmission line, so that it will act as the circuit load. This inductor is coupled to the SQUID and it undergoes changes in its nominal value according to the variation on the magnetic flux threading the SQUID. As a consequence the resonant frequency of the circuit will be changed.

Inserting the inductive load into the resonator terminal changes the resonant frequency behavior as follows:

$$\begin{aligned} 0 &= \frac{1}{i\omega_0 C_c} + Z_1 \frac{i\omega_0 L \cot\left(\frac{\omega_0 l}{v_p}\right) + iZ_1}{Z_1 \cot\left(\frac{\omega_0 l}{v_p}\right) - \omega_0 L} \\ &= (\omega_0 C_c Z_1)\left[\omega_0 L \cot\left(\frac{\omega_0 l}{v_p}\right) + Z_1\right] - Z_1 \cot\left(\frac{\omega_0 l}{v_p}\right) - \omega_0 L. \end{aligned} \tag{6.24}$$

After some algebraic manipulation and performing some approximations, the effective resonant frequency can be given by (MATES, 2011):

$$f_0 = \frac{f_1}{1 + 4 f_1 C_c Z_1 + \frac{4 f_1 L}{Z_1}}. \tag{6.25}$$

6.1.3.4 Inductive Load Variation

From 6.25, the resonant frequency ω_0 varies with the current value of L. The derivative of the frequency relative to L results in:

$$\begin{aligned} \frac{\partial \omega_0}{\partial L} &= \frac{-\omega_1}{\left(1 + \frac{2\omega_1 C_c Z_1}{\pi} + \frac{2\omega_1 L}{\pi Z_1}\right)^2} \left(\frac{2\omega_1}{\pi Z_1}\right) \\ &= \frac{2\omega_0^2}{\pi Z_1}, \end{aligned} \tag{6.26}$$

which implies in:

$$\frac{\partial f_0}{\partial L} = -\frac{4 f_0^2}{Z_1}. \tag{6.27}$$

Combining (6.27) with (6.11), which express the load inductance fluctuation due to the flux through the SQUID, it finally turns into (MATES, 2011):

$$f_0(\phi) \approx f_1 - 4 f_1^2 C_c Z_1 - \frac{4 f_1^2 L_c}{Z_1} + \frac{4 f_1^2 \eta M_c^2}{Z_1 L_S} \cos(\phi). \tag{6.28}$$

The emphasis is on the presentation of the characteristics related to the change in resonant frequency, but as can be seen in (MATES, 2011; KEMPF, 2012) other aspects are equally relevant to the circuit design and manufacture, such as resonator bandwidth, channel crosstalk, notch filter quality factor, energy stored in the resonator, power dissipated at the resonator terminals and more. These aspects are beyond the scope of this work, since it is not intended to produce a prototype circuit.

6.2 Flux Ramp Modulation

Once the resonant frequency variation is set, it is time to consider a modulation of this flux that threads the SQUID. A ramp sweeping integer multiples of one quantum magnetic flux Φ_0 is added to the system to linearize the SQUID response. Conventionally, the linearization of an individual SQUID is performed through an active feedback loop that set the operation at a specific polarization point. If several SQUIDs are to be used simultaneously, the same procedure is unfeasible, as it would be necessary to apply the feedback to each SQUID of the array.

The alternative is known as flux-ramp modulation, which consists of applying a periodic ramp, which can be sinusoidal, triangular or sawtooth (MATES et al., 2008). The modulation wave frequency must exceed the signal frequency. The input signal shifts the flux ramp vertically and culminates in a phase shift modulation in the SQUID periodic response, as seen in Figure 32.

The total flux in SQUID is the composition of external and internal sources. Ex-

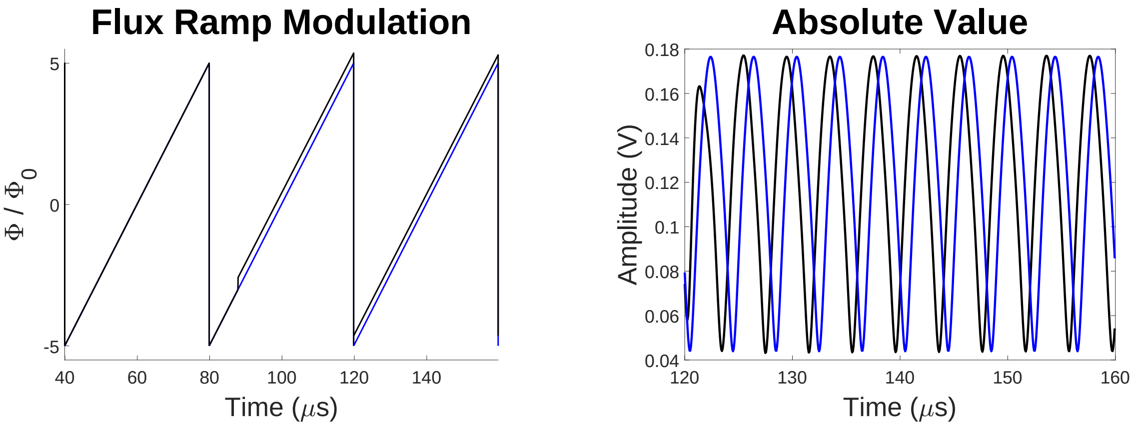

(a) Simulated sawtooth ramp. Due to an incident energy, the ramp gets vertically shifted.

(b) Reference carrier wave (blue curve) and phase modulated wave resulting from the incidence of a particle in the detector (black curve). Data were obtained by simulation.

Figure 32 – Sawtooth flux ramp (left) and absolute value of the complex carrier (right). Source: Author.

plicitly:

$$\Phi = \Phi_{ramp} + \Phi_{pulse} + \Phi_{loop}. \tag{6.29}$$

The contribution of the flux ramp is linear and the pulse shifts the ramp amplitude up or down while the magnetization changes. The internal flux produced by the loop depends on the factor η and can be kept small. Therefore, it is sufficient to read the phase and observe the points where its variation is no longer linear to obtain the flux due to an energy pulse.

A disadvantage of using this approach is that the readout noise level is increased, which is caused by measurements taken near to the edge of the SQUID response curve, where it becomes insensitive to magnetic flux. The noise is expected to be increased by $\sqrt{2}$ when compared to the feedback loop approach.

6.3 Software-defined Radio-based SQUID Multiplexer

The readout is performed in the digital domain, so that the signal should be digitized for signal processing purposes. It requires an infrastructure that connects all components of the system. Some stages of the system operate in analog domain and others in digital domain.

This section deals with the generation of the frequency comb that runs through the multiplexer. The chain of operations is explained, starting from signal generation until the chip-feeding and returning back to signal processing and storing. Afterward, the data is available for off-line processing.

The strategy used in the transmission stage to generate the microwave frequency comb and in the reception stage to channelize the signals and determine the amplitude and phase of each transmitted carrier signal is to employ the concept known as software-defined radio (SDR) implemented in FPGAs (SANDER et al., 2017).

Broadly speaking, frequencies are created in baseband in the range of 0 Hz to 100 MHz using two high speed digital-to-analog converters (DAC) connected to an FPGA. The comb is then mixed with an intermediate frequency that converts it to the operating region of the resonant circuits, the mixer is complex and handles in-phase and quadrature components (I/Q). The frequencies go through the chip located at the cryostat and at the other end are amplified by a HEMT. The road back to the baseband is paved using an I/Q mixer tunned at the same frequency. Both complex mixers have the same local oscillator (LO) stimulus. Returning to the FPGA, the signal is first digitized by an analog-to-digital converter (ADC).

The resulting in-phase and quadrature signals are in baseband and are channelized by an FPGA using an equivalent digital complex mixer. It separates the frequency comb

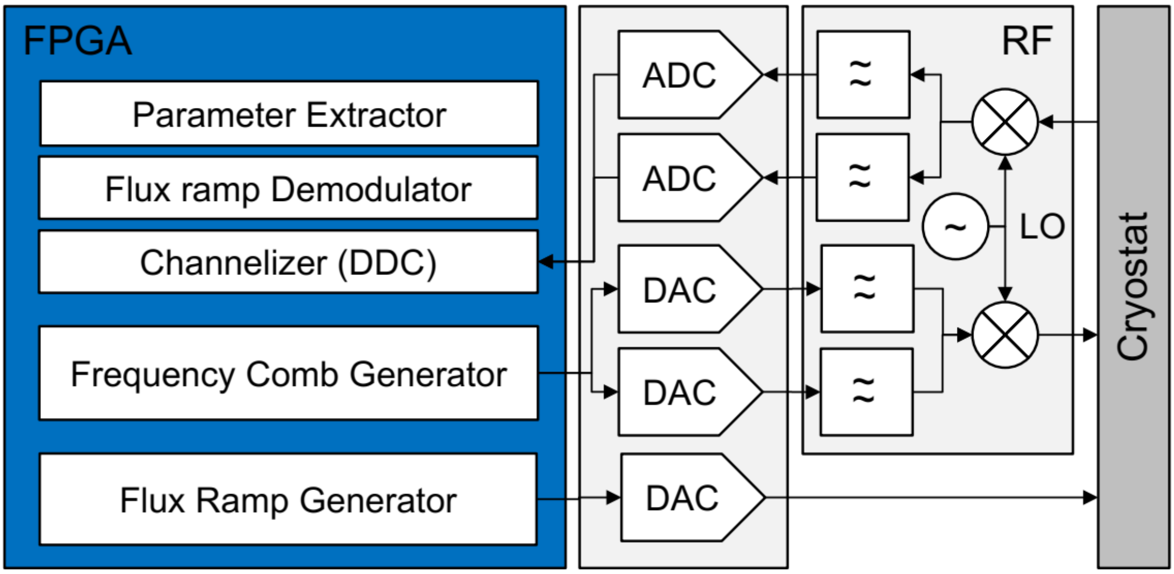

Figure 33 – Overview of the implemented hardware used on the SDR. Source: (SANDER et al., 2017).

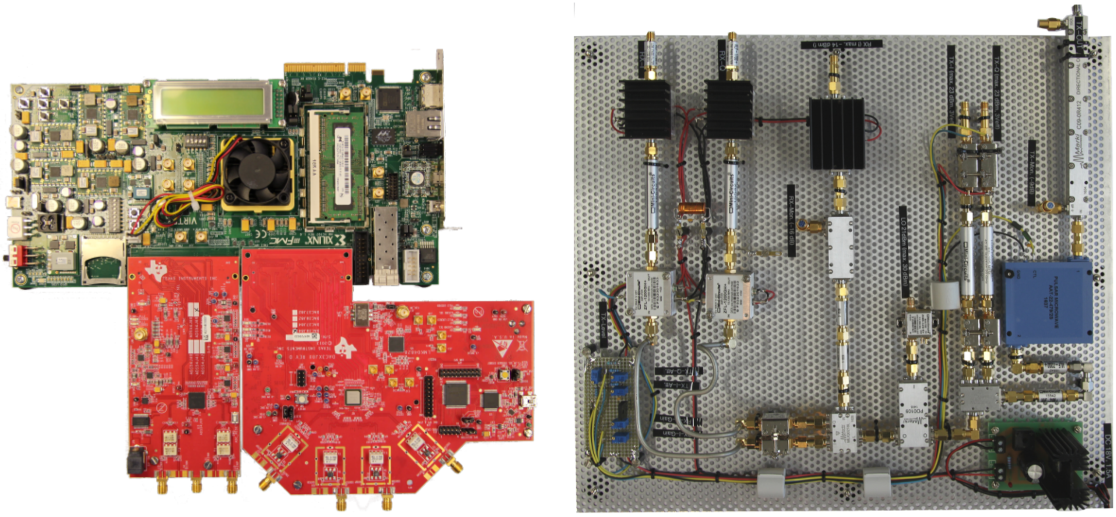

(a) FPGA board connected to the DAC and ACD boards.

(b) RF Frontend Prototype assembled in IPE/KIT by Dr.-Ing. O. Krömer. It was used for the first measurements.

Figure 34 – Whole system for signal readout in microwave SQUID multiplexing. Source: (KARCHER, 2016; SANDER et al., 2017).

into different carrier signals, determines the amplitude or phase of each carrier and determines the characteristic parameters of each detector signal (SANDER et al., 2017).

Figure 33 presents the signal path and the main operations implemented for information extraction. Figure 34a shows the FPGA VC707 (green) along with the DAC board on the right (red) and the ADC board on the left. Figure 34b presents the analog part of the signal processing.

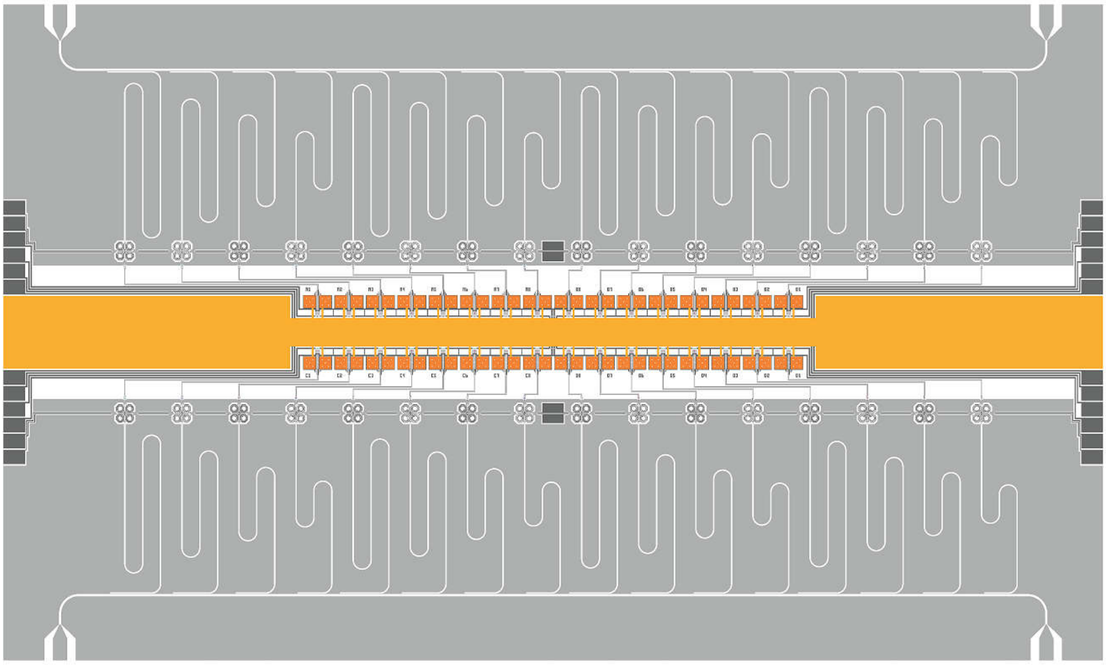

Figure 35 – Chip overview containing superconducting resonators and SQUIDs. There are two power lines for frequency comb feeding, the SQUIDs are spread over 2 lines and 16 columns. The pixels are positioned in the center of the chip, two of them coupled to each resonator summing up to 64. Source: (KARCHER, 2016).

6.3.1 ECHo Chip

The electron capture in holmium (ECHo) chip was used to measure the energy pulses of the incident particles in the sensors. A single chip gathers 64 pixels. Each two pixels are connected to a resonator, which is coupled to one of two available transmission conductors on the chip, as can be seen in Figure 35. The magnetic flux of the sensor is transfered to the rf-SQUIDs, such that each pixel is responsible for an energy pulse polarity (KARCHER, 2016).

The chip containing the pixels and resonators is mounted inside a cryostat, which enables the system to be cooled down to an extremely low-temperature. The cryostat used is based on a mixed cooling system, which provides the required temperature without the use of a compressor. Within the cryostat there are various stages and temperature zones, which through a vacuum region is isolated from the outside world. Cryostat can be divided into different layers, which are room temperature (300 K), one Nitrogen zone

(77.4 K), one Helium zone (4.2 K) and one cryogenic zone (1 K up to 20 mK). In the cryogenic region, cooling can be enhanced by using the ^{3}He and ^{4}He isotopes. Under these conditions a cooling capacity of the order of microwatt is achieved.

6.3.2 SDR Architecture

The current SDR concept for the next stage of the ECHo experiment employs 15 FPGA boards, each covering 4 GHz bandwidth. Considering a channel spacing of 10 MHz, the number of channels could probably reach 6000. It can be seen in Figure 33 that the architecture of the SDR is divided into three sections: the RF stage, the AD/DA stage, and digital processing through FPGA hardware. This is performed by a heterogeneous Xilinx Zynq Ultrascale+ FPGA, which is a combination of a Kintex Ultrascale+ FPGA with a powerful quad-core ARM A53 processor system (SANDER et al., 2017).

The frequency comb generator stores and reproduces previously computed waveforms and is therefore an arbitrary generator and the flux ramp is generated in the same way. On the receiver side, samples coming from the ADC are first processed in a channel block that separates the several channels. Subsequently, the flux ramp is demodulated for each channel, providing the detector signals. All relevant parameters are extracted at the last stage and the data is directed to the software layers, which organize the data in packet form and transmit it to the storage system.

Digitization is based on two 1 GS/s channels, 16-bit ADC with a JESD204b interface. The converter provides 1 GHz sampling of complex analog bandwidth. On the transmitter side there is 1 GS/s, four channel, 16-bit DAC to transform the I/Q samples into a complex baseband signal. Covering the 4 GHz range requires 5 ADCs and 3 DACs chips each covering 800 MHz of complex bandwidth (SANDER et al., 2017).

A high frequency prototype was assembled (KARCHER, 2016; WEGNER et al., 2018) for initial measurements and also served the purpose of a proof of concept for future manufacturing a dedicated board, which could be used for ECHo project experiments. In the transmission direction, there are two adjustable attenuators to set an appropriate and balanced input power before mixing the carrier with the local oscillator frequency. To generate the frequencies, a module that reads samples from a RAM block at 500 MS/s is used, these samples are interpolated and converted to analog mode through a 1 GS/s DAC39J84. The mixers are two Marki Microwave MLIQ0218L which are used for up and down conversion. There are also 105 MHz cut-off low-pass filters that have been chosen for DA reconstruction and to avoid aliasing. On the receiver side, there is a 50 dB amplifier before the waves are mixed down. Subsequently, an adjustable amplifier was employed to adjust and balance the signal level in AD conversion (WEGNER et al., 2018).

After AD conversion by a ADS54J69 500 MS/s two-channel converter, the digital signal is processed in an FPGA with firmware running on an Xilinx VC707 board. At first, the resonator signals are channeled through the digital down conversion (DDC) stage, which multiplies an input signal with a complex frequency to shift it in frequency. They are then filtered through a low pass filter and decimated to remove signals from other channels. During decimation the data rate is reduced from 2 GB/s to 125 MB/s. The demodulated signals are encapsulated in UDP packets and transmitted to a computer via a 10 GBit/s Ethernet cable (WEGNER et al., 2018).

6.3.3 Complex Mixer

The mixer's principles of operation recalls the multiplication of two sinusoidal waves. A multiplication in time represents a convolution in frequency which can be expressed as:

$$m(t) = z(t) \cdot r(t) \rightarrowtail Z(\omega) * R(\omega_{LO}). \tag{6.30}$$

If the intermediate frequency can be considered to be an ideal complex exponential wave, it will be represented by a Dirac delta in the frequency domain, or an impulse at the position $\omega = \omega_{LO}$, it follows that (KARCHER, 2016):

$$m(t) = z(t) \cdot \exp(-i\omega_{LO}t) \rightarrowtail Z(\omega) * \delta(\omega - \omega_{LO}) = Z(\omega - \omega_{LO}). \tag{6.31}$$

The use of an I/Q mixer presumes the existence of two signals, a cosine $i(t) = A\cos(\omega_i t + \theta_i)$ and a sine wave $q(t) = B\sin(\omega_q t + \theta_q)$, and therefore, they are shifted at the nominal phase of 90°, whereas $\theta_i = \theta_q = 0$. It represents a link between the complex baseband in digital signal processing and the real world. Signals I and Q are mixed with the intermediate frequency in individual mixers, so that the in-phase component is multiplied by the LO wave and the quadrature component is multiplied by the shifted version of the LO wave by 90°. Later, they are regrouped into an external conductor. For this reason, the mirror frequencies that arise during the multiplication process of each component are canceled.

Considering $\omega_{iq} = \omega_i = \omega_q$, $A = 1$ and $B = 1$, the complex carrier could be written as (KARCHER, 2016):

$$z(t) = \exp[i(-\omega_{iq})t] = i(t) - iq(t) = \cos(\omega_{iq}t) - i\sin(\omega_{iq}t), \tag{6.32}$$

which after the multiplication with the LO frequency provides:

$$\begin{aligned} m(t) &= i(t) \cdot \cos(\omega_{LO}t) + [-q(t)] \cdot [-\sin(\omega_{LO}t)] && (6.33)\\ &= \cos(\omega_{iq}t) \cdot \cos(\omega_{LO}t) + [-\sin(\omega_{iq}t)] \cdot [-\sin(\omega_{LO}t)] && (6.34)\\ &= \frac{1}{2}\{\cos[(\omega_{iq} - \omega_{LO})t] + \cos[(\omega_{iq} + \omega_{LO})t]\} && (6.35)\\ &+ \frac{1}{2}\{\cos[(\omega_{iq} - \omega_{LO})t] - \cos[(\omega_{iq} + \omega_{LO})t]\} && (6.36)\\ &= \cos[(\omega_{iq} - \omega_{LO})t] = \cos[(\omega_{LO} - \omega_{iq})t]. && (6.37) \end{aligned}$$

By performing those operations the lower-frequency signal is transported in the frequency domain to a region of the spectrum next to the local oscillator's frequency.

On the other hand, the same procedure can be conducted to remove the higher-frequency component, however, an additional step of low-pass filtering to discard the high-frequency components would be needed. The down-mixing is implemented in the reception stage, the output from the ECHo chip has its intermediate frequency discarded in the RF front-end, afterward, the same procedure is performed digitally inside the FPGA to channelize each SQUID response, so that the I and Q carriers are ready to be processed in order to recover the energy pulse.

6.3.4 The Readout of Information in the I/Q Carriers

In possession of both data sets I and Q, the problem consists of estimating the phase difference of the complex signal over time. Both signals are periodic and depend on the applied magnetic flux modulating wave to set the SQUID operation point.

Currently the readout of the phase shift is performed over the absolute value of the complex vector I/Q. The approach is supported by stochastic process theory and was proposed in (MATES et al., 2012).

The following procedure is described in detail.

6.3.4.1 Mates Approach

In the context of the microwave SQUID multiplexer, the approach to extract the phase information is presented in (MATES et al., 2012) as a Fourier calculation. However, it is equivalent to performing a maximum likelihood estimation and, in this section, we describe the mathematical background that support employing the currently used method for phase estimation.

In general, two criteria are the most applied for the estimation of signal parameters: the maximum likelihood criterion and the maximum a posteriori probability (MAP) criterion. In MAP, the $\boldsymbol{\theta}$ parameter vector is modeled as a random variable and is characterized by the a priori probability density function $p(\boldsymbol{\theta})$. In the maximum likelihood criterion, the signal parameter vector is treated as deterministic but unknown (PROAKIS; SALEHI, 2008).

According to (PROAKIS; SALEHI, 2008), if there is no prior knowledge of the $\boldsymbol{\theta}$ parameter vector, we can assume that $p(\boldsymbol{\theta})$ is uniform in the domain that defines the parameters. It follows that the estimates obtained by both MAP and ML will be identical.

Therefore, the parameter estimation treatment considers that the phase shift of the signal is unknown and deterministic. Then, the maximum likelihood criterion is used to obtain the energy pulse.

For the extraction of information a window of observation over a time interval $T_0 \geq T$ is required. Estimates obtained by observing only one interval are known as one-shot estimates. The probability distribution function of the random variable $r(t)$ can be expressed by (PROAKIS; SALEHI, 2008):

$$p(\mathbf{r}|\boldsymbol{\theta}) = \left(\frac{1}{\sqrt{2\pi}\sigma}\right)^N \exp\left\{-\sum_{n=1}^{N} \frac{\left[r_n - s_n\left(\boldsymbol{\theta}\right)\right]^2}{2\sigma^2}\right\}, \tag{6.38}$$

where

$$r_n = \int_{T_0} r(t)\phi_n(t)\mathrm{d}t, \tag{6.39}$$

$$s_n\left(\boldsymbol{\theta}\right) = \int_{T_0} s(t;\boldsymbol{\theta})\phi_n(t)\mathrm{d}t, \tag{6.40}$$

$r_n(t)$ and $s_n(\boldsymbol{\theta})$ are orthonormal expansions in the T_0 integration range of $r(t)$ and $s(t;\boldsymbol{\theta})$. The additive noise $e(t)$ is considered to be zero-mean white Gaussian.

It is important to note that the exponential function argument can be expressed in terms of the waveform of the considered signals. Proceeding in such a way to replace 6.39 and 6.40 in 6.38 gives:

$$\lim_{N\to\infty} \frac{1}{2\sigma^2}\sum_{n=1}^{N}\left[r_n - s_n(\boldsymbol{\theta})\right]^2 = \frac{1}{N_0}\int_{T_0}\left[r(t) - s(t;\boldsymbol{\theta})\right]^2 \mathrm{d}t. \tag{6.41}$$

As a consequence, the maximization of $p(\mathbf{r}|\boldsymbol{\theta})$ with respect to the parameters $\boldsymbol{\theta}$ of the signal is equivalent to maximizing the likelihood function:

$$\Lambda(\boldsymbol{\theta}) = \exp\left\{-\frac{1}{N_0}\int_{T_0}\left[r(t) - s(t;\boldsymbol{\theta})\right]^2 \mathrm{d}t\right\}. \tag{6.42}$$

This procedure is widely used in carrier synchronization in the process of receiving digital signals. For signal demodulation to occur in the most favorable situation possible, the receiving system must be synchronized with the received wave. Generally, the evaluated parameters are the delay τ and the carrier phase ϕ. If the delay is assumed to be null, $\tau = 0$, the ML function to be maximized is reduced to (PROAKIS; SALEHI, 2008):

$$\begin{aligned}\Lambda(\phi) &= \exp\left\{-\frac{1}{N_0}\int_{T_0}\left[r(t) - s(t;\phi)\right]^2 \mathrm{d}t\right\}\\ &= \exp\left\{-\frac{1}{N_0}\int_{T_0} r^2(t)\ \mathrm{d}t + \frac{2}{N_0}\int_{T_0} r(t)s(t;\phi)\ \mathrm{d}t - \frac{1}{N_0}\int_{T_0} s^2(t;\phi)\ \mathrm{d}t\right\}.\end{aligned} \tag{6.43}$$

Here, the first term is independent of the parameter ϕ and the third term is a constant equal to the signal energy in the T_0 observation interval. Only the second term, which is the cross-correlation between the received signal $r(t)$ and the signal$s(t;\phi)$, depends on the value of the parameter ϕ. So, the likelihood function can be written as:

$$\Lambda(\phi) = C \exp\left[\frac{2}{N_0}\int_{T_0} r(t)s(t;\phi)\ \mathrm{d}t\right], \tag{6.44}$$

where C is constant and independent of ϕ.

The ML estimate $\hat{\phi}_{ML}$ is the value ϕ that maximizes 6.44, or equivalent, is the value that maximizes the logarithm of $\Lambda(\phi)$, known as the log-likelihood function (PROAKIS; SALEHI, 2008):

$$\Lambda_L(\phi) = \frac{2}{N_0}\int_{T_0} r(t)s(t;\phi)\ \mathrm{d}t. \tag{6.45}$$

For the specific case of the microwave SQUID multiplexer, the SQUID response is periodic in multiples of the quantum magnetic flux Φ_0. Considering a magnetic flux modulation in the form of a sawtooth wave, the phase of the SQUID response will be linear, resulting essentially in a sine wave (MATES et al., 2012). This process can be understood as a phase modulation in which the input signal determines the instantaneous phase of the wave. Knowing the frequency of the carrier wave, one can write the received signal as:

$$r(t) = A\cos(2\pi f_c t + \phi) + e(t). \tag{6.46}$$

The parameter sought is the value ϕ that maximizes:

$$\Lambda_L(\phi) = \frac{2A}{N_0}\int_{T_0} r(t)\cos(2\pi f_c t + \phi)\ \mathrm{d}t. \tag{6.47}$$

Therefore, the derivative relative to ϕ must be zero:

$$\frac{d\Lambda_L(\phi)}{d\phi} = 0, \tag{6.48}$$

which yields the expression:

$$\int_{T_0} r(t)\sin\left(2\pi f_c t + \hat{\phi}_{ML}\right)\ \mathrm{d}t = 0, \tag{6.49}$$

and it can be finally rewritten using the arc sum of the sine function and expressed by (PROAKIS; SALEHI, 2008):

$$\hat{\phi}_{ML} = -\,\mathrm{atan}\left[\frac{\int_{T_0} r(t)\sin(2\pi f_c t)\ \mathrm{d}t}{\int_{T_0} r(t)\cos(2\pi f_c t)\ \mathrm{d}t}\right]. \tag{6.50}$$

In the context of the SQUID multiplexer, estimates are currently obtained from 6.50. The complex carrier, which carries the SQUID response modulated over the phase or on its envelope, is the result of the down-mixing process and the subsequent channeling. The modulating signal is essentially a sine wave. An observation interval T_0 is considered that meets the condition $T_{SQUID} \leq T_0 \leq T_{ramp}$, where T_{SQUID} is the SQUID response wave period and T_{ramp} is the period of the flux modulator ramp.

In practice the flux ramp is finite, so a sawtooth or triangular wave is employed. Multiple units of quantum magnetic flux are swept.

An issue arises when considering the flux ramp modulation approach, because on the turning point at the end of a period the system energy undergoes a slight instability. Any sudden transition in magnetic flux modulation can introduce transients into the system energy. To bypass this concern, it is necessary to define a window that guarantees minimum readout linearity, so that the phase is extracted in each ramp segment (MATES et al., 2012). Effectively, the output is sampled at the flux ramp frequency, i.e., each point of the energy pulse is relative to a ramp period. It is also possible to perform the phase estimation for each sample under some constraints.

Some simulations were conducted in Matlab in order to illustrate the estimation results. Figure 36 shows the estimated energy pulses in different SNR configurations considering that the signal is processed sample by sample, with a maximum phase shift of 24°, since the received signal is an ideal cosine function with zero-mean white Gaussian additive noise.

Figure 36a shows that the pulse adjustment is excellent for the ideal case, where there is no noise and the received signal is a perfect cosine. The residual resulting from the estimation is presented in Figure 36b, where it can be seen that the rise time is considerably increased. The estimated pulse rise time will be directly proportional to the number of points used to obtain an estimate and the sampling frequency, in other words, the length of the data vector and the delay between samples.

Figures 36c and 36d show the estimated pulses for received signals submitted to 20 dB and 10 dB SNRs, respectively. Noise affects the method's estimation quality.

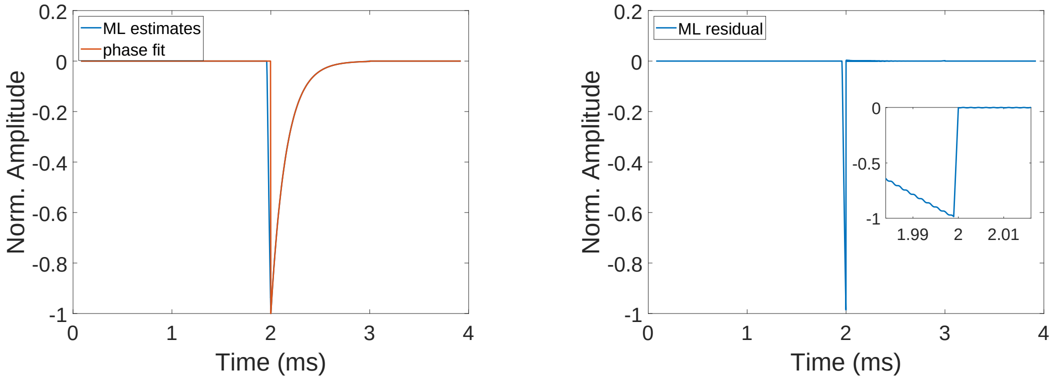

(a) Pulse with exponential decay retrieved through the maximum likelihood function for a minimum phase shift of −24°. The processed signal is an ideal cosine function and the noise power is assumed to be zero.

(b) Difference between original and estimated pulse. The pulse rise time is directly proportional to the size chosen to the processed data vector. A 25 kHz flux ramp is used, representing a rise time of 40 μs.

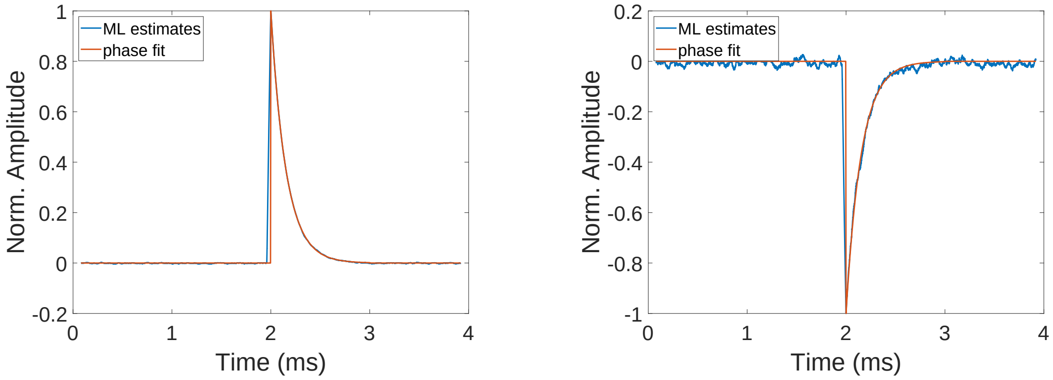

(c) Positive pulse with exponential decay recovered by the maximum likelihood criteria for an SNR = 20 dB.

(d) Negative pulse with exponential decay recovered by maximum likelihood function for an SNR = 10 dB.

Figure 36 – Maximum likelihood method applied in different SNR contexts for an absolute maximum phase shift of 24°. The red curve is the original pulse. (a) Estimated pulse for an SNR = ∞; (b) difference between the original and the estimated pulse; (c) SNR = 20 dB and (d) SNR = 10 dB. Source: Author.

7 Sensor Array-based Approach

7.1 Introduction

Recalling the *modus operandi* of SEAD method in DOA estimation, a sensor array-based approach is proposed in order to estimate the phase shift of carriers in the microwave SQUID multiplexer system. As seen in 2.5, the difference between the two largest eigenvalues of the spatial correlation matrix provides an estimate of the direction, in which a flat wave impinges the sensors. The source positions are related to the time delay between the induced signals in the circuits relative to each sensor. Therefore, the parameter of interest to be estimated is basically the signal phase shift.

For this reason, there is a motivation to apply those techniques to the energy pulse estimation problem in the microwave SQUID multiplexer. To build the bridge between the two problems, an analogy with an array consisting of two sensors is established ($K = 2$). One sensor provides a signal with no phase shift and acts like a reference vector, the other sensor provides the instantaneous values coming out from the DDC and it is updated with the received values for each new sample. Consequently, a spatial correlation matrix $\mathbf{R}$ of dimensions 2×2 can be estimated. Due to the limitations posed by the modulation wave's turning point, the SQUID modulation ramp cycle determines the length of the data vector. This procedure yields a number of $N = \frac{f_{sampling}}{f_{ramp}}$ values for each algorithm iteration. The length N represents the number of snapshots in analogy to the DOA problem.

In practice, the reference signal can be obtained from the measured data, once the system is idle (no events on the MMC).

The signal processing over the I/Q carriers is currently performed off-line through Matlab software by means of scripts developed for this purpose.

The developed scripts feature modularity. A main file calls functions that are performed throughout the data processing. In the program's header there are several defined parameters: measured or simulated data; in-phase and quadrature components stored individually in separate files or interleaved in the same file; frame size for splitting the data to be processed from the total data set; sampling frequency; decimation factor; set the I/Q amplitude and initial phase shift between $\mathbf{x}_R$ and $\mathbf{x}_T$; amplitude threshold for pulse detection; expected pulse duration for storing the estimates; several function enablers; filtering parameters; sample by sample or block by block processing mode; type of employed estimators; flux ramp parameters; set data vector length N; set the length of valid data in the ML method; among other aspects.

Processed signals undergo high pass filtering in order to discard the DC component.

The signals to be processed are the I/Q components in the case of the eigenvalue method and the I/Q magnitude in the case of the maximum likelihood method.

Depending on the settled goals, it is possible to process blocks of length N obtaining one estimate per block or process sample by sample in order to obtain as many estimates as samples. Of course, one must take into account the computational effort involved when aiming to process it on-line.

7.2 Mathematical Fundamentals of the Eigenvalue Method

It is already known from Linear Algebra that the linearly dependent lines produce eigenvalues equal to zero (MEYER, 2001; GOLUB; LOAN, 1996). Therefore, considering the matrix $\mathbf{R}[i]$ with dimensions 2×2, identical signals will produce one eigenvalue concentrating all power and another null-valued. If the signals are not equal for at least one point, then the first eigenvalue will be reduced and the second will be nonzero.

7.2.1 Complex Exponential Modeling

The eigenvalues of $\mathbf{R}$ are calculated through the characteristic polynomial, which is obtained by the eigenvalue decomposition process. Assuming that the in-phase and quadrature components have power equal to $\frac{\sqrt{2}}{2}$ and the same oscillation frequency, the reference and transmitted vectors can be considered ideal complex exponentials. Thus, the reference vector can be denoted by $\mathbf{x}_R[i]_{(1\times N)} = \mathbf{i}_R[i] - j\mathbf{q}_R[i] = \exp(-j\omega_{iq}T_S i - \theta_R)$ and the transmitted vector by $\mathbf{x}_T[i]_{(1\times N)} = \mathbf{i}_T[i] - j\mathbf{q}_T[i] = \exp(-j\omega_{iq}T_S i - \theta_T[i])$, both with dimensions $1 \times N$. The data matrix $\mathbf{X}_{2\times N}[i]$ can be written, according to Appendix D, as:

$$\mathbf{X}[i] = \begin{pmatrix} \mathbf{x}_R[i] \\ \\ \mathbf{x}_T[i] \end{pmatrix}_{2\times N} \tag{7.1}$$

and the spatial correlation matrix is obtained through the matrix product $\mathbf{X}[i]\ \mathbf{X}^*[i]$:

$$\mathbf{R}[i] = \begin{pmatrix} {}^{|\mathbf{x}_R[i]|^2}\!/_{N} & {}^{\langle \mathbf{x}_T[i], \mathbf{x}_R[i] \rangle}\!/_{N} \\ \\ {}^{\langle \mathbf{x}_R[i], \mathbf{x}_T[i] \rangle}\!/_{N} & {}^{|\mathbf{x}_T[i]|^2}\!/_{N} \end{pmatrix}. \tag{7.2}$$

In the ideal case where the signals are complex exponentials, the two eigenvalues present the behavior observed in Figure 37.

In both the first and second eigenvalues, the pulses are preceded by a peak generated by the phase-shifted data filling process. This peak is precisely the length of a data vector, i.e. it lasts N points. This directly affects the rise time of the pulse, which is an extremely important factor for the energy calculation.

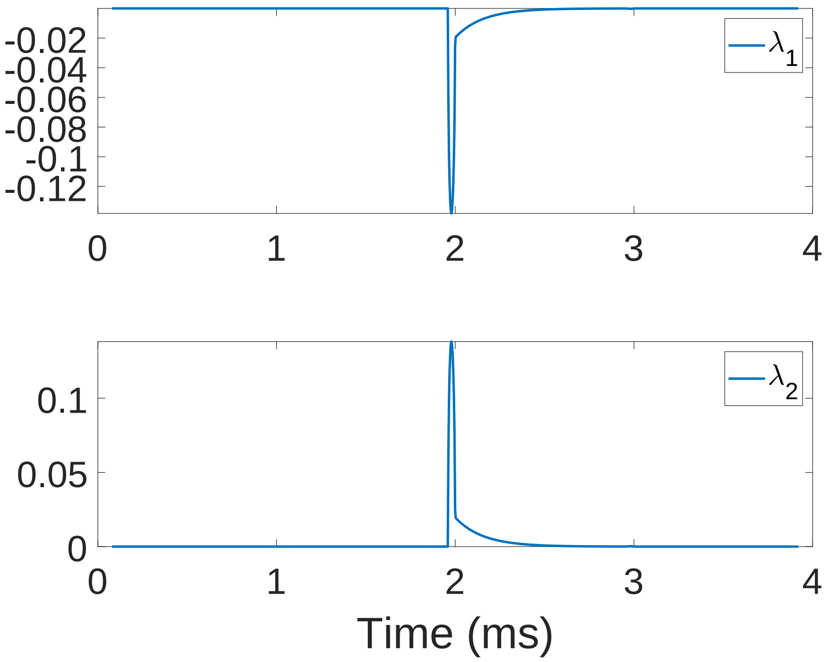

Figure 37 – Estimated pulses from ideal complex exponential input signals. At the top there are the λ_1 values, at the bottom λ_2 values. In both cases the square root was required to be extracted. Source: Author.

Following the approach used in the SEAD method, the difference between the two values is calculated. The behavior of the difference between values can be seen in Figure 38a, where the original and estimated pulses are overlapping, and 38b, where the negative pulse is emphasized. The values were manipulated to keep the baseline at zero and pulses with maximum unit amplitude.

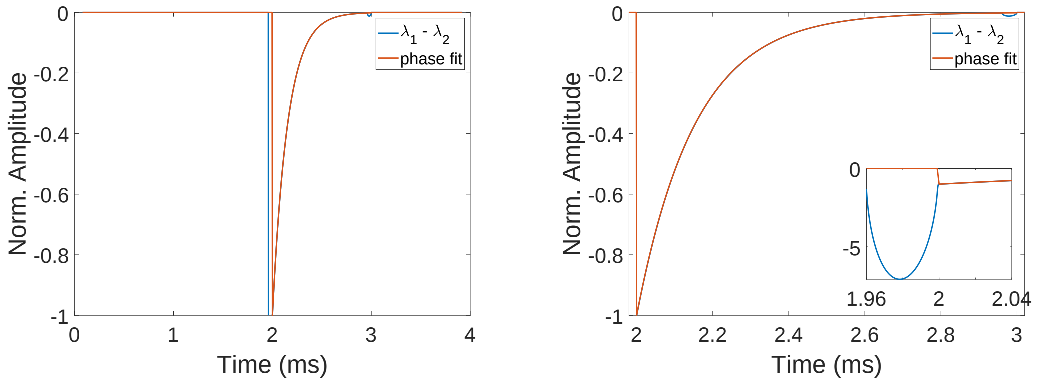

(a) Difference between both eigenvalues, $\lambda_1 - \lambda_2$.

(b) Highlighting a negative pulse.

Figure 38 – Estimates using the difference between λ_1 and λ_2. This approach is based in the idea developed in the SEAD method. Source: Author.

In this particular case, the polarity of the pulse is not detected because, as is shown in Figure 37 the largest eigenvalue is always an increasing exponential pulse, while the second is a decreasing exponential pulse, in accordance with the formulation delivered in Appendix F. In addition, it is necessary to remove the square root of each point so that the time constant of the exponential function (decay) is adjusted to the original pulse. These issues will be discussed in more depth in the following sections.

After obtaining the correlation matrix, the EVD of $\mathbf{R}[i]$ produces the decomposition into eigenvalues and eigenvectors, as presented in Appendix D. Since the matrix $\mathbf{R}[i]$ has dimensions 2 × 2, it is possible to deliver a formulation which is a function of the matrix entries. The characteristic polynomial relative to the matrix $\mathbf{R}[i]$ will have degree 2. Thus, the eigenvalues can be obtained as follows:

$$\lambda[i] = \frac{(|\mathbf{x}_R[i]|^2 + |\mathbf{x}_T[i]|^2)}{2N} \pm \frac{\sqrt{(|\mathbf{x}_R[i]|^2 - |\mathbf{x}_T[i]|^2)^2 + 4|\langle \mathbf{x}_R[i], \mathbf{x}_T[i]\rangle|^2}}{2N}. \tag{7.3}$$

The eigenvalues differ only by the term within the square root. This means that for the idle system, λ_1 will be twice the average signal power and λ_2 will be zero. On the other hand, whenever there is an energy pulse, λ_1 and λ_2 will have values in the range (0,2) depending on the maximum value of the phase shift in the transmitted signal. Furthermore, it can be observed that:

$$|\mathbf{x}_R[i]|^2 = \sum_{i=1}^{N} |\mathbf{x}_R[i]|^2 = \sum_{i=1}^{N} \left[\mathrm{Re}(\mathbf{x}_R[i])^2 + \mathrm{Im}(\mathbf{x}_R[i])^2\right] = const.; \tag{7.4}$$

$$|\mathbf{x}_T[i]|^2 = \sum_{i=1}^{N} |\mathbf{x}_T[i]|^2 = \sum_{i=1}^{N} \left[\mathrm{Re}(\mathbf{x}_T[i])^2 + \mathrm{Im}(\mathbf{x}_T[i])^2\right] = const.; \tag{7.5}$$

$$|\mathbf{x}_R[i]|^2 = |\mathbf{x}_T[i]|^2, \tag{7.6}$$

and the eigenvalues are given as a function of the signals' phase by:

1. in case $\theta_R = \theta_T[i]$:

$$\lambda_1[i] = \frac{1}{N}\left[|\mathbf{x}_R[i]|^2 + |\langle \mathbf{x}_R[i], \mathbf{x}_R[i]\rangle|\right] = |\mathbf{x}_R[i]|^2 + |\mathbf{x}_R[i]|^2 = 2; \tag{7.7}$$

$$\lambda_2[i] = \frac{1}{N}\left[|\mathbf{x}_R[i]|^2 - |\langle \mathbf{x}_R[i], \mathbf{x}_R[i]\rangle|\right] = |\mathbf{x}_R[i]|^2 - |\mathbf{x}_R[i]|^2 = 0. \tag{7.8}$$

2. in case $\theta_R \neq \theta_T[i]$:

$$\lambda_1[i] = \frac{1}{N}\left[|\mathbf{x}_R[i]|^2 + |\langle \mathbf{x}_R[i], \mathbf{x}_T[i]\rangle|\right] = 1 + \frac{|\langle \mathbf{x}_R[i], \mathbf{x}_T[i]\rangle|}{N}; \tag{7.9}$$

$$\lambda_2[i] = \frac{1}{N}\left[|\mathbf{x}_R[i]|^2 - |\langle \mathbf{x}_R[i], \mathbf{x}_T[i]\rangle|\right] = 1 - \frac{|\langle \mathbf{x}_R[i], \mathbf{x}_T[i]\rangle|}{N}. \tag{7.10}$$

Therefore, based on 7.9 and 7.10, it is important to observe the behavior of the inner product magnitude, as it exclusively determines the pulse amplitude for signals

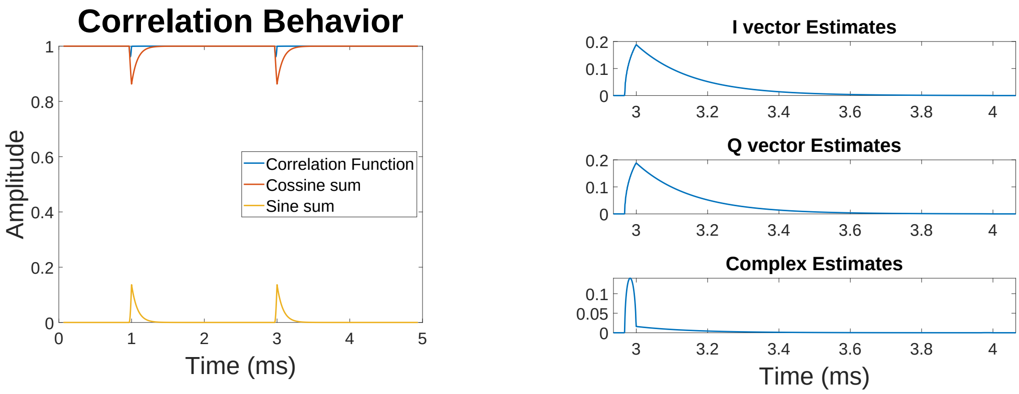

(a) Correlation function behavior for ideal complex exponentials.

(b) Estimates obtained by processing $\mathbf{i}_T$ (top), $\mathbf{q}_T$ (middle) and $\mathbf{x}_T = \mathbf{i}_T - j\mathbf{q}_T$ (bottom).

Figure 39 – The correlation function combines a cosine and a sine function in its calculation. It is also possible to estimate a pulse performing the calculations over the real and imaginary components individually. Source: Author.

modeled as complex exponentials. According to Appendix F, the magnitude of the inner product follows exclusively the phase-shifted values and it can be written as:

$$|\langle \mathbf{x}_R[i], \mathbf{x}_T[i]\rangle| = \left\{ \left[\sum_{i=1}^{N} \cos(\theta_T[i])\right]^2 + \left[\sum_{i=1}^{N} \sin(\theta_T[i])\right]^2 \right\}^{\frac{1}{2}} . \tag{7.11}$$

7.2.2 General Case

To understand how the pulse is generated it is necessary to mathematically analyze the operations performed and to identify how the amplitude, frequency and phase of the signals interfere the estimates. Once obtained the mathematical expression that rules the method it will be possible to discuss the aspects that contribute to optimize the pulse estimation. For the sake of easiness for presenting the expressions, the temporal index $[i]$ will be omitted.

According to 7.11, there are two functions of opposite behavior. The cosine function results in an upward curve after the data fill interval and the sine function results in a downward curve. As a consequence, the variation in the inner product is attenuated, however, this occurs under very specific circumstances. Figure 39a shows the composition for ideal signals generated with the aid of Matlab software for a maximum pulse phase shift of 24°.

In Figure 39b it is observed the behavior of estimated pulses using the cosine ($\mathbf{i}_R$), sine ($\mathbf{q}_R$) and the complex exponential function ($\mathbf{i}_R - j\mathbf{q}_R$), in which case the square root extraction of the values for curve fitting is demanded.

It is concluded that it is possible to estimate the pulse individually by the complex signal components, i.e., if $B = 0$ it turns out that $\mathbf{x}_R = \mathbf{i}_R$ and $\mathbf{x}_T = \mathbf{i}_T$, or if $A = 0$ the

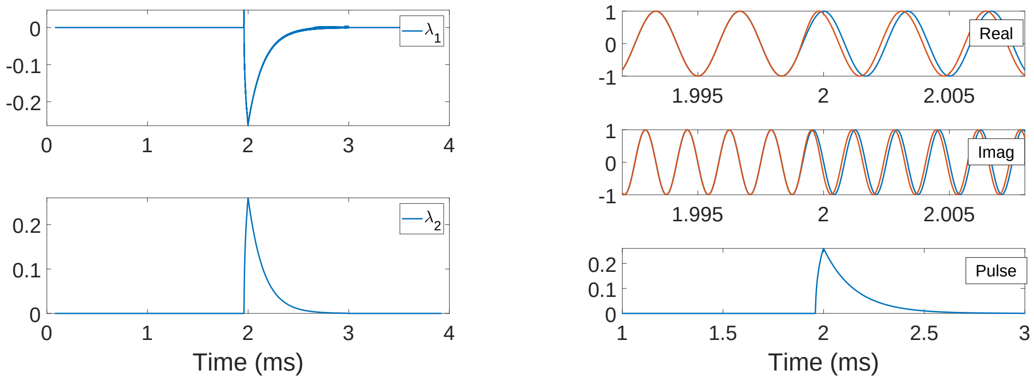

(a) Correlation matrix eigenvalues for I/Q signals with different frequencies.

(b) I and Q components and the pulse obtained through λ_2.

Figure 40 – A pulse of energy estimated through ideal signals where $\omega_q = 2\omega_i$. Source: Author.

signal vectors are written as $\mathbf{x}_R = -j\mathbf{q}_R$ and $\mathbf{x}_T = -j\mathbf{q}_T$, as seen in Figure 39b. Thus, by varying the parameters of the wave, significant results can be reached.

Therefore, it is necessary to define the reference and transmitted vectors in a broader sense:

$$\mathbf{x}_R = \mathbf{i}_R - j\mathbf{q}_R = A_R \cos(\omega_i T_S i - \theta_R) - jB_R \sin(\omega_q i T_S - \theta_R); \tag{7.12}$$

$$\mathbf{x}_T = \mathbf{i}_T - j\mathbf{q}_T = A_T \cos(\omega_i T_S i - \theta_T) - jB_T \sin(\omega_q i T_S - \theta_T), \tag{7.13}$$

however, it is common to have $A_R = A_T$ and $B_R = B_T$ by setting the complex signals' power equal to 1.

In addition to the case of different power for the real and imaginary vector components, one can analyze the case where the frequencies ω_i and ω_q are distinct. Figure 40a shows the pulse estimation for the case where $\omega_q = 2\omega_i$, besides, $A = B = 1$ and $\theta_R = \theta_T[0] = 0$. In Figure 40b the real and imaginary components of the complex signal and the pulse obtained through the second eigenvalue are presented. The pulse should be negative according to the behavior of the red curve (transmitted) that is now ahead of the blue wave (reference), as can be seen in the waveforms. However, the estimate obtained through the second eigenvalue is positive and the polarity of the pulse cannot be identified. The square root of the estimates must be extracted.

Next, the case of an initial phase shift between ideal complex exponential reference and transmitted signals is considered. As demonstrated in Appendix E, the behavior of the eigenvalues for any phase shift between the reference and the transmitted signal will produce an equivalent result to what is obtained for equal initial phases.

On the contrary, the estimates obtained exclusively through the in-phase components ($\mathbf{i}_R$ and $\mathbf{i}_T$) or quadrature components ($\mathbf{q}_R$ and $\mathbf{q}_T$) will have proper pulse polarity.

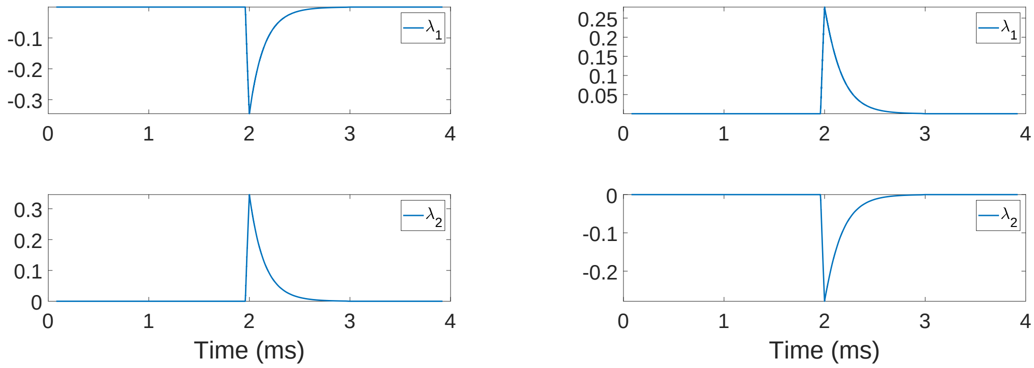

(a) Eigenvalues behavior in the presence of a positive pulse, 24° maximum, where $\theta_R = \theta_T[0] - \frac{\pi}{3}$, $A = 1$ and $B = 0$.

(b) Eigenvalues behavior in the presence of a negative pulse, $-24°$ minimum, where $\theta_R = \theta_T[0] - \frac{\pi}{3}$, $A = 1$ and $B = 0$.

Figure 41 – Estimated energy pulses for an ideal in-phase signal with initial phases $\theta_R = -\frac{\pi}{3}$ and $\theta_T[0] = 0$. Source: Author.

Figure 41 presents the estimated pulses for positive and negative original pulses. Note that both eigenvalues can provide estimates for the pulse.

7.3 Simulated Data

In this section, some results of simulations performed in Matlab are presented. Consider the vectors I and Q are synthesized cosine and sine functions, respectively. The power, phase and frequency parameters may be arbitrarily assigned according to the analysis interest.

To perform the simulations, a sampling rate of 15,625 MS/s, a sawtooth modulation ramp with frequency equal to 25 KHz, amplitude of 5 units of quantum magnetic flux, which imply in a block of length $N = 625$, was considered. In addition, the pulse has a maximum peak relative to a phase shift of ±24°.

The performance of the methods is assessed in terms of the Mean Squared Error (MSE) of 20 experiments in different scenarios. The maximum (or minimum) phase shift and the SNR are the parameters in the evaluation. The original and estimated pulses are normalized and their difference provides the residuals of the estimation.

In a simulated environment, the starting point of the pulse is known, such that, only the residuals relative to the pulse activity are calculated. The error due to the rise time will not be considered, this procedure measures how good the estimated pulse fit to the original one.

The noise is modeled as zero-mean white Gaussian added to data vectors by multiple sources. The reference and transmitted vectors are denoted respectively as:

$$\begin{aligned}\mathbf{y}_R &= (\mathbf{i}_R + \mathbf{e}_{R,i}) - j\,(\mathbf{q}_R + \mathbf{e}_{R,q}) \\ &= A_R \cos(\omega_i T_S i - \theta_R) - j B_R \sin(\omega_q T_S i - \theta_R) + \mathbf{e}_R; \qquad (7.14) \\ \mathbf{y}_T &= (\mathbf{i}_T + \mathbf{e}_{R,i}) - j\,(\mathbf{q}_T + \mathbf{e}_{T,q}) \\ &= A_T \cos(\omega_i T_S i - \theta_T[i]) - j B_T \sin(\omega_q T_S i - \theta_T[i]) + \mathbf{e}_T. \qquad (7.15)\end{aligned}$$

both are $1 \times N$. The eigenvalues are obtained as is shown on Appendix D as:

$$\lambda = \frac{(|\mathbf{x}_R|^2 + |\mathbf{x}_T|^2)}{2N} + \sigma_e^2 \pm \frac{\sqrt{(|\mathbf{x}_R|^2 - |\mathbf{x}_T|^2)^2 + 4|\langle \mathbf{x}_R, \mathbf{x}_T \rangle|^2}}{2N}. \qquad (7.16)$$

From the equation 7.16, one can apply simplifications by approximating and discarding terms that do not decisively aggregate in the results. In general, the two vectors $\mathbf{x}_R$ and $\mathbf{x}_T$ are very similar complex signals and, therefore, the difference between their norms will be small. It can be assumed that the difference between them will be irrelevant to the term within the square root, because the term referring to the inner product between the vectors will predominate over this difference, $4|\langle \mathbf{x}_R, \mathbf{x}_T \rangle|^2 \gg (|\mathbf{x}_R|^2 - |\mathbf{x}_T|^2)^2$. It follows that the eigenvalues can be approximated as:

$$\lambda_1 \approx \frac{1}{2N}\left[|\mathbf{x}_R|^2 + |\mathbf{x}_T|^2 + 2|\langle \mathbf{x}_R, \mathbf{x}_T \rangle|\right] + \sigma_e^2; \qquad (7.17)$$

$$\lambda_2 \approx \frac{1}{2N}\left[|\mathbf{x}_R|^2 + |\mathbf{x}_T|^2 - 2|\langle \mathbf{x}_R, \mathbf{x}_T \rangle|\right] + \sigma_e^2. \qquad (7.18)$$

An even stronger constraint can be imposed in special cases, and the expression can be rewritten as:

$$\lambda_1 \approx \frac{1}{N}\left[|\mathbf{x}_R|^2 + |\langle \mathbf{x}_R, \mathbf{x}_T \rangle|\right] + \sigma_e^2; \qquad (7.19)$$

$$\lambda_2 \approx \frac{1}{N}\left[|\mathbf{x}_R|^2 - |\langle \mathbf{x}_R, \mathbf{x}_T \rangle|\right] + \sigma_e^2. \qquad (7.20)$$

where the norm of $\mathbf{x}_R$ is constant whenever the data vector length is a multiple of the number of points in one magnetic flux ramp cycle.

7.3.1 Real and Imaginary Components with Equal Power

In the ideal case, considering the signals are zero-mean ideal complex exponential functions with null initial phases, the eigenvalue method produces pulses in a large range of phase shifts. The largest eigenvalue is strongly affected by the noise. Figure 42a shows the eigenvalues for SNR = 20 dB and an energy pulse corresponding to a maximum phase shift of 24°. In Figure 42b it is shown the in-phase and quadrature components in addition to the pulse generated by the second eigenvalue. For small phase shifts, the pulse amplitude is extremely low.

As expected, before subtracting the mean of estimates, the baseline was consistent with 7.16. First and second eigenvalue raw estimates were originally positioned at

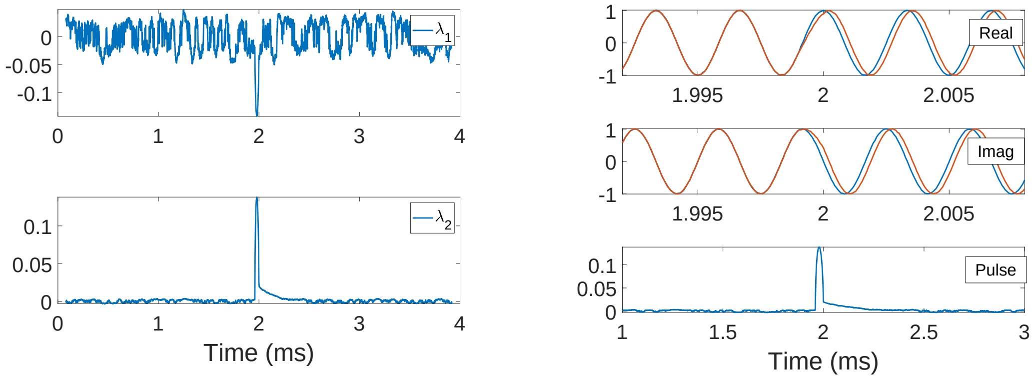

(a) Effect of noise on the eigenvalues.

(b) In-phase and quadrature components for a maximum phase shift of 24°.

Figure 42 – Pulse estimation through complex exponential signals. (a) Eigenvalues of the spatial correlation matrix, (b) real and imaginary components and pulse obtained by the second eigenvalue for a SNR of 20 dB. Source: Author.

heights $1,414166022655965$ and $1,0007416348917 \times 10^{-2}$, the estimates have a variance of $6.704855736524886 \times 10^{-4}$ and $3.221947715830095 \times 10^{-6}$, respectively.

The pulse cannot be estimated properly for a wide range of angles, once the noise easily corrupts the estimate values. The pulse behavior in this situation is very peculiar, presenting a higher peak during the process of phase-shifted data filling. The square root must be extracted and the polarity is not identified.

In order to assess the estimation capability, the MSEs of the estimates obtained by the assessed methods are presented in Figures 43, 44, 45, 46, and 47. In Figures 43 and 44, the MSE is evaluated for phase shifts in the range $(-1800°, 1800°)$ and SNRs ranging from 0 to 20 dB.

The eigenvalue method is able to estimate the pulses even for such a long angle range. For high SNRs, 16, 18, 20 dB, and for the angle range $\pm(200°, 700°)$, the order of magnitude of the error is -3. The ML method failed to provide estimates due to the fact that the magnitude of a zero-mean ideal complex exponential is constant.

On the other hand, if the signals are allowed to be non-zero-mean, the range of the possible phase shift is smaller, $(-180°, 180°)$. The maximum likelihood method performs very well and it outperforms the eigenvalue method, as seen in Figure 46. The ML has shown an error in the order of magnitude -4 for high SNRs, however, it fails to estimate in some region due to the limitation regarding the definition domain of the arctangent function, which is $(\frac{-\pi}{2}, \frac{\pi}{2})$. The eigenvalue method can be performed on complex and real signals, Figures 45 and 47 show very similar error performance.

All methods present bad performance for small angles, the noise prevails over the pulse amplitude and hamper the estimation.

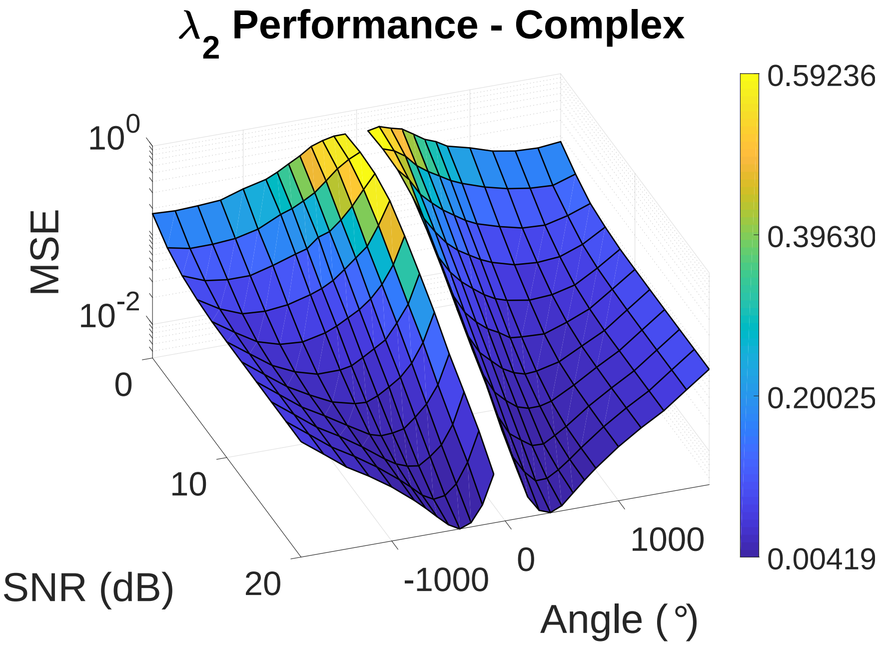

Figure 43 – MSE surfaces of the eigenvalue method (λ_2) for zero-mean complex exponential signals.

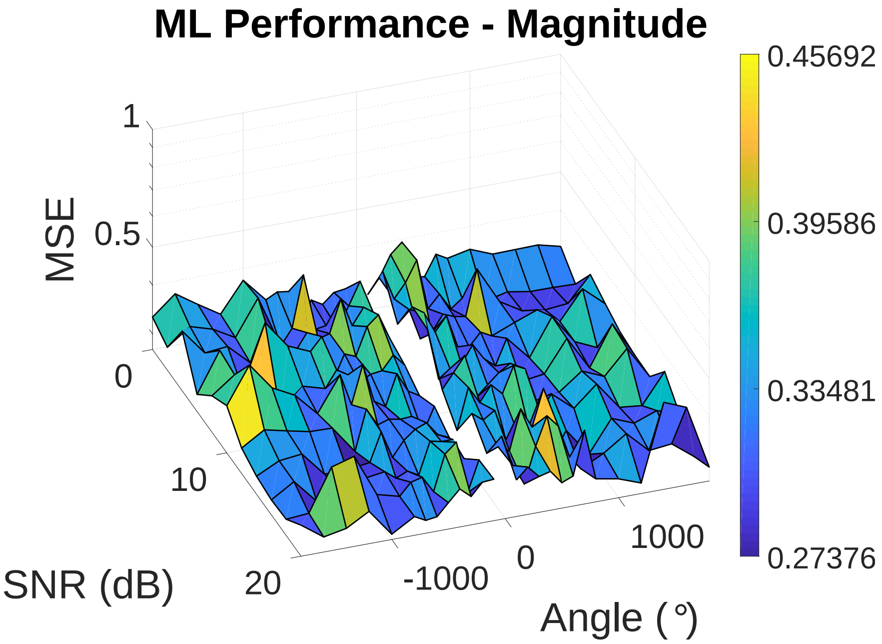

Figure 44 – MSE surfaces of the ML method applied to the magnitude of a zero-mean complex exponential.

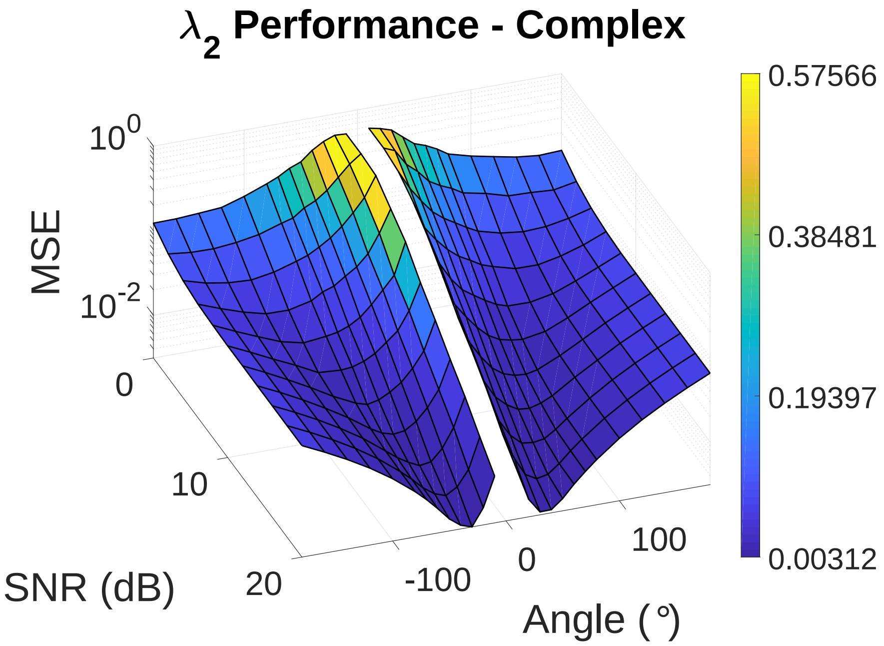

Figure 45 – MSE surfaces of the eigenvalue method (λ_2) for non-zero-mean complex exponential signals.

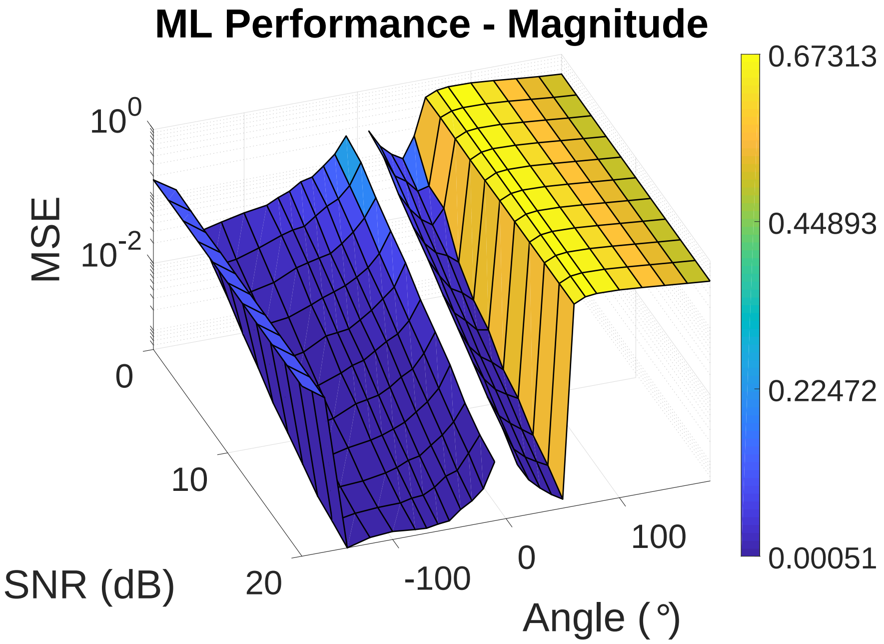

Figure 46 – MSE surfaces of the ML method applied to the magnitude of a non-zero-mean complex exponential.

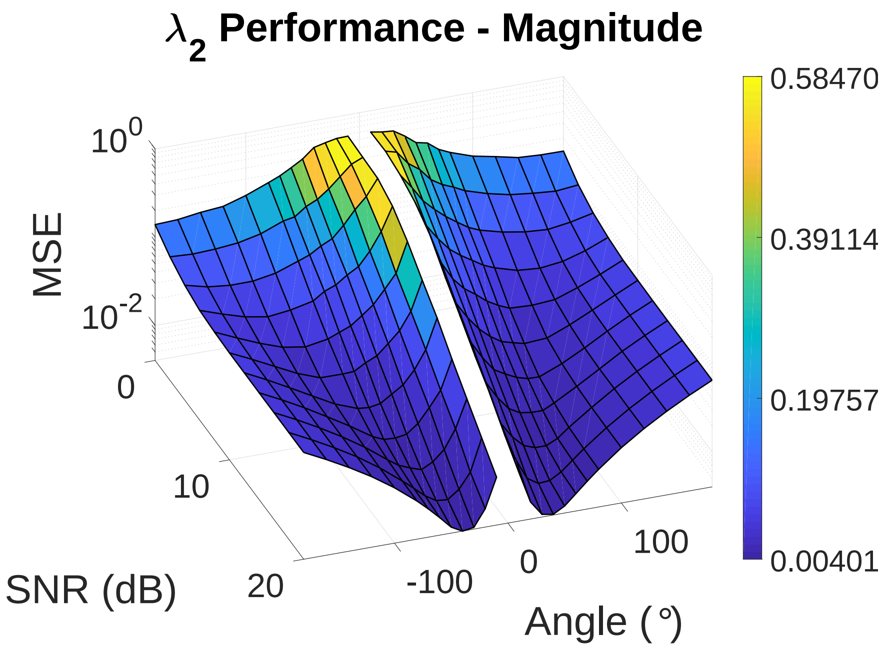

Figure 47 – MSE surfaces of the eigenvalue method (λ_2) applied to the magnitude of non-zero-mean complex exponential signals.

7.3.2 Real and Imaginary Components with Different Power

Different values can be assigned to the signal amplitudes and different $\frac{A}{B}$ relations can be reached, leading to a vast number of possibilities for the complex number distribution over the complex plan. A representative case of this situation of different power is presented in Figure 48, where $A = 1$ and $B = 0$. The SNR is set at 20 dB and the pulse corresponds to a maximum phase shift of 24°.

The energy pulse can be estimated from the second eigenvalue with a variance of approximately $2.193948181799515 \times 10^{-6}$ along the data related to an idle system. The largest eigenvalue is greatly affected by noise and has a variance of approximately $6,385636855268621 \times 10^{-4}$ along the idle state data.

The pulses have original base lines at 1.414093977030180, for λ_1, and 0.007071973939792, for λ_2, once again checking the formulation proposed. The noise shifts the baseline up by a factor of $\frac{\sqrt{2}}{2} \times 10^{-2}$ because the imaginary part is zero and does not contribute to the calculation. Only negative pulses are obtained from λ_1 and positive from λ_2.

The MSE surfaces are presented to evaluate the accuracy of the eigenvalue method in this situation. The estimated pulses were obtained considering an angle range from $-180°$ to $180°$ and SNR ranging from 0 to 20 dB. Figure 49 presents the performance of the eigenvalue method, using λ_2 as an estimator, applied to a phase-modulated cosine function according to the maximum phase shift indicated in the axis. Figure 50 presents the MSE for a sine function under the same conditions.

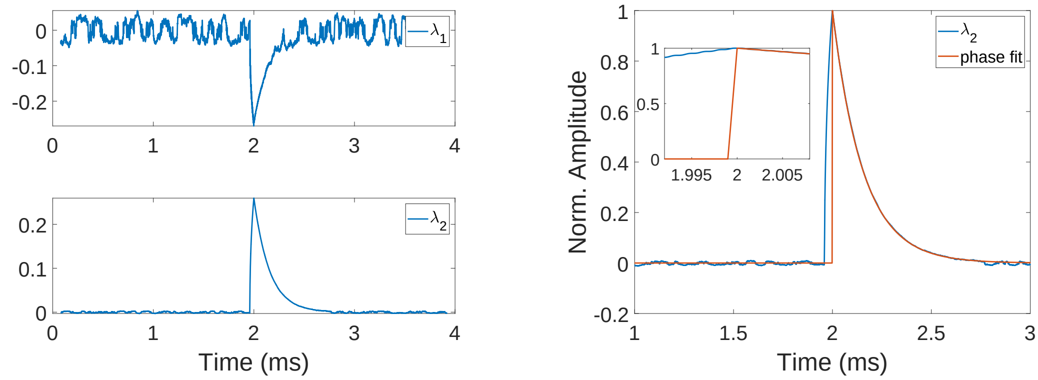

(a) Estimates of a positive pulse with maximum phase shift of 24° obtained with both eigenvalues.

(b) Estimates from the second eigenvalue and the original pulse. Despite the noise added to the carriers, the pulse estimates fit to the original pulse.

Figure 48 – Energy pulse estimation for signals containing real and imaginary parts with different power. (a) first and second eigenvalues and (b) superposition of original and estimated pulses Source: Author.

The method performed very well for high SNRs and angles ranging in $\pm(20°, 70°)$ in both cases. The estimation over the quadrature component has shown instability for low SNRs and small angles. For angles with absolute value greater than 100° the MSE increases very fast, which characterizes the region where the method fails to provide estimates.

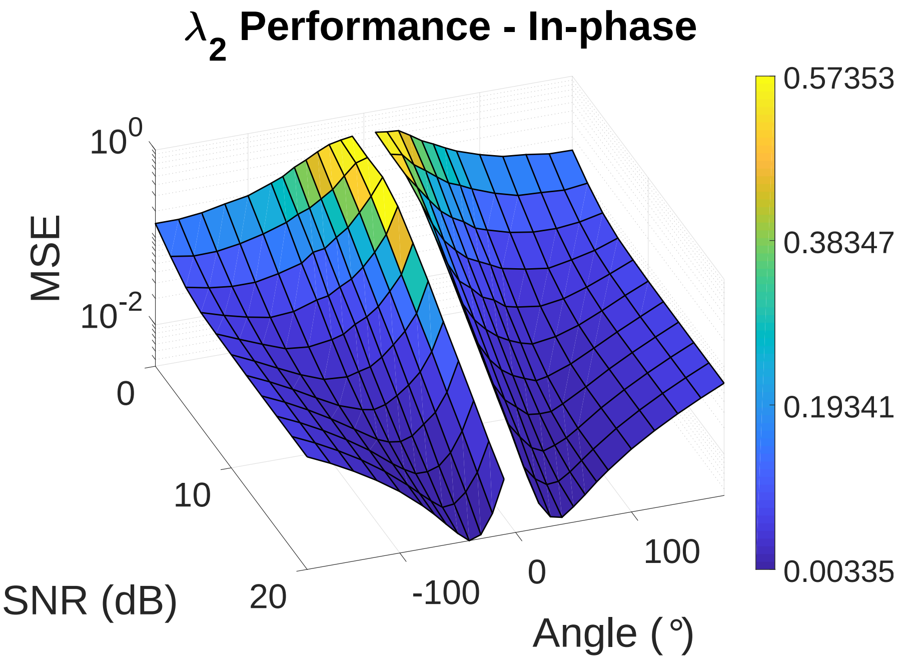

Figure 49 – MSE of estimates obtained by the eigenvalue method (λ_2) applied to the in-phase component, a zero-mean cosine function.

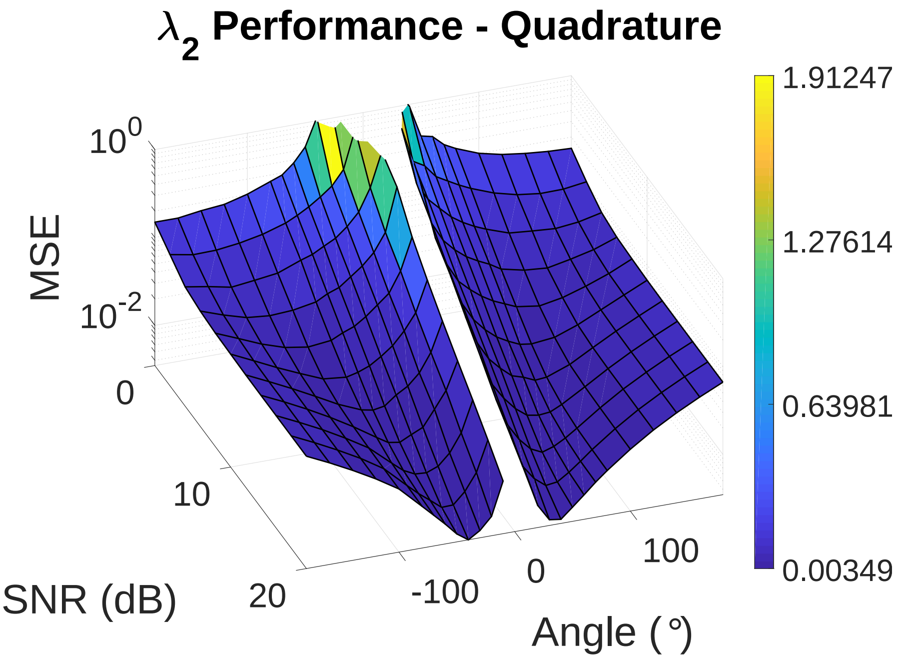

Figure 50 – MSE of estimates obtained by the eigenvalue method (λ_2) applied to the quadrature component, a zero-mean sine function.

7.3.3 Real and Imaginary Components with Different Frequencies

Figure 51 presents the estimated pulse obtained if the frequencies of the in-phase and quadrature components are different, in this simulation $\omega_q = 2\omega_i$, SNR $= 20$ dB and the pulse has a maximum amplitude relative to a 24° phase shift.

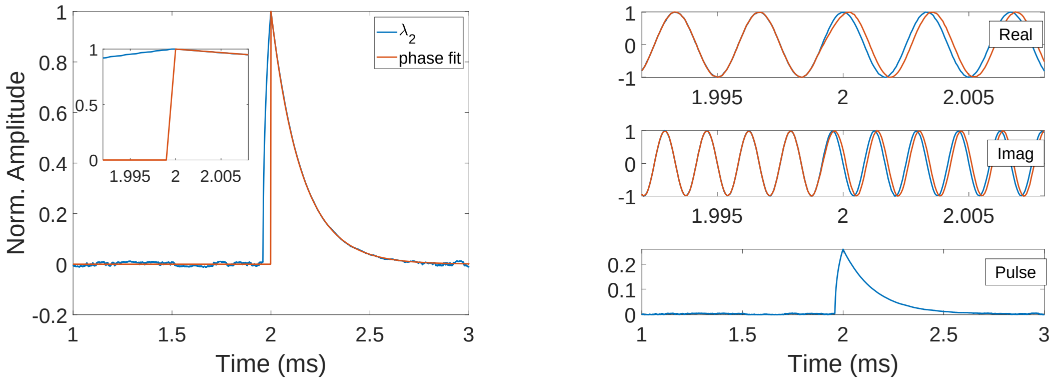

(a) The second eigenvalue used as a pulse estimator for the case where I and Q have different frequencies.

(b) I and Q components and the pulse obtained through λ_2.

Figure 51 – Simulations performed for $\omega_q = 2\omega_i$ at 20dB. The second eigenvalue provides the estimates for the pulse decay. Source: Author.

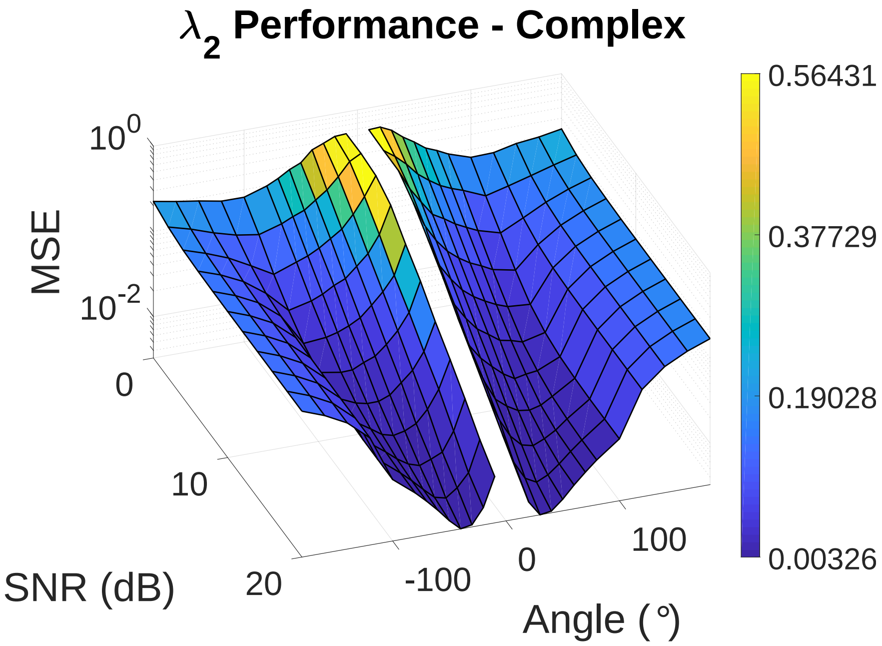

Figure 52 – MSE relative to the estimation through λ_2 for zero-mean complex signals considering $\omega_q = 2\omega_i$.

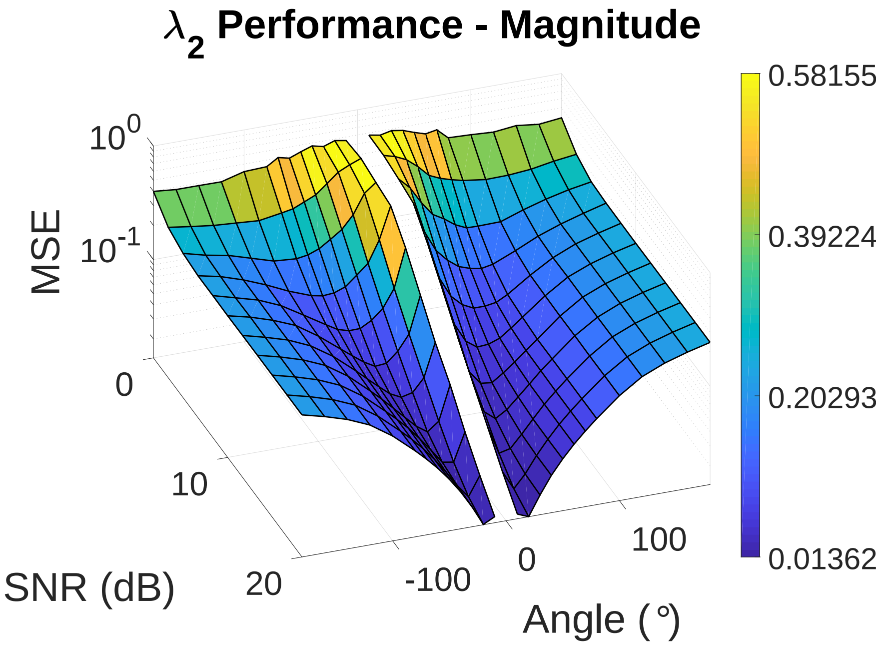

Figure 53 – MSE relative to the estimation through λ_2 for the magnitude of zero-mean complex signals $\omega_q = 2\omega_i$.

This approach still has the limitation of providing only negative pulses through the first eigenvalue and positive pulses through the second eigenvalue, not allowing the identification of the pulse polarity. Estimates of the pulse through the largest eigenvalue are harmed by noise, and the square root of both must be extracted so that the time

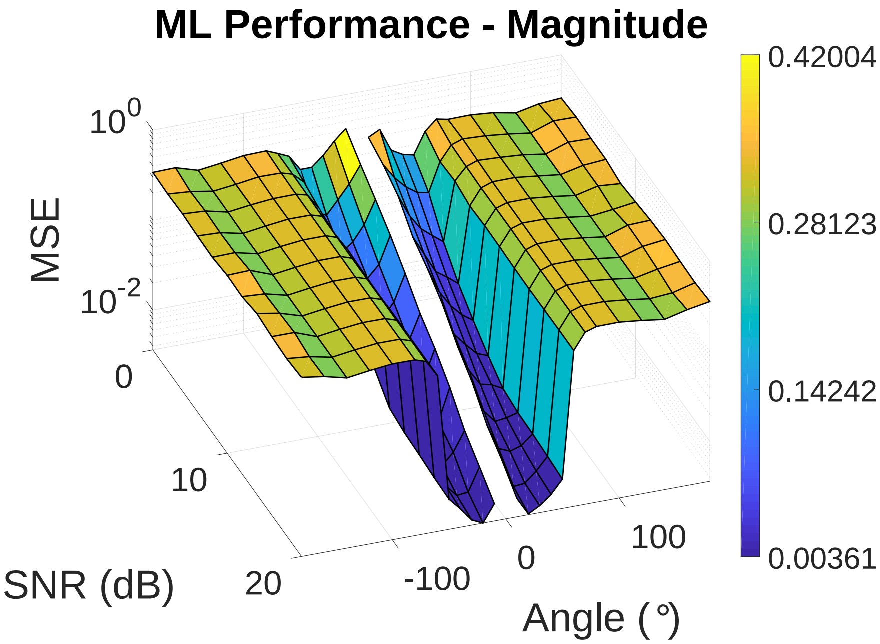

Figure 54 – MSE relative to the ML method for the magnitude of a zero-mean complex signal $\omega_q = 2\omega_i$.

constant is consistent with that of the original pulse. In Figure 51a the influence of the data vector length N on the pulse rise time is remarkable, it is essential to reduce it as much as possible.

For the synthesized pulse with the aid of Matlab software, there is a rise time of 1,024 μs. There are 16 samples representing the time that the sensor requires to go from idle to activity. This value is far from that obtained for the case without ramp modulation by a factor of approximately 8 times slower, which was reported in (KEMPF et al., 2017b) to be 130 ns. However, the rise time of the pulse turns into 410.24 ms when the data vector is of length $N = 625$, which may be harmful to the calculation accuracy of the scattered energy in the pulse.

Figures 52, 53, and 54 show the performances of the eigenvalue estimates obtained from zero-mean complex signals and also from its magnitude, besides the performance of the ML method for the magnitude of the zero-mean complex signal is presented. The eigenvalue method performed similarly to the previous cases showing minimum MSE for an angle range varying in $\pm(20, 70)$ in the order of magnitude -3.

On the other hand, the ML method performed worse presenting a minimum MSE in the order of magnitude -3, moreover, for angles larger than 50° (or less than $-50°$) it failed to provide estimates even for high SNR values.

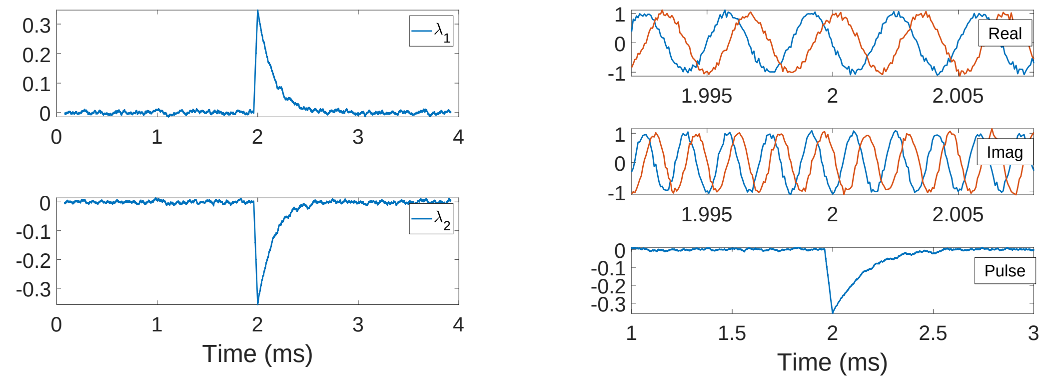

(a) The first and second eigenvalues provides estimates for the energy pulse.

(b) Real and imaginary components and the estimated pulse through λ_2.

Figure 55 – Estimated energy pulse considering SNR $= 10$ dB and $\theta_R = -\frac{\pi}{2}$. Source: Author.

7.3.4 Reference and Transmitted Complex Signals with Different Phases

The estimates obtained by setting different initial phases for the reference and transmitted vectors, for ideal complex exponential signals, is equivalent to the case where both signals are synchronized. However, if it is assumed that they are general complex signals with arbitrary power and frequencies, the estimates are provided by both eigenvalues. Compared to other cases, they are not affected by noise so dramatically due to avoiding the square root extraction.

Some benefits are that the square root extraction is not required, the largest eigenvalues shows greater robustness against the noise effects, the pulse amplitude is higher, and the pulse polarity can be determined if the signals are non-zero-mean. There are also limitations, for instance, the pulse fit rapidly degrades for large phase shifts.

Simulations were performed with the setup $A = B = 1$, $\omega_q = 2\omega_i$, and $\theta_R = \theta_T[0] - \frac{\pi}{2}$. For generating the MSE surfaces, the mean of each component was set to 10 when the magnitude of the complex signal is assessed.

Originally, both eigenvalues presented the baseline floating around the amplitude 1, when the input signal is a complex function. Figure 55a shows the behavior of the eigenvalues for the case where the reference signal is $\frac{\pi}{2}$ advanced relative to the transmitted signal, the SNR equals 10 dB and the pulse amplitude corresponds to 24°. Besides, in Figure 55b the in-phase and quadrature components are presented, as well as the pulse provided by the second eigenvalue.

In addition to the above discussed cases, it is also possible to obtain estimates by employing other combinations of the wave's parameters, which is what happens in practical situations.

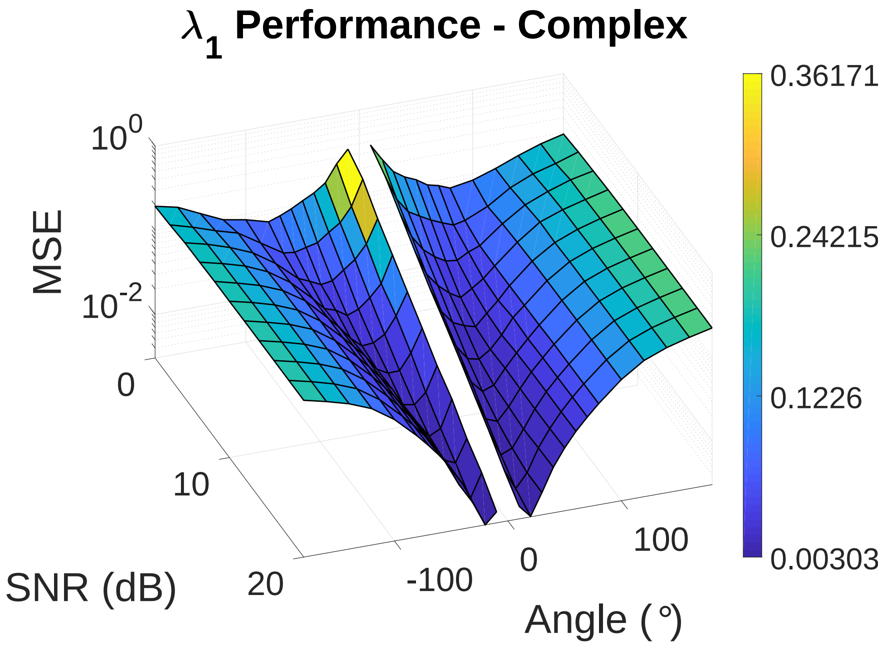

Figure 56 – MSE surface of the eigenvalue method using λ_1 to estimate the pulses from zero-mean complex signals considering different phases and frequencies.

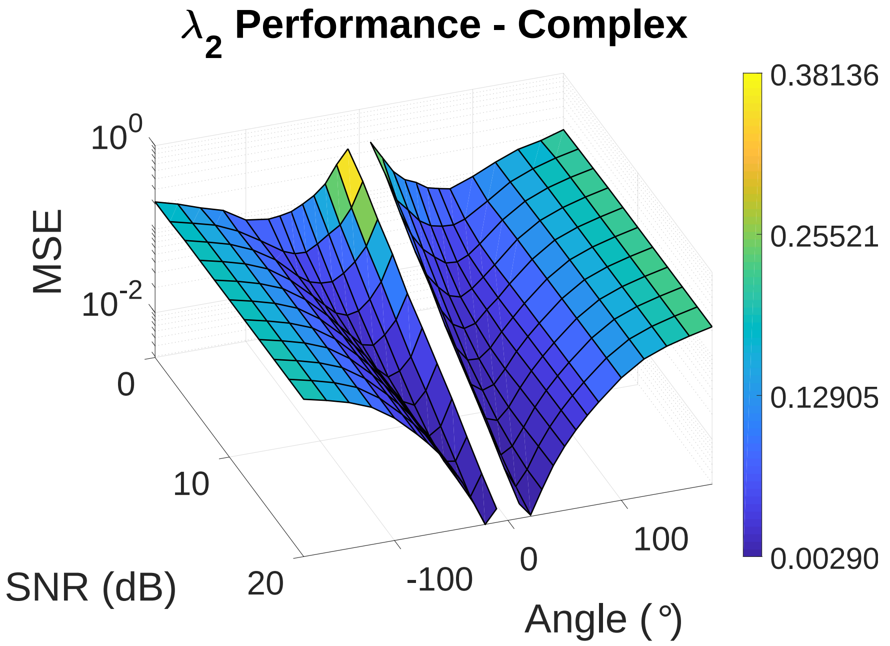

Figure 57 – MSE surface of the eigenvalue method using λ_2 to estimate the pulses from zero-mean complex signals considering different phases and frequencies.

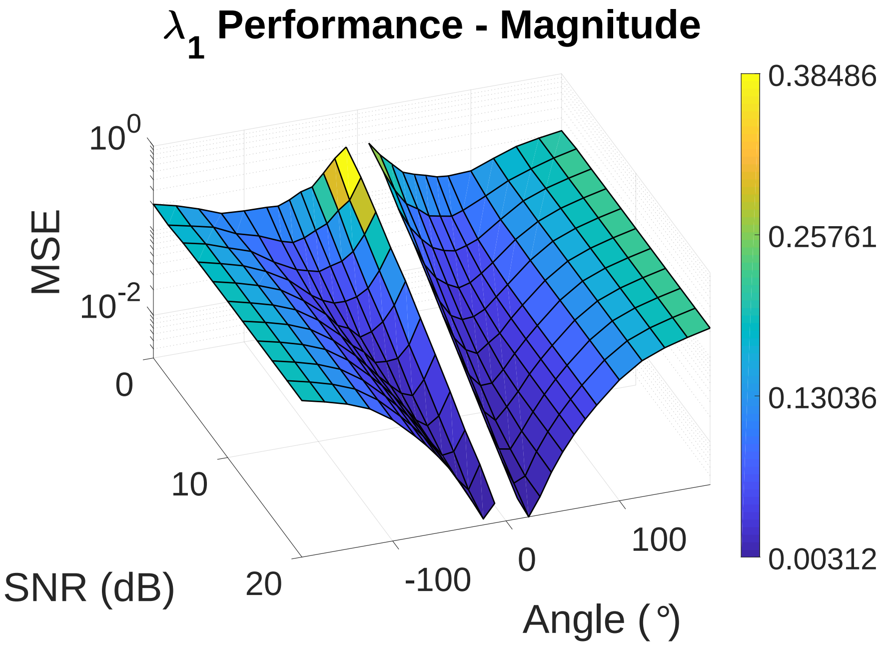

Figure 58 – MSE surface of λ_1 to estimate the pulses from the magnitude of non-zero-mean complex signals considering different phases and frequencies.

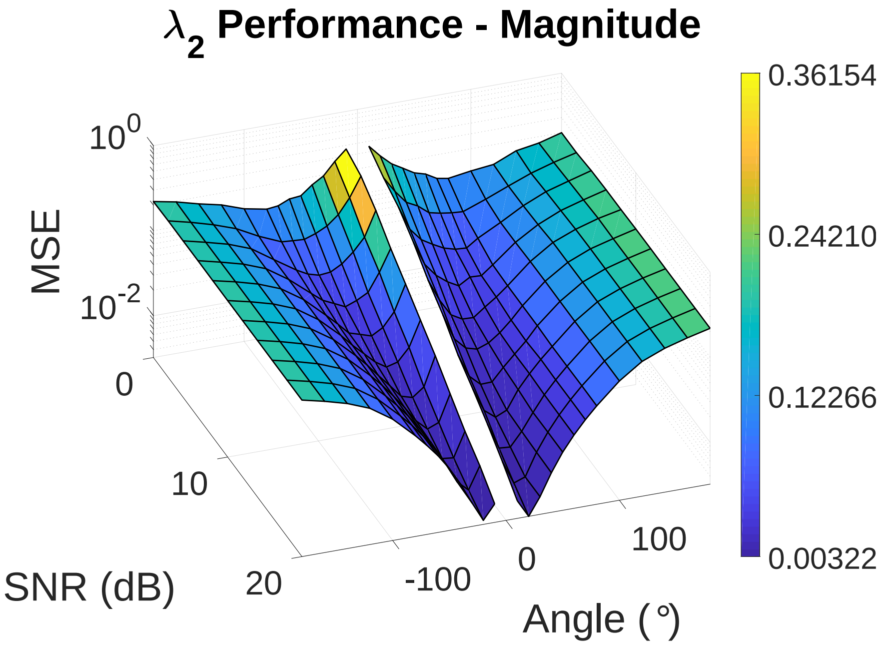

Figure 59 – MSE surface of λ_2 to estimate the pulses from the magnitude of non-zero-mean complex signals considering different phases and frequencies.

Figures 56, 57, 58, and 59 show the performance of the eigenvalue method, whereas the input signal is either a complex function or its magnitude. The performances of λ_1 and λ_2 are compared, it can be seen that all approaches provide similar results. The MSE increases very fast for angles greater than 50° (or less than $-50°$).

The ML method is not affected by setting a different phase for the reference signal, it performs equivalently to the case where there are different frequencies and it is not presented in this section.

In short, the simulated results prove the ability of estimating the energy pulses on the microwave SQUID multiplexer system. The wave parameters require previous knowledge from the absolute value of the phase shift in order to allow the methods providing suitable estimates. The eigenvalue method allows great flexibility to choose the wave parameters and its error surface has shown the competitive performance face to the maximum likelihood method. Besides, the eigenvalue method has shown compatible performance in all assessed cases.

7.4 Measured Data

The current section presents the obtained results for applying the eigenvalue method and the maximum likelihood method to the data measured in the context presented in section 6.3.

The system used for the measurements consists of the ECHo chip sited on a cryostat, an RF Frontend circuit and an FPGA. The data was stored in a memory device for subsequent off-line processing. After the data is made available through a data server, Matlab software scripts were used in order to obtain the pulses estimates.

The SQUID modulation ramp has two shapes: sawtooth and triangle. The sampling rate is 15,625 MS/s, the modulation ramp frequency is $f_{ramp} = 25$ KHz and the amplitude is set to 6 V for both ramp types, which theoretically produces waves with frequencies $f_{SQUID,\ s} = 2 \times 6 \times 25000 = 300$ KHz and $f_{SQUID,\ t} = 4 \times 6 \times 25000 = 600$ KHz. Due to the nonlinear processing of the SQUID response, the signals may behave slightly different than expected. The number of points in a modulating wave cycle is the relationship between sampling and ramp frequencies, i.e., $N = \frac{f_{sampling}}{f_{ramp}} = 625$.

In the context of the microwave SQUID multiplexer, the SQUID response is modulated in the magnitude and phase of a complex carrier, it is a challenging task to obtain analogous behavior to the ideal case, where the in-phase component is a pure cosine tone and the quadrature component is a pure sine tone. Therefore, it is considered only the cases where the frequencies are different, $\omega_i \neq \omega_q$, or the initial phases are different, $\theta_R \neq \theta_T[0]$.

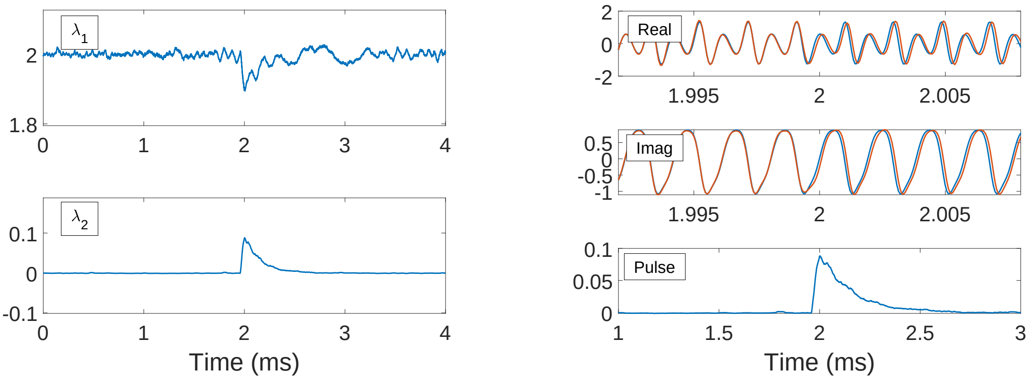

(a) Eigenvalues of the spatial correlation matrix $\hat{\mathbf{R}}$.

(b) Real and imaginary components and pulse from λ_2.

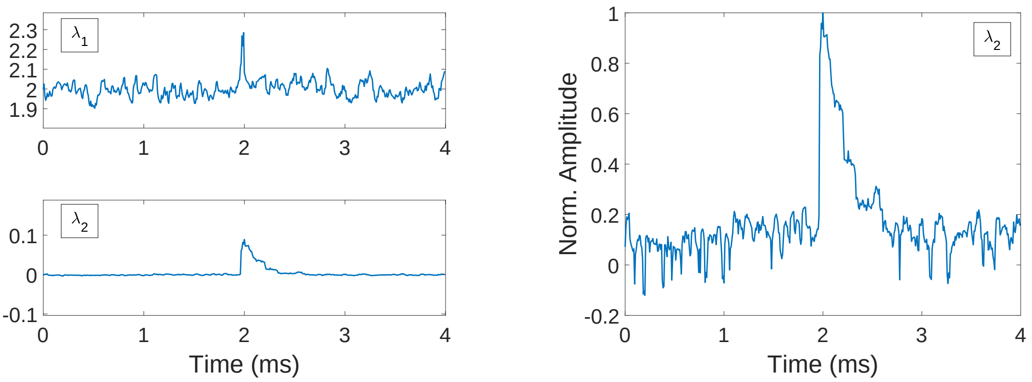

(c) Eigenvalues of the spatial correlation matrix $\hat{\mathbf{R}}$ for a sampling frequency equivalent to 125 KHz.

(d) Pulse obtained from λ_2 considering a decimation factor of 125.

Figure 60 – Energy pulse estimates for measured I/Q components with different frequencies (a) and (b). Estimates with a decimation factor of 125, which results in a data vector length of 5 samples per ramp cycle (c) and (d). The modulating ramp consists on a sawtooth-shaped wave. Source: Author.

7.4.1 Real and Imaginary Components with Different Frequencies

7.4.1.1 Sawtooth Ramp

After power adjustment, in-phase and quadrature components will have mean power equal to $\frac{\sqrt{2}}{2}$. This will produce a complex signal of power equal to 1. Figure 60 shows the estimates obtained by applying the eigenvalue method over the I/Q carriers, where it can be seen that the original pulse is positive. The ramp modulation is a sawtooth function. While the system is idle, the waves are superimposed, but when it occurs to fall an energetic particle on the pixel, the transmitted signal is shifted relative to the reference signal. This effect is visible from the mark of 2 ms on.

As observed for the case where the I/Q components were ideal, the largest eigenvalue is greatly affected by noise, while the second eigenvalue is more robust and provides better

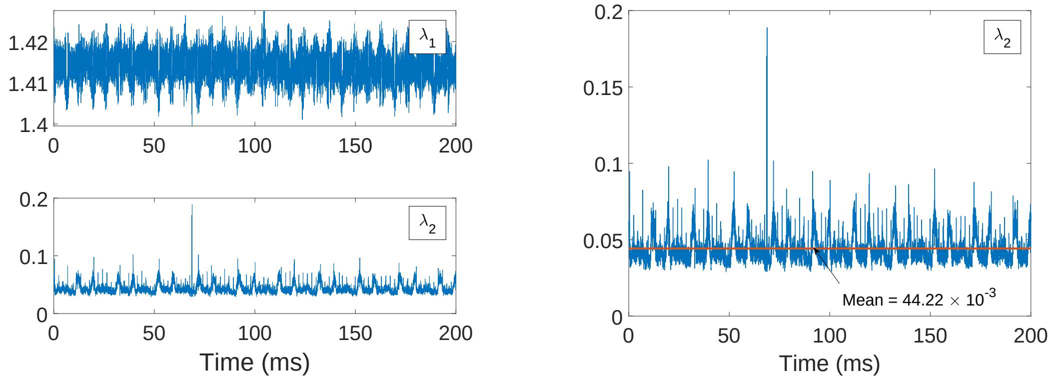

(a) Eigenvalues of the spatial correlation matrix.

(b) Second eigenvalue indicating noise power.

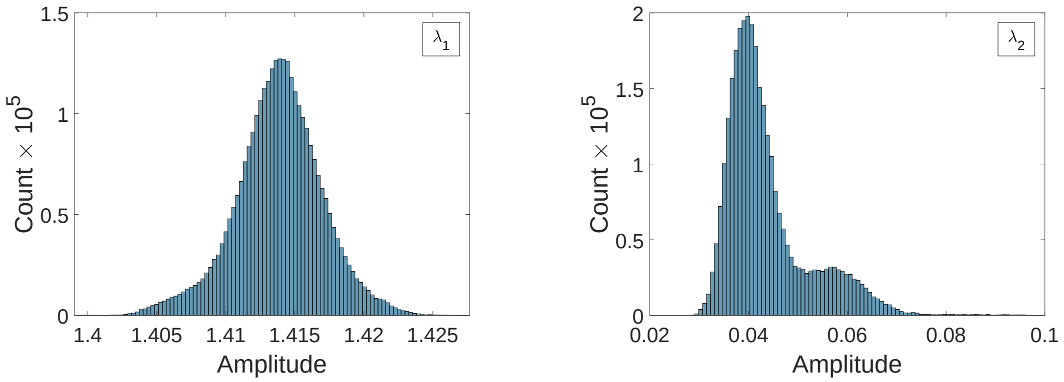

(c) Histogram of estimates from λ_1 divided into 101 bins.

(d) Histogram of estimates from λ_2 divided into 201 bins.

Figure 61 – Noise behavior in eigenvalues. Estimates are obtained considering 3125000 points with the system in standby state. Source: Author.

pulse estimates. Figure 60a presents the estimates without square root extraction and at their original positions for an idle system. As a consequence, λ_1 floats around the value 2 and λ_2 has its baseline around 0. Figure 60b shows the waveforms of the phase and quadrature components and the pulse obtained by λ_2.

As noted before, this procedure does not allow identification of positive and negative pulses. The first singular value will provide only negative pulses and the second will provide only positive pulses. After obtaining the estimates, the square root extraction is necessary, so that the decay of the exponential function is consistent with the decay of the original pulse.

It is also possible to estimate the pulse from a smaller set of samples by applying the decimation technique. In Figure 60d the square root is extracted and the base line of the pulse is adjusted to lay at the zero-mean level and the pulse itself have a maximum amplitude equal to 1. This procedure is equivalent to divide the current sampling rate by 125. The length of the data vector feeding the correlation matrix is reduced to 5 samples and, although the number of points is small, it is still possible to recover the energy pulses by the second eigenvalue.

Figure 61 presents the behavior of eigenvalues in the absence of pulses and the distribution of the values by means of a histogram. For the analysis of noise in the estimates, 3125000 signal samples were used, where $N = 625$. The square root has been extracted and the noise power can be measured by the vertical displacement relative to the horizontal axis in the λ_2 estimates, in which case $\sigma_e \approx 44.22 \times 10^{-3}$, which represents a SNR ≈ 13.5 dB.

However, λ_2 fluctuates over time and has periodic behavior with frequency of 50 Hz, as can be seen in Figure 61b. One can also observe the average of the values presented by a red line that has height 44.22×10^{-3}.

The histograms showed in Figures 61c and 61d reveal interesting features. Estimates obtained from λ_1 are roughly the shape of a Gaussian curve with average $\mu_{\lambda_1} = 1,413966236628566$ and standard deviation $\sigma_{\lambda_1} = 0.003165728355908$. Estimates of λ_2 have the occurrences apparently given by the overlap of two Gaussian curves, but the values closer to $40 \times 10{-}3$ are more likely to happen.

7.4.1.2 Triangle Ramp

The modulation ramp may also be triangular-shaped. The same considerations are made with respect to the power of the in-phase and quadrature components. For this modulation ramp a peculiar effect on phase shift is observed. In the case of incidence of a particle, the phase shift will depend on the slope of the triangular wave.

In the positive slope half-cycle, the displacement is analogous to the polarity of the original pulse, on the other hand, in the negative slope half-cycle, the displacement will have opposite value. This effect does not affect pulse estimation by the eigenvalue method for synchronized reference and transmitted signals.

Figure 62 shows the pulse estimate for a triangular ramp and overlapping carriers. It is not possible to obtain the energy pulse through the first eigenvalue, but the second eigenvalue provides the pulse estimates. Figure 62b highlights the time interval when the phase of the transmitted signal is reversed.

The histograms of 3125000 noisy estimates values are shown in Figures 62c and 62d. The noise has a frequency distribution similar to a Gaussian curve. Estimates obtained from λ_1 are roughly the shape of a Gaussian curve with average $\mu_{\lambda_1} = 1,416818717994598$ and standard deviation $\sigma_{\lambda_1} = 0.004318591512771$. Estimates of λ_2 have an average $\mu_{\lambda_2} = 0.056412341272159$, which represents an SNR of approximately 12.5 dB, and standard deviation $\sigma_{\lambda_2} = 0.005691281466710$.

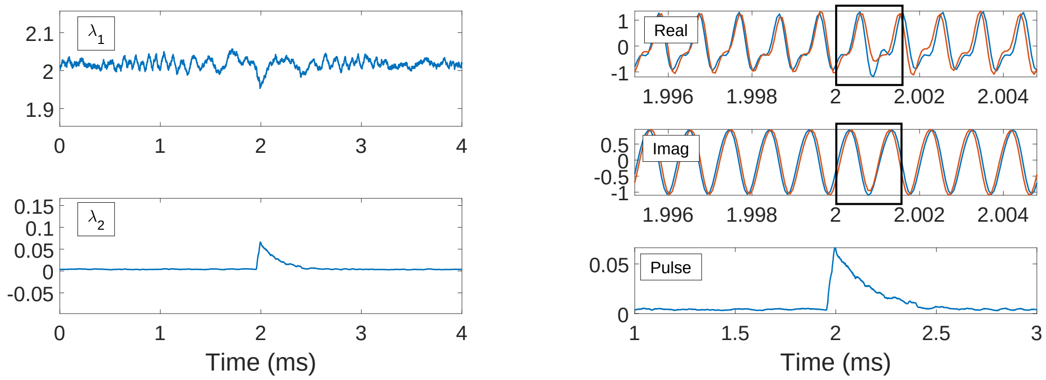

(a) Eigenvalues of the spatial correlation matrix.

(b) Real and imaginary components and the pulse obtained through λ_2 for a triangle flux ramp.

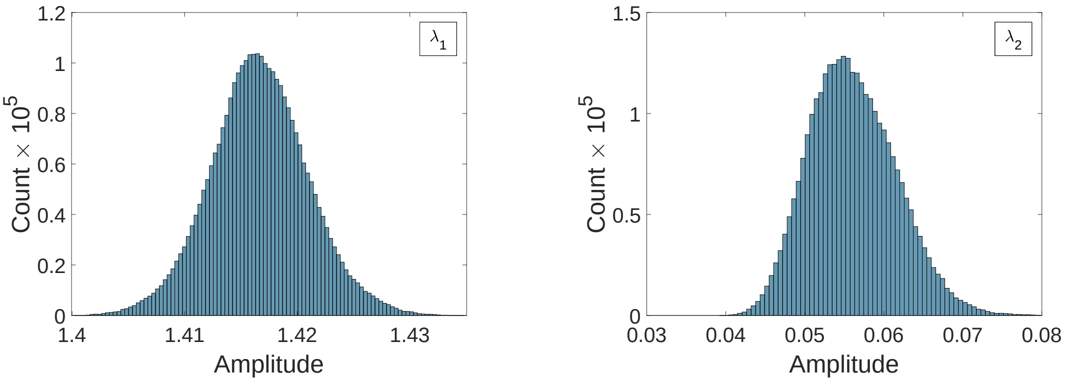

(c) Histogram of estimates obtained by λ_1 divided into 101 bins.

(d) Histogram of estimates obtained by λ_2 divided into 201 bins.

Figure 62 – Energy pulse estimates in the context of a triangle flux ramp (a) and (b). Noise behavior in the eigenvalues estimates considering the triangular ramp (c) and (d). The noise estimates were obtained over 3125000 samples with the system in standby state. Source: Author.

7.4.2 Reference and Transmitted Complex Signals with Different Phases

7.4.2.1 Sawtooth Ramp

The I and Q components' power are set equal to $\frac{\sqrt{2}}{2}$, so that $|\mathbf{y}_R|^2 = 1$. Figure 63 shows the obtained estimates, whereas the initial phase of the reference signal is approximately $-22.5°$, i.e., $\theta_R \approx \theta_T[0] - \frac{\pi}{8}$, with $N = 625$.

This approach avoids the necessity of square root extraction of the estimates. Note from Figure 63a that both eigenvalues, the first and second, provides pulse estimates. In Figure 63b I/Q waveforms are shown and it can be observed the time interval, in which there is a positive phase shift in the transmitted signal (red curve) relative to the reference (blue curve), it happens near the instant 1.998 ms.

In the context of different initial phases, it makes no sense to analyze the noise

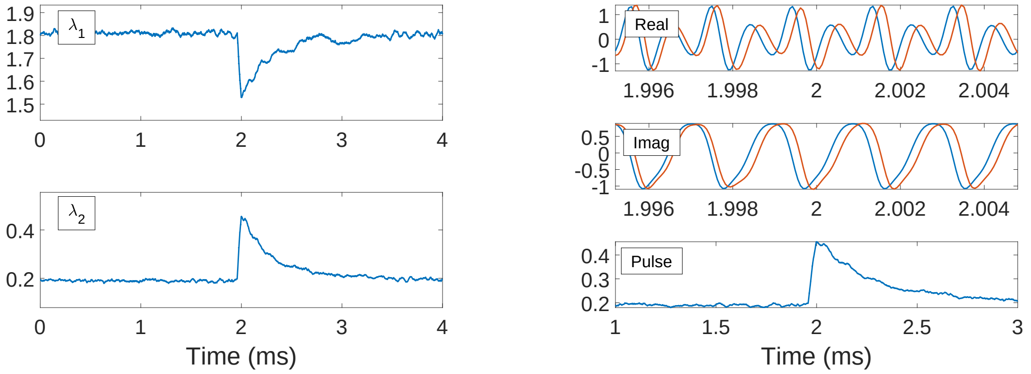

(a) Eigenvalues of $\hat{\mathbf{R}}$.

(b) Carriers and Pulse.

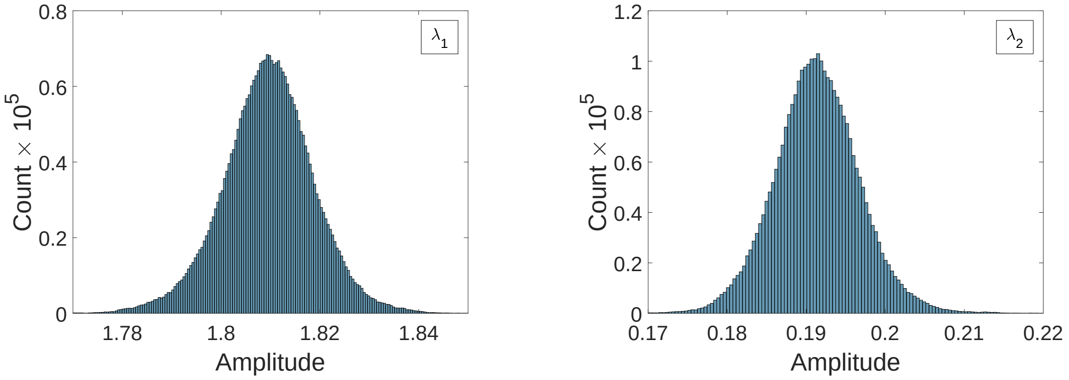

(c) Histogram of λ_1 into 201 bins.

(d) Histogram λ_2 into 201 bins.

Figure 63 – (a) Pulse estimates from measured data for distinct initial phases ($\mathbf{y}_R$ and $\mathbf{y}_T$); (b) in-phase and quadrature components and λ_2 estimates. Noise behavior in (c) λ_1 and (d) λ_2 for a sawtooth ramp. There are 3125000 samples, system in idle state. Source: Author.

power by the vertically shifted estimates. The reason is that, for non-synchronized signals, the correlation function floats around a specific value set by the phase shift between the signals. Estimates of λ_1 and λ_2 float around 1.8 and 0.2, respectively.

Figures 63c and 63d present the frequency of estimates for an idle system, which correspond to the estimated noise values. They present a Gaussian distribution shape with mean approximately 1.81 for λ_1 and 0.19 for λ_2.

Figure 63c and Figure 63d present the eigenvalue histograms. Both are approximately the shape of a Gaussian curve.

7.4.2.2 Triangle Ramp

Considering the same conditions for I/Q, it is observed that the estimates are not properly provided when using the triangle flux ramp. Due to the effect caused by different slopes, the opposite values cancel out and the pulse could not be recovered.

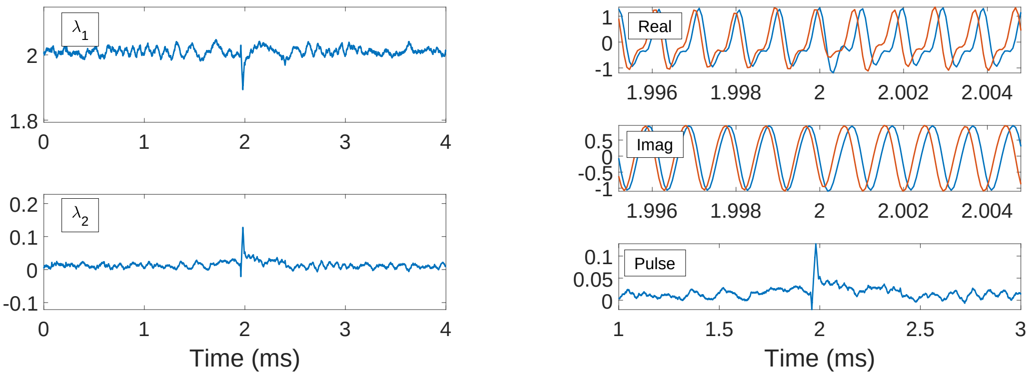

(a) Eigenvalues of the spatial correlation matrix.

(b) Real and imaginary components and values of λ_2.

Figure 64 – Estimates obtained for a triangle flux ramp with initial phase between the reference and transmitted signals. Source: Author.

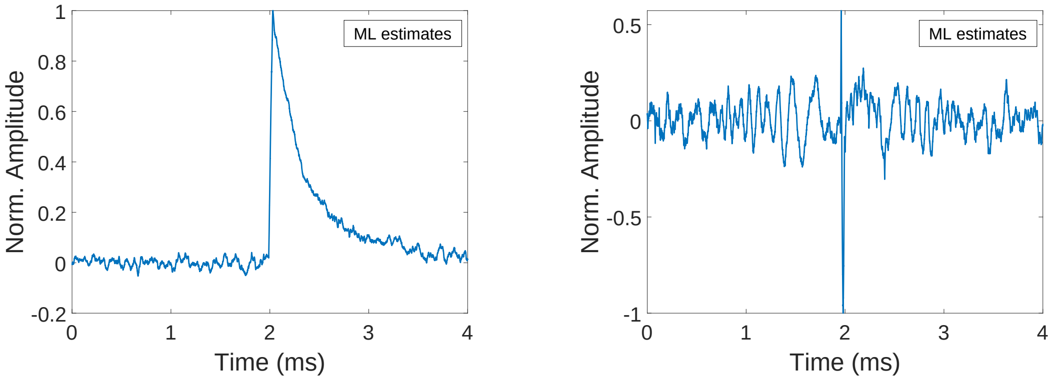

(a) ML estimates for a sawtooth flux ramp.

(b) ML estimates for a triangle flux ramp.

Figure 65 – Estimates obtained by the ML method for a (a) sawtooth and (b) triangular modulation ramp. Because there are opposite phase shifts for different inclinations the pulse in (b) cannot be satisfactorily recovered. Source: Author.

Figure 64 presents the results obtained by applying the eigenvalue method in this situation. In Figure 64a non of the estimators could recover the pulse information, despite their capability of detecting the pulse. The waveforms for an initial phase of approximately 45° relative to the transmitted signal phase can be seen in Figure 64b.

Within the same data block there is approximately the same amount of positive and negative phase shift data, which causes these values to be canceled. To circumvent this problem it is possible to perform the calculations for each modulating wave half-cycle, however, this increases the complexity of the system. In addition, pulse polarity cannot be established without prior knowledge of the triangular ramp operating slope.

7.4.3 Maximum Likelihood Estimates

The maximum likelihood method was also applied to the measured data and resulted in the estimates presented in Figure 65. The data vector in this method is the absolute value of the complex vector over time. Next, the continuous component of the obtained sinusoidal signal is filtered and a window is settled, which guarantees the linearity of the SQUID response, as described in (MATES et al., 2012).

For the sawtooth flux ramp the estimation is performed properly and a pulse is obtained, such as in Figure 65a. The pulse is positive according to what was observed in sections 7.4.1.1 and 7.4.2.1, where the same data set was used.

In case of a triangle flux ramp modulation, this method does not provide pulse estimates unless data manipulation is performed so that the wave half-cycles are identified and calculated separately. In this case, it is essential to synchronize the modulation ramp with the estimation block in order to use the different slope data separately. It follows directly from this observation that the estimation should be performed block by block, it is not possible to assess the data sample by sample. This behavior is analogous to that observed in the 7.4.2.2 section when using the eigenvalues' method.

Similar to the eigenvalue method, it is possible to obtain estimates even for lower sampling frequencies, whereas it is reduced by some decimation factor. It is true whenever the SQUID response frequency is known.

7.5 Practical Considerations

7.5.1 Inner Product Behavior

From the particular cases assessed in F, it is possible to underlie some alternative approaches for the implementation of the method.

7.5.1.1 Ideal Complex Exponential

Recalling the resulting formulation for the inner product or ideal complex exponential signals,

$$\langle \mathbf{x}_R, \mathbf{x}_T \rangle = \sum_{i=1}^{N} \cos(\theta_T[i]) + j \sum_{i=1}^{N} \sin(\theta_T[i]), \tag{7.21}$$

it follows that the real part will produce only positive pulses because the phase values are the argument of a cosine function. Considering the fact that the phase values of the transmitted vector is the argument of a sine function, the imaginary part will follow the pulse polarity and for small phase shifts it can be written as $\sin(\theta_T[i]) \approx \theta_T[i]$, so that the pulse is obtained directly from the mean values of the phase shift along N samples. Figure 66 shows the magnitude, the real part and the imaginary part of the inner product for two cases, whereas in the first case the phase shift is 24° as in Figure 66a and the second case the phase shift is $-24°$ as in Figure 66b.

7.5.1.2 I/Q Components with Different Amplitudes

The second situation presented in the Appendix F considers different amplitudes for the in-phase and quadrature components. The formulation, after some algebraic manipulation whereas $A \neq B$, with A, $B \in \mathbb{R}$, $\omega_i = \omega_q = \omega_{iq}$, $\{f_{iq} \in \mathbb{R} \mid \frac{-f_{sampling}}{2} \leq f_{iq} \leq \frac{f_{sampling}}{2}\}$, and $\theta_R = \theta_T[0] = 0$, turns into

$$\langle \mathbf{x}_R, \mathbf{x}_T \rangle = \sum_{i=1}^{N} \left[\frac{(A^2 - B^2)}{2} \cos(2\omega_{iq} T_S i) \cos(\theta_T[i]) + \right. \\ \left. + \frac{(A^2 + B^2)}{2} \cos(\theta_T[i]) \right] + j \left[AB \sum_{i=1}^{N} \sin(\theta_T[i]) \right]. \tag{7.22}$$

It can be seen that the same behavior holds for the imaginary part of the inner product. It is equivalent to what was observed in subsection 7.5.1.1, the sine function will provide pulses with the same polarity of the original pulse.

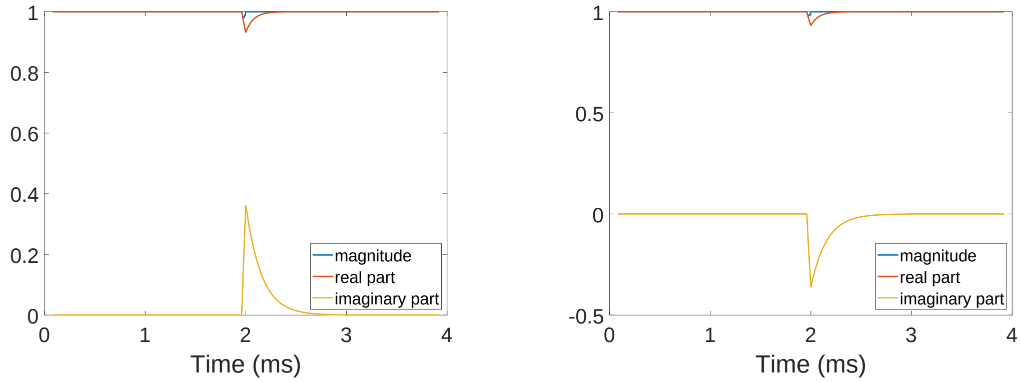

(a) Behavior of the magnitude, real and imaginary part of the inner product for ideal complex exponential signals in the presence of a positive pulse which causes a maximum phase shift of 24°.

(b) Behavior of the magnitude, real and imaginary part of the inner product for ideal complex exponential signals in the presence of a negative pulse which causes a maximum phase shift of $-24°$.

Figure 66 – Inner product behavior in case of ideal complex exponential signals. The estimated pulse follows the original pulse polarity. Source: Author.

7.5.1.3 I/Q Components with Different Frequencies

The third case considered in Appendix F is relative to different oscillation frequencies for I and Q. The inner product behavior can be modeled as

$$\langle \mathbf{x}_R, \mathbf{x}_T \rangle = \sum_{i=1}^{N} \Big\{ \cos(\theta_T[i]) + \cos(2\omega_i T_S i - \theta_T[i]) - \cos(4\omega_i T_S i - \theta_T[i]) \Big\} + \\ + j \left[\sum_{i=1}^{N} \sin(\theta_T[i]) \cos(-\omega_i T_S i) \right], \tag{7.23}$$

where $A = B = 1$, $\omega_q = 2\omega_i$, $\{f_i,\ f_q \in \mathbb{R} \mid \frac{-f_{sampling}}{2} \leq f_i,\ f_q \leq \frac{f_{sampling}}{2}\}$, and $\theta_R = \theta_T[0] = 0$.

From equation 7.23, the imaginary part has a zero-mean oscillating component which attenuate the sine function if the observation interval is equal to multiples of one wave period. It follows that all the relevant pulse information relies on the real part, which consists of a cosine function. Therefore, only positive pulses can be obtained through this approach.

It is reasonable, according to the inner product behavior for this situation, to modify the estimate formulation through the eigenvalues in terms of the real part instead of the magnitude calculation. The modified eigenvalues can be written as:

$$\lambda_1 \approx \frac{1}{2N} \left[|\mathbf{x}_R|^2 + |\mathbf{x}_T|^2 + 2\ \operatorname{Re}\{\langle \mathbf{x}_R, \mathbf{x}_T \rangle\} \right] + \sigma_e^2; \tag{7.24}$$

$$\lambda_2 \approx \frac{1}{2N} \left[|\mathbf{x}_R|^2 + |\mathbf{x}_T|^2 - 2\ \operatorname{Re}\{\langle \mathbf{x}_R, \mathbf{x}_T \rangle\} \right] + \sigma_e^2. \tag{7.25}$$

Figure 67 shows the inner product behavior for different I/Q frequencies and the estimated pulse by replacing the magnitude of the inner product by its real component. In Figure 67b, it can be observed that the estimated pulse overlaps the original pulse.

7.5.1.4 Reference and Transmitted Carriers with Different Initial Phases

The last case of interest concerns the initial phase from the reference and transmitted signals. If the amplitudes and frequencies are equal, it will be equivalent to the complex exponential case with an additional term on the argument of sine and cosine functions.

Any combination of parameters is possible, but one interesting setup is $A = B = 1$, $\omega_q = 2\omega_i$, $\{f_i, f_q \in \mathbb{R} \mid \frac{-f_{sampling}}{2} \leq f_i, f_q \leq \frac{f_{sampling}}{2}\}$, and $\theta_R = \frac{-\pi}{2}$, $\theta_T[0] = 0$. From Appendix F, the expression for the inner product can be written as:

$$\langle \mathbf{x}_R, \mathbf{x}_T \rangle = \sum_{i=1}^{N} \left[-\sin(\theta_T[i]) + \frac{\sin(2\omega_i T_S i - \theta_T[i]) + \sin(4\omega_i T_S i - \theta_T[i])}{2} \right] + \\ + j \sum_{i=1}^{N} \cos(\theta_T[i]) \cos(\omega_i T_S i), \tag{7.26}$$

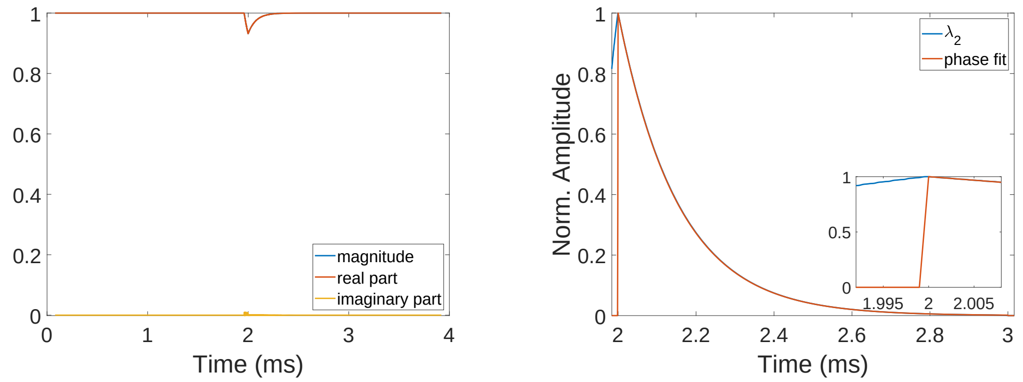

(a) Behavior of the inner product for complex signals with different frequencies. A positive pulse of 24° modulate the carriers.

(b) Pulse estimation through the modified eigenvalues formulation. Original pulse (red) and estimated pulse (blue), which fits to the exponential decay.

Figure 67 – Inner product behavior in the case of complex signals with different I/Q frequencies and the estimated pulse. Source: Author.

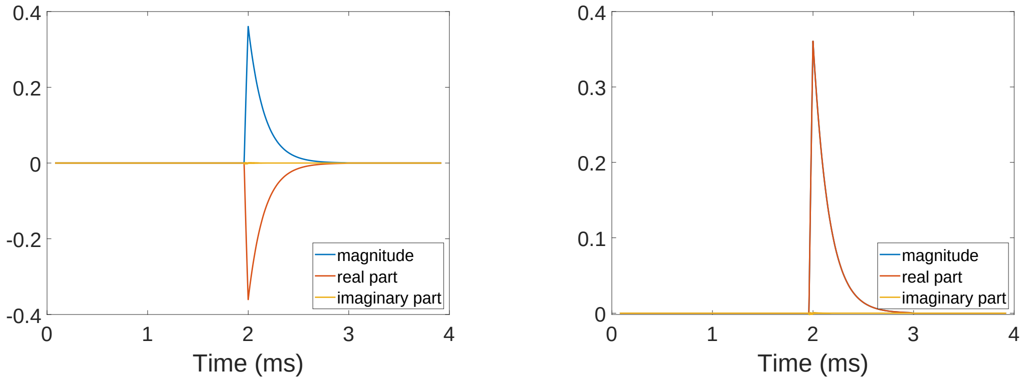

(a) Behavior of the magnitude, real and imaginary part of the inner product for complex signals with different frequencies in the presence of a positive pulse which causes a maximum phase shift of 24°.

(b) Behavior of the magnitude, real and imaginary part of the inner product for complex signals with different frequencies in the presence of a positive pulse which causes a maximum phase shift of $-24°$.

Figure 68 – Inner product behavior in the case of complex signals whereas the reference and transmitted signals are phase-shifted of $\frac{-\pi}{2}$ and the I/Q components have different frequencies. Source: Author.

where the real part consists of a sine function that is phase-shifted by a value of π, which produces pulses with the opposite polarity regarding the original pulse, and an additional oscillating component. The imaginary part is negligible.

In the Figure 68 two cases are highlighted, when there is a positive pulse as in Figure 68a and in case of a negative pulse as in Figure 68b

7.5.2 Hardware Implementation

Embedded systems such as FPGAs cab be used to implement the eigenvalue algorithm for on-line processing. Simple calculations and limited number of operations are required. The number of multiplications and additions are a critical factor and the need to perform functions that have a high computational cost must be avoided.

In the eigenvalue method, there is no need to perform all N multiplications for each new sample, instead, the correlation matrix should be simply updated. It is enough to subtract the correlation value relative to the first component of the current vector, add the correlation value for the new sample, and, finally, update the transmitted data vector in the device's storage module. The estimated correlation matrix can be updated as follows.

The $\hat{\mathbf{R}}[i]$ matrix is known to be given as:

$$\hat{\mathbf{R}}[i] = \begin{pmatrix} (|\hat{\mathbf{y}}_R[i]|^2+|\hat{\mathbf{y}}_R[i+1]|^2+\cdots+|\hat{\mathbf{y}}_R[i+N-1]|^2)/_N & (\hat{\mathbf{y}}_R^*[i]\cdot\hat{\mathbf{y}}_T[i]+\cdots+\hat{\mathbf{y}}_R^*[i+N-1]\cdot\hat{\mathbf{y}}_T[i+N-1])/_N \\ (\hat{\mathbf{y}}_T^*[i]\cdot\hat{\mathbf{y}}_R[i]+\cdots+\hat{\mathbf{y}}_T^*[i+N-1]\cdot\hat{\mathbf{y}}_R[i+N-1])/_N & (|\hat{\mathbf{y}}_T[i]|^2+|\hat{\mathbf{y}}_T[i+1]|^2+\cdots+|\hat{\mathbf{y}}_T[i+N-1]|^2)/_N \end{pmatrix}. \tag{7.27}$$

The correlation matrix update can be done recursively as:

$$\hat{\mathbf{R}}[i+1] = \begin{pmatrix} \left[\hat{\mathbf{R}}[i]\right]_{11}-(|\hat{\mathbf{y}}_R[i]|^2-|\hat{\mathbf{y}}_R[i+N]|^2)/_N & \left[\hat{\mathbf{R}}[i]\right]_{12}-(\hat{\mathbf{y}}_R^*[i]\cdot\hat{\mathbf{y}}_T[i]-\hat{\mathbf{y}}_R[i+N]\cdot\hat{\mathbf{y}}_T[i+N])/_N \\ \left[\hat{\mathbf{R}}[i]\right]_{21}-(\hat{\mathbf{y}}_T^*[i]\cdot\hat{\mathbf{y}}_R[i]-\hat{\mathbf{y}}_T^*[i+N]\cdot\hat{\mathbf{y}}_R[i+N])/_N & \left[\hat{\mathbf{R}}[i]\right]_{22}-(|\hat{\mathbf{y}}_T[i]|^2-|\hat{\mathbf{y}}_T[i+N]|^2)/_N \end{pmatrix}. \tag{7.28}$$

where each entry is calculated as a function of the past entry values.

The reference vector is obtained by cyclic repeating the reference data, which stands for one flux ramp cycle of the SQUID response. Therefore $\left[\hat{\mathbf{R}}[i]\right]_{11}$ will always have the same value for all $i \in \mathbb{N}$, which means that is enough to store this value once and use it for future calculations. In addition, $\left[\hat{\mathbf{R}}[i]\right]_{12} = \left[\hat{\mathbf{R}}[i]\right]_{21}^*$ implies that just one of them needs to be calculated, the other value is obtained by changing the sign of the imaginary part.

Thus, only 4 multiplications and 2 additions are required for each entry, summing up to 8 multiplications and 4 additions for the two entries $\left[\hat{\mathbf{R}}[i+1]\right]_{12}$ and $\left[\hat{\mathbf{R}}[i+1]\right]_{22}$ in order to update the matrix $\hat{\mathbf{R}}[i+1]$.

After updating the correlation matrix, the eigenvalues are calculated. The most critical operation is the magnitude calculation of the complex entry $\left[\hat{\mathbf{R}}[i]\right]_{12}$, which can be implemented by a look-up-table. Finally, the magnitude is multiplied by 2, which is implemented by shifting the bits to the left and, after that, it follows two additions and one division by 2, which is equivalent to shifting the bits to the right. The factor N can be omitted in calculations and inserted in a convenient later time, furthermore, it would be desirable to define a number of points for each flux ramp equal to a power of 2, by doing that the division by N would be much easier.

A final comment on this matter is relative to the pulse estimation over the in-phase and quadrature components individually. The magnitude calculation $|\langle \mathbf{x}_R, \mathbf{x}_T \rangle|$ will be equivalent to the absolute value of the inner product relative to the in-phase vector, $|\langle \mathbf{i}_R, \mathbf{i}_T \rangle|$, or the absolute value of the inner product relative to the quadrature vector, $|\langle \mathbf{q}_R, \mathbf{q}_T \rangle|$. The calculation of the absolute value of a real number does not require to calculate a square root. Table 3 shows the mean runtime of 20 experiments performed in Matlab for the eigenvalue method processing the in-phase component individually, the quadrature component individually, the magnitude of the complex signals and the complex signals; besides the mean runtime of the maximum likelihood.

Table 3 – Mean runtime of assessed methods in seconds.

In-phase	Quadrature	Magnitude	Complex	ML
0.0027	0.0027	0.0112	0.1265	0.0141

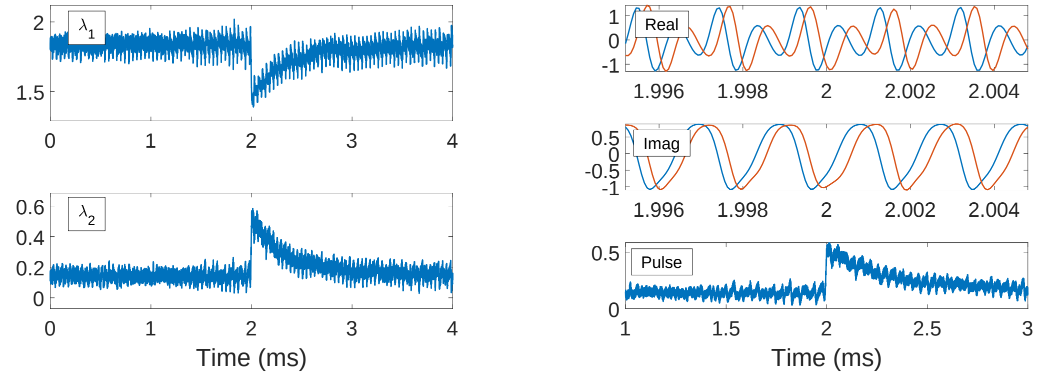

(a) Correlation matrix eigenvalues for sawtooth flux ramp, $L = 125$, and different initial phases.

(b) I/Q components and pulse obtained through λ_2.

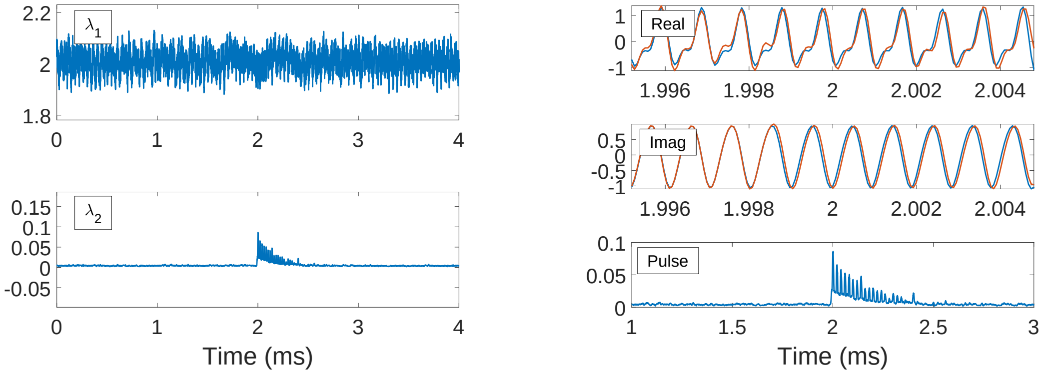

(c) Eigenvalues of the correlation matrix in case of a triangular flux ramp is used, $L = 125$ and equal initial phases.

(d) I/Q components and pulse obtained through λ_2.

Figure 69 – Results using $L = 125$. (a) Estimates for a sawtooth modulation ramp and (b) their respective I/Q components, for a phase shift of approximately $-\frac{\pi}{4}$ compared to the transmitted signal. (c) Estimates for a triangular modulation ramp and (d) their respective I/Q components. Source: Author.

7.5.3 Data Vector Length used to Processes the Information

The length of the data vector $L \in \mathbb{N}$ used to calculate the estimates is an extremely important parameter. On the previous analysis, it was considered to be equal to the number of points in one flux ramp cycle, $L = N$, but in this subsection, some comments are pointed out on the benefits of controlling this parameter. It is important to draw the balance between a fast rise time of the pulse and a sufficient amount of data for the estimation.

By controlling the number of points used, the rise time of the pulse can be controlled and the associated error should be minimized, which can be seen in Figure 36b. On the other hand, when less information is used, noise can become more detrimental due to asymptotic characteristics.

Figure 69 presents the result of employing shorter vectors on the calculation. It is observed that it is possible to estimate the pulses using either a sawtooth or a triangular ramp. Figure 69a shows the two eigenvalues that present the estimated pulse, but there are more intense oscillations when compared to Figure 64a. This is due to the smaller number of samples but also due to the turning point of the modulation ramp.

Similarly, for the triangle ramp there are more intense swings than in the case where $L = 625$. It can be seen from the estimates by λ_2 that the turning point of the modulation ramp drastically affects the estimation.

On the contrary, the results obtained with the ML method are not effective, it is observed that for a small number of samples the pulse cannot be estimated. ML estimates vary widely and does not trace the exponential decay pulse. Figure 70 presents the estimates obtained.

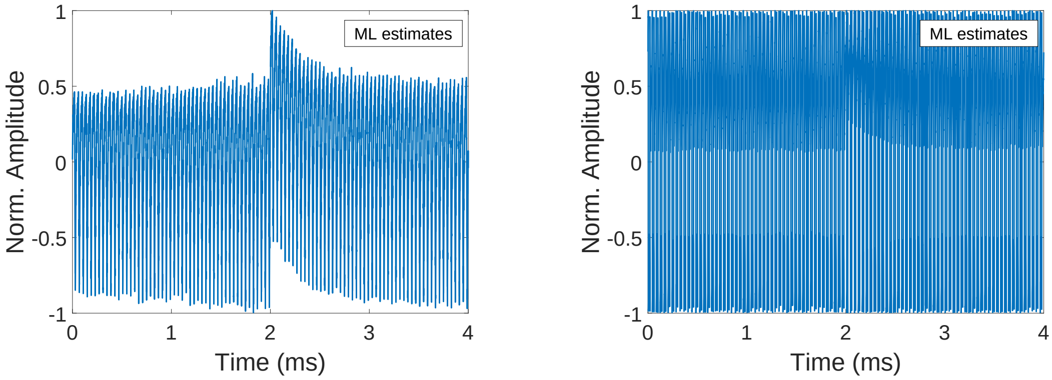

(a) ML estimates for sawtooth flux ramp with $L = 125$.

(b) ML estimates for triangle flux ramp with $L = 125$.

Figure 70 – Estimates obtained by the ML method for a (a) sawtooth and (b) triangle modulation ramp where $L = 125$. Source: Author.

7.6 Chapter Conclusions

By recalling the *modus operandi* of SEAD method in the DOA estimation, a sensor array-based approach was proposed in order to estimate the phase shift of carriers in the microwave SQUID multiplexer system. In the direction of arrival problem, the source positions are related to the phase shift on the signals relative to each sensor. In the microwave SQUID multiplexer, the signal of interest is also a phase shift of a complex wave which is provoked by the incidence of charged particles on the pixels attached to the ECHo chip.

To solve the problem of phase estimation on the SQUID multiplexer an analogy with the sensor array was established. It is assumed the existence of a virtual circuit, which is a reference signal, and of a real circuit, which is the actual signal being received throughout the experiment. The eigenvalues of the spatial correlation matrix solved the problem of energy estimation and constitute an alternative to the maximum likelihood estimator. The eigenvalues method showed to be robust against the effects of noise and, under certain constraints, it performed better than the other method. The second eigenvalue can provide a measure of the noise added to the signals, which is helpful to calculate an estimate of the SNR condition. Besides, the runtime for the eigenvalue method, considering real signals, is around 20% of the required by the maximum likelihood method.

8 Conclusion

This work intended to solve two major problems: to prove that the matrix norms are direction of arrival estimators and to propose the use of a SEAD-inspired method to estimate the pulse energy in the microwave SQUID multiplexer.

In the direction of arrival problem, the motivation laid on the analysis of the differential spectrum components, which is the difference between the two largest eigenvalues of the modified spatial correlation matrix. The differential spectrum was basically an empirical observation and the lacking of a theoretical framework that supports SEAD method as direction of arrival estimator straitened its acknowledgment. The differential spectrum definition was questioned resulting in the total differential spectrum, which proven to be a matrix norm calculation.

The matrix norms were investigated in terms of its fundamental formulation. By definition, each norm is a special combination of the absolute value of some selected entries. A mathematical formulation was delivered, which describes the relationship among the real direction of arrival angles and the test angle, which is added to the spatial correlation matrix to sweep the entire angular range in order to evaluate the positions of maximized power. It is a general expression, it is true for any number of sources, any number of sensors, any correlation factor, and direction of arrival angles. It is worth mentioning that the matrix norm approach profit from the correlation among sources, which is a big advantage for in-door and urban communication systems where the probability of reflected signals is very high.

The eigenvalues also play an important role in the differential spectrum calculation. The first eigenvalue shows peaks in positions relative to existing sources directions whilst the other eigenvalues in the signal subspace show valleys, such that, the difference between the largest and the second-largest eigenvalues will emphasize the peaks.

The matrix norms are suitable for obtaining candidate angles and all spectra were useful for indicating the position of sources through the prominent peaks, which have higher amplitude than other existing peaks. The same resolution issue on the differential spectrum is observed in matrix norms spectra, the number of sensors limits the thickness of the peaks.

SEAD method has shown outstanding performance for low SNR values, outperforming methods like the already well known MODEX method. Nonetheless, SEAD method using matrix norms as initial guess generators does not degrade the performance, on the contrary, for widely-spaced sources it has shown to be much more stable than the previous version of the method. Some simulations were performed to allow the analysis over the accuracy of the methods and to enable the comparison for different scenarios.

In the uncorrelated case and considering closely-spaced sources, the estimators achieved optimal CRB-compatible performance for high SNRs until the point where the breakdown effect is recognized. Improved SEAD provided better estimates with a threshold SNR in the proximity of -10 dB. For widely-spaced sources on the uncorrelated situation, SEAD-based methods using matrix norms outperformed the MODEX and improved-SEAD methods for low SNRs. All SEAD-based methods have limitations on high SNRs range, their performance tends to stagnate in a certain error.

Considering the correlated case, some issues were fixed regarding the error surface on improved-SEAD. The other SEAD-based methods performed slightly better for closely-spaced sources. For widely-spaced sources, the performance did not change dramatically and the stagnation on the error still exists for high SNRs.

Beyond these benefits, the proposal using matrix norms was very helpful for reducing the runtime on the initial guess step. By avoiding the EVD or SVD calculation, the overall runtime of the method was reduced and it was shown that for a number of sources greater than 4, the SEAD-based methods perform faster than MODEX-based methods. An astonishing result was reached by the 2-norm, it reduced the runtime of SEAD method around 40 %.

The matrix 2-norm (also known as the Frobenius norm) is then a strong candidate for substituting the eigenvalue/singular value decomposition on SEAD-based methods.

Some concerns arise from the observation that the performance of SEAD-based methods stagnate for high SNR values, which means that it is not asymptotically efficient. Another issue is the threshold amplitude that defines a minimum amplitude in which one peak is considered to be relative to a real source.

By changing gears a little bit, the focus relay on tracing a parallel that connects the direction of arrival estimation to the x-ray spectroscopy. Based on the approach used in SEAD method, a sensor array-based approach was proposed to estimate the phase shift of carriers in the microwave SQUID multiplexer system. In the microwave SQUID multiplexer, the signal of interest is also a phase shift of a complex wave, but in this case, it is provoked by the incidence of charged particles on MMCs.

It is assumed the existence of one virtual circuit and one physical circuit, the latter is the actual signal being received throughout the experiment and the first is a reference signal. Both signals are arranged in a matrix in order to obtain a spatial correlation matrix. The eigenvalues of this matrix solved the problem of energy estimation and constitute an alternative to the maximum likelihood estimator. The eigenvalues method has shown to be robust against the harmful effects of noise and, under certain constraints, it performed better than the other method. The second eigenvalue can provide a measure of the noise added to the signals, which is helpful to calculate an estimate of the SNR condition.

A complete formulation for the eigenvalues of the spatial correlation matrix was delivered, which is general in terms of the wave's parameters. The expression allows the understanding of the behavior of the eigenvalues for a wide variety of situations, some scenarios of most interest were addressed, so that, the advantages and disadvantages of the proposed method were discussed. It was found that the eigenvalues mainly depend on the magnitude of the inner product between the reference and transmitted vector.

Considering the context of simulated data, if the reference and transmitted signals are ideal complex exponential, the estimated pulse presented a larger peak during the shifted-phase values filling process. After that, the exponential pulse decay itself has shown a small amplitude. The noise added to the system was modeled as zero-mean white Gaussian, it hampers the estimation even for high SNR values, for instance, 10 dB. The formulation has shown that the method's performance can be improved by assigning different wave parameter's values. Three remarkable cases were presented and discussed: different I/Q amplitudes, different I/Q frequencies and different initial phase for the reference and transmitted vectors.

By varying the wave's parameters, the energy pulse could be estimated and the fit to the original pulse is reached by extracting the square root of the estimates specifically for the cases of different amplitudes and frequencies.

The reference and transmitted signals can also have different initial phases. In this case, the pulse can be estimated either by the largest eigenvalue or the second eigenvalue, furthermore, there is no need to extract the square root of the estimates. Furthermore, this approach provides robust estimates for lower SNR values around 6 dB.

The fit of the estimated pulse was assessed in terms of the MSE where the desired response was a simulated pulse. Different parameters assignment leads to characteristic error surfaces. The eigenvalue method has shown to be stable, whilst the maximum likelihood method performed better in some situations and has broken in others.

One strong limitation on the discussed methods is the length of the data vector used to calculate the estimates. The rise time of the estimated pulse is directly dependent on the number of samples, that is true for both approaches. However, the eigenvalue method has shown to be flexible in terms of the amount of data, while the maximum likelihood is very sensible to a limited number of samples.

The mean runtime of the methods is also an important measure criteria. The eigenvalue method performed over real signals requires 20% the runtime of the maximum likelihood, however, the eigenvalue method applied to complex signals is approximately 9 times slower than the maximum likelihood method.

For future work, the main challenge is to further exploit the common characteristics of both problems, for instance, to apply the methods used to estimate the direction of arrival on multiple inputs multiple outputs systems on the readout of multiple SQUIDs. Currently, only a single SQUID coupled to the termination of a transmission line is read out, the goal is to adapt algorithms such as the MUSIC, MODEX, SEAD and other methods to estimate a comb of frequencies modulated in a single resonator by multiple SQUIDs.

On the context of the direction of arrival estimation, it is straightforward to apply the discussed SEAD-based methods to estimate the arriving angle of planar waves in terms of azimuth and polar angles, which leads to the two-dimensional direction of arrival estimation problem.

Furthermore, the methods in both problems should be implemented in hardware in order to assess their capability to provide estimates on real situations and also to prove, if it is the case, that they can process information on-line.

Bibliography

ALVES, C. A. *Análise Teórica e Experimental de Métodos de Estimação de DOA e de Estimação de Freqüência com Alta Resolução*. Tese (Doutorado) — State University of Campinas, Jul 2004. Cited 7 times on page(s) 38, 43, 44, 53, 60, 62, and 63.

AMSTUTZ, C. *Evaluation of an Associative Memory and FPGA Based Concept for the CMS Track Trigger*. 168 f. p. Tese (Doutorado) — Fakultät für Elektrotechnik und Informationstechnik in Karlsruhe Institute für Technologie, Karlsruhe, Germany, jul 2016. Cited 9 times on page(s) 21, 99, 100, 101, 102, 103, 104, 105, and 106.

BANDLER, S. et al. Magnetically coupled microcalorimeters. *Journal of Low Temperature Physics*, USA, v. 167, n. 3/4, p. 254–268, may 2012. Cited on page 45.

BOLDRINI, J. L. et al. *Álgebra Linear*. 3rd edition. ed. São Paulo, Brasil: Harper & Row do Brasil, 1980. Cited 2 times on page(s) 73 and 169.

BRESLER, Y.; MACOVSKI, A. Exact maximum likelihood parameter estimation of superimposed exponential signals in noise. *IEEE Transactions on Acoustics, Speech, and Signal Processing*, v. 34, n. 5, p. 1081–1089, 1986. Cited 4 times on page(s) 58, 60, 61, and 62.

CERN-HISTORY. *CERN history*. Accessed: 2019–06–15. Disponível em: <https://home.cern/about/who-we-are/our-history>. Cited on page 100.

CERN-SCIENCE. *CERN science*. Accessed: 2019–06–15. Disponível em: <https://home.cern/science/physics/higgs-boson>. Cited on page 100.

FERREIRA, Y. R.; LEMOS, R. P. A new DOA estimation algorithm based on differential spectrum. In: *Proceedings of the Eighth International Symposium on Signal Processing and Its Applications*. Sydney, Australia: [s.n.], 2005. p. 303–307. Cited 2 times on page(s) 66 and 71.

GERSHMAN, A. B.; STOICA, P. New MODE-based techniques for direction finding with an improved threshold performance. *Signal Processing*, v. 76, p. 221–235, 1999. Cited 4 times on page(s) 64, 65, 66, and 81.

GOLUB, G. H.; LOAN, C. F. V. *Matrix Computations*. 3rd edition. ed. Baltimore, Maryland, USA: The Johns Hopkins University Press, 1996. Cited 3 times on page(s) 126, 169, and 170.

HALLIDAY, D.; RESNICK, R.; WALKER, J. *Fundamentals of Physics*. 9th edition. ed. New Jersey, USA: John Wiley & Sons, 2011. Cited 2 times on page(s) 99 and 100.

HUA, Y. The most efficient implementation of the IQML. *IEEE Trans. on Signal Processing*, v. 42, p. 2203–2204, Aug. 1994. Cited on page 55.

IRWIN, K. et al. Microwave SQUID multiplexers for low-temperature detectors. *Nuclear Instruments and Methods in Physics Research*, USA, v. 559, n. 2, p. 802–804, jan 2006. Cited 2 times on page(s) 45 and 107.

JúNIOR, G. C. et al. A new approach for the differential spectrum using the frobenius norm. In: *2014 Second International Conference on Artificial Intelligence, Modeling and Simulation*. Madrid, Spain: [s.n.], 2014. p. 350–354. Cited on page 191.

KARCHER, N. *Ein mehrkanaliges Software Defined Radio für supraleitende Mikrokalorimeter*. 114 p. Dissertação (Mestrado) — Karlsruher Institut für Technologie, Nov. 2016. Cited 5 times on page(s) 22, 116, 117, 118, and 119.

KAY, S. M. *Fundamentals of Statistical Signal Processing, Volume I: Estimation Theory*. Englewood Cliffs, NJ: Prentice Hall, 1993. Cited 2 times on page(s) 57 and 59.

KEMPF, S. *Entwicklung eines Mikrowellen-SQUID-Multiplexers auf der Grundlage nicht-hysteretischer rf-SQUIDs zur Auslesung metallischer magnetischer Kalorimeter*. 195 f. p. Tese (Doutorado) — Ruprecht-Karls-Universität Heidelberg, jul 2012. Cited 3 times on page(s) 44, 45, and 114.

KEMPF, S. et al. Microwave squid multiplexer for the readout of metallic magnetic calorimeters. *Journal of Low Temperature Physics*, USA, v. 175, n. 5/6, p. 850–862, jun 2014. Cited 3 times on page(s) 107, 108, and 109.

KEMPF, S. et al. Design, fabrication and characterization of a 64 pixel metallic magnetic calorimeter array with integrated, on-chip microwave SQUID multiplexer. *Superconductor Science and Technology*, USA, v. 30, n. 6, p. 1–16, may 2017. Cited 4 times on page(s) 21, 45, 46, and 109.

KEMPF, S. et al. Demonstration of a scalable frequency-domain readout of metallic magnetic calorimeters by means of a microwave SQUID multiplexer. *American Institute of Physics*, USA, v. 7, n. 1, p. 1–9, jan 2017. Cited 2 times on page(s) 45 and 140.

KEMPF, S. et al. Multiplexed readout of MMC detector arrays using non-hysteretic rf-SQUIDs. *Journal of Low Temperature Physics*, USA, v. 176, n. 3/4, p. 426–434, aug 2014. Cited on page 107.

KRUMMENAUER, R. et al. Improving the threshold perfomance of maximum likelihood estimation of direction of arrival. *Signal Processing*, v. 90, n. 11, p. 1582–1590, Nov 2010. Cited on page 66.

KUMARESAN, L.; SHAW, A. An algorithm for pole-zero modeling and spectral analysis. *IEEE Transactions on Acoustics, Speech and Signal Processing*, v. 34, n. 3, p. 637–640, 1986. Cited 3 times on page(s) 55, 58, and 60.

KUNZLER, J. A. et al. Further investigation on frobenius spectrum for DOA estimation. In: *2015 IEEE Latin American Symposium on Circuits & Systems (LASCAS)*. Montevideo, Uruguai: [s.n.], 2015. p. 1–4. Cited on page 81.

LI, J.; STOICA, P.; LIU, Z. Comparative study of IQML and MODE direction-of-arrival estimators. *IEEE Trans. on Signal Processing*, v. 46, p. 149–160, Jan. 1998. Cited on page 63.

LOPES, A. et al. Improving the MODEX algorithm for direction estimation. *Signal Processing*, v. 83, n. 9, p. 2047–2051, Sep 2003. Cited 2 times on page(s) 66 and 81.

MATES, J. A. B. *The Microwave SQUID Multiplexer*. 128 f. p. Tese (Doutorado) — University of Colorado at Boulder, 2011. Cited 8 times on page(s) 45, 46, 109, 110, 111, 112, 113, and 114.

MATES, J. A. B. et al. Demonstration of a multiplexer of dissipationless superconducting quantum interference devices. *Applied Physics Letters*, USA, v. 92, p. 1–9, 2008. Cited 5 times on page(s) 45, 46, 107, 108, and 114.

MATES, J. A. B. et al. Flux-ramp modulation for SQUID multiplexing. *Journal of Low Temperature Physics*, USA, v. 167, p. 707–712, feb 2012. Cited 4 times on page(s) 120, 122, 123, and 151.

MEYER, C. D. *Matrix Analysis and Applied Linear Algebra*. 1st edition. ed. Philadelphia, PA, USA: SIAM, 2001. Cited 5 times on page(s) 73, 81, 126, 169, and 170.

OTTERSTEN, B.; VIBERG, M. Analysis of subspace fitting based methods for sensor array processing. In: *Proceedings of the International Conference on Acoustic, Speech and Signal Processing*. Glasgow, Scotland: [s.n.], 1989. p. 2807–2810. Cited on page 58.

PILLAI, S. U. *Array Signal Processing*. New York, NY: Springer-Verlag, 1989. Cited 3 times on page(s) 37, 56, and 57.

PORST, J.-P. et al. Time domain multiplexed readout of magnetically coupled calorimeters. *IEEE TRANSACTIONS ON APPLIED SUPERCONDUCTIVITY*, USA, v. 23, n. 3, p. 1–5, jun 2013. Cited on page 45.

POZAR, D. M. *Microwave Engineering*. 4th edition. ed. New Jersey, USA: John Wiley & Sons, 2012. Cited on page 111.

PROAKIS, J. G.; SALEHI, M. *Digital Communications*. 5th edition. ed. New York, USA: McGraw-Hill, 2008. Cited 3 times on page(s) 120, 121, and 122.

SANDER, O. et al. Software defined radio based readout of microwave SQUID multiplexed metallic magnetic calorimeter arrays. In: *Topical Workshop on Electronics for Particle Physics (TWEPP-17)*. Santa Cruz, California: Proceedings of Science, 2017. p. 1–5. Cited 6 times on page(s) 21, 22, 108, 115, 116, and 118.

SILVA, H. V. L. et al. A branch-and-bound inspired technique to improve the computational efficiency of DOA estimation. *Signal Processing*, v. 93, n. 4, p. 947–956, Apr 2013. ISSN 0165-1684. Cited 8 times on page(s) 51, 67, 69, 70, 71, 72, 93, and 191.

SILVA, H. V. L. e. *Utilização de Filtragem Espacial e Otimização Numérica em um Método de Estimação de Direção de Chegada em Arranjos de Sensores*. 189 p. Tese (Doutorado) — Federal University of Uberlândia, Jun. 2017. Cited 3 times on page(s) 66, 71, and 81.

STOICA, P.; NEHORAI, A. Performance study of conditional and unconditional direction-of-arrival estimation. *IEEE Transactions on Acoustic, Speech and Signal Processing*, v. 38, n. 10, p. 1783–1795, Oct 1990. Cited 3 times on page(s) 54, 55, and 60.

STOICA, P.; SHARMAN, K. C. Novel eigenanalysis method for direction estimation. *IEE Proceedings F Radar and Signal Processing*, v. 137, n. 1, p. 19–26, Feb 1990. ISSN 0956-375X. Cited 3 times on page(s) 60, 62, and 63.

TREES, H. L. V. *Optimum Array Processing. Part IV of Detection, Estimation and Modulation Theory.* New York, NY: John Wiley and Sons, 2002. Cited 5 times on page(s) 37, 39, 41, 42, and 51.

VIBERG, M.; KRIM, H. Two decades of array signal processing research. *IEEE Signal Processing Magazine*, v. 13, n. 4, p. 67–94, jul 1996. ISSN 1053-5888. Cited 3 times on page(s) 53, 58, and 59.

WEGNER, M. et al. Microwave SQUID multiplexing of metallic magnetic calorimeters: Status of multiplexer performance and room-temperature readout electronics development. *Journal of Low Temperature Physics*, USA, v. 193, n. 3–4, p. 462–475, feb 2018. Cited 2 times on page(s) 118 and 119.

Appendices

APPENDIX A – Linear Algebra Definitions and Properties

Some techniques derived from Linear Algebra are extremely important within the present work, such as vectors and matrix operations. There are several references to their definitions and elementary properties as found in (MEYER, 2001; GOLUB; LOAN, 1996; BOLDRINI et al., 1980). Some advanced definitions and properties that are fundamental to the development of the thesis are presented in this section.

A.1 Trace Operator

The trace operator of a square matrix $K \times K$, with $K \in \mathbb{N}$, $\mathbf{A} = [a_{rc}]$, is defined as the sum of the main diagonal elements (MEYER, 2001):

$$\operatorname{tr}(\mathbf{A}) = \sum_{r=1}^{K} a_{rr}, \tag{A.1}$$

the indexes r and c refers to row and column, respectively.

The trace is a linear function, which means that given two matrices $K \times K$, $\mathbf{A} = [a_{rc}]$ and $\mathbf{B} = [b_{rc}]$:

$$\operatorname{tr}(\alpha\ \mathbf{A} + \mathbf{B}) = \sum_{r=1}^{K} (\alpha\ a_{rr} + b_{rr}) = \alpha \sum_{r=1}^{K} a_{rr} + \sum_{r=1}^{K} b_{rr} = \alpha\ \operatorname{tr}(\mathbf{A}) + \operatorname{tr}(\mathbf{B}). \tag{A.2}$$

A.2 Matrix Norms

The matrix norm for a vector space $\mathcal{V}$ is a function that transforms $\mathcal{V}$ into $\mathbb{R}$ and satisfies certain properties (MEYER, 2001). Given a generic matrix $\mathbf{A}$ of dimensions $R \times C$, its norm can be calculated by the so calling p-norm:

$$\|\mathbf{A}\|_p = \sqrt[p]{\sum_{r=1}^{R} \sum_{c=1}^{C} |a_{rc}|^p}, \tag{A.3}$$

where R, $C \in \mathbb{N}$.

Commonly found norms are $\|\mathbf{A}\|_1$, 1-norm or grade norm; $\|\mathbf{A}\|_2$, 2-norm or Frobenius norm, $\|\mathbf{A}\|_\infty$, ∞-norm, although it does not meet all matrix norm conditions unless an algebraic manipulation. They are defined as (MEYER, 2001; GOLUB; LOAN, 1996):

$$\|\mathbf{A}\|_1 = \sum_{r=1}^{R} \sum_{c=1}^{C} |a_{rc}|; \tag{A.4}$$

$$\|\mathbf{A}\|_2 = \|\mathbf{A}\|_F = \sqrt[2]{\sum_{r=1}^{R}\sum_{c=1}^{C}|a_{rc}|^2}; \tag{A.5}$$

$$\|\mathbf{A}\|_\infty = \max_{r,c}|a_{rc}|. \tag{A.6}$$

There are also matrix norms induced by vector norms. They are $\|\mathbf{A}\|_{1_i}$, 1_i-norm or maximum column sum norm, $\|\mathbf{A}\|_{2_i}$, 2_i-norm or the largest eigenvalue of $\mathbf{A}^*\mathbf{A}$ and $\|\mathbf{A}\|_{\infty_i}$, ∞_i-norm or maximum row sum norm. Thus, considering the matrix $\mathbf{A}$ and a unit vector $\mathbf{x}$ (GOLUB; LOAN, 1996), matrix norms are calculated as follows:

$$\|\mathbf{A}\|_{1_i} = \sup_{\mathbf{x}\neq 0}\frac{\|\mathbf{A}\mathbf{x}\|_1}{\|\mathbf{x}\|_1} = \max_{\|\mathbf{x}\|_1=1}\|\mathbf{A}\mathbf{x}\|_1 = \max_{c}\sum_{r=1}^{R}|a_{rc}|; \tag{A.7}$$

$$\|\mathbf{A}\|_{2_i} = \sup_{\mathbf{x}\neq 0}\frac{\|\mathbf{A}\mathbf{x}\|_2}{\|\mathbf{x}\|_2} = \max_{\|\mathbf{x}\|_2=1}\|\mathbf{A}\mathbf{x}\|_2 = \max\sqrt{\lambda}; \tag{A.8}$$

$$\|\mathbf{A}\|_{\infty_i} = \sup_{\mathbf{x}\neq 0}\frac{\|\mathbf{A}\mathbf{x}\|_\infty}{\|\mathbf{x}\|_\infty} = \max_{\|\mathbf{x}\|_\infty=1}\|\mathbf{A}\mathbf{x}\|_\infty = \max_{r}\sum_{c=1}^{C}|a_{rc}|. \tag{A.9}$$

A.3 Orthogonal Projector

It projects a vector in orthogonal space to the $\mathbf{A}$ column space (MEYER, 2001).

$$\mathbf{P}_A^{\perp} = \mathbf{I} - \mathbf{P}_A = \mathbf{I} - \mathbf{A}\mathbf{A}^{\dagger}, \tag{A.10}$$

where $\mathbf{A}^{\dagger} = \left(\mathbf{A}^*\mathbf{A}\right)^{-1}\mathbf{A}^*$ is the Moore-Penrose pseudoinverse.

A.4 Eigenvalue Decomposition (EVD)

An array $\mathbf{A}$ of dimensions $K \times K$ is diagonalizable if there is a complete set of independent eigenvalues, $\{\lambda_1,\lambda_2,\ldots,\lambda_K\}$. Associated with these values there are eigenvectors $\{\mathbf{x}_1,\mathbf{x}_2,\ldots,\mathbf{x}_K\}$ that satisfy the equation (MEYER, 2001):

$$\mathbf{A}\mathbf{x}_k = \mathbf{x}_k\lambda_k, \tag{A.11}$$

where $(\lambda_k,\mathbf{x}_k)$ is called the $\mathbf{A}$ eigenpair and $k = \{1,\ 2,\ldots,\ K\}$. The set of distinct eigenvalues is called the spectrum of $\mathbf{A}$. If all eigenvectors are put together, in such a manner $\mathbf{A}$ is similar to a diagonal matrix $\boldsymbol{\Lambda}$, the eigenvalue decomposition of $\mathbf{A}$ can be written as:

$$\mathbf{A} = \mathbf{X}\boldsymbol{\Lambda}\mathbf{X}^*. \tag{A.12}$$

The spectral matrix diagonalization theorem states that the matrix $\mathbf{A}$ can be decomposed as:

$$\mathbf{A} = \lambda_1\mathbf{X}_1 + \lambda_2\mathbf{X}_2 + \cdots + \lambda_K\mathbf{X}_K, \tag{A.13}$$

where $\mathbf{X}_k = \frac{x_k x_k^*}{x_k^* x_k}$ are spectral projectors relative to $\mathbf{A}$, $\mathbf{X}_i\mathbf{X}_j = \mathbf{0}$ when $i \neq j$, and $\mathbf{X}_1 + \mathbf{X}_2 + \cdots + \mathbf{X}_K = \mathbf{I}$.

A.5 Singular Value Decomposition (SVD)

For a matrix $\mathbf{A}$, where $\text{rank}(\mathbf{A}) = g$, the factorization $\mathbf{URV}^*$ comes from the orthogonal decomposition theorem, which is given by:

$$\mathbf{A} = \mathbf{URV}^* = \mathbf{U}\begin{pmatrix} \mathbf{C}_{g\times g} & \mathbf{0} \\ \mathbf{0} & \mathbf{0} \end{pmatrix}\mathbf{V}^*, \tag{A.14}$$

where $\mathbf{C}$ is a non-singular matrix.

The singular value decomposition of $\mathbf{A}$ is a later process which follows A.14. It diagonalizes the $\mathbf{C}$ matrix, obtaining a matrix $\mathbf{D}_{g\times g} = diag(\sigma_1, \sigma_2, \ldots, \sigma_g)$ so that:

$$\mathbf{A} = \mathbf{U}'\begin{pmatrix} \mathbf{D}_{g\times g} & \mathbf{0} \\ \mathbf{0} & \mathbf{0} \end{pmatrix}\mathbf{V}'^{\,*}, \tag{A.15}$$

com $\sigma_1 \geq \sigma_2 \geq \cdots \geq \sigma_g \geq 0$.

A.6 Normal Matrices

Even if a matrix $\mathbf{A}$ of rank g has a complete set of independent eigenvalues, there is no guarantee that this set is orthonormal. For $\mathbf{A}$ to be unitary and similar to a diagonal matrix the following condition must be met:

$$\mathbf{A}^*\mathbf{A} = \mathbf{A}\mathbf{A}^*. \tag{A.16}$$

An array that meets this condition is said to be normal and there will be a unitary matrix $\mathbf{U}$ whose columns are a complete set of orthogonal eigenvectors and $\mathbf{D}$ is a diagonal matrix whose entries are the associated eigenvalues. In addition to the inherent properties of normal matrices, symmetric and hermitian matrices have their eigenvalues in the set of real numbers.

An important feature of normal matrix is that the singular values of $\mathbf{A}$ are the positive square roots of the eigenvalues of $\mathbf{AA}^*$. If $\mathbf{A}$ is normal and has non-zero eigenvalues $\{\lambda_1,\lambda_2,\ldots,\lambda_g\}$, then the non-zero singular values of $\mathbf{A}$ are $\{\sigma_1 = |\lambda_1|, \sigma_2 = |\lambda_2|, \ldots, \sigma_g = |\lambda_g|\}$. This means that both EVD and SVD provide the same values.

APPENDIX B – The General Term for the Modified Spatial Correlation Matrix $\mathbf{R}_m$

The steering matrix and the correlation matrix can be written respectively as:

$$\mathbf{A} = \begin{pmatrix} 1 & 1 & \dots & 1 \\ \exp(j\omega_1) & \exp(j\omega_2) & \dots & \exp(j\omega_M) \\ \vdots & \vdots & \ddots & \vdots \\ \exp[j(K-1)\omega_1] & \exp[j(K-1)\omega_2] & \dots & \exp[j(K-1)\omega_M] \end{pmatrix}$$

and

$$\mathbf{P} = \begin{pmatrix} 1 & \rho_{12} & \dots & \rho_{1M} \\ \rho_{21} & 1 & \dots & \rho_{2M} \\ \vdots & \vdots & \ddots & \vdots \\ \rho_{M1} & \rho_{M2} & \dots & 1 \end{pmatrix}$$

Secondly, performing $\mathbf{APA}^*$, one obtains a matrix such that each entry $[\mathbf{APA}^*]_{rc}$ is given by

$$[\mathbf{APA}^*]_{rc} = \sum_{\beta=1}^{M}\sum_{\alpha=1}^{M} \rho_{\alpha\beta}\ \exp\{-j[(c-1)\omega_\alpha - (r-1)\omega_\beta]\}, \qquad \text{(B.1)}$$

where, ω_α and ω_β stand for the angular frequencies relative to the DOA angles. Taking a closer look into matrix columns, it follows that:

$$\mathbf{APA}^* = (r_1|r_2|\dots|r_i|\dots|r_K) \qquad \text{(B.2)}$$

where, r_i is a $(K \times 1)$ vector and $i = 1, 2, \dots, K$.

$$r_i = \begin{pmatrix} \sum_{\beta=1}^{M}\sum_{\alpha=1}^{M} \rho_{\alpha\beta}\ \exp[-j(i-1)\omega_\alpha] \\ \sum_{\beta=1}^{M}\sum_{\alpha=1}^{M} \rho_{\alpha\beta}\ \exp\{-j[(i-1)\omega_\alpha - \omega_\beta]\} \\ \vdots \\ \sum_{\beta=1}^{M}\sum_{\alpha=1}^{M} \rho_{\alpha\beta}\ \exp\{-j[(i-1)\omega_\alpha - (K-1)\omega_\beta]\} \end{pmatrix}$$

Thus, the general term of $\mathbf{R}_m(\omega_t)$ can be written as

$$[\mathbf{R}_m(\omega_t)]_{rc} = \left[\sum_{\beta=1}^{M}\sum_{\alpha=1}^{M} \rho_{\alpha\beta}\ \exp\{-j[(c-1)\omega_\alpha - (r-1)\omega_\beta]\}\right] + \\ +\ \exp[-j(c-r)\omega_t]. \tag{B.3}$$

APPENDIX C – RMSE Values for DOA Estimation Performance

The data used to plot the error surface in Chapter 4 are presented in this appendix in tabular form as a supplementary material to aid in understanding the results.

Despite of the SNR ranging from -15 to 15 dB in the figures presented in Chapter 4, the tables in this section will present the RMSE values in the range $(-12.5, 15)$ dB, because at this level the methods have already reached the breakdown effect.

C.1 Uncorrelated Sources

A series of 1000 experiments was performed and the RMSE of the estimates are presented in tabular form for the several assessed methods: 1-norm, 1_i-norm, 2-norm, 2_i-norm, Improved SEAD, MODEX, and Modified MODEX. The sources are assumed to be uncorrelated, which means that $\rho_{\alpha\beta} = 0$.

Table 4 presents the RMSE values for the case where the signals are uncorrelated. Table 4 refers to Figure 9.

Table 4 – RMSE of 1000 experiments for the 1-norm estimator considering uncorrelated signals.

$dB\rightarrow$ $(^\circ)\downarrow$	−12.5	−11.25	−10	−8.75	−7.5	−6.25	−5	−3.75	−2.5	−1.25	0	1.25	2.5	3.75	5	6.25	7.5	8.75	10	11.25	12.5	13.75	15
−40	4.05	2.00	0.80	0.63	0.52	0.44	0.38	0.32	0.29	0.25	0.22	0.19	0.17	0.16	0.15	0.14	0.13	0.13	0.12	0.12	0.11	0.11	0.11
−35	3.57	0.96	0.75	0.60	0.49	0.42	0.35	0.29	0.25	0.21	0.19	0.17	0.16	0.16	0.15	0.14	0.15	0.14	0.15	0.15	0.15	0.16	0.16
−30	2.39	1.93	0.72	0.59	0.49	0.39	0.34	0.29	0.24	0.21	0.18	0.17	0.14	0.12	0.11	0.09	0.09	0.07	0.06	0.05	0.05	0.05	0.04
−25	3.26	0.90	0.72	0.57	0.47	0.38	0.33	0.28	0.25	0.20	0.18	0.17	0.15	0.13	0.13	0.12	0.11	0.11	0.11	0.11	0.11	0.11	0.11
−20	3.37	1.26	0.72	0.57	0.45	0.39	0.32	0.28	0.23	0.20	0.18	0.17	0.16	0.14	0.14	0.14	0.14	0.14	0.14	0.14	0.13	0.13	0.13
−15	3.43	0.90	0.72	0.57	0.48	0.38	0.33	0.27	0.23	0.20	0.18	0.16	0.14	0.14	0.14	0.13	0.13	0.13	0.13	0.12	0.12	0.12	0.12
−10	5.03	0.88	0.73	0.57	0.48	0.39	0.32	0.28	0.24	0.21	0.18	0.17	0.16	0.15	0.15	0.15	0.14	0.14	0.14	0.14	0.14	0.14	0.14
−5	4.32	2.04	0.70	0.57	0.47	0.39	0.34	0.28	0.25	0.22	0.19	0.16	0.15	0.13	0.12	0.11	0.10	0.09	0.08	0.07	0.07	0.06	0.06
0	19.24	15.36	8.66	3.40	0.74	0.50	0.42	0.35	0.30	0.26	0.23	0.20	0.17	0.16	0.14	0.12	0.12	0.11	0.10	0.10	0.10	0.09	0.09
5	19.22	9.94	4.02	1.89	1.54	1.21	0.94	0.83	0.65	0.56	0.46	0.38	0.33	0.29	0.24	0.21	0.18	0.16	0.14	0.12	0.11	0.09	0.08
15	20.25	10.52	3.99	1.92	1.60	1.27	1.03	0.86	0.69	0.58	0.48	0.41	0.34	0.29	0.25	0.22	0.18	0.16	0.14	0.12	0.11	0.10	0.08
20	22.08	17.41	11.22	4.48	0.65	0.53	0.45	0.39	0.32	0.26	0.23	0.21	0.17	0.16	0.14	0.12	0.11	0.11	0.09	0.09	0.08	0.08	0.08
25	5.86	2.83	0.75	0.61	0.49	0.41	0.35	0.30	0.26	0.23	0.21	0.20	0.19	0.18	0.18	0.18	0.18	0.19	0.19	0.19	0.19	0.20	0.20
30	5.13	1.99	0.76	0.61	0.50	0.42	0.36	0.30	0.26	0.22	0.20	0.18	0.16	0.15	0.14	0.13	0.12	0.12	0.12	0.12	0.11	0.11	0.10
35	3.71	1.15	0.78	0.64	0.53	0.42	0.37	0.30	0.26	0.23	0.20	0.19	0.17	0.17	0.16	0.17	0.16	0.17	0.17	0.17	0.18	0.18	0.18
40	4.72	1.06	0.79	0.65	0.52	0.45	0.37	0.31	0.27	0.23	0.21	0.18	0.16	0.15	0.15	0.15	0.16	0.16	0.16	0.16	0.17	0.17	0.17
45	3.12	2.99	0.84	0.67	0.55	0.46	0.40	0.33	0.28	0.24	0.21	0.20	0.18	0.18	0.18	0.18	0.19	0.19	0.20	0.21	0.21	0.21	0.21
50	4.76	2.06	0.90	0.72	0.59	0.47	0.40	0.35	0.30	0.26	0.23	0.19	0.17	0.15	0.14	0.13	0.12	0.11	0.11	0.11	0.11	0.11	0.10
55	5.11	1.24	0.96	0.77	0.65	0.52	0.44	0.37	0.31	0.27	0.23	0.20	0.19	0.17	0.16	0.15	0.15	0.14	0.14	0.14	0.14	0.14	0.14
60	4.59	1.33	1.06	0.87	0.72	0.57	0.48	0.42	0.37	0.32	0.26	0.24	0.20	0.17	0.15	0.14	0.13	0.11	0.10	0.09	0.09	0.08	0.07

Table 5 presents the RMSE values for the case where the signals are uncorrelated. Table 5 refers to Figure 10.

Table 5 – RMSE of 1000 experiments for the 1_i-norm estimator considering uncorrelated signals.

(°)↓ dB→	−12.5	−11.25	−10	−8.75	−7.5	−6.25	−5	−3.75	−2.5	−1.25	0	1.25	2.5	3.75	5	6.25	7.5	8.75	10	11.25	12.5	13.75	15
−40	4.00	1.98	0.83	0.65	0.54	0.47	0.39	0.34	0.31	0.27	0.24	0.22	0.20	0.19	0.18	0.17	0.17	0.17	0.16	0.16	0.15	0.15	0.16
−35	4.00	1.71	0.77	0.62	0.51	0.44	0.36	0.31	0.28	0.25	0.23	0.22	0.21	0.20	0.19	0.19	0.18	0.18	0.18	0.19	0.18	0.19	0.19
−30	3.33	2.06	0.72	0.60	0.50	0.40	0.34	0.30	0.25	0.22	0.18	0.17	0.15	0.13	0.13	0.11	0.11	0.11	0.10	0.09	0.10	0.09	0.10
−25	4.58	1.28	0.74	0.59	0.50	0.39	0.35	0.31	0.28	0.24	0.21	0.20	0.19	0.17	0.17	0.16	0.15	0.15	0.15	0.15	0.15	0.15	0.15
−20	3.67	1.26	0.73	0.58	0.47	0.39	0.33	0.29	0.25	0.22	0.19	0.18	0.17	0.16	0.16	0.15	0.15	0.16	0.15	0.15	0.15	0.14	0.14
−15	3.15	1.13	0.83	0.58	0.49	0.39	0.35	0.30	0.26	0.24	0.22	0.20	0.19	0.19	0.18	0.18	0.18	0.18	0.17	0.17	0.17	0.17	0.17
−10	5.53	1.13	0.76	0.59	0.48	0.40	0.33	0.29	0.25	0.22	0.19	0.18	0.16	0.15	0.14	0.14	0.14	0.14	0.14	0.14	0.14	0.14	0.14
−5	4.10	2.67	2.85	1.92	0.70	1.10	0.33	0.27	0.24	0.20	0.18	0.16	0.15	0.13	0.12	0.11	0.10	0.09	0.11	0.08	0.08	0.08	0.08
0	13.19	12.51	12.52	10.47	6.14	4.07	2.58	1.72	0.92	0.61	0.61	0.36	0.31	0.32	0.22	0.29	0.20	0.21	0.19	0.16	0.20	0.18	0.16
5	25.62	21.31	17.03	10.40	3.76	1.45	0.97	0.83	0.65	0.56	0.46	0.38	0.33	0.29	0.24	0.21	0.18	0.15	0.14	0.12	0.10	0.09	0.08
15	26.66	23.22	17.08	9.55	4.23	1.67	1.13	0.86	0.69	0.58	0.48	0.41	0.34	0.29	0.25	0.22	0.18	0.16	0.14	0.12	0.11	0.09	0.08
20	15.43	15.20	13.89	10.93	7.83	4.48	2.24	1.39	0.66	0.43	0.36	0.38	0.35	0.27	0.20	0.19	0.16	0.16	0.13	0.13	0.15	0.13	0.14
25	7.29	3.99	2.34	0.91	0.81	0.71	0.35	0.30	0.25	0.26	0.24	0.18	0.19	0.17	0.16	0.16	0.16	0.20	0.16	0.15	0.15	0.15	0.16
30	5.87	1.99	0.76	0.61	0.50	0.43	0.37	0.31	0.28	0.25	0.24	0.22	0.22	0.22	0.21	0.21	0.21	0.22	0.22	0.22	0.22	0.22	0.22
35	4.39	1.17	0.81	0.68	0.56	0.46	0.40	0.36	0.31	0.29	0.27	0.26	0.25	0.25	0.24	0.25	0.24	0.23	0.25	0.25	0.25	0.25	0.24
40	4.93	1.49	0.80	0.66	0.53	0.46	0.39	0.32	0.28	0.24	0.23	0.20	0.19	0.18	0.18	0.17	0.17	0.17	0.18	0.18	0.18	0.19	0.18
45	4.08	2.91	1.10	0.68	0.56	0.48	0.41	0.35	0.30	0.26	0.24	0.22	0.21	0.20	0.20	0.20	0.20	0.20	0.20	0.20	0.20	0.20	0.20
50	5.28	2.87	0.93	0.74	0.60	0.50	0.43	0.38	0.33	0.27	0.25	0.21	0.19	0.18	0.18	0.17	0.17	0.17	0.16	0.16	0.16	0.16	0.16
55	6.00	1.26	0.99	0.79	0.67	0.54	0.46	0.40	0.35	0.31	0.28	0.26	0.25	0.24	0.23	0.23	0.23	0.23	0.23	0.23	0.23	0.23	0.23
60	5.42	1.36	1.08	0.87	0.74	0.59	0.50	0.43	0.39	0.32	0.27	0.25	0.22	0.20	0.17	0.17	0.16	0.15	0.15	0.15	0.15	0.15	0.15

Table 6 presents the RMSE values for the case where the signals are uncorrelated. Table 6 refers to Figure 11.

Table 6 – RMSE of 1000 experiments for the 2-norm estimator considering uncorrelated signals.

$dB\rightarrow$ $(°)\downarrow$	−12.5	−11.25	−10	−8.75	−7.5	−6.25	−5	−3.75	−2.5	−1.25	0	1.25	2.5	3.75	5	6.25	7.5	8.75	10	11.25	12.5	13.75	15
−40	3.97	2.00	0.80	0.63	0.52	0.44	0.38	0.32	0.29	0.26	0.23	0.20	0.17	0.16	0.15	0.14	0.13	0.12	0.11	0.11	0.11	0.11	0.11
−35	3.57	0.96	0.76	0.60	0.49	0.42	0.35	0.29	0.25	0.21	0.19	0.17	0.16	0.15	0.14	0.13	0.14	0.13	0.14	0.14	0.14	0.15	0.14
−30	2.51	1.93	0.72	0.59	0.49	0.39	0.33	0.29	0.24	0.21	0.18	0.16	0.14	0.12	0.11	0.09	0.08	0.07	0.06	0.05	0.05	0.04	0.04
−25	3.26	0.90	0.72	0.57	0.47	0.38	0.33	0.28	0.25	0.20	0.18	0.16	0.15	0.13	0.13	0.12	0.11	0.11	0.11	0.11	0.11	0.11	0.11
−20	3.37	1.26	0.72	0.57	0.46	0.39	0.32	0.28	0.23	0.20	0.18	0.17	0.15	0.14	0.14	0.14	0.14	0.14	0.13	0.13	0.12	0.11	0.11
−15	3.44	0.90	0.72	0.57	0.47	0.38	0.33	0.27	0.23	0.20	0.18	0.16	0.14	0.14	0.14	0.14	0.13	0.13	0.13	0.13	0.12	0.13	0.12
−10	5.04	0.88	0.73	0.58	0.48	0.39	0.32	0.28	0.24	0.21	0.18	0.17	0.16	0.15	0.15	0.15	0.14	0.14	0.14	0.14	0.14	0.14	0.14
−5	4.63	2.04	0.70	0.58	0.46	0.39	0.34	0.28	0.24	0.22	0.19	0.16	0.15	0.13	0.12	0.11	0.10	0.09	0.08	0.07	0.07	0.06	0.06
0	19.86	15.87	9.40	4.70	0.93	0.50	0.42	0.35	0.29	0.26	0.22	0.19	0.17	0.14	0.12	0.11	0.10	0.09	0.08	0.07	0.06	0.06	0.06
5	19.57	9.69	4.02	1.88	1.56	1.21	0.93	0.83	0.65	0.56	0.46	0.38	0.33	0.29	0.24	0.21	0.18	0.16	0.14	0.12	0.11	0.09	0.08
15	20.30	10.71	4.14	1.91	1.60	1.27	1.03	0.86	0.69	0.58	0.48	0.41	0.34	0.29	0.25	0.22	0.18	0.16	0.14	0.12	0.11	0.10	0.08
20	22.67	18.07	11.84	4.76	0.65	0.53	0.45	0.38	0.31	0.26	0.23	0.20	0.17	0.15	0.13	0.12	0.10	0.09	0.08	0.07	0.07	0.06	0.06
25	5.98	2.83	0.75	0.61	0.49	0.41	0.35	0.29	0.26	0.23	0.21	0.19	0.19	0.18	0.18	0.18	0.18	0.18	0.19	0.19	0.19	0.19	0.19
30	5.13	1.98	0.76	0.61	0.50	0.42	0.36	0.30	0.26	0.22	0.20	0.18	0.16	0.15	0.13	0.13	0.12	0.11	0.11	0.11	0.10	0.10	0.09
35	3.70	1.14	0.78	0.64	0.53	0.42	0.37	0.30	0.26	0.23	0.20	0.19	0.17	0.17	0.16	0.17	0.17	0.17	0.17	0.17	0.18	0.18	0.18
40	4.72	1.06	0.78	0.65	0.51	0.45	0.37	0.31	0.27	0.22	0.21	0.17	0.16	0.15	0.14	0.14	0.14	0.14	0.14	0.14	0.15	0.15	0.14
45	3.12	2.98	0.84	0.67	0.55	0.46	0.39	0.33	0.27	0.24	0.21	0.20	0.18	0.17	0.17	0.17	0.17	0.17	0.18	0.18	0.18	0.18	0.18
50	3.82	2.06	0.90	0.72	0.59	0.48	0.41	0.35	0.30	0.26	0.23	0.19	0.17	0.15	0.14	0.13	0.12	0.11	0.11	0.11	0.11	0.11	0.10
55	5.13	1.23	0.96	0.77	0.65	0.52	0.44	0.37	0.31	0.27	0.23	0.20	0.19	0.17	0.16	0.15	0.15	0.14	0.14	0.14	0.14	0.14	0.14
60	4.44	1.33	1.06	0.86	0.72	0.57	0.48	0.41	0.37	0.32	0.26	0.24	0.20	0.17	0.15	0.14	0.12	0.11	0.10	0.09	0.09	0.08	0.07

Table 7 presents the RMSE values for the case where the signals are uncorrelated. Table 7 refers to Figure 12.

Table 7 – RMSE of 1000 experiments for the 2_i-norm estimator considering uncorrelated signals.

(°)↓ dB→	−12.5	−11.25	−10	−8.75	−7.5	−6.25	−5	−3.75	−2.5	−1.25	0	1.25	2.5	3.75	5	6.25	7.5	8.75	10	11.25	12.5	13.75	15
−40	4.05	2.00	0.80	0.63	0.52	0.44	0.38	0.32	0.29	0.25	0.22	0.20	0.17	0.16	0.15	0.14	0.13	0.12	0.12	0.12	0.11	0.11	0.12
−35	3.57	0.96	0.76	0.60	0.49	0.42	0.35	0.29	0.25	0.21	0.19	0.17	0.16	0.16	0.15	0.14	0.14	0.14	0.15	0.15	0.15	0.16	0.15
−30	2.51	1.93	0.72	0.59	0.49	0.39	0.34	0.29	0.24	0.21	0.18	0.17	0.14	0.12	0.11	0.09	0.09	0.07	0.06	0.05	0.05	0.04	0.04
−25	3.26	0.90	0.72	0.57	0.47	0.38	0.33	0.28	0.25	0.21	0.18	0.17	0.15	0.13	0.13	0.12	0.11	0.11	0.11	0.11	0.11	0.11	0.11
−20	3.37	1.26	0.72	0.57	0.46	0.39	0.32	0.28	0.23	0.21	0.18	0.17	0.16	0.14	0.15	0.14	0.14	0.14	0.14	0.14	0.13	0.13	0.12
−15	3.43	0.90	0.72	0.57	0.48	0.38	0.33	0.27	0.23	0.20	0.18	0.16	0.15	0.14	0.14	0.14	0.13	0.13	0.13	0.13	0.12	0.13	0.12
−10	5.03	0.88	0.73	0.57	0.48	0.39	0.32	0.28	0.24	0.21	0.18	0.17	0.16	0.15	0.15	0.15	0.14	0.14	0.14	0.14	0.14	0.14	0.14
−5	4.55	2.04	0.70	0.57	0.46	0.39	0.34	0.28	0.24	0.22	0.19	0.16	0.15	0.13	0.12	0.11	0.10	0.09	0.08	0.07	0.07	0.06	0.06
0	19.50	15.43	8.67	3.81	0.74	0.50	0.42	0.35	0.30	0.26	0.22	0.19	0.17	0.15	0.13	0.11	0.10	0.10	0.09	0.09	0.08	0.08	0.08
5	19.24	9.74	3.93	1.88	1.55	1.21	0.93	0.83	0.65	0.57	0.46	0.38	0.33	0.29	0.24	0.21	0.18	0.16	0.14	0.12	0.10	0.09	0.08
15	20.20	10.50	4.02	1.91	1.60	1.27	1.03	0.86	0.69	0.58	0.48	0.41	0.34	0.29	0.25	0.22	0.18	0.16	0.14	0.12	0.11	0.10	0.08
20	22.27	17.67	11.27	4.49	0.65	0.53	0.45	0.39	0.31	0.26	0.23	0.20	0.17	0.15	0.13	0.12	0.11	0.10	0.09	0.08	0.08	0.07	0.07
25	5.86	2.83	0.75	0.61	0.49	0.41	0.35	0.30	0.26	0.23	0.21	0.20	0.19	0.18	0.18	0.18	0.18	0.19	0.19	0.19	0.19	0.20	0.20
30	5.13	1.98	0.76	0.61	0.50	0.42	0.36	0.30	0.26	0.22	0.21	0.18	0.17	0.16	0.15	0.14	0.14	0.14	0.13	0.13	0.12	0.13	0.12
35	3.71	1.14	0.78	0.64	0.53	0.42	0.37	0.30	0.26	0.23	0.20	0.19	0.18	0.17	0.17	0.17	0.17	0.17	0.18	0.18	0.19	0.18	0.18
40	4.72	1.06	0.79	0.65	0.52	0.46	0.38	0.31	0.26	0.23	0.21	0.18	0.17	0.15	0.16	0.15	0.16	0.16	0.17	0.17	0.17	0.17	0.17
45	3.12	2.99	0.84	0.67	0.55	0.46	0.40	0.33	0.27	0.24	0.21	0.20	0.18	0.18	0.18	0.18	0.18	0.18	0.19	0.19	0.19	0.19	0.19
50	4.18	2.06	0.90	0.72	0.59	0.47	0.41	0.35	0.30	0.26	0.23	0.19	0.17	0.15	0.14	0.13	0.12	0.12	0.11	0.11	0.11	0.11	0.11
55	5.11	1.24	0.96	0.77	0.65	0.52	0.44	0.37	0.31	0.27	0.23	0.20	0.19	0.17	0.17	0.15	0.15	0.15	0.14	0.14	0.14	0.14	0.14
60	4.44	1.33	1.06	0.87	0.72	0.57	0.48	0.41	0.37	0.32	0.26	0.24	0.20	0.17	0.15	0.14	0.12	0.11	0.10	0.09	0.09	0.08	0.07

Table 8 presents the RMSE values for the case where the signals are uncorrelated. Table 8 refers to Figure 13.

Table 8 – RMSE of 1000 experiments for the Improved SEAD estimator considering uncorrelated signals.

(°)↓ dB→	−12.5	−11.25	−10	−8.75	−7.5	−6.25	−5	−3.75	−2.5	−1.25	0	1.25	2.5	3.75	5	6.25	7.5	8.75	10	11.25	12.5	13.75	15
−40	5.43	2.88	0.81	2.26	1.66	1.07	0.38	0.33	0.29	0.26	0.23	0.20	0.18	0.17	0.16	0.15	0.14	0.14	0.13	0.13	0.13	0.13	0.14
−35	4.28	2.71	1.98	1.18	0.49	0.42	0.35	0.29	0.26	0.22	0.21	0.18	0.18	0.17	0.17	0.16	0.16	0.16	0.16	0.16	0.17	0.17	0.17
−30	4.11	3.16	2.21	0.59	0.96	0.85	0.34	0.29	0.24	0.22	0.18	0.16	0.14	0.12	0.11	0.09	0.09	0.08	0.07	0.06	0.05	0.05	0.05
−25	3.75	2.37	2.01	1.43	1.16	0.38	0.34	0.29	0.25	0.21	0.19	0.17	0.16	0.15	0.14	0.14	0.13	0.13	0.13	0.13	0.13	0.13	0.14
−20	3.74	1.69	0.72	0.58	0.46	0.39	0.32	0.28	0.24	0.21	0.19	0.17	0.17	0.16	0.16	0.16	0.16	0.16	0.15	0.16	0.15	0.15	0.15
−15	3.64	2.04	1.37	0.70	0.48	0.39	0.34	0.28	0.24	0.21	0.19	0.18	0.16	0.16	0.16	0.16	0.15	0.16	0.16	0.16	0.15	0.15	0.15
−10	5.17	1.28	0.73	0.73	0.58	0.60	0.33	0.29	0.25	0.21	0.19	0.17	0.15	0.15	0.14	0.14	0.14	0.13	0.14	0.14	0.13	0.13	0.13
−5	4.72	3.11	0.70	0.61	0.46	0.39	0.33	0.28	0.24	0.21	0.18	0.15	0.14	0.13	0.11	0.10	0.09	0.08	0.08	0.07	0.06	0.06	0.05
0	17.07	12.42	6.50	3.14	0.86	0.50	0.42	0.35	0.29	0.26	0.22	0.19	0.16	0.14	0.12	0.10	0.09	0.09	0.08	0.07	0.06	0.06	0.05
5	10.25	3.93	2.17	1.83	1.52	1.20	0.93	0.83	0.65	0.56	0.46	0.38	0.33	0.29	0.24	0.21	0.18	0.15	0.14	0.12	0.11	0.09	0.08
15	10.79	4.13	2.24	1.84	1.58	1.25	1.03	0.86	0.69	0.58	0.48	0.41	0.34	0.29	0.25	0.22	0.18	0.16	0.14	0.12	0.11	0.10	0.08
20	18.95	12.19	7.52	2.63	0.68	0.54	0.45	0.38	0.31	0.26	0.23	0.20	0.17	0.15	0.13	0.12	0.10	0.09	0.08	0.07	0.07	0.06	0.06
25	6.52	2.60	0.86	0.64	0.48	0.40	0.34	0.29	0.26	0.24	0.22	0.20	0.19	0.18	0.18	0.18	0.18	0.18	0.18	0.18	0.18	0.18	0.18
30	4.62	1.75	1.08	0.94	0.51	0.43	0.38	0.32	0.29	0.27	0.26	0.24	0.23	0.23	0.23	0.23	0.23	0.23	0.23	0.23	0.23	0.23	0.23
35	4.96	1.56	1.40	0.88	0.53	0.68	0.37	0.31	0.28	0.25	0.23	0.21	0.20	0.20	0.19	0.20	0.19	0.19	0.20	0.20	0.20	0.20	0.21
40	4.49	1.12	1.05	0.95	0.52	0.45	0.37	0.31	0.27	0.23	0.21	0.19	0.18	0.17	0.18	0.17	0.18	0.18	0.18	0.18	0.19	0.19	0.19
45	4.27	2.83	2.02	1.06	0.55	0.47	0.40	0.34	0.28	0.25	0.23	0.21	0.20	0.20	0.20	0.20	0.21	0.21	0.21	0.21	0.22	0.21	0.22
50	5.88	3.31	2.02	1.84	0.59	0.49	0.41	0.35	0.31	0.26	0.23	0.19	0.18	0.16	0.15	0.14	0.13	0.13	0.13	0.13	0.13	0.13	0.13
55	5.49	3.29	1.56	1.48	1.47	0.52	0.44	0.37	0.32	0.28	0.25	0.22	0.20	0.20	0.19	0.18	0.18	0.17	0.17	0.17	0.17	0.17	0.17
60	5.12	3.07	2.34	0.87	1.61	0.57	0.49	0.42	0.37	0.33	0.27	0.24	0.20	0.18	0.15	0.14	0.13	0.11	0.11	0.10	0.09	0.08	0.08

Table 9 presents the RMSE values for the case where the signals are uncorrelated. Table 9 refers to Figure 14.

Table 9 – RMSE of 1000 experiments for the MODEX estimator considering uncorrelated signals.

$(^\circ)\downarrow$ $dB\rightarrow$	−12.5	−11.25	−10	−8.75	−7.5	−6.25	−5	−3.75	−2.5	−1.25	0	1.25	2.5	3.75	5	6.25	7.5	8.75	10	11.25	12.5	13.75	15
−40	3.95	1.84	0.91	0.67	0.54	0.44	0.36	0.29	0.26	0.21	0.18	0.15	0.12	0.11	0.10	0.08	0.07	0.06	0.05	0.05	0.04	0.03	0.03
−35	4.46	1.12	0.83	0.63	0.49	0.42	0.34	0.27	0.24	0.20	0.17	0.15	0.13	0.11	0.09	0.08	0.07	0.06	0.05	0.05	0.04	0.03	0.03
−30	3.31	2.20	0.76	0.59	0.49	0.39	0.32	0.27	0.22	0.19	0.16	0.14	0.12	0.10	0.09	0.08	0.07	0.06	0.05	0.04	0.04	0.03	0.03
−25	3.68	1.41	0.78	0.59	0.48	0.38	0.32	0.27	0.23	0.19	0.16	0.14	0.12	0.10	0.09	0.08	0.07	0.06	0.05	0.04	0.04	0.03	0.03
−20	4.10	1.40	0.81	0.60	0.47	0.38	0.30	0.26	0.22	0.19	0.15	0.14	0.12	0.10	0.09	0.07	0.06	0.06	0.05	0.04	0.04	0.03	0.03
−15	3.81	1.36	0.80	0.61	0.49	0.38	0.32	0.26	0.22	0.19	0.16	0.14	0.11	0.10	0.09	0.07	0.06	0.05	0.05	0.04	0.03	0.03	0.03
−10	5.39	1.35	0.80	0.60	0.48	0.39	0.32	0.26	0.22	0.19	0.16	0.14	0.12	0.10	0.09	0.07	0.06	0.05	0.05	0.04	0.04	0.03	0.03
−5	4.55	1.12	0.78	0.62	0.47	0.39	0.32	0.26	0.22	0.18	0.15	0.13	0.12	0.10	0.08	0.07	0.06	0.05	0.05	0.04	0.04	0.03	0.03
0	6.96	3.64	1.67	1.04	0.74	0.58	0.46	0.37	0.30	0.26	0.22	0.18	0.16	0.13	0.11	0.09	0.08	0.08	0.06	0.06	0.05	0.04	0.04
5	20.39	17.35	13.65	9.30	4.67	2.12	1.70	1.43	1.17	0.96	0.71	0.50	0.40	0.34	0.26	0.21	0.18	0.15	0.13	0.12	0.10	0.08	0.12
15	22.42	18.12	14.17	9.98	6.21	2.77	1.67	1.44	1.22	1.05	0.85	0.64	0.46	0.37	0.31	0.24	0.20	0.17	0.14	0.12	0.10	0.09	0.07
20	5.71	3.59	1.58	1.26	0.94	0.74	0.61	0.46	0.37	0.29	0.25	0.21	0.17	0.15	0.12	0.11	0.09	0.08	0.07	0.06	0.05	0.04	0.04
25	4.73	1.65	0.93	0.72	0.58	0.49	0.38	0.30	0.25	0.20	0.17	0.14	0.12	0.11	0.09	0.08	0.07	0.06	0.05	0.04	0.04	0.03	0.03
30	5.46	2.06	0.98	0.68	0.55	0.45	0.36	0.30	0.24	0.20	0.17	0.15	0.13	0.11	0.09	0.08	0.07	0.06	0.05	0.04	0.04	0.03	0.03
35	5.69	1.79	1.24	0.90	0.70	0.54	0.43	0.32	0.26	0.22	0.18	0.16	0.13	0.11	0.10	0.08	0.07	0.06	0.05	0.05	0.04	0.03	0.03
40	6.88	2.78	1.51	1.26	0.99	0.74	0.54	0.37	0.29	0.23	0.20	0.16	0.13	0.11	0.10	0.09	0.07	0.06	0.05	0.05	0.04	0.04	0.03
45	6.55	4.50	1.54	1.23	1.03	0.82	0.65	0.45	0.34	0.27	0.22	0.18	0.15	0.13	0.11	0.09	0.08	0.07	0.06	0.05	0.04	0.04	0.03
50	5.17	2.90	1.34	1.10	0.93	0.75	0.62	0.51	0.39	0.32	0.26	0.20	0.18	0.15	0.12	0.10	0.09	0.08	0.06	0.06	0.05	0.04	0.04
55	5.92	1.90	1.89	1.01	0.89	0.68	0.58	0.55	0.44	0.39	0.28	0.27	0.22	0.19	0.16	0.14	0.12	0.10	0.09	0.07	0.06	0.05	0.05
60	6.26	1.88	1.46	1.19	1.02	0.77	0.67	0.54	0.45	0.38	0.30	0.25	0.22	0.18	0.15	0.13	0.11	0.09	0.08	0.07	0.06	0.05	0.04

Table 10 presents the RMSE values for the case where the signals are uncorrelated. Table 10 refers to Figure 15.

Table 10 – RMSE of 1000 experiments for the Modified MODEX estimator considering uncorrelated signals.

$(°)\downarrow$ $dB\rightarrow$	−12.5	−11.25	−10	−8.75	−7.5	−6.25	−5	−3.75	−2.5	−1.25	0	1.25	2.5	3.75	5	6.25	7.5	8.75	10	11.25	12.5	13.75	15
−40	10.08	4.08	1.66	0.64	0.52	0.43	0.36	0.29	0.26	0.21	0.18	0.15	0.12	0.11	0.10	0.08	0.07	0.06	0.05	0.05	0.04	0.04	0.03
−35	8.19	3.33	0.82	0.62	0.49	0.41	0.34	0.27	0.23	0.19	0.17	0.15	0.13	0.11	0.09	0.08	0.07	0.06	0.05	0.05	0.04	0.03	0.03
−30	7.89	3.81	1.24	0.60	0.49	0.38	0.32	0.27	0.22	0.19	0.16	0.14	0.12	0.10	0.09	0.08	0.07	0.06	0.05	0.04	0.04	0.03	0.03
−25	8.44	3.27	0.81	0.59	0.47	0.37	0.32	0.27	0.23	0.19	0.16	0.14	0.12	0.10	0.09	0.08	0.07	0.06	0.05	0.04	0.04	0.03	0.03
−20	6.74	3.08	0.83	0.58	0.45	0.37	0.30	0.26	0.22	0.18	0.15	0.14	0.12	0.10	0.09	0.07	0.06	0.06	0.05	0.04	0.04	0.03	0.03
−15	5.69	2.07	1.00	0.59	0.47	0.37	0.32	0.26	0.22	0.19	0.16	0.14	0.11	0.10	0.09	0.07	0.06	0.05	0.05	0.04	0.03	0.03	0.03
−10	6.07	2.86	1.52	0.59	0.47	0.38	0.31	0.26	0.22	0.18	0.16	0.13	0.12	0.10	0.09	0.07	0.06	0.05	0.05	0.04	0.04	0.03	0.03
−5	6.50	3.60	1.66	0.63	0.46	0.38	0.32	0.25	0.22	0.18	0.15	0.13	0.11	0.10	0.08	0.07	0.06	0.05	0.05	0.04	0.04	0.03	0.03
0	5.52	3.13	2.08	1.35	0.85	0.56	0.45	0.36	0.29	0.25	0.21	0.18	0.16	0.13	0.11	0.09	0.08	0.08	0.06	0.06	0.05	0.04	0.04
5	15.14	13.18	9.19	6.14	3.38	2.13	1.50	1.24	0.85	0.63	0.49	0.39	0.34	0.29	0.24	0.21	0.17	0.15	0.13	0.12	0.10	0.08	0.07
15	15.35	12.21	10.01	6.44	3.77	2.34	1.53	1.16	0.83	0.64	0.51	0.42	0.35	0.29	0.25	0.22	0.18	0.16	0.14	0.12	0.10	0.09	0.07
20	5.70	3.64	2.36	1.32	0.79	0.58	0.46	0.38	0.31	0.26	0.22	0.19	0.16	0.14	0.12	0.11	0.09	0.08	0.07	0.06	0.05	0.04	0.04
25	9.18	4.85	2.21	0.64	0.49	0.39	0.33	0.27	0.23	0.19	0.17	0.14	0.12	0.10	0.09	0.08	0.07	0.06	0.05	0.04	0.04	0.03	0.03
30	8.05	3.33	1.13	0.61	0.49	0.40	0.34	0.28	0.23	0.19	0.17	0.14	0.12	0.11	0.09	0.08	0.07	0.06	0.05	0.04	0.04	0.03	0.03
35	7.21	2.28	0.86	0.67	0.53	0.41	0.36	0.29	0.24	0.21	0.18	0.15	0.13	0.11	0.10	0.08	0.07	0.06	0.05	0.05	0.04	0.03	0.03
40	7.84	2.67	0.90	0.66	0.50	0.43	0.35	0.29	0.24	0.20	0.18	0.15	0.13	0.11	0.10	0.08	0.07	0.06	0.05	0.05	0.04	0.04	0.03
45	8.77	3.86	1.06	0.68	0.54	0.44	0.37	0.31	0.26	0.22	0.19	0.16	0.14	0.12	0.10	0.09	0.08	0.07	0.06	0.05	0.04	0.04	0.03
50	8.25	4.73	0.96	0.72	0.58	0.47	0.39	0.33	0.28	0.24	0.20	0.17	0.15	0.13	0.11	0.09	0.08	0.07	0.06	0.05	0.05	0.04	0.04
55	11.21	4.23	1.26	0.77	0.64	0.51	0.43	0.35	0.30	0.25	0.22	0.18	0.16	0.14	0.12	0.10	0.09	0.08	0.07	0.06	0.05	0.04	0.04
60	12.45	4.78	2.07	0.87	0.70	0.56	0.46	0.39	0.34	0.29	0.23	0.21	0.18	0.15	0.13	0.11	0.10	0.08	0.07	0.06	0.05	0.05	0.04

C.2 Correlated Sources

A series of 1000 experiments was performed and the RMSE of the estimates are presented in tabular form for the several assessed methods: 1-norm, 1_i-norm, 2-norm, 2_i-norm, Improved SEAD, MODEX, and Modified MODEX. The sources are assumed to be correlated, with correlation factor $\rho_{\alpha\beta} = 0.9$.

Table 11 presents the RMSE values for the case where the signals are correlated. Table 11 refers to Figure 16.

Table 11 – RMSE of 1000 experiments for the 1-norm estimator considering correlated signals.

$(^\circ)\downarrow$ $dB\rightarrow$	−12.5	−11.25	−10	−8.75	−7.5	−6.25	−5	−3.75	−2.5	−1.25	0	1.25	2.5	3.75	5	6.25	7.5	8.75	10	11.25	12.5	13.75	15
−40	3.85	1.57	0.80	0.64	0.55	0.46	0.40	0.34	0.30	0.25	0.24	0.21	0.20	0.20	0.19	0.20	0.20	0.20	0.20	0.20	0.21	0.21	0.21
−35	3.88	1.10	0.76	0.62	0.50	0.43	0.36	0.31	0.26	0.23	0.22	0.20	0.20	0.19	0.18	0.18	0.18	0.18	0.18	0.18	0.18	0.19	0.19
−30	3.89	1.10	0.81	0.67	0.52	0.45	0.37	0.31	0.28	0.22	0.18	0.16	0.14	0.11	0.10	0.09	0.08	0.07	0.07	0.07	0.06	0.06	0.06
−25	4.03	1.55	0.72	0.60	0.51	0.43	0.36	0.32	0.29	0.24	0.20	0.19	0.17	0.15	0.13	0.12	0.11	0.08	0.07	0.06	0.06	0.06	0.06
−20	3.37	0.95	0.74	0.62	0.48	0.40	0.34	0.29	0.25	0.22	0.21	0.19	0.18	0.19	0.19	0.19	0.20	0.20	0.20	0.20	0.21	0.21	0.21
−15	4.27	1.19	1.29	0.60	0.51	0.42	0.35	0.32	0.27	0.24	0.21	0.19	0.17	0.15	0.15	0.14	0.14	0.14	0.14	0.14	0.14	0.14	0.14
−10	3.85	1.24	0.70	0.57	0.47	0.38	0.32	0.27	0.25	0.21	0.19	0.17	0.16	0.14	0.13	0.13	0.12	0.11	0.11	0.11	0.11	0.11	0.11
−5	5.59	1.72	1.21	0.93	0.70	0.58	0.48	0.39	0.33	0.29	0.25	0.23	0.20	0.19	0.18	0.17	0.16	0.16	0.15	0.14	0.14	0.14	0.14
0	9.91	3.01	1.92	1.01	0.82	0.71	0.56	0.50	0.42	0.35	0.29	0.24	0.22	0.18	0.16	0.15	0.13	0.13	0.12	0.12	0.11	0.11	0.11
5	12.05	4.99	2.60	2.12	1.71	1.47	1.18	0.93	0.77	0.63	0.51	0.43	0.36	0.30	0.26	0.22	0.19	0.17	0.14	0.13	0.11	0.09	0.08
15	11.22	5.21	2.50	2.21	1.90	1.53	1.24	1.03	0.81	0.65	0.54	0.45	0.38	0.31	0.27	0.23	0.19	0.17	0.14	0.13	0.11	0.10	0.09
20	11.58	5.27	1.33	1.02	0.84	0.73	0.60	0.50	0.41	0.34	0.30	0.25	0.22	0.18	0.16	0.14	0.12	0.11	0.10	0.09	0.09	0.09	0.08
25	5.96	2.35	1.46	1.14	0.89	0.71	0.54	0.48	0.38	0.34	0.30	0.28	0.27	0.26	0.24	0.22	0.20	0.19	0.18	0.16	0.15	0.15	0.14
30	4.91	1.42	0.76	0.62	0.50	0.41	0.36	0.31	0.27	0.25	0.22	0.20	0.20	0.19	0.19	0.19	0.19	0.19	0.19	0.20	0.19	0.20	0.20
35	6.38	2.14	0.79	0.65	0.54	0.44	0.38	0.34	0.31	0.27	0.25	0.25	0.24	0.22	0.22	0.21	0.20	0.20	0.19	0.19	0.19	0.18	0.18
40	4.63	2.06	0.89	0.73	0.61	0.50	0.42	0.34	0.30	0.25	0.23	0.21	0.20	0.19	0.19	0.19	0.19	0.20	0.20	0.20	0.20	0.20	0.21
45	4.92	1.10	0.84	0.71	0.54	0.46	0.39	0.34	0.30	0.27	0.25	0.24	0.24	0.24	0.24	0.24	0.25	0.25	0.25	0.25	0.25	0.25	0.25
50	5.57	1.21	0.88	0.71	0.60	0.50	0.44	0.38	0.34	0.31	0.29	0.27	0.26	0.25	0.25	0.24	0.24	0.24	0.25	0.25	0.25	0.25	0.25
55	6.14	2.54	1.05	0.82	0.65	0.55	0.46	0.40	0.36	0.32	0.29	0.27	0.26	0.24	0.22	0.21	0.20	0.19	0.18	0.18	0.17	0.17	0.17
60	5.91	2.64	1.17	0.97	0.77	0.66	0.55	0.49	0.40	0.35	0.31	0.26	0.22	0.20	0.19	0.18	0.17	0.17	0.17	0.17	0.17	0.17	0.17

The Table 12 presents the RMSE values for the case where the signals are correlated. Table 12 refers to Figure 17.

Table 12 – RMSE of 1000 experiments for the 1_i-norm estimator considering correlated signals.

$(^\circ)\downarrow$ $dB\rightarrow$	−12.5	−11.25	−10	−8.75	−7.5	−6.25	−5	−3.75	−2.5	−1.25	0	1.25	2.5	3.75	5	6.25	7.5	8.75	10	11.25	12.5	13.75	15
−40	4.45	1.58	0.80	0.64	0.55	0.46	0.39	0.33	0.30	0.25	0.22	0.19	0.17	0.16	0.14	0.13	0.13	0.12	0.11	0.10	0.10	0.10	0.10
−35	3.89	1.51	0.77	0.62	0.50	0.44	0.37	0.32	0.27	0.24	0.22	0.21	0.20	0.17	0.18	0.17	0.16	0.16	0.16	0.16	0.16	0.17	0.17
−30	3.24	0.99	0.80	0.67	0.53	0.46	0.38	0.32	0.29	0.24	0.19	0.17	0.15	0.13	0.12	0.10	0.09	0.08	0.08	0.07	0.07	0.06	0.06
−25	3.29	1.57	0.71	0.59	0.49	0.41	0.35	0.29	0.26	0.21	0.18	0.16	0.14	0.12	0.10	0.09	0.08	0.07	0.07	0.06	0.06	0.06	0.05
−20	3.18	1.21	0.74	0.62	0.48	0.40	0.34	0.29	0.25	0.21	0.19	0.16	0.15	0.15	0.14	0.14	0.14	0.13	0.13	0.13	0.13	0.13	0.13
−15	4.43	1.20	0.79	0.61	0.51	0.42	0.35	0.30	0.25	0.23	0.21	0.19	0.18	0.17	0.17	0.16	0.16	0.16	0.16	0.16	0.16	0.16	0.16
−10	3.96	1.13	0.71	0.58	0.48	0.40	0.33	0.28	0.25	0.22	0.20	0.18	0.16	0.15	0.15	0.14	0.13	0.13	0.13	0.13	0.13	0.13	0.13
−5	4.95	1.93	1.20	0.93	0.71	0.60	0.50	0.41	0.35	0.30	0.27	0.24	0.21	0.19	0.16	0.14	0.13	0.11	0.10	0.09	0.08	0.07	0.07
0	8.25	3.23	1.44	1.09	0.87	0.74	0.58	0.50	0.42	0.36	0.29	0.24	0.22	0.18	0.17	0.15	0.13	0.12	0.11	0.10	0.09	0.09	0.08
5	21.90	14.57	6.93	3.90	1.80	1.50	1.18	0.93	0.78	0.63	0.51	0.43	0.36	0.30	0.25	0.22	0.19	0.17	0.14	0.13	0.11	0.09	0.08
15	21.48	14.42	7.42	3.58	1.90	1.63	1.24	1.03	0.81	0.65	0.54	0.45	0.38	0.31	0.27	0.23	0.20	0.18	0.15	0.13	0.11	0.10	0.09
20	9.80	3.38	1.53	1.08	0.88	0.76	0.62	0.50	0.42	0.35	0.30	0.26	0.22	0.19	0.17	0.15	0.13	0.12	0.11	0.10	0.09	0.09	0.08
25	5.89	2.17	1.68	1.15	0.91	0.74	0.58	0.52	0.42	0.36	0.32	0.29	0.26	0.25	0.24	0.21	0.20	0.19	0.18	0.17	0.16	0.15	0.15
30	3.47	1.52	0.75	0.62	0.51	0.42	0.37	0.33	0.29	0.28	0.26	0.26	0.26	0.25	0.25	0.25	0.25	0.24	0.24	0.24	0.24	0.24	0.24
35	5.73	2.29	1.44	0.66	0.53	0.44	0.37	0.33	0.29	0.27	0.24	0.24	0.23	0.22	0.21	0.21	0.21	0.20	0.20	0.20	0.20	0.19	0.19
40	4.87	1.90	0.89	0.73	0.63	0.52	0.44	0.36	0.32	0.26	0.25	0.20	0.17	0.16	0.14	0.13	0.12	0.11	0.11	0.11	0.11	0.11	0.10
45	5.09	1.10	0.85	0.72	0.56	0.47	0.40	0.35	0.28	0.25	0.23	0.20	0.20	0.19	0.19	0.20	0.20	0.20	0.20	0.20	0.20	0.20	0.20
50	6.03	1.23	0.89	0.71	0.62	0.49	0.43	0.37	0.31	0.27	0.23	0.21	0.20	0.20	0.19	0.19	0.19	0.19	0.19	0.20	0.20	0.20	0.20
55	5.16	2.57	1.06	0.83	0.64	0.55	0.46	0.40	0.34	0.30	0.27	0.24	0.23	0.21	0.20	0.19	0.19	0.19	0.19	0.19	0.19	0.19	0.19
60	6.07	1.57	1.15	0.94	0.75	0.64	0.54	0.48	0.38	0.34	0.29	0.25	0.21	0.20	0.19	0.17	0.16	0.16	0.15	0.15	0.15	0.14	0.14

Table 13 presents the RMSE values for the case where the signals are correlated. Table 13 refers to Figure 18.

Table 13 – RMSE of 1000 experiments for the 2-norm estimator considering correlated signals.

$(^\circ)\downarrow$ $dB\rightarrow$	−12.5	−11.25	−10	−8.75	−7.5	−6.25	−5	−3.75	−2.5	−1.25	0	1.25	2.5	3.75	5	6.25	7.5	8.75	10	11.25	12.5	13.75	15
−40	3.73	1.57	0.79	0.64	0.55	0.46	0.40	0.33	0.30	0.24	0.21	0.19	0.17	0.15	0.14	0.14	0.14	0.13	0.13	0.12	0.12	0.12	0.12
−35	3.88	1.10	0.76	0.61	0.50	0.43	0.36	0.31	0.26	0.23	0.21	0.20	0.19	0.18	0.18	0.18	0.18	0.19	0.19	0.19	0.18	0.19	0.18
−30	3.89	1.19	0.80	0.67	0.52	0.46	0.37	0.31	0.28	0.23	0.19	0.16	0.14	0.12	0.11	0.09	0.08	0.08	0.07	0.07	0.06	0.06	0.06
−25	4.03	1.55	0.71	0.60	0.50	0.42	0.36	0.29	0.26	0.20	0.15	0.13	0.11	0.09	0.09	0.08	0.08	0.08	0.08	0.08	0.08	0.08	0.08
−20	3.35	0.95	0.74	0.62	0.48	0.40	0.33	0.29	0.25	0.21	0.19	0.17	0.17	0.16	0.16	0.16	0.15	0.15	0.15	0.15	0.15	0.15	0.15
−15	4.21	1.19	1.29	0.60	0.50	0.41	0.35	0.30	0.26	0.23	0.21	0.20	0.18	0.17	0.15	0.15	0.14	0.12	0.12	0.11	0.11	0.10	0.10
−10	3.80	1.24	0.70	0.57	0.47	0.38	0.32	0.27	0.24	0.21	0.19	0.16	0.15	0.13	0.12	0.12	0.11	0.11	0.11	0.11	0.11	0.11	0.11
−5	5.62	1.72	1.20	0.93	0.71	0.58	0.49	0.39	0.34	0.29	0.27	0.23	0.20	0.20	0.17	0.16	0.15	0.13	0.12	0.11	0.10	0.10	0.10
0	9.91	3.24	1.98	1.01	0.82	0.71	0.56	0.49	0.42	0.35	0.29	0.24	0.22	0.18	0.16	0.15	0.13	0.12	0.12	0.11	0.11	0.10	0.09
5	12.24	5.17	2.59	2.12	1.72	1.47	1.19	0.93	0.77	0.63	0.52	0.43	0.36	0.30	0.25	0.22	0.19	0.17	0.14	0.13	0.11	0.09	0.08
15	11.29	5.20	2.48	2.21	1.91	1.54	1.24	1.03	0.81	0.65	0.54	0.45	0.38	0.31	0.27	0.23	0.20	0.17	0.15	0.13	0.11	0.10	0.09
20	11.63	5.38	1.33	1.02	0.84	0.73	0.60	0.50	0.41	0.34	0.30	0.25	0.22	0.18	0.16	0.14	0.12	0.11	0.10	0.10	0.09	0.09	0.08
25	5.96	2.36	1.46	1.14	0.90	0.72	0.55	0.49	0.40	0.35	0.31	0.28	0.26	0.26	0.23	0.21	0.20	0.19	0.17	0.16	0.16	0.15	0.14
30	4.91	1.42	0.76	0.62	0.50	0.41	0.35	0.31	0.26	0.23	0.20	0.18	0.16	0.14	0.12	0.12	0.11	0.10	0.10	0.09	0.09	0.08	0.07
35	6.37	2.14	0.79	0.65	0.53	0.44	0.37	0.33	0.30	0.27	0.24	0.23	0.22	0.21	0.21	0.20	0.20	0.19	0.19	0.18	0.18	0.18	0.18
40	4.88	2.06	0.89	0.73	0.61	0.49	0.41	0.34	0.30	0.24	0.23	0.21	0.19	0.18	0.18	0.18	0.18	0.18	0.18	0.18	0.18	0.18	0.18
45	4.91	1.09	0.84	0.71	0.54	0.46	0.39	0.34	0.29	0.26	0.24	0.22	0.21	0.21	0.21	0.21	0.21	0.21	0.22	0.22	0.22	0.22	0.22
50	5.55	1.21	0.88	0.71	0.59	0.49	0.43	0.37	0.33	0.31	0.28	0.26	0.24	0.23	0.23	0.22	0.22	0.22	0.22	0.23	0.23	0.23	0.24
55	6.18	2.55	1.05	0.81	0.64	0.55	0.46	0.39	0.35	0.31	0.28	0.26	0.24	0.22	0.20	0.19	0.18	0.18	0.18	0.18	0.17	0.17	0.17
60	5.91	1.60	1.18	0.97	0.78	0.67	0.56	0.50	0.40	0.35	0.30	0.26	0.21	0.18	0.17	0.14	0.13	0.12	0.11	0.11	0.11	0.10	0.09

Table 14 presents the RMSE values for the case where the signals are correlated. Table 14 refers to Figure 19.

Table 14 – RMSE of 1000 experiments for the 2_i-norm estimator considering correlated signals.

$dB\rightarrow$ $(^\circ)\downarrow$	−12.5	−11.25	−10	−8.75	−7.5	−6.25	−5	−3.75	−2.5	−1.25	0	1.25	2.5	3.75	5	6.25	7.5	8.75	10	11.25	12.5	13.75	15
−40	3.81	1.57	0.80	0.64	0.55	0.46	0.40	0.34	0.30	0.25	0.23	0.20	0.18	0.17	0.16	0.16	0.16	0.15	0.15	0.14	0.14	0.14	0.14
−35	3.87	1.10	0.76	0.62	0.50	0.43	0.36	0.31	0.26	0.23	0.22	0.20	0.20	0.19	0.18	0.19	0.19	0.19	0.19	0.19	0.19	0.20	0.19
−30	3.89	1.19	0.81	0.67	0.52	0.46	0.37	0.31	0.28	0.22	0.18	0.16	0.14	0.11	0.10	0.09	0.07	0.07	0.07	0.06	0.06	0.06	0.06
−25	4.03	1.55	0.72	0.59	0.50	0.42	0.36	0.30	0.26	0.20	0.15	0.13	0.11	0.09	0.09	0.09	0.08	0.08	0.08	0.08	0.08	0.08	0.08
−20	3.49	0.95	0.74	0.62	0.48	0.40	0.33	0.29	0.25	0.21	0.20	0.18	0.17	0.17	0.16	0.16	0.16	0.16	0.16	0.15	0.15	0.15	0.15
−15	4.27	1.19	1.29	0.60	0.50	0.42	0.35	0.31	0.27	0.24	0.22	0.20	0.18	0.17	0.16	0.15	0.15	0.15	0.15	0.15	0.15	0.15	0.15
−10	3.85	1.24	0.70	0.57	0.47	0.38	0.32	0.27	0.25	0.21	0.19	0.17	0.16	0.14	0.13	0.12	0.11	0.11	0.11	0.11	0.11	0.11	0.11
−5	5.62	1.73	1.21	0.93	0.70	0.58	0.48	0.39	0.33	0.29	0.26	0.23	0.20	0.19	0.17	0.16	0.15	0.14	0.13	0.12	0.12	0.12	0.12
0	9.91	3.00	1.92	1.01	0.82	0.71	0.56	0.50	0.42	0.35	0.29	0.24	0.22	0.18	0.17	0.15	0.13	0.13	0.12	0.12	0.11	0.11	0.11
5	11.89	4.99	2.59	2.12	1.71	1.45	1.18	0.93	0.77	0.63	0.51	0.43	0.36	0.30	0.26	0.22	0.19	0.17	0.14	0.13	0.11	0.10	0.08
15	10.98	5.02	2.49	2.20	1.89	1.53	1.24	1.03	0.81	0.65	0.54	0.45	0.38	0.31	0.27	0.23	0.19	0.17	0.14	0.13	0.11	0.10	0.09
20	11.60	5.37	1.33	1.02	0.84	0.72	0.60	0.50	0.41	0.34	0.30	0.25	0.22	0.18	0.16	0.14	0.12	0.11	0.10	0.09	0.09	0.09	0.08
25	5.96	2.36	1.46	1.14	0.89	0.71	0.54	0.48	0.39	0.34	0.31	0.29	0.28	0.27	0.25	0.23	0.21	0.20	0.18	0.17	0.16	0.15	0.14
30	4.91	1.42	0.76	0.62	0.50	0.41	0.36	0.31	0.27	0.24	0.22	0.20	0.19	0.17	0.17	0.17	0.17	0.17	0.17	0.17	0.17	0.17	0.17
35	6.38	2.14	0.79	0.65	0.53	0.44	0.37	0.34	0.30	0.28	0.25	0.25	0.24	0.22	0.22	0.21	0.20	0.20	0.19	0.19	0.19	0.19	0.18
40	4.83	2.06	0.89	0.73	0.61	0.49	0.41	0.33	0.29	0.24	0.23	0.21	0.19	0.19	0.18	0.18	0.18	0.18	0.18	0.18	0.18	0.18	0.18
45	4.92	1.09	0.84	0.71	0.54	0.46	0.38	0.34	0.29	0.27	0.24	0.23	0.22	0.22	0.22	0.22	0.23	0.23	0.23	0.23	0.24	0.24	0.24
50	5.57	1.22	0.88	0.71	0.60	0.49	0.43	0.37	0.34	0.31	0.28	0.27	0.25	0.25	0.24	0.23	0.23	0.23	0.23	0.23	0.23	0.23	0.23
55	6.13	2.55	1.05	0.82	0.65	0.55	0.46	0.40	0.36	0.32	0.29	0.27	0.26	0.24	0.23	0.21	0.20	0.20	0.20	0.20	0.20	0.20	0.20
60	5.91	1.60	1.17	0.97	0.77	0.67	0.56	0.50	0.40	0.36	0.30	0.26	0.22	0.20	0.18	0.17	0.15	0.15	0.15	0.14	0.14	0.13	0.12

Table 15 presents the RMSE values for the case where the signals are correlated. Table 15 refers to Figure 20.

Table 15 – RMSE of 1000 experiments for the Improved SEAD estimator considering correlated signals.

$(°)\downarrow$ $dB\rightarrow$	−12.5	−11.25	−10	−8.75	−7.5	−6.25	−5	−3.75	−2.5	−1.25	0	1.25	2.5	3.75	5	6.25	7.5	8.75	10	11.25	12.5	13.75	15
−40	3.67	1.58	0.79	0.64	0.55	0.46	0.40	0.34	0.30	0.25	0.23	0.21	0.19	0.18	0.17	0.16	0.16	0.15	0.15	0.15	0.15	0.14	0.14
−35	4.03	1.11	0.76	0.62	0.49	0.43	0.36	0.31	0.26	0.23	0.22	0.20	0.20	0.19	0.18	0.19	0.19	0.19	0.19	0.19	0.19	0.19	0.19
−30	3.55	1.00	0.80	0.66	0.52	0.46	0.37	0.31	0.28	0.22	0.18	0.16	0.14	0.11	0.10	0.09	0.07	0.07	0.07	0.06	0.06	0.06	0.06
−25	3.88	0.95	0.71	0.58	0.49	0.42	0.36	0.30	0.26	0.20	0.15	0.13	0.11	0.09	0.09	0.08	0.08	0.08	0.08	0.08	0.08	0.08	0.08
−20	2.52	0.95	0.74	0.61	0.48	0.40	0.33	0.29	0.25	0.21	0.20	0.18	0.17	0.17	0.16	0.16	0.16	0.16	0.15	0.15	0.15	0.15	0.15
−15	4.36	0.98	0.78	0.60	0.50	0.41	0.35	0.31	0.27	0.24	0.22	0.20	0.18	0.17	0.16	0.15	0.15	0.14	0.14	0.14	0.14	0.14	0.15
−10	3.07	1.11	0.72	0.58	0.47	0.39	0.33	0.28	0.25	0.22	0.19	0.17	0.16	0.14	0.13	0.13	0.12	0.11	0.11	0.11	0.11	0.11	0.11
−5	4.97	1.47	1.20	0.94	0.70	0.58	0.48	0.38	0.33	0.28	0.25	0.23	0.20	0.20	0.18	0.17	0.17	0.16	0.15	0.14	0.14	0.14	0.14
0	9.11	2.62	1.18	0.99	0.80	0.70	0.56	0.49	0.41	0.35	0.29	0.25	0.22	0.18	0.17	0.15	0.13	0.13	0.12	0.11	0.11	0.11	0.10
5	4.56	2.76	2.42	2.07	1.68	1.45	1.18	0.93	0.77	0.63	0.51	0.43	0.35	0.30	0.26	0.22	0.19	0.17	0.14	0.13	0.11	0.10	0.08
15	4.32	2.72	2.41	2.15	1.87	1.53	1.24	1.03	0.81	0.65	0.54	0.45	0.38	0.31	0.27	0.23	0.19	0.17	0.14	0.13	0.11	0.10	0.09
20	10.18	3.70	1.30	0.99	0.82	0.71	0.59	0.49	0.40	0.34	0.30	0.25	0.22	0.18	0.16	0.14	0.12	0.12	0.10	0.10	0.09	0.09	0.09
25	4.58	1.67	1.45	1.15	0.89	0.72	0.54	0.48	0.38	0.33	0.29	0.28	0.26	0.25	0.23	0.22	0.20	0.19	0.18	0.16	0.15	0.15	0.14
30	3.50	1.39	0.77	0.62	0.51	0.41	0.36	0.32	0.28	0.25	0.23	0.21	0.20	0.19	0.19	0.19	0.19	0.19	0.20	0.20	0.20	0.20	0.20
35	5.21	2.11	0.78	0.65	0.53	0.44	0.37	0.33	0.29	0.26	0.23	0.22	0.21	0.19	0.19	0.18	0.18	0.17	0.16	0.16	0.16	0.16	0.16
40	4.24	1.54	0.89	0.73	0.61	0.49	0.41	0.33	0.30	0.24	0.23	0.21	0.19	0.19	0.18	0.18	0.18	0.18	0.18	0.18	0.18	0.18	0.18
45	4.27	1.10	0.85	0.71	0.55	0.46	0.39	0.33	0.29	0.26	0.24	0.23	0.22	0.22	0.22	0.22	0.23	0.23	0.23	0.23	0.24	0.24	0.24
50	5.28	2.42	0.88	0.70	0.59	0.49	0.43	0.38	0.34	0.32	0.29	0.28	0.26	0.26	0.25	0.24	0.24	0.24	0.24	0.23	0.23	0.24	0.23
55	5.30	2.39	1.05	0.81	0.64	0.55	0.46	0.40	0.35	0.32	0.29	0.27	0.25	0.24	0.23	0.21	0.20	0.19	0.19	0.19	0.18	0.18	0.18
60	4.88	1.58	1.16	0.96	0.77	0.67	0.56	0.50	0.40	0.35	0.31	0.26	0.22	0.20	0.19	0.17	0.16	0.15	0.15	0.14	0.14	0.14	0.13

Table 16 presents the RMSE values for the case where the signals are correlated. Table 16 refers to Figure 14.

Table 16 – RMSE of 1000 experiments for the MODEX estimator considering correlated signals.

$(^\circ)\downarrow$ $dB\rightarrow$	-12.5	-11.25	-10	-8.75	-7.5	-6.25	-5	-3.75	-2.5	-1.25	0	1.25	2.5	3.75	5	6.25	7.5	8.75	10	11.25	12.5	13.75	15
-40	3.77	1.65	0.84	0.67	0.54	0.43	0.36	0.30	0.25	0.21	0.18	0.15	0.13	0.11	0.09	0.08	0.07	0.06	0.05	0.05	0.04	0.03	0.03
-35	4.02	1.50	0.75	0.62	0.48	0.41	0.34	0.29	0.23	0.20	0.17	0.14	0.13	0.11	0.09	0.08	0.07	0.06	0.05	0.04	0.04	0.03	0.03
-30	3.75	1.09	0.75	0.61	0.49	0.41	0.34	0.28	0.25	0.20	0.17	0.14	0.13	0.11	0.09	0.08	0.07	0.06	0.05	0.05	0.04	0.03	0.03
-25	4.32	0.96	0.70	0.59	0.46	0.38	0.32	0.27	0.23	0.19	0.16	0.14	0.12	0.10	0.09	0.07	0.07	0.06	0.05	0.04	0.04	0.03	0.03
-20	3.17	1.22	0.74	0.59	0.46	0.38	0.32	0.27	0.22	0.19	0.16	0.13	0.11	0.10	0.09	0.08	0.06	0.06	0.05	0.04	0.04	0.03	0.03
-15	4.78	1.39	0.82	0.64	0.50	0.41	0.33	0.28	0.23	0.20	0.17	0.14	0.12	0.10	0.09	0.08	0.07	0.06	0.05	0.04	0.04	0.03	0.03
-10	3.50	1.20	0.73	0.58	0.47	0.38	0.31	0.26	0.22	0.19	0.16	0.13	0.12	0.10	0.08	0.07	0.07	0.05	0.05	0.04	0.04	0.03	0.03
-5	4.12	1.45	0.94	0.77	0.59	0.49	0.40	0.34	0.28	0.23	0.20	0.17	0.14	0.13	0.10	0.09	0.08	0.07	0.06	0.05	0.04	0.04	0.03
0	7.81	3.81	1.56	1.33	1.01	0.80	0.61	0.51	0.41	0.35	0.28	0.23	0.21	0.17	0.15	0.13	0.11	0.10	0.08	0.07	0.06	0.05	0.05
5	22.00	20.04	16.41	13.19	8.08	4.87	3.40	1.50	1.31	1.11	0.90	0.66	0.50	0.36	0.29	0.24	0.20	0.17	0.14	0.12	0.11	0.09	0.08
15	23.94	21.60	19.01	15.18	11.24	5.86	3.47	1.83	1.32	1.16	0.96	0.75	0.59	0.42	0.34	0.29	0.21	0.18	0.15	0.13	0.11	0.09	0.08
20	7.47	3.51	1.64	1.40	1.17	0.96	0.79	0.62	0.49	0.38	0.32	0.26	0.22	0.18	0.15	0.13	0.11	0.10	0.08	0.07	0.06	0.05	0.05
25	5.54	2.59	1.28	1.02	0.85	0.73	0.57	0.47	0.38	0.30	0.24	0.21	0.17	0.15	0.13	0.10	0.09	0.08	0.07	0.06	0.05	0.04	0.04
30	3.82	1.44	0.77	0.66	0.54	0.43	0.36	0.29	0.24	0.21	0.17	0.15	0.12	0.11	0.09	0.08	0.07	0.06	0.05	0.04	0.04	0.03	0.03
35	4.48	3.34	1.12	0.86	0.74	0.56	0.42	0.33	0.26	0.22	0.17	0.15	0.13	0.11	0.10	0.08	0.07	0.06	0.06	0.05	0.04	0.03	0.03
40	4.92	2.75	1.45	1.22	0.99	0.79	0.56	0.42	0.31	0.24	0.21	0.17	0.14	0.12	0.11	0.09	0.08	0.07	0.06	0.05	0.04	0.04	0.03
45	5.25	2.48	1.42	1.22	1.02	0.83	0.67	0.50	0.35	0.28	0.22	0.18	0.14	0.12	0.11	0.09	0.08	0.07	0.06	0.05	0.04	0.04	0.03
50	5.83	2.93	1.20	0.99	0.84	0.74	0.61	0.52	0.39	0.31	0.25	0.21	0.17	0.14	0.12	0.10	0.09	0.07	0.06	0.06	0.05	0.04	0.04
55	5.87	2.83	1.29	1.07	0.82	0.75	0.60	0.53	0.50	0.42	0.34	0.29	0.27	0.20	0.17	0.15	0.12	0.10	0.08	0.07	0.06	0.05	0.04
60	5.35	1.84	1.49	1.14	0.96	0.86	0.71	0.56	0.44	0.37	0.31	0.26	0.21	0.18	0.16	0.13	0.11	0.10	0.08	0.07	0.06	0.05	0.04

Table 17 presents the RMSE values for the case where the signals are correlated. Table 17 refers to Figure 22.

Table 17 – RMSE of 1000 experiments for the Modified MODEX estimator considering correlated signals.

$(^\circ)\downarrow$ $dB\rightarrow$	−12.5	−11.25	−10	−8.75	−7.5	−6.25	−5	−3.75	−2.5	−1.25	0	1.25	2.5	3.75	5	6.25	7.5	8.75	10	11.25	12.5	13.75	15
−40	5.96	1.54	0.83	0.66	0.53	0.43	0.35	0.29	0.25	0.21	0.18	0.15	0.13	0.11	0.10	0.08	0.07	0.06	0.05	0.05	0.04	0.03	0.03
−35	5.52	2.00	0.79	0.62	0.48	0.41	0.34	0.29	0.23	0.20	0.17	0.14	0.13	0.11	0.09	0.08	0.07	0.06	0.05	0.04	0.04	0.03	0.03
−30	4.85	2.02	0.86	0.63	0.50	0.42	0.34	0.28	0.25	0.20	0.17	0.14	0.13	0.11	0.09	0.08	0.07	0.06	0.05	0.05	0.04	0.03	0.03
−25	5.87	2.57	0.88	0.59	0.47	0.39	0.32	0.27	0.23	0.19	0.16	0.14	0.12	0.10	0.09	0.07	0.07	0.06	0.05	0.04	0.04	0.03	0.03
−20	4.52	1.89	1.03	0.59	0.45	0.37	0.31	0.27	0.22	0.19	0.16	0.13	0.12	0.10	0.09	0.08	0.06	0.06	0.05	0.04	0.04	0.03	0.03
−15	4.17	1.46	0.80	0.58	0.47	0.38	0.32	0.27	0.23	0.20	0.17	0.14	0.12	0.10	0.09	0.08	0.07	0.06	0.05	0.04	0.04	0.03	0.03
−10	4.58	1.51	1.02	0.55	0.44	0.36	0.30	0.25	0.22	0.18	0.16	0.13	0.12	0.10	0.08	0.07	0.07	0.05	0.05	0.04	0.04	0.03	0.03
−5	5.51	2.56	1.66	0.85	0.56	0.47	0.40	0.33	0.28	0.23	0.20	0.17	0.14	0.13	0.10	0.09	0.08	0.07	0.06	0.05	0.04	0.04	0.03
0	6.84	4.42	2.88	1.91	1.08	0.75	0.58	0.48	0.40	0.34	0.28	0.23	0.21	0.17	0.15	0.13	0.11	0.10	0.08	0.07	0.06	0.05	0.05
5	16.33	14.61	11.68	8.18	5.79	3.69	2.16	1.49	1.17	0.91	0.61	0.45	0.36	0.30	0.26	0.22	0.19	0.17	0.14	0.12	0.11	0.09	0.08
15	16.03	14.11	11.93	8.40	6.81	3.57	2.60	1.46	1.12	0.81	0.60	0.46	0.38	0.31	0.27	0.23	0.19	0.17	0.14	0.12	0.10	0.09	0.08
20	8.59	5.44	3.58	1.95	1.22	0.84	0.59	0.48	0.40	0.34	0.29	0.25	0.21	0.18	0.15	0.13	0.11	0.10	0.08	0.07	0.06	0.05	0.05
25	7.29	4.39	2.17	1.04	0.74	0.58	0.45	0.40	0.33	0.27	0.23	0.20	0.16	0.14	0.12	0.10	0.09	0.08	0.07	0.06	0.05	0.04	0.04
30	6.52	2.83	1.12	0.62	0.49	0.38	0.32	0.27	0.23	0.20	0.17	0.14	0.12	0.11	0.09	0.08	0.07	0.06	0.05	0.04	0.04	0.03	0.03
35	4.52	1.75	1.01	0.67	0.53	0.42	0.35	0.29	0.25	0.21	0.17	0.15	0.13	0.11	0.10	0.08	0.07	0.06	0.06	0.05	0.04	0.03	0.03
40	4.25	1.76	0.90	0.70	0.57	0.46	0.38	0.31	0.27	0.22	0.20	0.16	0.14	0.12	0.11	0.09	0.08	0.07	0.06	0.05	0.04	0.04	0.03
45	6.43	2.01	0.87	0.68	0.50	0.43	0.35	0.30	0.26	0.22	0.19	0.16	0.13	0.12	0.10	0.09	0.08	0.06	0.06	0.05	0.04	0.04	0.03
50	7.15	2.47	1.95	0.68	0.55	0.45	0.38	0.32	0.27	0.24	0.19	0.17	0.14	0.13	0.11	0.09	0.08	0.07	0.06	0.05	0.05	0.04	0.03
55	10.33	3.80	1.86	0.79	0.61	0.52	0.42	0.36	0.31	0.26	0.21	0.19	0.16	0.14	0.12	0.10	0.09	0.08	0.07	0.06	0.05	0.04	0.04
60	8.56	3.62	1.32	0.86	0.69	0.58	0.47	0.41	0.34	0.29	0.25	0.21	0.18	0.16	0.14	0.12	0.10	0.09	0.08	0.06	0.06	0.05	0.04

APPENDIX D – Sensor Array-based Method Derivation

In general, the amplitude, frequency and phase of a trigonometric function are parameters which can be arbitrated. Let

$$\mathbf{x}_R(t) = \mathbf{i}_R(t) - j\mathbf{q}_R(t) = A_R\cos(\omega_i t - \theta_R) - jB_R\sin(\omega_q t - \theta_R) \tag{D.1}$$

$$\mathbf{x}_T(t) = \mathbf{i}_T(t) - j\mathbf{q}_T(t) = A_T\cos(\omega_i t - \theta_T(t)) - jB_T\sin(\omega_q t - \theta_T(t)) \tag{D.2}$$

be the reference and transmitted carriers.

Considering a digital signal, the expressions can be written as:

$$\mathbf{x}_R[i] = \mathbf{i}_R[i] - j\mathbf{q}_R[i] = A_R\cos(\omega_i T_S i - \theta_R) - jB_R\sin(\omega_q T_S i - \theta_R); \tag{D.3}$$

$$\mathbf{x}_T[i] = \mathbf{i}_T[i] - j\mathbf{q}_T[i] = A_T\cos(\omega_i T_S i - \theta_T[i]) - jB_T\sin(\omega_q T_S i - \theta_T[i]), \tag{D.4}$$

where the sampling period is T_S, and dimension of the vector is equal to multiples of one cycle, i.e., $N = g \cdot \frac{f_{sampling}}{\min\{f_i, f_q\}}, g \in \mathbb{N}$, and $i = \{0,\, 1,\, 2, \ldots,\, N-1\}$.

The signals are interfered with by various noisy sources, so that the noise is assumed to be white Gaussian with zero-mean. Thus, the reference and transmitted signals are modeled as:

$$\mathbf{y}_R[i] = \mathbf{x}_R[i] + \mathbf{e}_R[i]; \tag{D.5}$$

$$\mathbf{y}_T[i] = \mathbf{x}_T[i] + \mathbf{e}_T[i]. \tag{D.6}$$

By acquiring the reference and transmitted vectors, the snapshot matrix $\mathbf{Y}$ is settled. It is assumed that the noise power in both signals is equal, i.e., $\sigma_{e,R} = \sigma_{e,T} = \sigma_e$, so:

$$\mathbf{Y}[i] = \begin{pmatrix} \mathbf{y}_R[i] \\ \mathbf{y}_T[i] \end{pmatrix}_{2\times N}, \tag{D.7}$$

consequently, the spatial correlation matrix comes from the product $\mathbf{Y}[i]\ \mathbf{Y}^*[i]$ (SILVA et al., 2013; JúNIOR et al., 2014).

$$\mathbf{R}[i] = \frac{1}{N}\left(\mathbf{Y}[i]\ \mathbf{Y}^*[i]\right) = \frac{1}{N}\begin{pmatrix} \mathbf{y}_R[i] \\ \mathbf{y}_T[i] \end{pmatrix}\begin{pmatrix} \bar{\mathbf{y}}_R[i] & \bar{\mathbf{y}}_T[i] \end{pmatrix}$$

$$= \begin{pmatrix} {}^{\langle \mathbf{x}_R[i], \mathbf{x}_R[i]\rangle}\!/_{N} + \sigma_e^2 & {}^{\langle \mathbf{x}_T[i], \mathbf{x}_R[i]\rangle}\!/_{N} \\ {}^{\langle \mathbf{x}_R[i], \mathbf{x}_T[i]\rangle}\!/_{N} & {}^{\langle \mathbf{x}_T[i], \mathbf{x}_T[i]\rangle}\!/_{N} + \sigma_e^2 \end{pmatrix}, \tag{D.8}$$

where $[\bullet]^*$ denotes the conjugate transpose operation and $[i]$ stands for the sampling instant relative to the first entry in a data vector, which will be omitted from here on for the sake of notation simplicity.

The spatial correlation matrix consists of the autocorrelation of both vectors and the cross-correlation between the different vectors, it is important to analyze the behavior of these components. In the following each term is algebraically analyzed.

The first term is the autocorrelation of $\mathbf{x}_R$, and the inner product can be written as:

$$\begin{aligned}\langle \mathbf{x}_R, \mathbf{x}_R \rangle &= (\mathbf{i}_R - j\mathbf{q}_R)^* (\mathbf{i}_R - j\mathbf{q}_R) \\ &= |\mathbf{i}_R|^2 - j\langle \mathbf{i}_R, \mathbf{q}_R \rangle + j\langle \mathbf{q}_R, \mathbf{i}_R \rangle + |\mathbf{q}_R|^2 \\ &= |\mathbf{i}_R|^2 + |\mathbf{q}_R|^2 \\ &= |\mathbf{x}_R|^2, \end{aligned} \tag{D.9}$$

which is a constant equal to the squared Euclidean norm of $\mathbf{x}_R$.

The second term is the cross-correlation between both vectors, whereas the reference vector is transposed and conjugated. It follows that:

$$\begin{aligned}\langle \mathbf{x}_R, \mathbf{x}_T \rangle &= (\mathbf{i}_R - j\mathbf{q}_R)^* (\mathbf{i}_T - j\mathbf{q}_T) \\ &= \langle \mathbf{i}_R, \mathbf{i}_T \rangle - j\langle \mathbf{i}_R, \mathbf{q}_T \rangle + j\langle \mathbf{q}_R, \mathbf{i}_T \rangle + \langle \mathbf{q}_R, \mathbf{q}_T \rangle \\ &= \langle \mathbf{i}_R, \mathbf{i}_T \rangle + \langle \mathbf{q}_R, \mathbf{q}_T \rangle + j\left(\langle \mathbf{q}_R, \mathbf{i}_T \rangle - \langle \mathbf{i}_R, \mathbf{q}_T \rangle\right), \end{aligned} \tag{D.10}$$

it depends on the inner products of the in-phase and quadrature components of each vector.

The third term is also a cross-correlation, however, in this case the transmitted vector is transposed and conjugated.

$$\begin{aligned}\langle \mathbf{x}_T, \mathbf{x}_R \rangle &= (\mathbf{i}_T - j\mathbf{q}_T)^* (\mathbf{i}_R - j\mathbf{q}_R) \\ &= \langle \mathbf{i}_T, \mathbf{i}_R \rangle - j\langle \mathbf{i}_T, \mathbf{q}_R \rangle + j\langle \mathbf{q}_T, \mathbf{i}_R \rangle + \langle \mathbf{q}_T, \mathbf{q}_R \rangle \\ &= \langle \mathbf{i}_T, \mathbf{i}_R \rangle + \langle \mathbf{q}_T, \mathbf{q}_R \rangle + j\left(\langle \mathbf{q}_T, \mathbf{i}_R \rangle - \langle \mathbf{i}_T, \mathbf{q}_R \rangle\right) \\ &= \overline{\langle \mathbf{x}_R, \mathbf{x}_T \rangle}, \end{aligned} \tag{D.11}$$

which also depends on the inner products of the complex vector components, furthermore, it is the complex conjugate of $\langle \mathbf{x}_R, \mathbf{x}_T \rangle$.

$$\begin{aligned}\langle \mathbf{x}_T, \mathbf{x}_T \rangle &= (\mathbf{i}_T - j\mathbf{q}_T)^* (\mathbf{i}_T - j\mathbf{q}_T) \\ &= |\mathbf{i}_T|^2 - j\langle \mathbf{i}_T, \mathbf{q}_T \rangle + j\langle \mathbf{q}_T, \mathbf{i}_T \rangle + |\mathbf{q}_T|^2 \\ &= |\mathbf{i}_T|^2 + |\mathbf{q}_T|^2 \\ &= |\mathbf{x}_T|^2, \end{aligned} \tag{D.12}$$

which is equal to the squared Euclidean norm of $\mathbf{x}_T$ and depends on the phase variation.

Therefore, the matrix $\mathbf{R}$ can be written as

$$\mathbf{R} = \begin{pmatrix} {}^{|\mathbf{x}_R|^2}/_N + \sigma_e^2 & {}^{\overline{\langle \mathbf{x}_R, \mathbf{x}_T \rangle}}/_N \\ {}^{\langle \mathbf{x}_R, \mathbf{x}_T \rangle}/_N & {}^{|\mathbf{x}_T|^2}/_N + \sigma_e^2 \end{pmatrix}, \tag{D.13}$$

and the characteristic polynomial follows from the determinant of $\mathbf{R}$ by setting it equal to zero:

$$\begin{aligned} \det(\ \mathbf{R}\ ) &= 0 \\ \det \begin{pmatrix} {}^{|\mathbf{x}_R|^2}/_N + \sigma_e^2 - \lambda & {}^{\overline{\langle \mathbf{x}_R, \mathbf{x}_T \rangle}}/_N \\ {}^{\langle \mathbf{x}_R, \mathbf{x}_T \rangle}/_N & {}^{|\mathbf{x}_T|^2}/_N + \sigma_e^2 - \lambda \end{pmatrix} &= 0 \end{aligned}$$

$$\begin{aligned} \lambda^2 - \frac{\lambda}{N}\left(|\mathbf{x}_R|^2 + |\mathbf{x}_T|^2 + 2N\sigma_e^2\right) &+ \\ + \left(\frac{|\mathbf{x}_R|^2}{N} + \sigma_e^2\right)\left(\frac{|\mathbf{x}_T|^2}{N} + \sigma_e^2\right) - \left(\frac{\langle \mathbf{x}_R, \mathbf{x}_T \rangle}{N}\right)\left(\frac{\overline{\langle \mathbf{x}_R, \mathbf{x}_T \rangle}}{N}\right) &= 0 \end{aligned}$$

$$\begin{aligned} \lambda^2 - \frac{\lambda}{N}\left(|\mathbf{x}_R|^2 + |\mathbf{x}_T|^2 + 2N\sigma_e^2\right) &+ \\ + \frac{|\mathbf{x}_R|^2|\mathbf{x}_T|^2 - |\langle \mathbf{x}_R, \mathbf{x}_T \rangle|^2}{N^2} + \frac{\sigma_e^2\left(|\mathbf{x}_R|^2 + |\mathbf{x}_T|^2\right)}{N} + \sigma_e^4 &= 0. \end{aligned} \tag{D.14}$$

And then, it follows the eigenvalue decomposition:

$$\begin{aligned} \lambda = \frac{\left(|\mathbf{x}_R|^2 + |\mathbf{x}_T|^2\right)}{2N} + \sigma_e^2 \pm \frac{1}{2}\Bigg[\left(\frac{|\mathbf{x}_R|^2 + |\mathbf{x}_T|^2 + 2N\sigma_e^2}{N}\right)^2 - \\ - 4\left(\frac{|\mathbf{x}_R|^2|\mathbf{x}_T|^2 - |\langle \mathbf{x}_R, \mathbf{x}_T \rangle|^2}{N^2} + \frac{\sigma_e^2\left(|\mathbf{x}_R|^2 + |\mathbf{x}_T|^2\right)}{N} + \sigma_e^4\right)\Bigg]^{\frac{1}{2}} \end{aligned} \tag{D.15}$$

The term inside the square root should be analyzed individually, such that:

$$\begin{aligned} (I) &= \left(\frac{1}{N}|\mathbf{x}_R|^2 + |\mathbf{x}_T|^2 + 2N\sigma_e^2\right)^2 \\ &= \frac{1}{N^2}\left[|\mathbf{x}_R|^4 + |\mathbf{x}_R|^2|\mathbf{x}_T|^2 + |\mathbf{x}_R|^2\left(2N\sigma_e^2\right)\right] + \\ &+ \frac{1}{N^2}\left[|\mathbf{x}_T|^2|\mathbf{x}_R|^2 + |\mathbf{x}_T|^4 + |\mathbf{x}_T|^2\left(2N\sigma_e^2\right)\right] + \\ &+ \frac{1}{N^2}\left[|\mathbf{x}_R|^2\left(2N\sigma_e^2\right) + |\mathbf{x}_T|^2\left(2N\sigma_e^2\right) + 4N^2\sigma_e^4\right] \\ &= \frac{1}{N^2}\left[|\mathbf{x}_R|^4 + |\mathbf{x}_T|^4 + 4N^2\sigma_e^4 + 2|\mathbf{x}_R|^2|\mathbf{x}_T|^2 + 4N\sigma_e^2\left(|\mathbf{x}_R|^2 + |\mathbf{x}_T|^2\right)\right], \end{aligned} \tag{D.16}$$

and

$$\begin{aligned} (II) &= -4\left(\frac{|\mathbf{x}_R|^2|\mathbf{x}_T|^2 - |\langle \mathbf{x}_R, \mathbf{x}_T \rangle|^2}{N^2} + \frac{\sigma_e^2\left(|\mathbf{x}_R|^2 + |\mathbf{x}_T|^2\right)}{N} + \sigma_e^4\right) \\ &= \frac{1}{N^2}\left[-4|\mathbf{x}_R|^2|\mathbf{x}_T|^2 + 4|\langle \mathbf{x}_R, \mathbf{x}_T \rangle|^2 - 4N\sigma_e^2\left(|\mathbf{x}_R|^2 + |\mathbf{x}_T|^2\right) - 4N^2\sigma_e^4\right]. \end{aligned} \tag{D.17}$$

Therefore, the eigenvalues are expressed in terms of the signals' mean power and the cross-correlation between $\mathbf{x}_R$ and $\mathbf{x}_T$, as follows:

$$\begin{aligned}\lambda &= \frac{(|\mathbf{x}_R|^2 + |\mathbf{x}_T|^2)}{2N} + \sigma_e^2 \pm \sqrt{(I) + (II)}\\ &= \frac{(|\mathbf{x}_R|^2 + |\mathbf{x}_T|^2)}{2N} + \sigma_e^2 \pm \frac{\sqrt{(|\mathbf{x}_R|^4 - 2|\mathbf{x}_R|^2|\mathbf{x}_T|^2 + |\mathbf{x}_T|^4 + 4|\langle \mathbf{x}_R, \mathbf{x}_T\rangle|^2)}}{2N}\\ &= \frac{(|\mathbf{x}_R|^2 + |\mathbf{x}_T|^2)}{2N} + \sigma_e^2 \pm \frac{\sqrt{(|\mathbf{x}_R|^2 - |\mathbf{x}_T|^2)^2 + 4|\langle \mathbf{x}_R, \mathbf{x}_T\rangle|^2}}{2N}. \end{aligned} \tag{D.18}$$

APPENDIX E – The Behavior of each Component of the Formulation

The terms that varies according to a phase shift are $|\mathbf{x}_T|^2$ and $|\langle \mathbf{x}_R, \mathbf{x}_T \rangle|^2$, which the latter interrelates the reference signal and the transmitted signal. The term $|\mathbf{x}_R|^2$ will oscillate only if the length of the vector is different from the number of points in one signal cycle, and it can be written in terms of the in-phase and quadrature components as:

$$\begin{aligned} |\mathbf{x}_R|^2 &= |\mathbf{i}_R|^2 + |\mathbf{q}_R|^2 \\ &= \sum_{i=1}^{N} \Big[A_R^2 \cos^2(\omega_i T_S i - \theta_R) + B_R^2 \sin^2(\omega_q T_S i - \theta_R) \Big] . \end{aligned} \tag{E.1}$$

In the same manner, the transmitted signal vector (the index [i] is explicitly indicated to emphasize the time dependency of the transmitted signal phase) can be written as:

$$\begin{aligned} |\mathbf{x}_T|^2 &= |\mathbf{i}_T|^2 + |\mathbf{q}_T|^2 \\ &= \sum_{i=1}^{N} \Big[A_T^2 \cos^2(\omega_i T_S i - \theta_T[i]) + B_T^2 \sin^2(\omega_q T_S i - \theta_T[i]) \Big] . \end{aligned} \tag{E.2}$$

To explicit the inner product in terms of the trigonometric functions, it follows that:

$$\begin{aligned} \langle \mathbf{x}_R, \mathbf{x}_T \rangle &= \langle \mathbf{i}_R, \mathbf{i}_T \rangle + \langle \mathbf{q}_R, \mathbf{q}_T \rangle + j \left(\langle \mathbf{i}_T, \mathbf{q}_R \rangle - \langle \mathbf{q}_T, \mathbf{i}_R \rangle \right) \\ &= \sum_{i=1}^{N} \Big[A_R \cos(\omega_i T_S i - \theta_R) \cdot A_T \cos(\omega_i T_S i - \theta_T[i]) + \\ &+ B_R \sin(\omega_q T_S i - \theta_R) \cdot B_T \sin(\omega_q T_S i - \theta_T[i]) \Big] - \\ &- j \sum_{i=1}^{N} \Big[A_T \cos(\omega_i T_S i - \theta_T[i]) \cdot B_R \sin(\omega_q T_S i - \theta_R) - \\ &- B_T \sin(\omega_q T_S i - \theta_T[i]) \cdot A_R \cos(\omega_i T_S i - \theta_R) \Big]. \end{aligned} \tag{E.3}$$

Solving for each term individually, the first multiplication turns into:

$$
\begin{aligned}
\langle \mathbf{i}_R, \mathbf{i}_T \rangle &= A_R A_T \sum_{i=1}^{N} [\cos(\omega_i T_S i - \theta_T[i]) \cos(\omega_i T_S i - \theta_R)] = \\
&= A_R A_T \sum_{i=1}^{N} [\cos(\omega_i T_S i) \cos(\theta_T[i]) + \sin(\omega_i T_S i) \sin(\theta_T[i])] \cdot \\
&\cdot \sum_{i=1}^{N} [\cos(\omega_i T_S i) \cos(\theta_R) + \sin(\omega_i T_S i) \sin(\theta_R)] \\
&= A_R A_T \sum_{i=1}^{N} \Big[\cos^2(\omega_i T_S i) \cos(\theta_T[i]) \cos(\theta_R) + \\
&+ \cos(\omega_i T_S i) \sin(\omega_i T_S i) \cos(\theta_T[i]) \sin(\theta_R) + \\
&+ \cos(\omega_i T_S i) \sin(\omega_i T_S i) \cos(\theta_R) \sin(\theta_T[i]) + \sin^2(\omega_i T_S i) \sin(\theta_T[i]) \sin(\theta_R) \Big] \\
&= A_R A_T \sum_{i=1}^{N} \Big\{ \cos^2(\omega_i T_S i) \cos(\theta_T[i]) \cos(\theta_R) + \sin^2(\omega_i T_S i) \sin(\theta_T[i]) \sin(\theta_R) + \\
&+ \cos(\omega_i T_S i) \sin(\omega_i T_S i) [\cos(\theta_T[i]) \sin(\theta_R) + \cos(\theta_R) \sin(\theta_T[i])] \Big\}, \qquad \text{(E.4)}
\end{aligned}
$$

whereas the amplitude of both cosine functions can be arbitrated, in particular, $A_R = A_T = A$. Thus,

$$
\begin{aligned}
\langle \mathbf{i}_R, \mathbf{i}_T \rangle = A^2 \sum_{i=1}^{N} \Big\{ & \cos^2(\omega_i T_S i) \cos(\theta_T[i]) \cos(\theta_R) + \sin^2(\omega_i T_S i) \sin(\theta_T[i]) \sin(\theta_R) + \\
& + \frac{1}{2} \sin(2\omega_i T_S i) \sin(\theta_R + \theta_T[i]) \Big\}. \qquad \text{(E.5)}
\end{aligned}
$$

The second multiplication brings:

$$
\begin{aligned}
\langle \mathbf{q}_R, \mathbf{q}_T \rangle &= B_R B_T \sum_{i=1}^{N} [\sin(\omega_q T_S i - \theta_R) \sin(\omega_q T_S i - \theta_T[i])] = \\
&= B_R B_T \sum_{i=1}^{N} [\sin(\omega_q T_S i) \cos(\theta_R) - \sin(\theta_R) \cos(\omega_q T_S i)] \cdot \\
&\cdot \sum_{i=1}^{N} [\sin(\omega_q T_S i) \cos(\theta_T[i]) - \sin(\theta_T[i]) \cos(\omega_q T_S i)] \\
&= B_R B_T \sum_{i=1}^{N} \Big[\sin^2(\omega_q T_S i) \cos(\theta_R) \cos(\theta_T[i]) - \\
&- \sin(\omega_q T_S i) \cos(\omega_q T_S i) \cos(\theta_R) \sin(\theta_T[i]) - \\
&- \cos(\omega_q T_S i) \sin(\omega_q T_S i) \sin(\theta_R) \cos(\theta_T[i]) + \cos^2(\omega_q T_S i) \sin(\theta_R) \sin(\theta_T[i]) \Big] \\
&= B_R B_T \sum_{i=1}^{N} \Big\{ \sin^2(\omega_q T_S i) \cos(\theta_R) \cos(\theta_T[i]) + \cos^2(\omega_q T_S i) \sin(\theta_R) \sin(\theta_T[i]) - \\
&- \cos(\omega_q T_S i) \sin(\omega_q T_S i) [\sin(\theta_R) \cos(\theta_T[i]) + \sin(\theta_T[i]) \cos(\theta_R)] \Big\}, \qquad \text{(E.6)}
\end{aligned}
$$

whereas the amplitude of both sine functions can be arbitrated, in particular, $B_R = B_T = B$. Thus,

$$\begin{aligned}\langle \mathbf{q}_R, \mathbf{q}_T \rangle = B^2 \sum_{i=1}^{N} \Big\{ & \sin^2(\omega_q T_S i)\cos(\theta_R)\cos(\theta_T[i]) + \cos^2(\omega_q T_S i)\sin(\theta_R)\sin(\theta_T[i]) - \\ & - \frac{1}{2}\sin(2\omega_q T_S i)\sin(\theta_R + \theta_T[i])\Big\}. \end{aligned} \tag{E.7}$$

Next comes:

$$\begin{aligned}\langle \mathbf{i}_T, \mathbf{q}_R \rangle &= BA\sum_{i=1}^{N}[\cos(\omega_i T_S i - \theta_T[i])\sin(\omega_q T_S i - \theta_R)] = \\ &= BA\sum_{i=1}^{N}[\cos(\omega_i T_S i)\cos(\theta_T[i]) + \sin(\omega_i T_S i)\sin(\theta_T[i])]\cdot \\ &\cdot [\sin(\omega_q T_S i)\cos(\theta_R) - \sin(\theta_R)\cos(\omega_q T_S i)] \\ &= BA\sum_{i=1}^{N}\Big[\cos(\omega_i T_S i)\sin(\omega_q T_S i)\cos(\theta_T[i])\cos(\theta_R) - \\ &- \cos(\omega_i T_S i)\cos(\omega_q T_S i)\cos(\theta_T[i])\sin(\theta_R) + \\ &+ \sin(\omega_i T_S i)\sin(\omega_q T_S i)\sin(\theta_T[i])\cos(\theta_R) - \\ &- \sin(\omega_i T_S i)\cos(\omega_q T_S i)\sin(\theta_T[i])\sin(\theta_R)\Big], \end{aligned} \tag{E.8}$$

and

$$\begin{aligned}\langle \mathbf{q}_T, \mathbf{i}_R \rangle &= BA\sum_{i=1}^{N}[\sin(\omega_q T_S i - \theta_T[i])\cos(\omega_i T_S i - \theta_R)] = \\ &= BA\sum_{i=1}^{N}[\sin(\omega_q T_S i)\cos(\theta_T[i]) - \cos(\omega_q T_S i)\sin(\theta_T[i])]\cdot \\ &\cdot [\cos(\omega_i T_S i)\cos(\theta_R) + \sin(\omega_i T_S i)\sin(\theta_R)] \\ &= BA\sum_{i=1}^{N}\Big[\sin(\omega_q T_S i)\cos(\omega_i T_S i)\cos(\theta_T[i])\cos(\theta_R) + \\ &+ \sin(\omega_q T_S i)\sin(\omega_i T_S i)\cos(\theta_T[i])[i]\sin(\theta_R) - \\ &- \cos(\omega_q T_S i)\cos(\omega_i T_S i)\cos(\theta_R)\sin(\theta_T[i]) - \\ &- \cos(\omega_q T_S i)\sin(\omega_i T_S i)\sin(\theta_T[i])\sin(\theta_R)\Big]. \end{aligned} \tag{E.9}$$

Therefore, by summing everything up and algebraically handling the results, the real and imaginary parts are given by:

$$\begin{aligned}\mathrm{Re}\{\langle \mathbf{x}_R, \mathbf{x}_T \rangle\} = \sum_{i=1}^{N}\Big\{ & \cos(\theta_R)\cos(\theta_T[i])\Big[A^2\cos^2(\omega_i T_S i) + B^2\sin^2(\omega_q T_S i)\Big] + \\ & + \sin(\theta_R)\sin(\theta_T[i])\Big[A^2\sin^2(\omega_i T_S i) + B^2\cos^2(\omega_q T_S i)\Big] + \\ & + \frac{1}{2}\sin(\theta_R + \theta_T[i])\,[\sin(2\omega_i T_S i) - \sin(2\omega_q T_S i)]\Big\}, \end{aligned} \tag{E.10}$$

and

$$\begin{aligned}\mathrm{Im}\{\langle \mathbf{x}_R, \mathbf{x}_T\rangle\} &= AB\sum_{i=1}^{N}\Big\{\cos(\omega_i T_S i)\cos(\omega_q T_S i)\left[\sin(\theta_T[i])\cos(\theta_R) - \cos(\theta_T[i])\sin(\theta_R)\right] + \\ &+ \sin(\omega_i T_S i)\sin(\omega_q T_S i)\left[\sin(\theta_T[i])\cos(\theta_R) - \cos(\theta_T[i])\sin(\theta_R)\right]\Big\} \\ &= AB\sum_{i=1}^{N}\sin(\theta_T[i] - \theta_R)\cos(\omega_i T_S i - \omega_q T_S i). \qquad \text{(E.11)}\end{aligned}$$

This is the general formulation for the inner product $\langle \mathbf{x}_R, \mathbf{x}_T\rangle$. It is a function of time $T_S i$ with the parameters A, B, ω_i, ω_q, θ_R and θ_T.

APPENDIX F – Some Interesting Cases

Especial cases can be considered, where some parameters are arbitrated.

1. **ideal complex exponential**. It means that $A = B = 1$, $\omega_i = \omega_q = \omega_{iq}$, $\{f_{iq} \in \mathbb{R} \mid \frac{-f_{sampling}}{2} \leq f_{iq} \leq \frac{f_{sampling}}{2}\}$, and $\theta_R = \theta_T[0] = 0$.

$$\langle \mathbf{x}_R, \mathbf{x}_T \rangle = \sum_{i=1}^{N} \cos(\theta_T[i]) + j \sum_{i=1}^{N} \sin(\theta_T[i]), \tag{F.1}$$

thus, the absolute value is equal to:

$$|\langle \mathbf{x}_R, \mathbf{x}_T \rangle|^2 = \left[\sum_{i=1}^{N} \cos(\theta_T[i])\right]^2 + \left[\sum_{i=1}^{N} \sin(\theta_T[i])\right]^2 . \tag{F.2}$$

It follows that the squared magnitude of the inner product will provide only positive pulses.

2. **I/Q components with different amplitudes**. In this case, the parameters are $A \neq B$, where A, $B \in \mathbb{R}$, $\omega_i = \omega_q = \omega_{iq}$, $\{f_{iq} \in \mathbb{R} \mid \frac{-f_{sampling}}{2} \leq f_{iq} \leq \frac{f_{sampling}}{2}\}$, and $\theta_R = \theta_T[0] = 0$.

$$\begin{aligned}
\langle \mathbf{x}_R, \mathbf{x}_T \rangle &= \sum_{i=1}^{N} \cos(\theta_T[i]) \left[A^2 \cos^2(\omega_{iq} T_S i) + B^2 \sin^2(\omega_{iq} T_S i)\right] + \\
&+ j \left[AB \sum_{i=1}^{N} \sin(\theta_T[i])\right] \\
&= \sum_{i=1}^{N} \cos(\theta_T[i]) \left\{\frac{A^2}{2} \left[\cos(2\omega_{iq} T_S i) + 1\right] + \frac{B^2}{2} \left[1 - \cos(2\omega_{iq} T_S i)\right]\right\} + \\
&+ j \left[AB \sum_{i=1}^{N} \sin(\theta_T[i])\right] \\
&= \sum_{i=1}^{N} \left[\frac{(A^2 - B^2)}{2} \cos(2\omega_{iq} T_S i) \cos(\theta_T[i]) + \right. \\
&+ \left. \frac{(A^2 + B^2)}{2} \cos(\theta_T[i])\right] + j \left[AB \sum_{i=1}^{N} \sin(\theta_T[i])\right] .
\end{aligned} \tag{F.3}$$

3. **I/Q components with different frequencies**. In this case, the parameters are

$A = B = 1$, $\omega_i \neq \omega_q$, $\{f_i,\, f_q \in \mathbb{R} \mid \frac{-f_{sampling}}{2} \leq f_i,\, f_q \leq \frac{f_{sampling}}{2}\}$, and $\theta_R = \theta_T[0] = 0$.

$$\begin{aligned}
\langle \mathbf{x}_R, \mathbf{x}_T \rangle &= \sum_{i=1}^{N} \Big\{ \cos(\theta_T[i]) \Big[\cos^2(\omega_i T_S i) + \sin^2(\omega_q T_S i)\Big] \; + \\
&+ \frac{1}{2} \sin(\theta_T[i]) \left[\sin(2\omega_i T_S i) - \sin(2\omega_q T_S i)\right] \Big\} + \\
&+ j \left[\sum_{i=1}^{N} \sin(\theta_T[i]) \cos(\omega_i T_S i - \omega_q T_S i)\right] \\
&= \sum_{i=1}^{N} \frac{1}{2} \Big\{ \cos(\theta_T[i]) \left[\cos(2\omega_i T_S i) + 1\right] + \cos(\theta_T[i]) \left[1 - \cos(2\omega_q T_S i)\right] \; + \\
&+ \frac{1}{2} \left[\sin(\theta_T[i]) \sin(2\omega_i T_S i) - \sin(\theta_T[i]) \sin(2\omega_q T_S i)\right] \Big\} + \\
&+ j \left[\sum_{i=1}^{N} \sin(\theta_T[i]) \cos(\omega_i T_S i - \omega_q T_S i)\right] \\
&= \sum_{i=1}^{N} \Big\{ \cos(\theta_T[i]) + \cos(2\omega_i T_S i - \theta_T[i]) - \cos(2\omega_q T_S i - \theta_T[i]) \Big\} + \\
&+ j \left[\sum_{i=1}^{N} \sin(\theta_T[i]) \cos(\omega_i T_S i - \omega_q T_S i)\right]. \qquad \text{(F.4)}
\end{aligned}$$

4. **I/Q components with different frequencies and $\mathbf{x}_R$, and $\mathbf{x}_T$ with different initial phases**. In this case, the parameters are $A = B = 1$, $\omega_q = 2\omega_i$, $\{f_i, f_q \in \mathbb{R} \mid \frac{-f_{sampling}}{2} \leq f_i, f_q \leq \frac{f_{sampling}}{2}\}$, and $\theta_R = \frac{-\pi}{2}$, $\theta_T[0] = 0$.

$$\begin{aligned}
\langle \mathbf{x}_R, \mathbf{x}_T \rangle &= \sum_{i=1}^{N} \left[- \sin(\theta_T[i]) + \frac{\sin(2\omega_i T_S i - \theta_T[i]) + \sin(4\omega_i T_S i - \theta_T[i])}{2} \right] + \\
&+ j \sum_{i=1}^{N} \cos(\theta_T[i]) \cos(\omega_i T_S i). \qquad \text{(F.5)}
\end{aligned}$$

Furthermore, any combination of the above mentioned cases and different parameters' assignment are also possible.

APPENDIX G – MSE Values for X-Ray Spectroscopy Performance

The data used to plot the error surface in Chapter 7 are presented in this appendix in tabular form as a supplementary material to aid in understanding the results.

G.1 Real and Imaginary Components with Equal Power

For the case where the real and imaginary components have equal power and equal frequencies, the signals are ideal complex exponential functions. Table 18 refers to Figure 43.

Table 18 – MSE of 20 experiments for the estimator λ_2 considering zero-mean ideal complex exponential signals.

$dB\rightarrow$ $(^{\circ})\downarrow$	0	2	4	6	8	10	12	14	16	18	20
−1800	0.1728	0.1251	0.0978	0.0889	0.0841	0.0834	0.0829	0.0827	0.0828	0.0828	0.0828
−1600	0.1628	0.1035	0.0793	0.0632	0.0573	0.0554	0.0543	0.0540	0.0539	0.0539	0.0539
−1400	0.1672	0.1069	0.0688	0.0510	0.0410	0.0371	0.0354	0.0352	0.0350	0.0349	0.0349
−1200	0.1850	0.1172	0.0709	0.0486	0.0355	0.0292	0.0263	0.0254	0.0249	0.0249	0.0249
−1000	0.2229	0.1355	0.0815	0.0509	0.0341	0.0239	0.0194	0.0178	0.0173	0.0170	0.0169
−800	0.2587	0.1651	0.0973	0.0601	0.0377	0.0245	0.0169	0.0130	0.0114	0.0109	0.0108
−700	0.3062	0.1873	0.1118	0.0681	0.0414	0.0252	0.0165	0.0121	0.0095	0.0086	0.0084
−600	0.3423	0.2221	0.1344	0.0805	0.0484	0.0305	0.0181	0.0120	0.0080	0.0069	0.0063
−500	0.4132	0.2625	0.1623	0.0960	0.0598	0.0354	0.0212	0.0131	0.0081	0.0058	0.0048
−400	0.4958	0.3217	0.2062	0.1222	0.0751	0.0445	0.0273	0.0163	0.0099	0.0057	0.0042
−300	0.5337	0.4333	0.2707	0.1715	0.1017	0.0598	0.0355	0.0214	0.0122	0.0076	0.0047
−200	0.5862	0.5245	0.4181	0.2560	0.1565	0.0964	0.0568	0.0354	0.0200	0.0118	0.0070
−100	0.5528	0.5800	0.5653	0.4726	0.3242	0.2046	0.1213	0.0737	0.0463	0.0253	0.0154
0	NaN	NaN	NaN	NaN	NaN	NaN	NaN	NaN	NaN	NaN	NaN
100	0.5649	0.5924	0.5685	0.4727	0.3179	0.2010	0.1239	0.0706	0.0441	0.0271	0.0148
200	0.5636	0.5162	0.3981	0.2629	0.1592	0.0961	0.0598	0.0335	0.0201	0.0127	0.0070
300	0.5288	0.4271	0.2725	0.1606	0.1007	0.0621	0.0369	0.0215	0.0125	0.0076	0.0047
400	0.4794	0.3293	0.2006	0.1258	0.0731	0.0425	0.0269	0.0161	0.0097	0.0059	0.0042
500	0.3956	0.2562	0.1566	0.0982	0.0583	0.0355	0.0221	0.0126	0.0081	0.0057	0.0049
600	0.3384	0.2173	0.1423	0.0781	0.0496	0.0298	0.0186	0.0118	0.0084	0.0066	0.0064
700	0.2876	0.1880	0.1114	0.0668	0.0422	0.0254	0.0165	0.0116	0.0094	0.0086	0.0084
800	0.2516	0.1704	0.1023	0.0600	0.0374	0.0240	0.0168	0.0127	0.0113	0.0110	0.0108
1000	0.2185	0.1293	0.0846	0.0512	0.0328	0.0239	0.0195	0.0178	0.0171	0.0170	0.0169
1200	0.1813	0.1127	0.0723	0.0481	0.0342	0.0282	0.0259	0.0253	0.0249	0.0249	0.0248
1400	0.1740	0.1077	0.0721	0.0500	0.0406	0.0368	0.0357	0.0351	0.0350	0.0350	0.0349
1600	0.1696	0.1072	0.0781	0.0629	0.0575	0.0553	0.0542	0.0540	0.0539	0.0540	0.0540
1800	0.1748	0.1209	0.0982	0.0887	0.0841	0.0833	0.0831	0.0828	0.0827	0.0828	0.0828

The eigenvalues will show different behavior if it is considered a mean value for the real and imaginary components. Table 19 refers to Figure 45.

Table 19 – MSE of 20 experiments for the estimator λ_2 considering non-zero-mean ideal complex exponential signals, where $mean(\mathbf{i}_R) = mean(\mathbf{q}_R) = mean(\mathbf{i}_T) = mean(\mathbf{q}_T) = 10$.

$(^\circ)\downarrow$ $dB\rightarrow$	0	2	4	6	8	10	12	14	16	18	20
−180	0.1227	0.0915	0.0759	0.0687	0.0665	0.0653	0.0653	0.0650	0.0650	0.0650	0.0649
−160	0.1238	0.0853	0.0637	0.0546	0.0506	0.0493	0.0489	0.0488	0.0488	0.0488	0.0487
−140	0.1290	0.0845	0.0576	0.0445	0.0391	0.0367	0.0359	0.0357	0.0357	0.0357	0.0357
−120	0.1353	0.0898	0.0556	0.0381	0.0307	0.0277	0.0260	0.0254	0.0253	0.0253	0.0253
−100	0.1639	0.1000	0.0616	0.0377	0.0266	0.0204	0.0183	0.0177	0.0173	0.0171	0.0170
−80	0.2073	0.1219	0.0744	0.0435	0.0285	0.0195	0.0136	0.0117	0.0110	0.0107	0.0107
−70	0.2368	0.1329	0.0828	0.0525	0.0301	0.0201	0.0125	0.0099	0.0087	0.0083	0.0082
−60	0.2828	0.1660	0.0981	0.0584	0.0338	0.0222	0.0133	0.0090	0.0072	0.0062	0.0060
−50	0.3195	0.1915	0.1193	0.0723	0.0406	0.0261	0.0156	0.0094	0.0063	0.0050	0.0043
−40	0.4140	0.2395	0.1543	0.0882	0.0543	0.0335	0.0193	0.0115	0.0066	0.0045	0.0034
−30	0.4980	0.3241	0.2123	0.1195	0.0767	0.0433	0.0268	0.0158	0.0090	0.0054	0.0031
−20	0.5602	0.4389	0.3036	0.1977	0.1084	0.0708	0.0409	0.0246	0.0150	0.0082	0.0050
−10	0.5496	0.5507	0.5223	0.3635	0.2536	0.1445	0.0891	0.0530	0.0329	0.0188	0.0111
0	*NaN*	*NaN*	*NaN*	*NaN*	*NaN*	*NaN*	*NaN*	*NaN*	*NaN*	*NaN*	*NaN*
10	0.5753	0.5757	0.5194	0.3865	0.2545	0.1510	0.0863	0.0557	0.0334	0.0183	0.0114
20	0.5392	0.5083	0.3137	0.1838	0.1191	0.0683	0.0418	0.0245	0.0145	0.0091	0.0050
30	0.4899	0.3318	0.2111	0.1258	0.0744	0.0459	0.0265	0.0152	0.0092	0.0055	0.0034
40	0.3841	0.2582	0.1481	0.0915	0.0524	0.0324	0.0185	0.0116	0.0071	0.0046	0.0034
50	0.3035	0.1873	0.1175	0.0719	0.0428	0.0246	0.0149	0.0098	0.0068	0.0049	0.0044
60	0.2732	0.1576	0.0984	0.0611	0.0353	0.0209	0.0135	0.0095	0.0071	0.0062	0.0061
70	0.2353	0.1385	0.0823	0.0512	0.0299	0.0195	0.0132	0.0103	0.0087	0.0083	0.0082
80	0.1943	0.1157	0.0703	0.0461	0.0271	0.0188	0.0141	0.0119	0.0111	0.0108	0.0107
100	0.1646	0.1022	0.0598	0.0391	0.0269	0.0209	0.0186	0.0177	0.0172	0.0172	0.0171
120	0.1452	0.0858	0.0556	0.0388	0.0304	0.0272	0.0258	0.0253	0.0255	0.0253	0.0254
140	0.1287	0.0842	0.0573	0.0442	0.0386	0.0370	0.0363	0.0360	0.0358	0.0358	0.0358
160	0.1204	0.0809	0.0643	0.0536	0.0503	0.0494	0.0491	0.0489	0.0488	0.0487	0.0488
180	0.1238	0.0912	0.0758	0.0690	0.0661	0.0656	0.0651	0.0650	0.0650	0.0650	0.0650

The ML method performs the estimation over the magnitude value of the complex function. For an ideal complex exponential with mean value equal 10 for both components the magnitude will oscillate according to the point distribution on the complex plane. Table 20 refers to Figure 46.

Table 20 – MSE of 20 experiments for the ML estimator considering the magnitude of a non-zero-mean ideal complex exponential, where $mean(\mathbf{i}_R) = mean(\mathbf{q}_R) = mean(\mathbf{i}_T) = mean(\mathbf{q}_T) = 10$.

$(^\circ)\downarrow$ $dB\rightarrow$	0	2	4	6	8	10	12	14	16	18	20
−180	0.1768	0.1790	0.1791	0.1783	0.1790	0.1791	0.1791	0.1791	0.1791	0.1791	0.1791
−160	0.1086	0.1063	0.1037	0.1056	0.1039	0.1039	0.1044	0.1045	0.1045	0.1045	0.1045
−140	0.0222	0.0136	0.0090	0.0054	0.0036	0.0022	0.0016	0.0011	0.0007	0.0006	0.0005
−120	0.0269	0.0152	0.0101	0.0067	0.0039	0.0027	0.0016	0.0012	0.0009	0.0007	0.0006
−100	0.0319	0.0194	0.0121	0.0074	0.0046	0.0030	0.0019	0.0014	0.0009	0.0008	0.0007
−80	0.0360	0.0261	0.0173	0.0099	0.0069	0.0039	0.0028	0.0016	0.0011	0.0008	0.0006
−70	0.0434	0.0291	0.0192	0.0117	0.0072	0.0047	0.0030	0.0018	0.0012	0.0008	0.0006
−60	0.0504	0.0307	0.0210	0.0134	0.0076	0.0053	0.0032	0.0021	0.0014	0.0009	0.0007
−50	0.0649	0.0407	0.0228	0.0154	0.0096	0.0068	0.0040	0.0024	0.0015	0.0011	0.0007
−40	0.0712	0.0531	0.0299	0.0191	0.0125	0.0087	0.0052	0.0032	0.0021	0.0015	0.0009
−30	0.0968	0.0637	0.0414	0.0247	0.0173	0.0105	0.0064	0.0042	0.0027	0.0016	0.0012
−20	0.1356	0.0936	0.0626	0.0375	0.0241	0.0154	0.0102	0.0063	0.0040	0.0028	0.0017
−10	0.2362	0.1933	0.1163	0.0756	0.0514	0.0297	0.0198	0.0129	0.0071	0.0048	0.0039
0	*NaN*	*NaN*	*NaN*	*NaN*	*NaN*	*NaN*	*NaN*	*NaN*	*NaN*	*NaN*	*NaN*
10	0.2416	0.2009	0.1144	0.0744	0.0494	0.0301	0.0193	0.0123	0.0076	0.0053	0.0031
20	0.1340	0.0977	0.0635	0.0397	0.0265	0.0151	0.0097	0.0064	0.0037	0.0024	0.0017
30	0.0944	0.0756	0.0415	0.0269	0.0160	0.0108	0.0063	0.0042	0.0027	0.0017	0.0012
40	0.0754	0.0503	0.0320	0.0227	0.0128	0.0073	0.0049	0.0033	0.0020	0.0013	0.0009
50	0.1530	0.0557	0.0525	0.0168	0.0093	0.0068	0.0035	0.0027	0.0015	0.0011	0.0007
60	0.5379	0.5473	0.5394	0.5300	0.5315	0.5384	0.5353	0.5368	0.5371	0.5372	0.5373
70	0.6378	0.6389	0.6444	0.6419	0.6453	0.6433	0.6424	0.6430	0.6426	0.6429	0.6428
80	0.6706	0.6667	0.6707	0.6731	0.6701	0.6718	0.6718	0.6713	0.6711	0.6709	0.6706
100	0.6635	0.6589	0.6607	0.6563	0.6577	0.6568	0.6570	0.6572	0.6572	0.6571	0.6570
120	0.6223	0.6228	0.6169	0.6197	0.6176	0.6172	0.6176	0.6171	0.6175	0.6172	0.6174
140	0.5754	0.5761	0.5755	0.5762	0.5752	0.5747	0.5748	0.5749	0.5750	0.5750	0.5749
160	0.5355	0.5333	0.5340	0.5357	0.5356	0.5357	0.5356	0.5355	0.5354	0.5354	0.5355
180	0.5060	0.5021	0.5003	0.4988	0.4999	0.5000	0.4996	0.4997	0.4997	0.4999	0.4999

The eigenvalue method is also useful when the signal is real, so that the magnitude of the complex number is also assessed regarding the estimation error. Table 21 refers to Figure 47.

Table 21 – MSE of 20 experiments for the estimator λ_2 considering the magnitude of non-zero-mean ideal complex exponential signals, where $mean(\mathbf{i}_R) = mean(\mathbf{q}_R) = mean(\mathbf{i}_T) = mean(\mathbf{q}_T) = 10$.

$dB\rightarrow$ $(^\circ)\downarrow$	0	2	4	6	8	10	12	14	16	18	20
−180	0.1388	0.1007	0.0804	0.0702	0.0669	0.0654	0.0653	0.0651	0.0652	0.0650	0.0650
−160	0.1425	0.0973	0.0695	0.0574	0.0517	0.0497	0.0489	0.0487	0.0488	0.0486	0.0487
−140	0.1547	0.0999	0.0651	0.0481	0.0405	0.0372	0.0359	0.0357	0.0356	0.0356	0.0356
−120	0.1630	0.1057	0.0654	0.0434	0.0329	0.0279	0.0261	0.0254	0.0253	0.0253	0.0252
−100	0.1952	0.1205	0.0725	0.0465	0.0299	0.0224	0.0190	0.0179	0.0174	0.0171	0.0170
−80	0.2460	0.1519	0.0896	0.0530	0.0331	0.0223	0.0152	0.0123	0.0113	0.0109	0.0108
−70	0.2782	0.1603	0.0999	0.0648	0.0373	0.0227	0.0148	0.0108	0.0093	0.0086	0.0084
−60	0.3268	0.1992	0.1195	0.0727	0.0419	0.0269	0.0156	0.0107	0.0082	0.0067	0.0063
−50	0.3882	0.2281	0.1376	0.0892	0.0522	0.0307	0.0189	0.0112	0.0074	0.0056	0.0047
−40	0.4981	0.2841	0.1848	0.1057	0.0657	0.0401	0.0229	0.0140	0.0087	0.0054	0.0040
−30	0.5345	0.3719	0.2634	0.1501	0.0931	0.0532	0.0321	0.0201	0.0113	0.0067	0.0042
−20	0.5680	0.4872	0.3529	0.2369	0.1341	0.0836	0.0516	0.0301	0.0185	0.0100	0.0065
−10	0.5718	0.5526	0.5370	0.4358	0.2920	0.1783	0.1119	0.0642	0.0384	0.0232	0.0140
0	*NaN*	*NaN*	*NaN*	*NaN*	*NaN*	*NaN*	*NaN*	*NaN*	*NaN*	*NaN*	*NaN*
10	0.5737	0.5847	0.5252	0.4315	0.3087	0.1777	0.1081	0.0645	0.0402	0.0230	0.0139
20	0.5454	0.5405	0.3642	0.2231	0.1420	0.0831	0.0502	0.0298	0.0172	0.0112	0.0062
30	0.5312	0.3824	0.2423	0.1518	0.0892	0.0544	0.0322	0.0192	0.0115	0.0066	0.0043
40	0.4421	0.3108	0.1843	0.1097	0.0658	0.0385	0.0224	0.0136	0.0087	0.0055	0.0041
50	0.3534	0.2259	0.1449	0.0882	0.0537	0.0300	0.0190	0.0116	0.0078	0.0056	0.0048
60	0.3316	0.1884	0.1187	0.0739	0.0427	0.0249	0.0164	0.0111	0.0078	0.0066	0.0063
70	0.2664	0.1671	0.0982	0.0616	0.0363	0.0230	0.0152	0.0110	0.0090	0.0085	0.0083
80	0.2336	0.1445	0.0867	0.0545	0.0319	0.0214	0.0150	0.0128	0.0114	0.0109	0.0107
100	0.1908	0.1206	0.0743	0.0459	0.0311	0.0222	0.0191	0.0178	0.0172	0.0170	0.0170
120	0.1697	0.1057	0.0672	0.0438	0.0324	0.0282	0.0259	0.0252	0.0253	0.0251	0.0252
140	0.1491	0.0987	0.0645	0.0471	0.0399	0.0373	0.0362	0.0359	0.0357	0.0356	0.0356
160	0.1440	0.0938	0.0702	0.0561	0.0508	0.0497	0.0492	0.0488	0.0487	0.0487	0.0487
180	0.1430	0.0996	0.0803	0.0714	0.0665	0.0657	0.0650	0.0648	0.0649	0.0649	0.0649

G.2 Real and Imaginary Components with Different Power

In the first case, an ideal cosine function is used as the reference and transmitted signals, moreover, there is no initial phase shift between them. Table 22 refers to Figure 49

Table 22 – MSE of 20 experiments for the estimator λ_2 considering the in-phase component of the complex signals.

$(^\circ)\downarrow$ $dB\rightarrow$	0	2	4	6	8	10	12	14	16	18	20
−180	0.1410	0.1045	0.0793	0.0703	0.0664	0.0657	0.0653	0.0653	0.0652	0.0652	0.0651
−160	0.1411	0.0945	0.0691	0.0585	0.0522	0.0501	0.0495	0.0495	0.0495	0.0494	0.0495
−140	0.1549	0.0961	0.0647	0.0481	0.0408	0.0381	0.0365	0.0363	0.0362	0.0361	0.0361
−120	0.1677	0.1034	0.0696	0.0434	0.0336	0.0283	0.0264	0.0258	0.0254	0.0254	0.0254
−100	0.1937	0.1192	0.0730	0.0447	0.0308	0.0228	0.0191	0.0178	0.0171	0.0169	0.0169
−80	0.2410	0.1468	0.0913	0.0541	0.0329	0.0215	0.0154	0.0123	0.0110	0.0105	0.0104
−70	0.2707	0.1702	0.1015	0.0624	0.0380	0.0224	0.0148	0.0107	0.0088	0.0081	0.0078
−60	0.3305	0.1840	0.1137	0.0721	0.0444	0.0266	0.0157	0.0105	0.0075	0.0062	0.0058
−50	0.3724	0.2265	0.1475	0.0836	0.0505	0.0305	0.0183	0.0113	0.0074	0.0053	0.0043
−40	0.4583	0.2838	0.1741	0.1081	0.0655	0.0391	0.0237	0.0140	0.0087	0.0051	0.0036
−30	0.5542	0.3807	0.2373	0.1526	0.0919	0.0544	0.0317	0.0191	0.0108	0.0064	0.0041
−20	0.5991	0.5309	0.3819	0.2354	0.1373	0.0821	0.0497	0.0306	0.0169	0.0097	0.0063
−10	0.5334	0.5559	0.5061	0.4424	0.3009	0.1789	0.1099	0.0641	0.0390	0.0230	0.0136
0	NaN	NaN	NaN	NaN	NaN	NaN	NaN	NaN	NaN	NaN	NaN
10	0.5523	0.5527	0.5667	0.4427	0.2956	0.1856	0.1035	0.0640	0.0373	0.0214	0.0140
20	0.5505	0.5101	0.3638	0.2294	0.1397	0.0851	0.0510	0.0312	0.0182	0.0105	0.0061
30	0.5338	0.4045	0.2490	0.1500	0.0917	0.0538	0.0324	0.0180	0.0117	0.0064	0.0041
40	0.4713	0.2904	0.1733	0.1064	0.0651	0.0382	0.0246	0.0139	0.0090	0.0055	0.0041
50	0.3601	0.2309	0.1453	0.0853	0.0500	0.0317	0.0190	0.0120	0.0078	0.0058	0.0049
60	0.3121	0.1886	0.1146	0.0702	0.0434	0.0260	0.0156	0.0109	0.0083	0.0069	0.0066
70	0.2795	0.1688	0.1042	0.0621	0.0371	0.0239	0.0158	0.0112	0.0096	0.0089	0.0087
80	0.2276	0.1507	0.0863	0.0530	0.0321	0.0210	0.0157	0.0130	0.0118	0.0113	0.0113
100	0.1926	0.1181	0.0736	0.0460	0.0312	0.0230	0.0194	0.0183	0.0177	0.0177	0.0176
120	0.1659	0.1049	0.0663	0.0444	0.0333	0.0284	0.0268	0.0262	0.0258	0.0257	0.0257
140	0.1558	0.0945	0.0641	0.0480	0.0402	0.0378	0.0365	0.0362	0.0359	0.0359	0.0360
160	0.1458	0.0968	0.0690	0.0562	0.0513	0.0498	0.0491	0.0489	0.0488	0.0488	0.0487
180	0.1437	0.1007	0.0796	0.0712	0.0659	0.0652	0.0651	0.0648	0.0647	0.0647	0.0647

In the second case, an ideal sine function is used as the reference and transmitted signals, no initial phase shift as well.

Table 23 – MSE of 20 experiments for the estimator λ_2 considering the quadrature component of the complex signals.

$dB\rightarrow$ $(^\circ)\downarrow$	0	2	4	6	8	10	12	14	16	18	20
−180	0.1496	0.1059	0.0810	0.0716	0.0680	0.0665	0.0663	0.0661	0.0661	0.0661	0.0660
−160	0.1464	0.0966	0.0708	0.0585	0.0525	0.0505	0.0503	0.0499	0.0497	0.0498	0.0498
−140	0.1609	0.0980	0.0672	0.0480	0.0405	0.0383	0.0369	0.0368	0.0367	0.0365	0.0365
−120	0.1689	0.1063	0.0665	0.0442	0.0337	0.0293	0.0270	0.0263	0.0260	0.0260	0.0259
−100	0.2034	0.1269	0.0724	0.0471	0.0306	0.0230	0.0197	0.0184	0.0178	0.0177	0.0176
−80	0.2515	0.1516	0.0887	0.0539	0.0334	0.0215	0.0158	0.0124	0.0111	0.0105	0.0104
−70	0.2982	0.1682	0.1000	0.0608	0.0361	0.0238	0.0151	0.0103	0.0087	0.0081	0.0079
−60	0.3456	0.1995	0.1196	0.0742	0.0425	0.0267	0.0155	0.0103	0.0074	0.0062	0.0058
−50	0.5541	0.2358	0.1455	0.0871	0.0519	0.0307	0.0184	0.0118	0.0075	0.0050	0.0042
−40	0.7438	0.3145	0.1837	0.1136	0.0678	0.0394	0.0244	0.0137	0.0088	0.0051	0.0034
−30	1.4673	0.4637	0.2600	0.1490	0.0903	0.0523	0.0316	0.0189	0.0109	0.0068	0.0040
−20	1.3394	1.1911	0.5450	0.2419	0.1303	0.0872	0.0511	0.0306	0.0182	0.0104	0.0063
−10	1.1978	1.3993	1.3344	1.2555	0.3244	0.1841	0.1065	0.0646	0.0387	0.0230	0.0142
0	*NaN*	*NaN*	*NaN*	*NaN*	*NaN*	*NaN*	*NaN*	*NaN*	*NaN*	*NaN*	*NaN*
10	1.6752	1.1903	1.7418	0.6852	0.3044	0.1810	0.1100	0.0635	0.0392	0.0232	0.0136
20	1.7595	1.5217	0.4508	0.2412	0.1395	0.0831	0.0470	0.0301	0.0192	0.0104	0.0063
30	0.9588	0.4612	0.2517	0.1549	0.0934	0.0541	0.0317	0.0188	0.0116	0.0068	0.0041
40	0.6480	0.3464	0.1758	0.1088	0.0678	0.0411	0.0241	0.0141	0.0086	0.0053	0.0039
50	0.4380	0.2368	0.1428	0.0852	0.0528	0.0310	0.0184	0.0117	0.0077	0.0057	0.0049
60	0.3444	0.1998	0.1192	0.0699	0.0428	0.0258	0.0157	0.0108	0.0083	0.0070	0.0066
70	0.2965	0.1749	0.1040	0.0617	0.0381	0.0236	0.0156	0.0113	0.0096	0.0090	0.0087
80	0.2494	0.1531	0.0912	0.0529	0.0327	0.0213	0.0157	0.0129	0.0119	0.0113	0.0113
100	0.1961	0.1180	0.0734	0.0459	0.0302	0.0229	0.0197	0.0183	0.0177	0.0177	0.0177
120	0.1735	0.1048	0.0665	0.0441	0.0333	0.0289	0.0274	0.0265	0.0261	0.0261	0.0261
140	0.1585	0.0978	0.0656	0.0478	0.0408	0.0384	0.0371	0.0367	0.0365	0.0366	0.0366
160	0.1481	0.0980	0.0712	0.0576	0.0518	0.0506	0.0500	0.0497	0.0496	0.0496	0.0495
180	0.1439	0.1032	0.0797	0.0711	0.0667	0.0660	0.0659	0.0659	0.0656	0.0657	0.0657

G.3 Real and Imaginary Components with Different Frequencies

For the case where the real and imaginary components have different frequencies, the eigenvalue method is applied to the complex signal and its magnitude for zero-mean signals. The maximum likelihood method as well is assessed for the magnitude of a zero-mean complex signal. Table 24 shows the MSE due to the eigenvalue method using the second eigenvalue to estimate the energy pulses and it refers to Figure 52.

Table 24 – MSE of 20 experiments for the estimator λ_2 considering complex signals.

$(^{\circ})\downarrow$ $dB\rightarrow$	0	2	4	6	8	10	12	14	16	18	20
−180	0.2244	0.1924	0.1766	0.1714	0.1694	0.1689	0.1684	0.1684	0.1682	0.1682	0.1681
−160	0.2010	0.1630	0.1451	0.1389	0.1359	0.1348	0.1345	0.1342	0.1341	0.1341	0.1341
−140	0.1829	0.1323	0.1148	0.1042	0.1007	0.0996	0.0988	0.0986	0.0985	0.0985	0.0985
−120	0.1633	0.1118	0.0834	0.0680	0.0628	0.0604	0.0597	0.0592	0.0591	0.0590	0.0590
−100	0.1627	0.1015	0.0595	0.0384	0.0269	0.0211	0.0185	0.0177	0.0173	0.0172	0.0172
−80	0.1980	0.1219	0.0743	0.0445	0.0285	0.0190	0.0142	0.0120	0.0111	0.0107	0.0107
−70	0.2297	0.1403	0.0831	0.0507	0.0308	0.0192	0.0132	0.0098	0.0087	0.0083	0.0081
−60	0.2761	0.1578	0.0972	0.0606	0.0349	0.0222	0.0133	0.0091	0.0072	0.0062	0.0060
−50	0.3147	0.1969	0.1188	0.0691	0.0411	0.0249	0.0150	0.0097	0.0065	0.0047	0.0043
−40	0.4230	0.2453	0.1457	0.0913	0.0546	0.0324	0.0198	0.0112	0.0073	0.0044	0.0033
−30	0.4774	0.3320	0.2057	0.1219	0.0745	0.0446	0.0261	0.0156	0.0084	0.0055	0.0035
−20	0.5445	0.4741	0.3149	0.1933	0.1097	0.0690	0.0412	0.0254	0.0141	0.0078	0.0052
−10	0.5549	0.5581	0.5242	0.4050	0.2422	0.1527	0.0874	0.0537	0.0319	0.0181	0.0114
0	NaN	NaN	NaN	NaN	NaN	NaN	NaN	NaN	NaN	NaN	NaN
10	0.5551	0.5410	0.5373	0.3856	0.2422	0.1493	0.0859	0.0522	0.0312	0.0185	0.0112
20	0.5643	0.4372	0.3118	0.1979	0.1148	0.0688	0.0388	0.0255	0.0155	0.0083	0.0049
30	0.4902	0.3367	0.2066	0.1256	0.0754	0.0449	0.0262	0.0148	0.0093	0.0051	0.0033
40	0.3870	0.2434	0.1402	0.0889	0.0533	0.0319	0.0198	0.0116	0.0070	0.0044	0.0034
50	0.3204	0.1945	0.1184	0.0699	0.0422	0.0261	0.0153	0.0098	0.0065	0.0050	0.0045
60	0.2578	0.1600	0.0972	0.0580	0.0355	0.0210	0.0128	0.0094	0.0074	0.0064	0.0062
70	0.2284	0.1401	0.0838	0.0508	0.0306	0.0198	0.0137	0.0101	0.0089	0.0085	0.0083
80	0.1969	0.1260	0.0729	0.0435	0.0274	0.0180	0.0142	0.0121	0.0113	0.0110	0.0109
100	0.1612	0.0976	0.0614	0.0385	0.0261	0.0209	0.0186	0.0178	0.0174	0.0174	0.0174
120	0.1641	0.1144	0.0827	0.0688	0.0628	0.0607	0.0599	0.0594	0.0593	0.0593	0.0592
140	0.1883	0.1357	0.1131	0.1041	0.1008	0.0996	0.0989	0.0988	0.0987	0.0987	0.0987
160	0.2014	0.1620	0.1449	0.1381	0.1354	0.1348	0.1342	0.1342	0.1341	0.1342	0.1341
180	0.2247	0.1907	0.1769	0.1719	0.1691	0.1689	0.1684	0.1685	0.1683	0.1684	0.1684

Table 25 refers to Figure 53. The magnitude of complex signals are used as an input to the eigenvalue method and the second eigenvalue provides the pulse estimates.

Table 25 – MSE of 20 experiments for the estimator λ_2 considering the magnitude of complex signals.

$(^\circ)\downarrow$ $dB\rightarrow$	0	2	4	6	8	10	12	14	16	18	20
−180	0.3984	0.2878	0.2541	0.2418	0.2420	0.2407	0.2419	0.2424	0.2425	0.2428	0.2429
−160	0.3812	0.2695	0.2257	0.2190	0.2134	0.2158	0.2148	0.2158	0.2157	0.2162	0.2163
−140	0.3806	0.2541	0.2070	0.1889	0.1879	0.1865	0.1874	0.1876	0.1877	0.1881	0.1881
−120	0.3788	0.2459	0.1803	0.1573	0.1549	0.1550	0.1535	0.1545	0.1545	0.1549	0.1548
−100	0.4291	0.2377	0.1570	0.1277	0.1177	0.1150	0.1141	0.1144	0.1142	0.1143	0.1142
−80	0.4374	0.2561	0.1516	0.1075	0.0890	0.0812	0.0785	0.0777	0.0775	0.0777	0.0778
−70	0.5051	0.2674	0.1571	0.1027	0.0778	0.0683	0.0640	0.0633	0.0632	0.0631	0.0631
−60	0.4789	0.2953	0.1712	0.1046	0.0728	0.0578	0.0527	0.0507	0.0508	0.0502	0.0503
−50	0.5231	0.3269	0.1988	0.1137	0.0731	0.0509	0.0437	0.0406	0.0394	0.0387	0.0387
−40	0.5659	0.3939	0.2329	0.1380	0.0828	0.0519	0.0390	0.0325	0.0300	0.0289	0.0288
−30	0.5362	0.4781	0.3016	0.1688	0.1014	0.0636	0.0412	0.0279	0.0225	0.0210	0.0204
−20	0.5806	0.5322	0.4475	0.2613	0.1462	0.0866	0.0534	0.0331	0.0216	0.0161	0.0137
−10	0.5580	0.5816	0.5356	0.4991	0.3189	0.1830	0.1050	0.0668	0.0384	0.0237	0.0154
0	NaN	NaN	NaN	NaN	NaN	NaN	NaN	NaN	NaN	NaN	NaN
10	0.5743	0.5691	0.5304	0.4850	0.3071	0.1809	0.1062	0.0640	0.0390	0.0235	0.0150
20	0.5508	0.5346	0.4261	0.2585	0.1516	0.0896	0.0511	0.0341	0.0220	0.0160	0.0136
30	0.5795	0.4819	0.3031	0.1713	0.1015	0.0611	0.0389	0.0285	0.0232	0.0208	0.0203
40	0.5587	0.4028	0.2283	0.1352	0.0821	0.0520	0.0379	0.0328	0.0298	0.0290	0.0290
50	0.5153	0.3226	0.2005	0.1140	0.0735	0.0529	0.0443	0.0408	0.0390	0.0387	0.0389
60	0.4798	0.2916	0.1705	0.1054	0.0734	0.0575	0.0530	0.0509	0.0506	0.0503	0.0503
70	0.5004	0.2725	0.1537	0.1011	0.0761	0.0678	0.0643	0.0639	0.0632	0.0632	0.0631
80	0.4087	0.2577	0.1529	0.1056	0.0858	0.0809	0.0776	0.0779	0.0779	0.0777	0.0779
100	0.4010	0.2419	0.1540	0.1282	0.1169	0.1153	0.1142	0.1148	0.1140	0.1144	0.1144
120	0.3895	0.2437	0.1806	0.1587	0.1536	0.1551	0.1546	0.1543	0.1549	0.1548	0.1549
140	0.4097	0.2535	0.2066	0.1870	0.1870	0.1870	0.1872	0.1881	0.1879	0.1882	0.1882
160	0.3876	0.2747	0.2303	0.2143	0.2145	0.2151	0.2152	0.2163	0.2163	0.2165	0.2164
180	0.4075	0.2912	0.2495	0.2426	0.2415	0.2407	0.2417	0.2423	0.2428	0.2431	0.2430

Table 26 presents the MSE in case of ML method is used over the magnitude of a zero-mean complex signal as presented in Figure 54.

Table 26 – MSE of 20 experiments for the ML estimator considering the magnitude of the complex signal.

$(^\circ)\downarrow$ $dB\rightarrow$	0	2	4	6	8	10	12	14	16	18	20
−180	0.3387	0.3303	0.3370	0.3255	0.3199	0.3419	0.3361	0.3697	0.3476	0.3361	0.3528
−160	0.3430	0.3160	0.3260	0.3180	0.3235	0.3488	0.3239	0.3351	0.3472	0.3175	0.3236
−140	0.2886	0.2867	0.2854	0.2800	0.2825	0.2809	0.2809	0.2808	0.2810	0.2810	0.2809
−120	0.3114	0.3070	0.3078	0.3040	0.3053	0.3041	0.3045	0.3044	0.3045	0.3045	0.3045
−100	0.3396	0.3344	0.3256	0.3264	0.3245	0.3243	0.3249	0.3243	0.3244	0.3243	0.3244
−80	0.3444	0.3317	0.3270	0.3255	0.3250	0.3239	0.3230	0.3236	0.3232	0.3237	0.3231
−70	0.3059	0.3055	0.3037	0.2991	0.2954	0.2945	0.2947	0.2948	0.2939	0.2940	0.2939
−60	0.2693	0.2372	0.2072	0.1879	0.1990	0.1934	0.1906	0.1937	0.1930	0.1936	0.1936
−50	0.1823	0.1035	0.0458	0.0286	0.0187	0.0155	0.0097	0.0088	0.0085	0.0080	0.0078
−40	0.1824	0.0909	0.0597	0.0333	0.0218	0.0141	0.0097	0.0077	0.0059	0.0062	0.0058
−30	0.2336	0.1278	0.0738	0.0495	0.0305	0.0194	0.0109	0.0080	0.0057	0.0046	0.0041
−20	0.3217	0.1821	0.1087	0.0668	0.0431	0.0268	0.0171	0.0099	0.0077	0.0047	0.0036
−10	0.4200	0.2831	0.1968	0.1335	0.0852	0.0520	0.0360	0.0225	0.0127	0.0085	0.0056
0	NaN	NaN	NaN	NaN	NaN	NaN	NaN	NaN	NaN	NaN	NaN
10	0.3008	0.2525	0.1938	0.1139	0.0849	0.0583	0.0342	0.0228	0.0128	0.0090	0.0057
20	0.3491	0.1721	0.1107	0.0700	0.0454	0.0260	0.0175	0.0105	0.0068	0.0044	0.0037
30	0.1950	0.1289	0.0753	0.0427	0.0302	0.0190	0.0117	0.0076	0.0060	0.0045	0.0043
40	0.1660	0.1064	0.0600	0.0350	0.0226	0.0143	0.0109	0.0079	0.0066	0.0059	0.0055
50	0.1551	0.1004	0.0484	0.0282	0.0186	0.0129	0.0094	0.0086	0.0084	0.0081	0.0076
60	0.2687	0.2098	0.2171	0.1946	0.1997	0.1979	0.1935	0.1920	0.1933	0.1946	0.1944
70	0.3487	0.3052	0.2975	0.2927	0.2943	0.2953	0.2933	0.2941	0.2942	0.2943	0.2944
80	0.3279	0.3373	0.3302	0.3240	0.3235	0.3245	0.3233	0.3233	0.3235	0.3230	0.3231
100	0.3303	0.3286	0.3212	0.3253	0.3240	0.3233	0.3245	0.3244	0.3243	0.3244	0.3246
120	0.3143	0.3090	0.3078	0.3037	0.3048	0.3037	0.3046	0.3042	0.3046	0.3044	0.3046
140	0.2809	0.2848	0.2820	0.2826	0.2810	0.2807	0.2809	0.2808	0.2810	0.2811	0.2810
160	0.3172	0.3489	0.3439	0.3220	0.3224	0.3000	0.3403	0.3353	0.3177	0.2940	0.3237
180	0.3315	0.3462	0.3389	0.3374	0.3077	0.3257	0.3476	0.3591	0.3481	0.3421	0.3588

G.4 Reference and Transmitted Complex Signals with Different Phases

For different initial phases the eigenvalue method provides estimates through both eigenvalues. The ML method is equivalent to the observed in section G.3. The MSE for λ_1 over zero-mean complex signals is presented in Table 27 and it refers to Figure 56.

Table 27 – MSE of 20 experiments for the eigenvalue method using λ_1 considering zero-mean complex signals.

$(^\circ)\downarrow$ $dB\rightarrow$	0	2	4	6	8	10	12	14	16	18	20
−180	0.1931	0.1999	0.2115	0.2141	0.2181	0.2184	0.2206	0.2210	0.2214	0.2215	0.2216
−160	0.1682	0.1681	0.1815	0.1846	0.1866	0.1895	0.1899	0.1912	0.1917	0.1917	0.1918
−140	0.1268	0.1369	0.1488	0.1549	0.1569	0.1587	0.1607	0.1609	0.1614	0.1615	0.1617
−120	0.0960	0.1148	0.1154	0.1185	0.1225	0.1238	0.1258	0.1262	0.1264	0.1268	0.1269
−100	0.0859	0.0784	0.0773	0.0793	0.0827	0.0824	0.0830	0.0834	0.0840	0.0843	0.0843
−80	0.0727	0.0535	0.0459	0.0452	0.0463	0.0466	0.0472	0.0475	0.0481	0.0482	0.0482
−70	0.0810	0.0515	0.0403	0.0328	0.0338	0.0344	0.0343	0.0346	0.0350	0.0352	0.0352
−60	0.0927	0.0558	0.0348	0.0297	0.0237	0.0250	0.0243	0.0242	0.0247	0.0249	0.0250
−50	0.1097	0.0600	0.0366	0.0245	0.0183	0.0167	0.0169	0.0162	0.0163	0.0167	0.0168
−40	0.1285	0.0755	0.0465	0.0274	0.0188	0.0142	0.0103	0.0106	0.0104	0.0102	0.0105
−30	0.1601	0.0929	0.0585	0.0356	0.0225	0.0143	0.0097	0.0071	0.0064	0.0056	0.0057
−20	0.2546	0.1373	0.0848	0.0494	0.0352	0.0220	0.0130	0.0083	0.0056	0.0036	0.0030
−10	0.3617	0.2740	0.1601	0.1020	0.0644	0.0410	0.0253	0.0175	0.0103	0.0069	0.0041
0	NaN	NaN	NaN	NaN	NaN	NaN	NaN	NaN	NaN	NaN	NaN
10	0.3595	0.2609	0.1611	0.0998	0.0626	0.0416	0.0270	0.0170	0.0109	0.0066	0.0043
20	0.2326	0.1335	0.0832	0.0513	0.0320	0.0211	0.0138	0.0086	0.0056	0.0038	0.0031
30	0.1572	0.0903	0.0553	0.0357	0.0223	0.0143	0.0101	0.0077	0.0063	0.0056	0.0056
40	0.1281	0.0758	0.0431	0.0274	0.0194	0.0134	0.0113	0.0108	0.0101	0.0104	0.0105
50	0.1126	0.0644	0.0362	0.0230	0.0178	0.0165	0.0170	0.0168	0.0166	0.0167	0.0170
60	0.0924	0.0565	0.0349	0.0279	0.0244	0.0232	0.0245	0.0251	0.0252	0.0251	0.0253
70	0.0857	0.0504	0.0415	0.0346	0.0329	0.0353	0.0342	0.0350	0.0352	0.0354	0.0354
80	0.0759	0.0539	0.0467	0.0462	0.0464	0.0467	0.0471	0.0480	0.0479	0.0482	0.0483
100	0.0844	0.0709	0.0761	0.0791	0.0813	0.0821	0.0826	0.0830	0.0834	0.0835	0.0837
120	0.1038	0.1059	0.1142	0.1232	0.1212	0.1241	0.1246	0.1255	0.1260	0.1259	0.1262
140	0.1325	0.1385	0.1476	0.1545	0.1558	0.1590	0.1597	0.1605	0.1606	0.1607	0.1609
160	0.1638	0.1650	0.1818	0.1830	0.1869	0.1890	0.1897	0.1906	0.1907	0.1910	0.1911
180	0.1916	0.2026	0.2080	0.2143	0.2172	0.2192	0.2199	0.2203	0.2205	0.2209	0.2209

The MSE for estimates obtained by λ_2 applied to zero-mean complex signals is presented in Table 28 and it refers to Figure 57.

Table 28 – MSE of 20 experiments for the eigenvalue method using λ_2 considering zero-mean complex signals.

$dB\rightarrow$ (°)↓	0	2	4	6	8	10	12	14	16	18	20
−180	0.2118	0.2127	0.2196	0.2197	0.2203	0.2213	0.2217	0.2221	0.2222	0.2223	0.2223
−160	0.1786	0.1825	0.1877	0.1899	0.1911	0.1915	0.1919	0.1922	0.1924	0.1925	0.1926
−140	0.1441	0.1549	0.1581	0.1599	0.1603	0.1613	0.1616	0.1621	0.1622	0.1624	0.1625
−120	0.1201	0.1177	0.1213	0.1245	0.1256	0.1261	0.1270	0.1271	0.1275	0.1276	0.1276
−100	0.0826	0.0806	0.0826	0.0818	0.0830	0.0837	0.0841	0.0843	0.0847	0.0848	0.0849
−80	0.0756	0.0539	0.0470	0.0470	0.0471	0.0476	0.0475	0.0482	0.0483	0.0483	0.0485
−70	0.0782	0.0478	0.0381	0.0349	0.0339	0.0344	0.0348	0.0351	0.0352	0.0354	0.0355
−60	0.0832	0.0471	0.0348	0.0264	0.0248	0.0244	0.0243	0.0245	0.0249	0.0250	0.0251
−50	0.0967	0.0560	0.0343	0.0235	0.0180	0.0160	0.0162	0.0161	0.0165	0.0166	0.0167
−40	0.1160	0.0694	0.0409	0.0251	0.0169	0.0122	0.0107	0.0101	0.0101	0.0100	0.0103
−30	0.1516	0.0846	0.0532	0.0327	0.0212	0.0136	0.0091	0.0068	0.0058	0.0058	0.0055
−20	0.2436	0.1287	0.0770	0.0500	0.0303	0.0189	0.0129	0.0084	0.0055	0.0036	0.0029
−10	0.3572	0.2517	0.1536	0.1011	0.0593	0.0398	0.0258	0.0169	0.0103	0.0064	0.0042
0	*NaN*	*NaN*	*NaN*	*NaN*	*NaN*	*NaN*	*NaN*	*NaN*	*NaN*	*NaN*	*NaN*
10	0.3814	0.2708	0.1600	0.0974	0.0655	0.0383	0.0251	0.0166	0.0107	0.0066	0.0043
20	0.2409	0.1268	0.0839	0.0488	0.0314	0.0194	0.0123	0.0083	0.0053	0.0038	0.0030
30	0.1529	0.0915	0.0538	0.0330	0.0203	0.0131	0.0099	0.0075	0.0064	0.0058	0.0058
40	0.1158	0.0643	0.0412	0.0245	0.0171	0.0129	0.0110	0.0102	0.0101	0.0104	0.0105
50	0.1014	0.0531	0.0329	0.0223	0.0187	0.0165	0.0159	0.0164	0.0166	0.0168	0.0169
60	0.0827	0.0496	0.0321	0.0266	0.0258	0.0243	0.0244	0.0248	0.0250	0.0251	0.0252
70	0.0765	0.0486	0.0369	0.0346	0.0339	0.0342	0.0349	0.0351	0.0353	0.0355	0.0356
80	0.0719	0.0541	0.0472	0.0459	0.0469	0.0474	0.0476	0.0481	0.0483	0.0485	0.0486
100	0.0904	0.0796	0.0817	0.0830	0.0828	0.0836	0.0839	0.0844	0.0847	0.0848	0.0849
120	0.1199	0.1205	0.1227	0.1246	0.1262	0.1265	0.1267	0.1271	0.1275	0.1275	0.1276
140	0.1530	0.1551	0.1587	0.1594	0.1608	0.1609	0.1615	0.1620	0.1623	0.1623	0.1624
160	0.1743	0.1866	0.1894	0.1905	0.1907	0.1913	0.1920	0.1923	0.1924	0.1925	0.1926
180	0.2107	0.2144	0.2171	0.2200	0.2211	0.2214	0.2218	0.2220	0.2222	0.2223	0.2224

The MSE for estimates obtained by λ_1 applied to the magnitude of non-zero-mean complex signals is presented in Table 29 and it refers to Figure 58.

Table 29 – MSE of 20 experiments for the eigenvalue method using λ_1 considering the magnitude of non-zero-mean complex signals.

$(^\circ)\downarrow$ $dB\rightarrow$	0	2	4	6	8	10	12	14	16	18	20
-180	0.2051	0.2000	0.2117	0.2162	0.2183	0.2199	0.2199	0.2206	0.2209	0.2213	0.2213
-160	0.1766	0.1749	0.1846	0.1860	0.1886	0.1889	0.1909	0.1912	0.1913	0.1915	0.1916
-140	0.1453	0.1518	0.1486	0.1571	0.1581	0.1595	0.1614	0.1608	0.1613	0.1612	0.1615
-120	0.1152	0.1140	0.1212	0.1207	0.1252	0.1256	0.1263	0.1263	0.1266	0.1269	0.1268
-100	0.1106	0.0962	0.0813	0.0853	0.0841	0.0847	0.0844	0.0842	0.0844	0.0845	0.0846
-80	0.1092	0.0743	0.0592	0.0507	0.0517	0.0499	0.0493	0.0485	0.0486	0.0485	0.0484
-70	0.1069	0.0683	0.0544	0.0417	0.0363	0.0363	0.0354	0.0359	0.0358	0.0357	0.0355
-60	0.1199	0.0733	0.0504	0.0367	0.0317	0.0287	0.0254	0.0257	0.0254	0.0254	0.0251
-50	0.1411	0.0850	0.0553	0.0364	0.0237	0.0204	0.0189	0.0178	0.0175	0.0171	0.0171
-40	0.1529	0.0967	0.0598	0.0390	0.0260	0.0199	0.0143	0.0119	0.0112	0.0108	0.0106
-30	0.2105	0.1310	0.0739	0.0467	0.0322	0.0204	0.0128	0.0097	0.0074	0.0067	0.0063
-20	0.2977	0.1643	0.1109	0.0714	0.0477	0.0281	0.0187	0.0119	0.0078	0.0047	0.0037
-10	0.3849	0.2889	0.1935	0.1257	0.0870	0.0548	0.0349	0.0220	0.0132	0.0089	0.0053
0	NaN	NaN	NaN	NaN	NaN	NaN	NaN	NaN	NaN	NaN	NaN
10	0.3827	0.2984	0.1884	0.1295	0.0833	0.0520	0.0330	0.0208	0.0131	0.0085	0.0055
20	0.2632	0.1722	0.1090	0.0672	0.0428	0.0269	0.0168	0.0108	0.0067	0.0045	0.0031
30	0.1961	0.1132	0.0748	0.0444	0.0275	0.0186	0.0121	0.0080	0.0063	0.0052	0.0051
40	0.1471	0.0933	0.0559	0.0354	0.0233	0.0159	0.0122	0.0110	0.0098	0.0096	0.0094
50	0.1316	0.0730	0.0488	0.0304	0.0239	0.0200	0.0167	0.0159	0.0157	0.0156	0.0155
60	0.1212	0.0687	0.0458	0.0331	0.0277	0.0248	0.0244	0.0240	0.0238	0.0237	0.0236
70	0.1101	0.0648	0.0502	0.0405	0.0367	0.0351	0.0344	0.0342	0.0341	0.0340	0.0340
80	0.1067	0.0720	0.0565	0.0513	0.0485	0.0477	0.0471	0.0470	0.0471	0.0470	0.0470
100	0.1098	0.0956	0.0865	0.0862	0.0841	0.0837	0.0838	0.0839	0.0837	0.0838	0.0838
120	0.1385	0.1298	0.1284	0.1265	0.1270	0.1269	0.1268	0.1268	0.1266	0.1266	0.1266
140	0.1713	0.1604	0.1619	0.1622	0.1617	0.1617	0.1617	0.1615	0.1616	0.1615	0.1615
160	0.1930	0.1929	0.1915	0.1924	0.1923	0.1922	0.1917	0.1918	0.1918	0.1917	0.1917
180	0.2116	0.2224	0.2210	0.2221	0.2221	0.2220	0.2218	0.2216	0.2215	0.2216	0.2216

The MSE for estimates obtained by λ_2 applied to the magnitude of non-zero-mean complex signals is presented in Table 30 and it refers to Figure 59.

Table 30 – MSE of 20 experiments for the eigenvalue method using λ_2 considering the magnitude of non-zero-mean complex signals.

dB→ (°)↓	0	2	4	6	8	10	12	14	16	18	20
−180	0.2202	0.2236	0.2232	0.2237	0.2232	0.2232	0.2232	0.2234	0.2233	0.2234	0.2233
−160	0.1955	0.1927	0.1925	0.1928	0.1940	0.1937	0.1934	0.1937	0.1937	0.1937	0.1937
−140	0.1663	0.1618	0.1637	0.1638	0.1638	0.1639	0.1635	0.1636	0.1636	0.1636	0.1636
−120	0.1449	0.1306	0.1301	0.1300	0.1293	0.1290	0.1289	0.1290	0.1289	0.1290	0.1289
−100	0.1170	0.0953	0.0869	0.0871	0.0867	0.0862	0.0865	0.0863	0.0863	0.0862	0.0862
−80	0.1039	0.0735	0.0587	0.0534	0.0506	0.0502	0.0498	0.0495	0.0494	0.0492	0.0494
−70	0.1077	0.0718	0.0499	0.0420	0.0381	0.0366	0.0365	0.0364	0.0362	0.0362	0.0361
−60	0.1228	0.0705	0.0458	0.0365	0.0282	0.0277	0.0260	0.0257	0.0256	0.0256	0.0258
−50	0.1266	0.0782	0.0472	0.0317	0.0257	0.0209	0.0188	0.0178	0.0173	0.0172	0.0172
−40	0.1613	0.0907	0.0557	0.0356	0.0233	0.0172	0.0134	0.0118	0.0112	0.0108	0.0106
−30	0.1942	0.1170	0.0729	0.0418	0.0277	0.0187	0.0123	0.0089	0.0069	0.0063	0.0061
−20	0.2723	0.1752	0.1031	0.0683	0.0403	0.0263	0.0155	0.0101	0.0067	0.0048	0.0036
−10	0.3615	0.2978	0.2014	0.1233	0.0807	0.0522	0.0340	0.0209	0.0129	0.0087	0.0053
0	NaN	NaN	NaN	NaN	NaN	NaN	NaN	NaN	NaN	NaN	NaN
10	0.3501	0.2543	0.1973	0.1310	0.0799	0.0532	0.0313	0.0212	0.0140	0.0087	0.0052
20	0.2553	0.1669	0.1028	0.0681	0.0443	0.0265	0.0166	0.0113	0.0070	0.0046	0.0032
30	0.1949	0.1176	0.0734	0.0480	0.0282	0.0197	0.0126	0.0089	0.0068	0.0052	0.0052
40	0.1637	0.1011	0.0614	0.0381	0.0238	0.0181	0.0128	0.0102	0.0098	0.0096	0.0094
50	0.1368	0.0798	0.0524	0.0324	0.0235	0.0202	0.0179	0.0169	0.0155	0.0156	0.0156
60	0.1253	0.0745	0.0481	0.0389	0.0296	0.0253	0.0243	0.0245	0.0238	0.0236	0.0235
70	0.1055	0.0712	0.0471	0.0382	0.0367	0.0337	0.0329	0.0342	0.0337	0.0338	0.0337
80	0.0999	0.0696	0.0581	0.0485	0.0472	0.0471	0.0470	0.0459	0.0461	0.0465	0.0463
100	0.1095	0.0875	0.0800	0.0800	0.0816	0.0820	0.0814	0.0813	0.0817	0.0816	0.0815
120	0.1172	0.1121	0.1127	0.1160	0.1224	0.1226	0.1231	0.1238	0.1235	0.1240	0.1241
140	0.1523	0.1421	0.1476	0.1520	0.1568	0.1585	0.1580	0.1583	0.1587	0.1587	0.1589
160	0.1684	0.1710	0.1767	0.1820	0.1886	0.1872	0.1882	0.1894	0.1893	0.1888	0.1891
180	0.1996	0.1995	0.2102	0.2144	0.2150	0.2182	0.2190	0.2186	0.2189	0.2190	0.2192